INAUGURAL - DISSERTATION

submitted to the

Combined Faculties for the Natural Sciences and for Mathematics

of the Ruperto-Carola University of Heidelberg, Germany

for the degree of

Doctor of Natural Sciences

Put forward by

M.Sc. Charlotte Christiane Debus

Born in: Frankfurt am Main, Germany

Oral examination: July 12th, 2016

Integrative multimodal image analysis using physical models for characterization of brain tumors in radiotherapy

Referees: Prof. Dr. Dr. Jürgen Debus
Prof. Dr. João Seco

Integrative multimodal image analysis using physical models for characterization of brain tumors in radiotherapy

Therapy failure with subsequent tumor progress is a common problem in radiotherapy of high grade glioma. Definition of treatment volumes with CT and MRI is limited due to uncertainties concerning tumor outlines. The goal of the presented work was to enable assessment of tumor physiology and prediction of progression patterns using multi-modal image analysis and thus, improve target delineation. Physiological imaging modalities, such as ^{18}F-FET PET, diffusion and perfusion MRI were used to predict recurrence patterns. The Medical Imaging Interaction ToolKit together with own software implementation enabled side-by-side evaluation of all image modalities. These included tools for PET analysis and a module for voxel wise fitting of dynamic data with pharmacokinetic models. Robustness and accuracy of parameter estimates were studied on synthetic perfusion data. Parameter feasibility for progression prediction was investigated on DCE MRI and ^{18}F-FET PET data. Using the developed software tools, a pipeline for prediction of tumor progression patterns based on multi-modal image classification with a random forest machine learning algorithm was established. Exemplary prediction analysis was applied on a small patient set for illustration of workflow functionality and classification results.

Integrative multimodale Bildgebungsanalyse mit physikalischen Modellen zur Charakterisierung von Hirntumoren in der Strahlentherapie

Fortschreitendes Tumorwachstum aufgrund von Therapieversagen ist ein häufiges Problem bei der Bestrahlung von hochgradigen Gliomen. Die Definition der Bestrahlungsvolumina mithilfe der Bildgebungsverfahren CT und MRT ist aufgrund von Unsicherheiten über die Tumorbegrenzung limitiert. Ziel der vorgestellten Arbeit war es, Messmethoden der Tumorphysiologie zu untersuchen und die Progression der Tumore durch multimodale Bildanalysen vorherzusagen, um die Zielvolumendefinition zu verbessern. Physiologische Bildgebungsmodalitäten, wie ^{18}F-FET PET, Diffusions- und Perfusions-MRT, wurden zur Vorhersage von Rekurrenzmustern verwendet. Das Medical Imaging Interaction ToolKit wurde mit eigenen Implementierungen erweitert, um eine gleichzeitige Auswertung aller relevanten Bilder zu ermöglichen. Dabei wurde Software zur Auswertung von PET-Bildern, sowie ein Modul für voxelbasiertes Fitten von dynamischen Daten mit pharmakokinetischen Modellen entwickelt. Robustheit und Genauigkeit der pharmakokinetischen Modellierung in der Perfusions-MRT wurde an synthetischen Daten untersucht. Studien zu Nutzung von Parametern aus Perfusions-MRT und ^{18}F-FET PET wurden zur Vorhersage von Progressionsmustern durchgeführt. Mithilfe der entwickelten Software wurde eine Pipeline zur Vorhersage von Tumorwachstumsmustern implementiert, die auf Klassifikation mittels maschinellen Lernens durch Random Forest Algorithmen basiert. Eine exemplarische Analyse wurde anhand eines kleinen Patientenkollektivs durchgeführt, um Funktionalität und Ergebnisse der Auswerteroutine zu illustrieren.

Contents

Abbreviations

ADC	Apparent Diffusion Coefficient
AIF	Arterial Input Function
AUC	Area Under the Curve
AUMC	Area Under the first Moment Curve
CA	Contrast Agent
CBF	Cerebral Blood Flow
CBV	Cerebral Blood Volume
CNR	Contrast-to-Noise Ratio
CT	Computed Tomography
DCE	Dynamic Contrast Enhanced
DSC	Dynamic Susceptibility Contrast
DWI	Diffusion Weighted Imaging
EES	Extracellular Extravascular Space
eTM	extended Tofts Model
FA	Fractionated Anisotropy
FID	Free Induction Decay
FLAIR	FLuid Attenuated Inversion Recovery
FLASH	Fast Low Angle SHot
GUI	Graphical User Interface
MITK	Medical Imaging Interaction Toolkit
MPRAGE	Magnetization Prepared RApid Gradient Echo
MRI	Magnetic Resonance Imaging
MRT	Mean Residence Time
MTT	Mean Transit Time
NLLS	Non-Linear Least Squares
NMR	Nuclear Magnetic Resonance
PET	Positron Emission Tomography

RF	RadioFrequency
SPECT	Single Photon Emission Computed Tomography
SUV	Standardized Uptake Value
TE	Echo Time
TI	Inversion Time
TR	Repetition Time
TUR	Tumor-specific Uptake Ratio
VIBE	Volumetric Interpolated Breath-hold Examination

^{18}**F-FET**	O-(2-[^{18}F]fluoroethyl)-l-tyrosine
^{18}**F-FDG**	[^{18}F]-fluoro-2-deoxy-D-glucose
2CXM	Two Compartment Exchange Model
1TCM	One Tissue Compartment Model
2TCM	Two Tissue Compartment Model

1 Introduction

Therapy failure with subsequent tumor progress is one of the most common problems in radiotherapy of patients diagnosed with high grade glioma. These tumors present with rapid growth and strong infiltration of the surrounding healthy brain tissue, making them difficult to address with surgery. Radiotherapy in combination with chemotherapy has been established as standard treatment procedure. However, median survival remains poor, as treatment planning of radiotherapy is confronted with a number of challenges. One major hurdle is the definition of tumor outlines due to micro-invasions into the surrounding healthy tissue. Magnetic resonance imaging (MRI) provides good soft tissue contrast. Furthermore, the break-down of the blood-brain-barrier, commonly observed in high grade glioma, induces leakage and hence, accumulation of the contrast agent in the interstitial volume, causing bright image contrast of the lesion. Therefore, standard target definition in radiotherapy is based on contrast enhanced T_1 weighted MRI together with a planning computed tomographic (CT) image. Microscopic outliers of the tumor, however, are difficult to assess with these modalities. The possibly resulting underdosage of brain tissue at risk poses the danger of progression, which leads to recurrence of the tumor. Furthermore, tumor heterogeneity presents with additional challenges, as different parts of the lesion require different radiation doses. Hypoxic conditions, for example, decrease the tissues sensitivity to radiation and thus higher doses need to be applied in order to induce cell death.

The aim of the presented thesis was to somehow "visualize" and assess the physiology of malignant and healthy brain tissue, in particular the tumor heterogeneity, for identification of potentially malignant tissue and estimation of the recurrence probability. Gained information could be used as prediction of the physiological tumor extent and could thus improve radiotherapy target delineation and inhibit progress formation.

Recent developments in the field of radiologic imaging have given rise to metabolic, (molecular-) biological and functional imaging modalities, which enable more detailed assessment of the tissue physiology in the brain rather than just anatomical structures. Due to increased amino acid transport, probably originating from enhanced protein synthesis, amino acid tracers, such as [^{18}F]-fluoro-ethyl-tyrosin (^{18}F-FET), have shown accumulation in brain tumors in positron emission tomography (PET) imaging. Thus, they provide a good opportunity to identify metabolically active tumor tissue with high sensitivity and specificity. Assessment of hemodynamic parameters, such as cerebral blood flow and cerebral blood volume, with dynamic contrast enhanced MRI (DCE MRI) provides interesting measurement parameters in various pathologies in the brain as they enable quantification of tissue micro-circulation and micro-vascularization. Diffusion MRI has been established as a useful diagnostic tool in various brain diseases, including stroke and hemorrhages, and is frequently consulted in neuro-oncology.

However, until now, these imaging options have been considered and investigated individually, and mostly with respect to their concordance with standard techniques. The goal of the presented work was not to replace information acquired with standard images but to draw additional information from these physiological modalities and to evaluate them with respect to tumor progression patterns. Furthermore, information from different modalities was not considered individually but as an entity.

The ultimate goal would be to combine the different parameters to a functional relation giving the probability of a tissue element to become malignant. It is obvious, that such a relation is difficult to "find by hand", as tumors and patients present with strong heterogeneity and large variation in the parameter characteristics. A good example for this inter-patient variability is the standard uptake value, derived from PET images. It is difficult to define fixed value thresholds for definition of pathological uptake, since the degree of tracer uptake varies greatly between patients.

A solution to the above described problem could be found by using machine learning approaches for pattern recognition. The classification algorithms present with the opportunity to evaluate large data sets with the aim to find empirical classification rules amongst multiple patients and parameters. Thus, they are good candidates for the task at hand of finding multi-modal multi-parametric models for tumor progression predictions. The presented work aimed to develop a workflow, which enables the use of available image data for prediction of tumor progression growth by using classification algorithms to determine pixels of tissue at risk of becoming tumor.

During the course of this thesis, a workflow for such a multi-modal, multi-parametric image analysis for tumor progression prediction was established. Focus was laid especially on parameters derived from dynamic contrast enhanced perfusion MRI and ^{18}F-FET PET. The software implementations, required to enable side by side evaluation and preprocessing of all imaging modalities, are presented. Several feasibility studies of DCE MRI and ^{18}F-FET PET data were done, in order to quantify the ability of the resulting parameters for aiding the cause of tissue classification and to determine the extent of their validity.

The chapter **Theory** briefly reviews advances and challenges in treatment of glioma, and the fundamental physical principles, up on which radiological imaging (CT, MRI and PET) and radiotherapy are based. In **Methods** the different imaging techniques and analysis approaches used in this thesis are introduced, with special focus on the surrogate values of parameters derived from them. Furthermore, software concepts of image processing methods relevant to this work are discussed. In the chapter **Results**, methodological developments and their applications are presented. Results from several studies on DCE MRI and ^{18}F-FET PET data are shown. This chapter concludes with an exemplary presentation of the developed workflow for multimodal image classification. All developments and study findings, their validity, advantages and drawbacks as well as improvements and an outlook to further research are reviewed in chapter **Discussion**.

2 Theory

The following chapter introduces the basic physical concepts relevant to this work. Sections 2.1 and 2.2 start with a general overview over the disease of cancer and the special challenges posed by high grade glioma. Radiotherapy as well as several modalities of radiological imaging are based on the fundamental principles describing interaction of ionizing radiation with matter. Images acquired with computed tomography (CT) derive from the interactions of photons with matter. Nuclear medicine in general uses radioactive materials for both diagnostic and therapeutic applications, and positron emission tomography (PET) in particular acquires images by detection of annihilation photons from tissue interactions with β^+ isotopes. Radiotherapy uses the biological effects of particle interactions with the patient body in order to kill cells. Conventional radiotherapy uses photon beams, were as in particle therapy patients are irradiated with ions, i.e. charged particles. Therefore, the physical theory of radiation and its interaction with matter is discussed in detail in section 2.3. The concept of dose and the biological effects of radiation are briefly introduced as they play a role in both radiology and radiooncology. Magnetic resonance imaging (MRI) derives from the interaction of particle spins with external magnetic fields and the phenomenon of nuclear magnetic resonance. Hence, the theoretical basics thereof are described in section 2.4. Finally, section 2.5 reviews the basic concepts of radiotherapy and current standard target delineation.

2.1 Cancer

With over 14 million incidences and 8.2 million related deaths worldwide, cancer is among the leading causes of death in modern society [*WHO Cancer Fact Sheet N° 297*, 2015]. In Germany, 500 thousand new cases and a mortality of 224 thousand cases were reported in 2015 [*Deutsche Krebshilfe*, 2016]. In general, cancer is an umbrella term for disease including the formation of malignant neoplasms, which can originate from any part of the body. The formation of such tumors is due to unregulated, abnormal cell growth and proliferation, forming a bulky tissue mass. Their malignancy is defined by rapid growth, infiltration of surrounding healthy tissue and the ability to spread through the body and form distant secondary tumor sites, so-called metastasis.

Cancer formation has been related to genetics and increasing age as well as environmental factors such as diet, smoking, infections and radiation damage. However the true cause of individual diseases is a complex interplay between many factors and cannot always be identified. For male patients, the most frequent tumor entities are lung, prostate and colorectal carcinoma (see figure 2.1). In women the primary site of cancer is the breast, followed by colorectum, lung and cervix [*Deutsche Krebshilfe*, 2016]. The three major treatment options for malignant tumors include surgery, chemotherapy and radiation

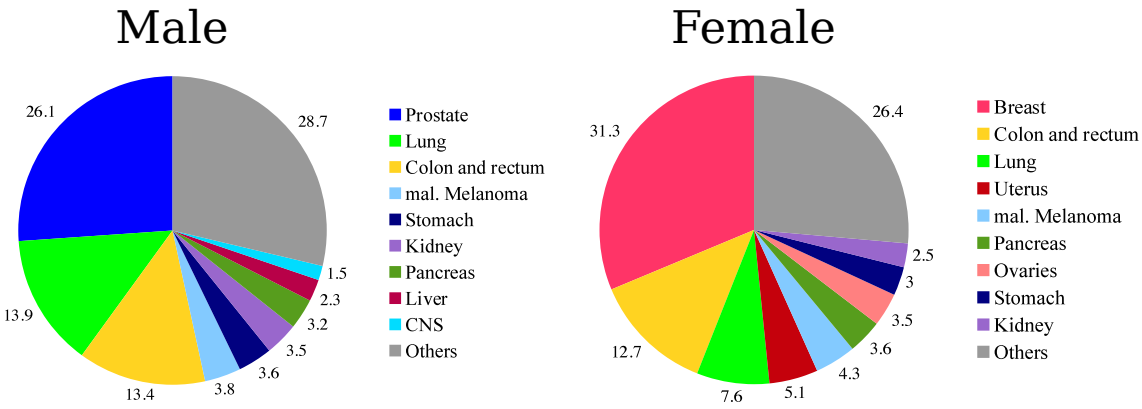

Figure 2.1: Cancer incidence rates in 2010 in Germany for men and women [*DKFZ Atlas of Cancer Mortality*, 2010].

therapy. Chemotherapy makes use of cytotoxic chemical substances that target rapidly growing cells. Radiotherapy uses the biological effects of ionizing radiation to induce localized cell death.

2.2 Glioma

Glioma is a tumor entity deriving from the supportive tissue of the brain, namely the glia cells. Depending on the concrete cell of origin, one can distinguish between various subtypes. The WHO[1] classifies them based on histological characteristics into *low grade* (I and II) and *high grade* (III and IV) glioma. Grading is associated with patient prognosis and survival.

Low grade gliomas are considered benign brain tumors with good prognosis, as they are well-differentiated and grow slowly. High grade glioma, including glioblastoma (grade IV), exhibit rapid tumor growth. Glioblastoma are the most frequent and aggressive form of primary brain tumors in adults, with poor median overall survival. They are divided into primary (de novo) tumors and secondary tumors, which develop gradually from low grade glioma. Due to their location and diffuse infiltration patterns in surrounding normal brain tissue, high grade glioma constitute augmented therapeutic challenges. With surgery alone, overall survival of glioblastoma lies between 3 and 5 month. Additional radiotherapy treatment has been shown to improve median survival to 9-12 months [Walker et al., 1979].

For diagnostics of glioma, magnetic resonance imaging is the method of choice, due to its high soft tissue contrast, followed by computed tomographic images. Surgery with maximal tumor resection is the first step of treatment, followed by a combination of chemotherapy, e.g. with temozolomide, and radiation therapy. For management of high-grade glioma, radiotherapy has been established as common treatment option, either in combination with chemotherapy or as sole treatment [Stupp et al., 2005]. Current standard definition of tumor target volumes in radiotherapy planning for high grade glioma is based on contouring anatomical information from contrast agent enhanced T_1 weighted

[1] World Health Organization

MRI, as leakage of contrast agent into tissue regions with disturbed blood brain barrier and increased vascularization results in clear visibility of the macroscopic tumor extent. Detection of invasive tumor fronts with these imaging techniques is limited though and contributes to uncertainties in defining the actual tumor boarder in radiotherapy planning. Therefore, local tumor recurrence is the predominant pattern of therapy failure in these patients leading to poor overall survival. In 80% of the cases recurrence patterns occur within $2-3\,\mathrm{cm}$ margins from the primary tumor [Gaspar et al., 1992]. A second course of radiotherapy for management of recurrent high grade glioma is difficult due to the high risk of treatment related side effects. Recent developments in the field of ion therapy have opened the possibility for irradiation of recurrent high grade glioma through their ability of precise dose delivery (section 2.3.1).

2.3 Radiation

Many methods in radiology and radiation oncology are based on the physical principles of interaction of radiation with matter. Thus, a short review of these processes is beneficial and required for a better understanding of methods and effects in both fields. More detailed information can be found in many physics textbooks. This chapter is oriented on the work of Bille and Schlegel [2002], which presents an adequate overview for medical applications.

2.3.1 Interaction of Radiation with Matter

In general, one can distinguish between ionizing and non-ionizing radiation. For medical purposes, the effects of ionizing radiation are of high interest.

Directly ionizing Radiation

Charged particles are considered directly ionizing radiation. They slowly lose their energy through Coulomb interactions until they come to rest. The incident radiation particle can interact with both orbital electrons and nuclei of the absorber atoms, resulting in either elastic or inelastic collisions. In elastic collisions, the particle is deflected without energy loss. Inelastic collisions can be soft, hard or nuclear, depending on the impact radius and the interaction partner. Coulomb interactions with orbital electrons are discriminated by the energy transfer from incident particle to the target electron. In soft collision, only a small part of the particles energy is transferred to the orbital electron. This leads to atomic excitation as the orbital electron is lifted to an energetically higher shell. Hard collision on the other hand are processes in which a significant amount of the incident energy ($\leq 50\%$) is transferred to the orbital electron. The energy transfer yields ejection of the orbital electron and hence, ionization of the interacting atom. Both types of energy loss through collisions are described by the collision stopping power in the Bethe-formula:

$$S_{col} = -\frac{dE}{dx} = 2\pi r_e^2 m_e c^2 \cdot \rho \frac{Z}{A} N_a \cdot \frac{z^2}{\beta^2} \cdot \left[ln\left(\frac{2m_e c^2 \cdot (\gamma\beta)^2 \cdot W_{max}}{I^2} \right) - \beta^2 \right] \tag{2.1}$$

where W_{max} is the maximum energy transfer of single collision, I the mean excitation potential, z the effective charge of projectile and β the projectile velocity. ρ, Z and A describe the traversed medium in terms of density, atomic and mass number. Coulomb interactions with the atomic nucleus lead to radiation loss through bremsstrahlung. This effect is described by the radiative stopping power.

The total linear stopping power, which describes the mean energy loss dE of a charged particle per path length dx in a material, is the sum of both contributions together with an additional component of nuclear stopping power from elastic scattering. Whereas electrons undergo only Coulomb interaction, ions exhibit further nuclear reactions in fragmentation process, and medium effects such as Cerenkov radiation. For heavy charged particles the radiative stopping power is considered negligible.

Indirectly Ionizing Radiation

Neutral, uncharged particles are defined as indirectly ionizing radiation as they deposit energy in two steps. First, the energy is transferred to secondary charged particles, which in terms deposit the energy as described above. Most medical applications are based on the interactions of photons with matter, which can be summarized in the linear attenuation coefficient $\mu(E_\gamma)$. The attenuation coefficient, also referred to absorption coefficient, is the probability of a photon interaction with an absorber atom per unit path length. The *Lambert-Beer* law describes the correlation between absorption, depth and interaction properties of the traversed medium:

$$I(\Delta x) = I(0) \cdot e^{-\mu(E_\gamma)\Delta x} \tag{2.2}$$

Δx is the length of the traversed medium and $I(x)$ the beam intensity. In the energy regimes used for radiotherapy, energy loss of photons originates from three interaction processes: the photon can be either absorbed completely while its energy is transferred to light charged particles (e^-, e^+) or scattered, both elastically or inelastically.

The **photoelectric effect** describes the process of total disintegration of the photon by ionization of an atom. A part of the photon energy E_γ is used to overcome the ionization potential and release a bound electron from the atomic shell. The rest is transferred to the electron as kinetic energy. The photo effect can be seen as true absorption without any photon scattering.

Compton scattering is inelastic scattering of the incident photon on the electrons of the medium, where only a part of the photon energy E_γ is used for ionization and kinetic energy of the target electron. The remaining energy is transported away from the interaction point by the scattered photon. Due to the fact that the incident photon energy is usually much larger than the binding energy of the atom, the process is assumed to be inelastic scattering on free electrons at rest. Elastic scattering of the photon can also occur, however since no energy is transferred to the medium it is of minor interest to the considerations of radiotherapy and will not be discussed in this work.

Pair production can occur from the interaction of the incident photon with the electro-

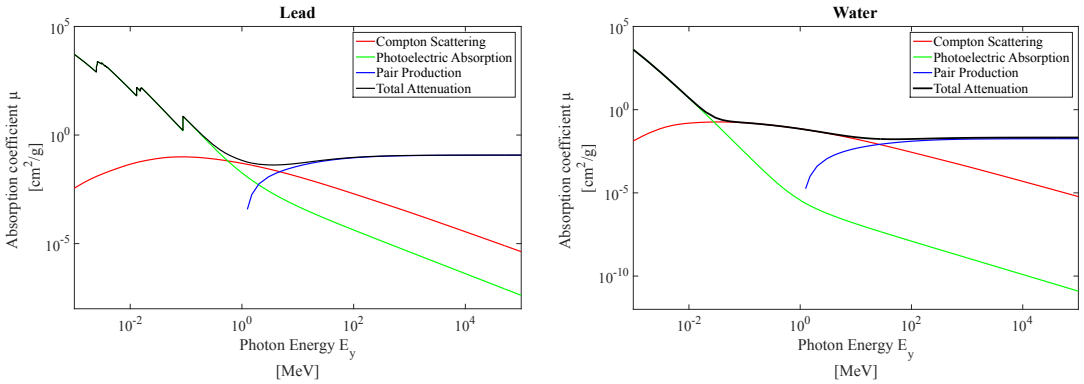

Figure 2.2: Absorption coefficients depending on the photon energy E_γ, for Compton scattering (red), photoelectric absorption (green) and pair production(blue) in lead and water.

magnetic field of the atomic nucleus. If the photon energy exceeds two times the electron mass, i.e. $E_\gamma > 1.022\,\text{MeV}$, it can disintegrate spontaneously into an electron-positron pair. The electron deposits its energy as described above while the positron travels a few millimeters through the tissue until it binds with an electron from the tissue into a state called positronium. The positronium then disintegrates under emission of two back-to-back photons of each 0.511 MeV, which undergo further interactions.

All of the above processes have in common that free electrons with ranges up to a few millimeters are produced, that in terms deposit the energy locally via Coulomb interaction. The respective cross section of each process and hence the absorption contribution depends on the photon energy and the traversed matter, as illustrated in figure 2.2. All these aspects have to be considered for both radiological imaging with x-rays and photon based radiation therapy.

2.3.2 Biological Effects of Radiation

Radiation effects on biological systems result from direct and indirect ionization of biomolecules. Direct effects are the ionization of DNA molecules, leading to single- and double-strand breaks, and of enzymes and cell membranes. Indirect damage is caused via radiolysis of water and hence the production of hydroxyl-radicals, which lead to inflammatory responses as well as destruction or mutation of the DNA. As a result the sensitivity to radiation is decreased under anoxic and hypoxic conditions compared to normal oxygenation.

An important quantity concerning directly ionizing charged particles is the *linear energy transfer* (LET), which is used to describe the mean energy loss of the particles via local transfer to the medium per path length. LET is dependent on the velocity and charge of incident particle as well as the nuclear composition of the traversed medium. Higher LET does not necessarily lead to a higher energy transfer at individual interactions but much rather on a more dense deposition of energy "packages" along the particle tracks. This in terms means that irradiation with low LET radiation leads to homogeneous dose depositions, whereas high LET radiation deposits high local doses. The biological

effectiveness of a type of radiation is highly dependent on its LET. Experiments have shown, that for high LET radiation much less dose is needed to achieve the same biological effect compared to low LET radiation. Since the concept of dose is not sufficient to describe these effects, a biological-physical quantity called *relative biological effectiveness* (RBE) has been introduced. RBE is explicitly defined for a certain biological effect as the ratio of doses needed for two different radiation types to cause this effect and is primarily dependent on the radiation types LET. Aside from the steep dose gradients, an increased RBE is argued as an advantage of ion irradiation compared to photons. Fractionation of applied total dose has been shown to increase the tumor control probability, since it allows regeneration and repair mechanisms in normal tissue, whereas these effects are much less expressed in tumor tissue.

The effects of radiation on tissue are diverse and depend on the affected organ. Both anatomic and functional deficits can be observed including inflammations, edema and vascular abnormalities up to radio necrosis. These side effects play an important role in the aftermath of radiation therapy for the discrimination between radiation damage and tumor growth progress or recurrence.

2.3.3 Dose Concepts

The microscopic effects of radiation are described on a macroscopic scale by the concept of energy dose, which is defined as the amount of deposited energy ΔE in a sufficiently small enough mass element of tissue Δm

$$D := \frac{\Delta E}{\Delta m} \tag{2.3}$$

in units of Grey $\mathrm{Gy} = \frac{\mathrm{J}}{\mathrm{kg}}$. The energy is deposited by free electrons produced in the ionization processes. These electrons have little energy of a few electron volts (eV) and consequently short ranges up to a few millimeters. Thus, it can be assumed that they deposit their energy locally in cascade processes of scattering and further ionization. The detailed interactions of radiation with matter depend on both radiation type and beam energy. The dose in depth x can be derived as.

$$D(x) = \Phi(x)\frac{\mu_{ab}}{\rho}E_\gamma \tag{2.4}$$

$\Phi(x)$ assigns the photon fluence (number of photons N passing a surface A) in depth x following the exponential decay of the Lambert-Beer law (c.f. 2.2):

$$\Phi(x) = \frac{N(x)}{A} = \Phi_0 e^{\int_0^x -\mu(E_\gamma)dx} \tag{2.5}$$

Hence the dose deposition in dependence of x, so-called *depth-dose curves* should exhibit a decreasing exponential course. However it can be observed that the depth-dose curves show a *build-up effect* within the entrance region of the photon beam. This effect is due to

the *secondary electron equilibrium*, i.e. the compensation of energy loss and energy gain from electrons, which is only reached after a depth of one electron range.

The dose deposited by photons depends on the corresponding total absorption coefficient μ. For charged particle radiation such as electrons and protons, the mean differential energy loss, described by the Bethe formula, is the important physical quantity to characterize energy deposition. The depth-dose curves of heavy charged particles exhibit an increased ionization potential at the end of the particles course. This phenomenon is called Bragg peak and is a result of electron capture processes at low velocities, which decrease the ration Z/β in the Bethe formula. It can be observed that the Bragg peak is lower and wider with increasing depth in material, meaning that ions at same energies exhibit different ranges. This effect is called range straggling and is due to the stochastic nature of the interaction processes.

2.4 Nuclear Magnetic Resonance

The effects of nuclear magnetic resonance (NMR) form the basis of magnetic resonance imaging (MRI), an important diagnostic tool in neuro-oncology. The following section reviews the underlying physical principles, based on literature from E. Yankeelov and Price. [2011] and Abragam [2007].

2.4.1 Nuclear Spin and Magnetic Moment

Nuclear particles, e.g. protons and neutrons, feature an intrinsic quantum mechanical property called spin, which is responsible for the hyperfine structure splitting in atomic spectra. It can have half-integer values for fermions or integer values for bosons. The spin of a nucleus results from the entity of the spins of the component nucleons. The spin represents a quantum mechanical angular momentum, characterized by two quantum numbers: the spin quantum number I and the magnetic quantum number m_I. m_I can take values between $\{-I, ..., I\}$ The momentum states $|I, m_I\rangle$ are eigenstates of the spin operator $\hat{\boldsymbol{I}}^2$ and its z-component

$$\hat{\boldsymbol{I}}^2 |I, m_I\rangle = I(I+1)\hbar^2 |I, m_I\rangle \tag{2.6}$$

$$\hat{I}_z |I, m_I\rangle = m_I \hbar |I, m_I\rangle \tag{2.7}$$

The spin is coupled to a magnetic dipole moment

$$\hat{\boldsymbol{\mu}} = \gamma \hat{\boldsymbol{I}} \tag{2.8}$$

with the *gyromagnetic ratio* γ being a nucleus specific, experimentally determined constant. For protons, ^{1}H, the gyromagnetic ratio is $\gamma/2\pi = 42.58$ MHz/T. Without perturbations via external fields, the states of $\hat{\boldsymbol{I}}$ are degenerated into $(2I+1)$ values. The interaction of

an external magnetic field $\boldsymbol{B}$ with the magnetic dipole moment is described by the following Hamiltonian:

$$\hat{\mathcal{H}} = -\hat{\boldsymbol{\mu}}\boldsymbol{B} \tag{2.9}$$

If $\boldsymbol{B}$ points along the z-axis ($\boldsymbol{B} = B_0\hat{e_z}$) the states of $|I, m_I\rangle$ are also eigenstates of $\mathcal{H}$ with energy eigenvalues E_{m_I}:

$$\hat{\mathcal{H}} = -\gamma\hbar B_0\hat{I}_z \tag{2.10}$$

$$E_{m_I} = -\gamma\hbar B_0 m_I \tag{2.11}$$

The solution is described by a harmonic oscillator with discrete energy states

$$E_n = \left(n + \frac{1}{2}\right)\hbar\omega_0 \tag{2.12}$$

Hence the energy levels will split in $(2I + 1)$ equidistant levels, as illustrated in figure 2.3A, where the difference between two states yields $\Delta E = \gamma\hbar B_0 = \hbar\omega_0$ with the *Larmor frequency* $\omega_0 := \omega_L$. This process is called *Zeeman splitting*.

For medical applications, the hydrogen nucleus, i.e. a single proton, is of particular interest. Protons carry spin $I = \frac{1}{2}$ and hence in an external magnetic field, the spin has $(2I+1) = 2$ energy states with either higher or lower energy. These states are commonly called parallel to $\boldsymbol{B}$ and antiparallel to $\boldsymbol{B}$.

2.4.2 Multi-Particle Systems

For an ensemble of N particles, the spins form a net magnetization $\boldsymbol{M}$. Without external magnetic field, the magnetic moments of all particles point into random directions, which leads to $\boldsymbol{M} = \sum_N \hat{\boldsymbol{\mu}} = 0$. In an external magnetic field $\boldsymbol{B} = (0, 0, B_0)$, the spins will align parallel or anti-parallel with the z-axis. Since the parallel state is energetically more favorable, one would assume, that all N spins align parallel with the magnetic field. However due to thermal movement, some of the N particles have enough energy to occupy the antiparallel state. Hence the occupation probability of the state m follows Boltzmann statistics:

$$p_m = \frac{e^{-\gamma\hbar m B_0/k_B T}}{\sum_{m=-I}^{+I} e^{-\gamma\hbar m B_0/k_B T}} \tag{2.13}$$

With this, the ground state macroscopic magnetization in an external magnetic field, which is the expectation value of the magnetic moments per volume, can be approximated as

$$\boldsymbol{M} = -N \sum_{m_I=-I}^{+I} p_m \langle m_I|\,\hat{\boldsymbol{\mu}}\,|m_I\rangle = \frac{N\gamma^2\hbar^2 I(I+1)}{3k_B T}\boldsymbol{B} \tag{2.14}$$

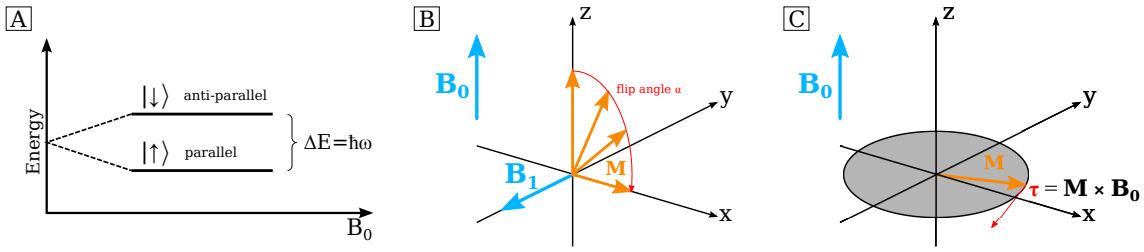

Figure 2.3: A: *Zeeman splitting* of the spin states into parallel and anti-parallel with the external magnetic field. B: If the spin is aligned parallel to an external magnetic field $\boldsymbol{B_0}$ along the z-axis, perturbation from $\boldsymbol{B_1}$ satisfying the resonance condition $\omega_L = \gamma B_1$ will rotate the magnetization $\boldsymbol{M}$ will rotate into the xy-plane by the flip-angle α. C: The external magnetic field $\boldsymbol{B_0}$ acts orthogonally as torque $\boldsymbol{\tau} = \boldsymbol{M} \times \boldsymbol{B_0}$ on the magnetization $\boldsymbol{M}$. This leads to the process of *precession*.

For typical MRI field strengths of a few tesla, this yields a very small ratio of $1 : 10^6$ of spins aligned in parallel with the magnetic field compared to those which align anti-parallel, so the magnetization is very close to the equilibrium state. Thus measurements have to be very precise to assess the signal of this small magnetization effect.

2.4.3 NMR and Precession

The alignment with the external magnetic field acts orthogonally as torque. Unless $\boldsymbol{M}$ and $\boldsymbol{B}$ are perfectly aligned, the magnetic moment will trace a circular path around the axis of $\boldsymbol{B}$ with the frequency $\omega_L = \gamma \cdot B_0$ (see figure 2.3C). The circular motion of the magnetization is called *precession*.

Nuclear magnetic resonance occurs, when the magnetization $\boldsymbol{M}$ is tipped away from its equilibrium state. If the spin of a proton is aligned parallel to an external magnetic field $\boldsymbol{B} = B_0\hat{e_z}$, a perturbation from a second magnetic field $\boldsymbol{B'} = B_1\hat{e}_x$ satisfying the resonance condition $\omega_L = \gamma B_1$ will lead to precession of the magnetization around $\hat{e}_z$. Thus, $\boldsymbol{M}$ will rotate into the xy-plane by a so-called flip-angle α, which is dependent on the time that the perturbation is active (figure 2.3B). After removal of $\boldsymbol{B}$, the magnetization will precess around $\boldsymbol{B}$ in the xy-plane. As every system seeks equilibrium, a second motion, the so-called nutation will move $\boldsymbol{M}$ from the transversal plane back into alignment with $\boldsymbol{B}$. Hence the magnetic moment will undergo two rotations, leading to a spiraling path.

2.4.4 Bloch Equations and Relaxation Times

The Bloch equations describe the temporal change in magnetization $\boldsymbol{M}$ caused by a perturbation in form of an external magnetic field B. In the Equilibrium State ($\boldsymbol{M} \parallel \boldsymbol{B}$) they derive as

$$\frac{dM_x}{dt} = \gamma(\boldsymbol{M} \times \boldsymbol{B})_x = 0 \tag{2.15}$$
$$\frac{dM_y}{dt} = \gamma(\boldsymbol{M} \times \boldsymbol{B})_y = 0 \tag{2.16}$$
$$\frac{dM_z}{dt} = \gamma(\boldsymbol{M} \times \boldsymbol{B})_z = 0 \tag{2.17}$$

Tipping the magnetization away from its equilibrium state with a 90° pulse leads to $\boldsymbol{B} \perp \boldsymbol{M}$, which yields for the Bloch equations:

$$\frac{dM_x}{dt} = \gamma M_y B_z \tag{2.18}$$
$$\frac{dM_y}{dt} = -\gamma M_x B_z \tag{2.19}$$
$$\frac{dM_z}{dt} = 0 \tag{2.20}$$

As mentioned before, $\boldsymbol{M}$ will not stay in the xy-plane. The time evaluation of the signal is known as relaxation process, and derives from interactions in tissue and external forces. The magnetization will strive back to equilibrium, which is described by the so called *longitudinal relaxation time* T_1. Mathematically, this leads to an empirical extension to the z-component of the Bloch equations:

$$\frac{dM_z}{dt} = \gamma(\boldsymbol{M} \times \boldsymbol{B})_z - \frac{M_z - M_0}{T1} \tag{2.21}$$

As the z-magnetization will recover exponentially $\propto e^{-t/T_1}$, T_1 represents the time that it takes the z-magnetization to recover. As the spins in the ensemble are not independent but interact with each other, the magnetic field varies locally due to different shielding from the molecules etc. The Larmor precession frequency is directly linked to the perturbing magnetic field, thus the spins composing the overall system magnetization will have slightly different angular precession frequencies. As a result, the transversal magnetization $\boldsymbol{M}_\perp$ will disperse, which is called transversal relaxation. Extension of the transversal component of the Bloch equations yields

$$\frac{dM_x}{dt} = \gamma(\boldsymbol{M} \times \boldsymbol{B})_x - \frac{M_x}{T_2} \tag{2.22}$$
$$\frac{dM_y}{dt} = \gamma(\boldsymbol{M} \times \boldsymbol{B})_y - \frac{M_y}{T_2} \tag{2.23}$$

For transversal relaxation, two factors contribute to the signal decay: the molecular spin-spin interactions, with the native T_2, and static local field inhomogeneities. T_2 decay is a function of completely random interactions between spins. However, the external B_0 field is not completely homogeneous. leading to a faster observed decay time

$$\frac{1}{T_2^*} = \frac{1}{T_2} + \frac{1}{T_2'} \tag{2.24}$$

The T_2' component can be counteracted for example by refocusing the transversal magnetization by applying a 180° pulse, leading to a so called spin echo signal, from which T_2 can be deduced. Since different tissue types exhibit different T_1 and T_2 relaxation times, measurements of NMR can be used for imaging.

2.5 Radiotherapy and Treatment Planning

Radiotherapy is considered a loco-regional treatment form of cancer and other diseases. It can be used for locally confined tissue destruction, but at the same time offers the possibility for regional large-volume treatment of microscopic tumor extensions in the same way that chemotherapy does. Oncological radiotherapy can be applied with curative intents as well as palliative. It is usually applied in combination with other treatment approaches such as surgery and chemotherapy. In general the goal of radiotherapy can be stated as using the biological effects of ionizing radiation for destruction of tumor tissue without causing severe damage in surrounding healthy tissue.

The radiotherapy treatment aim is to use these DNA destructive effects to induce cell death. Even though radiotherapy refers to various strategies for the irradiation of tissue, including intra-operative irradiation (IORT) and brachytherapy, the presented work is confined to teletherapy. For teletherapy, usage of different radiation types is possible, depending on tumor entity and location site. The most common approach is to use photons, originating from either isotope sources, like ^{60}Co, or electron accelerators through bremsstrahlung such as linear accelerators.

The physical principles of dose deposition are based on the absorption of photons in a medium. The reason photons are widely used for radiotherapy is their advantageous depth-dose profiles for deep-seated tumors. Production of secondary electrons results in a build-up region of the depth dose. This effect is of high clinical relevance as it enables sparing of the skin tissue. The maximum of the dose deposition shifts to greater depths with increasing energy. The depth dose profiles of electrons show a very narrow region of build-up and a rapid drop off, which makes them a good choice for treatment of superficial tumors, e.g. melanoma, and for IORT. Novel approaches for radiotherapy include treatment with ions, such as ^{1}H and ^{12}C. Their energy loss in matter is described by the mass stopping power in equation 2.1. Together with a plateau shape of low entrance dose, the steep dose gradient of the Bragg peak leads to an advantageous depth dose profile of good tumor coverage with concurrent skin and healthy tissue sparing. Furthermore due to different interaction processes, irradiation with ions yields different biological effects. The most often used therapeutic ion is the proton. Current research studies the applicability of

treatment with carbon, helium and oxygen ions. For those particles, fragmentation of both projectile and target, which result in further nuclear processes, has to be considered.

The amount of tumor cells killed by radiation is stochastically dependent on the applied energy dose. Hence radiotherapy aims to apply very high, conformal doses in the tumor or target volume and at the same time keep the dose to the surrounding health tissue low. An important part is the sparing of certain organs in the neighborhood of the tumor, so called *organs at risk* (OAR), where the dose has to be kept under a certain organ specific threshold.
In an ideal therapy, the dose prescribed by the physician would be deposited completely in the tumor, whereas the neighboring healthy tissue is spared. Unfortunately the preservation of the surrounding tissue is only possible to an extent, thus a compromise between sufficient tumor damage and the exposure of normal tissue has to be found. The dose distribution can be optimized by careful choice of radiation type, prescribed dose and precise confinement of the irradiated areas. This optimization is part of the treatment planning process. Crucial for the definition of the irradiation treatment plan is the definition of target volumes and organs at risk.

According to the ICRU[2] report n^{o} 50 and 62 [Chavaudra and Bridier, 2001], the treated tumor is defined by three sub-volumes, illustrated on a recurrent high grade glioma patient in figure 2.4. The macroscopic visible extent of the tumor is called the *gross tumor volume* (GTV). Malignant neoplasms grow highly invasive and cannot always be clearly delineated, whereas benign tumors are non-invasive and are confined more distinctively. Therefore the *clinical target volume* (CTV) includes margins for possible extensions of the tumor and infiltrations of the surrounding tissue. Finally the *planning target volume* (PTV) introduces a safety area around the tumor in order to accounts for patient mispositioning, organ movement and other uncertainties in dose delivery. The responsible physician prescribes minimum doses for the target volume PTV together with the fractionation scheme as well as maximum dose values for each of the surrounding organs at risk, depending on their sensibility to radiation. Values for both total dose and fractionation are based on experience and depend on the tumor entity and treatment intent as well as the patient's general state of health.

Target delineation is usually performed based on the planning CT image (figure 2.4, left). In some cases, especially brain tumors, additional information for MRI (figure 2.4, right) is used, due to the enhanced soft tissue contrast. These prescriptions lead to an irradiation scheme for the number and direction of fields, conformity, intensity of each beam etc. According to this scheme dose calculations are performed based on electron density information from CT and knowledge of physical processes of radiation, in order to estimate delivered dose distribution.

[2]International Commission on Radiation Units and Measurements

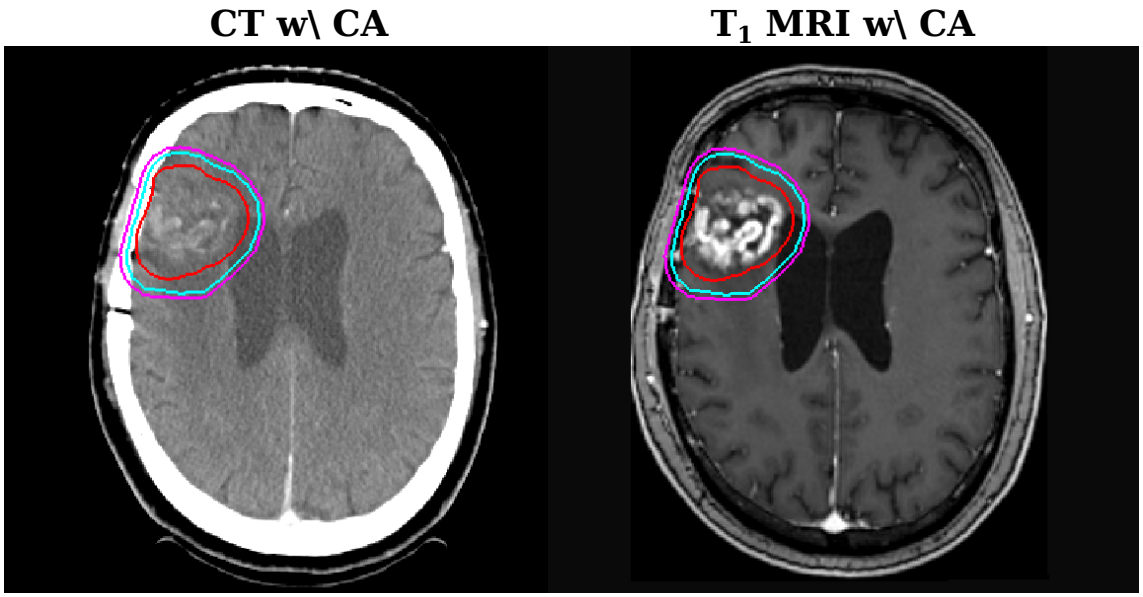

Figure 2.4: RT planning target contours gross tumor volume (red), clinical target volume (cyan) and planning target volume (magenta) of a brain tumor patient, displayed in the contrast enhanced planning CT (left) and the contrast enhanced T_1 weighted MRI (right).

Various techniques for estimation of the distribution of dose based on the physical interactions of the radiation exist, such as convolution algorithms from analytical model, and Monte Carlo simulations based on the various physical interaction processes between radiation and matter. Based on the dose calculations the treatment plan is gradually optimized with respect to dose prescription in target and sparing of surrounding healthy tissue and OAR.

3 Methods

The presented work aims to investigate multimodal image data from recurrent high grade glioma patients with respect to possible surrogate parameters in order to find patterns of tumor recurrence and growth prediction.

In the first part of the following chapter, the different image modalities are presented and their physiological correlates are discussed. After a general introduction on computed tomography (CT) and standard magnetic resonance imaging (MRI) (sections 3.1 and 3.2), dedicated focus is set on physiological (functional and metabolic) imaging modalities, such as perfusion and diffusion weighted MRI (sections 3.2.4 and 3.2.5), and amino acid positron emission tomography (PET) (section 3.3). Since most of the presented studies dealt with dynamic image series of PET and MRI, the underlying physical principles of pharmacokinetic modeling are discussed in more detail in section 3.4.

In the second part, software concepts used for analysis and post processing of the various images, are introduced. The multi-modal approach of finding tumor progression patterns was based on machine learning classification concepts and random forests. Hence, these approaches are reviewed in section 3.6. The medical imaging interaction toolkit (MITK) is presented in section 3.7, as it was used as base framework for all software developments and image analysis steps. Acquisition details of the used data from recurrent high grade glioma patients are presented in section 3.8.

3.1 Computed Tomography

Due to the fact, that the absorption coefficient depends on the atomic number and density of the material, the absorption of photons in matter leads to a contrast between materials of different densities. This effect can be used for imaging. Radiography acquires 2D projection images of the patients distribution of absorption coefficients $\mu(x, y, z)$, however the poor soft tissue contrast and missing depth information of the projections are often insufficient for detailed diagnosis. To overcome these limitations and resolve the superposition of structures, *computed tomography* (CT) uses the acquisition of several 2D projection images taken under different angles within an arc of at least 180°. As mentioned in chapter 2.3.1, the absorption coefficient depends on the traversed material and the energy of the incident photon. The energy distribution of the photon beam results from bremsstrahlung spectra and characteristic x-rays of the utilized x-ray tube and is influenced by the tube voltage, target anode material, angle of the anode and beam filters. Thus, the images produced at CT scanners with different x-ray tubes are not comparable. To enable inter-scanner

Figure 3.1: Transversal slice of a CT scan in a brain tumor patient. The *level window* is set to $C/W = (35/60)$ HU, covering the soft tissue range. More dense structures, like the skull bone, with higher HU values are displayed in white, less dense structures with lower HU values in black.

comparison, the Hounsfield value HU was introduced as normalization of the absorption coefficient μ to water:

$$\mathrm{HU}(\mu) := \frac{\mu - \mu_{H_2O}}{\mu_{H_2O}} \cdot 1000 \tag{3.1}$$

From the Hounsfield value, electron densities can be approximated for dose calculations via different interpolation methods.

Computed tomography is a sensitive method to assess bone structures as well as lung, abdominal and pelvic diseases. Today high resolution in the sub-millimeter range and fast acquisition times of a few seconds are possible. Fast acquisition methods enable cardiac imaging of the coronary arteries. In head and neck, CT is used especially for imaging of infarction, calcifications and hemorrhage. An example of a transversal slice of a treatment planning CT image is shown in figure 3.1. CT imaging can also be applied for tumor diagnosis in the brain, however MRI provides superior soft tissue contrast. On the other hand, MRI requires long acquisition times and is expensive. Thus, CT is an essential part in diagnosis and treatment of glioma. It plays a major role in radiation oncology, since the 3D patient electron density distribution is crucial for dose calculations.

3.2 Magnetic Resonance Imaging

Magnetic resonance imaging (MRI) is a valuable diagnostic imaging modality. Contrast in MRI is based on different relaxation times T_1 and T_2 of different morphological structures. With technical advances and increasing applications, further methods to measure functional and physiological processes from NMR effects have been developed. For diagnosis and treatment planning of brain tumors, MRI is superior to CT due to its distinct soft tissue contrast.

3.2.1 Image Acquisition

The precession movement of the magnetization $\boldsymbol{M}$ in a static magnetic field $\boldsymbol{B_0}$ after perturbation from a radio frequency (RF) pulse, as described in nuclear magnetic resonance (NMR), induces a voltage in a receiver coil. This offers the possibility to measure the signal of the magnetization, since the precession movement of $\boldsymbol{M}$ around $\boldsymbol{B}$ is a change in magnetic flux. In a nearby conductor, a signal proportional to the transversal magnetization $S \propto \omega_L M_\perp$ can be detected. The signal will follow the decay of the transversal magnetization $M_\perp$ precessing in the xy-plane, represented by a sinusoidal curve oscillating with the Larmor frequency. This signal, shown in figure 3.2, is called *free induction decay* (FID).

Using equation 2.14 for the transversal magnetization, proportionality of the signal with the squared magnetic field strength can be derived:

$$S \propto N \frac{B_0^2}{k_B T} \tag{3.2}$$

where N is the number of spins (see section 2.4.2). Hence, higher magnetic fields lead to greater potential signals. With the classical NMR experiment, the FID will be a sum over all protons in the examined volume (i.e. the body), precessing at Larmor frequency ω_L. For imaging, spatial encoding of the signal contributions from different locations is needed.

The precession frequency ω_L is directly proportional to the applied magnetic field strength $\boldsymbol{B_0}$. Using a linearly varying magnetic field along one axis, called *magnetic field gradient* G_z, will result in a spatially varying Larmor frequency:

$$\omega(z) = \gamma(B_0 + G_z \cdot z) \tag{3.3}$$

For an RF excitation pulse B_1, there is exactly one position x, at which the Larmor frequency $\omega_L(z)$ satisfies the resonance condition. This frequency dependent excitation is called slice selection. A slice of thickness Δz in position space corresponds to a band width $\Delta\omega$ in frequency space. If $B_1(\omega)$ is chosen to be a band function (step function) in frequency space it can be related to a *sinc*-function in position space $B_1(t)$ via Fourier transformation (FT).

After slice selection during the excitation pulse, only spins in a 2D plane are excited and (in homogeneous matter) precess with the same frequency. Application of a gradient G_y along one axis (perpendicular to the slice selecting gradient) for a time t will cause the spins to

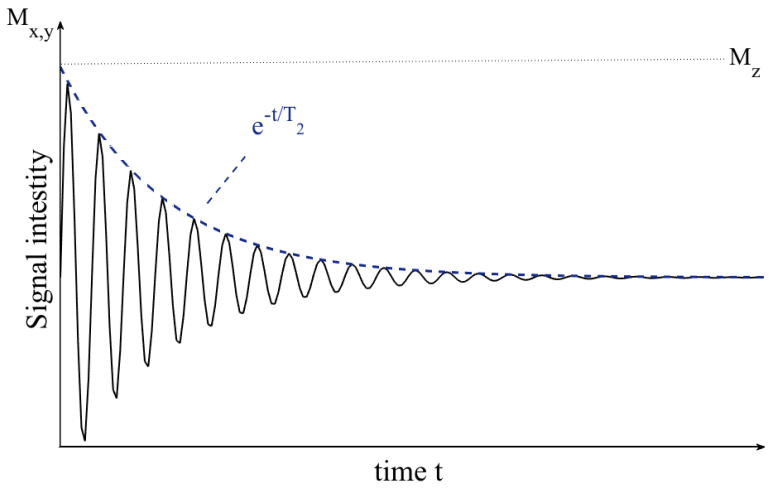

Figure 3.2: *Free induction decay*: The time dependent signal intensity of an NMR signal, induced in a receiver coil by the precession movement of the transversal magnetization $M_{x,y} = M_\perp$.

dephase due to spatially dependent precession frequencies $\omega(y) = \gamma(B_0 + G_y \cdot y)$, as some precess faster and others slower. After switching off the gradient, the magnetization at position y will again precess with the same frequency, but with position-dependent phase angles $\phi(y) = (\gamma G_y y) \cdot t := k_y \cdot y$. Hence the signal contributions from different locations are *phase encoded* with the *spatial frequency* $k_y = \gamma G_y t$. Repeating the phase encoding gradient N times with linearly increasing gradient field strength will result in projections of the signal

$$S(t) \propto P_y(x) = \int M(x,y) e^{ik_y y} dy \tag{3.4}$$

from which the spatial position y can be recovered from Fourier transformation.

In principle, phase encoding can be applied in the missing third direction as well, however, acquisition of each projection requires N repetitions of excitation and acquisition, which leads to long measurement times. Thus the concept of *frequency encoding* is often used. Application of a third gradient G_x during the image acquisition time T_{RO} leads to different precession frequencies $\omega(x)$ of the spin contributions at different locations x. The FID signal will then not have a single oscillation frequency but contributions from all $\omega(x)$, that can be recovered through Fourier analysis

$$S_x(t) = \int M(x) e^{i\omega(x) T_{RO}} \tag{3.5}$$

Thus the magnetization contribution from location x is encoded with a respective spatial

frequency k_x. In total, the 2D magnetization distribution $M_\perp(x, y, z)$ is related to the FID signal $S(t)$ by a 2D Fourier transformation.

$$S(t) = \int\int M_\perp(x, y, z) \cdot e^{ik_y \cdot y} \cdot e^{ik_x \cdot x} dxdy \tag{3.6}$$

k_x and k_y span the so-called *k-space*, and image acquisition is performed by discrete sampling of this k-space.

3.2.2 Contrast Agents

MRI provides high soft tissue contrast without the use of ionizing radiation. *Contrast agents* (CA) can further improve sensitivity and specificity by influencing the relaxation times. Their application is used for example in the diagnosis of high grade glioma, where CT and native MRI do not provide enough information for distinct visualization of the tumor outline. In the brain, contrast agents are usually confined to the intravascular space due to the *blood-brain-barrier* (BBB). Highly malignant brain tumors often exhibit disruption and leakage of the BBB. Thus, extravasation of the contrast agent into the *extravascular extracellular space* (EES) is possible, which can be detected as signal changes in the images. Furthermore, high grade glioma are highly vascularized hence, application of contrast agents leads to increased contrast and visibility of the vessels.

The effects of contrast agents are based on alterations of the relaxation times. Compared to other modalities, contrast agent in MRI are never visualized directly, but through their effects on the spin relaxation. There are mainly two types of MRI contrast agents: Gadolinium-based, paramagnetic chelates and iron-oxide-based, super-paramagnetic chelates. Gadolinium based contrast agents are the most widely used. Gadolinium Ga^{3+} is a paramagnetic ion, whose unpaired electrons shorten the longitudinal relaxation time T_1 via dipole-dipole interactions. The effects on relaxation rate $R_1 = \frac{1}{T_1}$ can be assumed linearly with the CA concentration c

$$R_1 = \frac{1}{T_1} = R_{1,0} + r_1 \cdot c \tag{3.7}$$

where $R_{1,0}$ is the relaxation rate without presence of contrast agent and r_1 is the CA specific relaxivity. In addition, the paramagnetism leads to local magnetic field inhomogeneities between spaces, that contain CA and those that do not. These field gradients yield further dephasing of proton spins and hence a reduction of the T_2 transversal relaxation time. Both the dipole-dipole interaction and the local field inhomogeneities are short ranging effects. Hence, gadolinium contrast agents only affect their immediate neighborhood tissue. Among other applications, gadolinium-based contrast agents are used for imaging brain tumors, especially in permeability and perfusion assessment. The interaction of iron-oxide-based contrast agents with the adjacent tissue mainly leads to shortened T_2 times, however they also effect T_1 times.

3.2.3 Sequences

The interplay of radio-frequency (RF) stimulation, magnetic field gradient and image acquisition is referred to as MRI *pulse sequence*. The time between successive pulse sequences applied to the same slice is referred to as *repetition time* (T_R). For a better understanding, a short review of the basic sequences of magnetic resonance imaging and those used in this work is presented. More detailed information can be found for example in Bernstein et al. [2004]. Special focus will be given to the prognostic and physiological meaning of the sequences for imaging of glioma. The principles of diffusion and perfusion MRI are covered in dedicated sections (3.2.4 and 3.2.5).

Spin echo (SE) pulse sequences use a 90° pulse, followed by a 180° refocusing pulse. The 90° pulse tips the magnetization into the transversal plain. Local field inhomogeneities lead to dephasing of the spins, characterized by the T_2 relaxation time. The 180° RF pulse is used to flip the spins into the opposite direction in the transversal plane, which causes the dephased spins to refocus. This refocusing induces an echo signal. The time between the application of the 90° pulse and the echo signal is called echo time (T_E). *Gradient echo* sequences (GRE) are an alternative technique that use gradient fields to create dephasing of the spins. A second, rephasing gradient acts in the same way as the 180° pulse in SE sequences, inducing an echo signal. GRE sequences use flip angles usually smaller than 90°. The low flip angles preserve parts of the original longitudinal magnetization and thus, the build-up time for longitudinal magnetization is significantly reduced. With this technique, gradient echo sequences allow fast image acquisition. *Inversion recovery* (IR) pulse sequences are SE sequences that use an initial 180° RF pulse to invert the magnetization. The following 90° RF pulse flips the longitudinal magnetization into the transversal plane. However at that time, the initial longitudinal magnetizations of different tissues has been separated due to different T_1 times, which enhances image contrast. The time between the two pulses is called inversion time (T_I). *Fast low angle shot (FLASH)* sequences are gradient echo sequences which set the transverse magnetization to zero after readout, which allows for even shorter acquisition times.

The **magnetization prepared rapid gradient echo** (MP-RAGE) sequence [Mugler and Brookeman, 1990] uses an initial 180° inversion pulse to create enhanced T_1 contrast. After the inversion time, this pulse is followed by a FLASH sequence for image acquisition. During data acquisition, T_1 relaxation is still in process. In order to avoid contrast artifacts, the MP-RAGE includes a time period for magnetization recovery after the FLASH. Measurement parameters such as T_R, T_E and the flip angle can be made small, since the inversion pulse ensures sufficient T_1 contrast. Thus, MP-RAGE yields short acquisition times around 1 minute [Mugler and Brookeman, 1991]. The improvement in diagnosis of brain tumors by usage of MP-RAGE has been shown for example by Nöth et al. [2015]. An example of an image derived from MP-RAGE with and without administration of a contrast agent is shown in figure 3.3.

In the diagnosis of brain lesions, the hyper intense signal from *cerebrospinal fluid* (CSF) can cause problems in T_2 weighted images. The **fluid-attenuated inversion-recovery** (FLAIR) sequence [Hajnal et al., 1992] uses an inversion recovery pulse sequence and long T_1, since the longitudinal relaxation time of CSF is considerably longer than those of brain

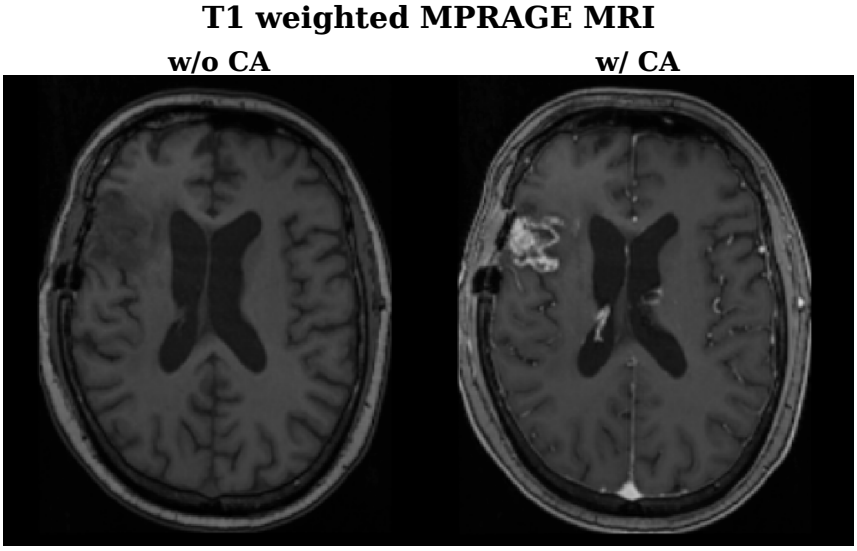

Figure 3.3: Standard T_1 weighted MPRAGE MRI in a recurrent glioma patient with and without contrast agent (CA) enhancement. The CA shortens T_1 relaxation in its surrounding tissue, leading to an increased signal. Thus, CA accumulating regions appear brighter in the image. The CA is confined to the plasma space in presence of an intact blood brain barrier. The main accumulation regions are the blood vessels and the lesion, due to a disrupted blood-brain-barrier.

parenchyma and most lesions. Thus, FLAIR sequences remove the effects of free fluid, that are not bound in tissue, in order to create a heavy T_2 weighting among tissues other than CSF. Figure 3.4 shows a transversal slice of a head acquired with a T_2 FLAIR sequence. Several study showed the prognostic value of T_2 weighted FLAIR imaging in different pathologies of the brain [Essig et al., 1998; Rydberg et al., 1994; De Coene et al., 1992]. Considering T_2 weighted FLAIR yields superior results for tumor delineation close to CSF in gliomas patients compared to conventional imaging due to an improved differentiation between tumor and edema [Essig et al., 2001; Husstedt et al., 2000].

Volumetric interpolated breath-hold examination (VIBE) is an interpolated 3D T_1-weighted GRE sequence developed for abdominal imaging. The sequence offers short acquisition times and improved resolution by using asymmetric k-space sampling and interpolation. It was shown, that VIBE can also be used to form rapid, high-spatial-resolution images of the brain [Wetzel et al., 2002]. With fast acquisition times, VIBE constitutes a good candidate for dynamic MRI.

3.2.4 Diffusion Weighted MRI

Diffusion weighted imaging (DWI) measures the diffusion process of water molecules with a special MRI sequence. Free molecules move random due to Brownian thermal motion. If no physical boundaries or constraints are present, this movement is isotropic. After a certain time t, the molecules have traveled

$$\sqrt{\langle x^2 \rangle} = \sqrt{2Dt} \tag{3.8}$$

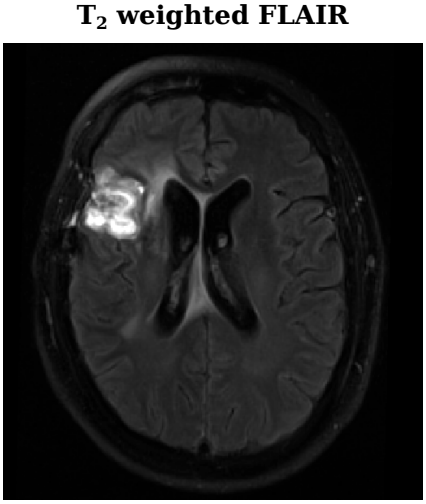

Figure 3.4: T_2 weighted FLAIR MRI in a recurrent glioma patient. The sequence suppresses signal from free fluids, thus the ventricles appear dark. With removal of the hyper intense signal from free fluids, it causes a strong T_2 weighting for detection of fluids bound in tissue (edema) as can be found in the surrounding of the lesion.

on average. D is the diffusion coefficient. This diffusion movement can be measured with the following sequence principle. Initially, a 90° RF pulse is applied, rotating the magnetization into the transversal plane. A gradient field is applied in one direction, causing spins at different locations to precess with different frequencies $\omega(x)$, which leads to dephasing of the magnetization. A subsequent 180° pulse inverts the magnetization in the transversal plain. A second gradient, equal in strength to the first one but with reversed polarity, is applied. If the molecules are stationary, the second gradient refocuses the spins, leading to a standard spin echo signal. However, due to diffusion motion, the molecules move between the 90° and 180° pulse. Hence, refocusing with the second gradient is not complete, as the spins experience different rephasing and dephasing frequencies, depending on their respective locations before and after the 180° pulse. This causes a measurable signal loss, containing information on the particle motion.
In tissue, the assumption of free diffusion is invalid due to cell membranes limiting molecule motion. Therefore, D is referred to as the apparent diffusion D_{app}, which is a measure for cellularity or cell density.
In nerve fibers, free diffusion is possible along the axons. Perpendicular to the nerve fibers diffusion is restricted. As diffusion motion can occur in all three dimensions, gradients along each of the patient axes x_i are applied. The diffusion tensor is used to map diffusion within the 3 space dimensions. $\boldsymbol{D}$ is a symmetrical matrix with six independent directions $x_i\, x_j$. From the diffusion tensor, two rotational invariant quantities can be deduced: The *apparent diffusion coefficient* (ADC) and the *fractionated anisotropy* (FA), with $0 \leq FA \leq 1$. $FA = 0$ represents isotropic diffusion whereas $FA = 1$ represents completely directional diffusion. Figure 3.5 shows exemplary maps of the ADC and FA in a transversal slice of a head, acquired with diffusion weighted MRI.

DWI is widely used in examinations of the brain for detection of ischemic strokes, characterization and differentiation of brain tumors and diagnosis of intracranial infections.

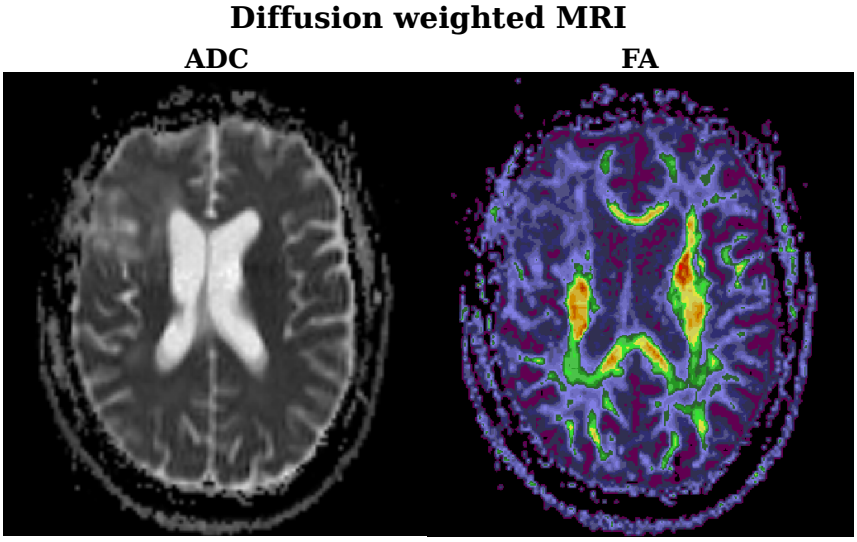

Figure 3.5: Parameter maps of the *ADC* and the *FA* from diffusion weighted MRI in a recurrent glioma patient. In liquids, such as the CSF in the ventricle, diffusion is more free compared to tissue, where the cells restrict diffusion. This leads to an enhanced *ADC*, indicated by a brighter image signal. In the *FA*, nerve fiber structures are indicated since they induce more directed diffusion compared to regions of isotropic diffusion such as the CSF.

Physiologically, the *ADC* reflects the degree of diffusion of water molecules in the extracellular water compartments and has been correlated with cellularity in various studies [Rowley et al., 1999; Sugahara et al., 1999; Ellingson et al., 2012]. Hence, it can be used to describe tumor physiology through changes in cell density, edema and necrosis. Destruction of water diffusion boundaries from decreasing cancer cell density leads to an increased *ADC*. On the other hand, a decrease in *ADC* indicates enhanced cellularity of the tumor and thus proliferation. These changes in *ADC* can be used as surrogate biomarker for the structure of the tumor physiology [Brynolfsson et al., 2014].

3.2.5 Dynamic Contrast Enhanced MRI

Tissue perfusion can be assessed through dynamic MRI by measuring the time course of the contrast agent concentration after bolus administration. Hemodynamic parameters, describing tissue perfusion and permeability, can be derived from these curves by using pharmacokinetic theory. As described before, paramagnetic CA such as gadolinium based chelates, primarily shorten T_1 relaxation times, which lead to an increased MRI signal. These effects are used in *dynamic contrast enhanced MRI* (DCE MRI) with T_1 weighted acquisition. Furthermore the contrast agents paramagnetism produces local magnetic field inhomogeneities which shorten the transversal T_2 relaxation time. The resulting decrease of signal intensity is the basis of *dynamic susceptibility contrast MRI* (DSC MRI). DCE can be applied to measure permeability parameters in most organs, since they offer large blood volume and easy extravasation of the contrast medium to the EES. This results in a total amount of CA large enough to cause strong signal changes. The quantification of tumor angiogenesis through measurement of micro-vascularization is used in numerous

studies for malignancy characterization and monitoring of treatment response in various tumor entities, such breast [Brix et al., 2004] and prostate [Buckley et al., 2004].

In the brain, however, the setting is different. Apart from the low blood volume, the BBB prevents contrast agent extravasation to the EES, so that the tracer is confined to the vessels. These conditions lead to only small changes in DCE MRI, thus DSC MRI was traditionally the method of choice for brain perfusion measurements. Absolute quantification of the hemodynamics with DSC MRI is difficult though [Rosen et al., 1991; Rempp et al., 1994]. Quantification of the *cerebral blood flow* (CBF) is usually done by assessment of the *mean transit time* (MTT) and *cerebral blood volume* (CBV). This approach however poses a number of difficulties. In reality, one does not deal with an ideal delta-function shaped bolus [Knutsson et al., 2010]. Furthermore determination of the CBV required calculation of the area under the arterial CA concentration (*arterial input function* AIF). Calculation thereof is hindered by the fact, that the T_2^* relaxivities of contrast agents are different in tissue and arterial blood. Relative values of CBV can be obtained by assuming a constant value for the integral AIF for the entire brain, but this complicates inter-patient comparisons or follow-up studies. An additional challenge is the reduction of the local magnetic field gradients through leakage of the contrast agent into the EES in case of a disrupted blood-brain-barrier and the resulting loss of susceptibility contrast. This leakage also leads to accumulation in the EES, which in terms yields an increase of T_1 effects. For all of the above named reasons, both Sourbron et al. [2009] and Larsson et al. [2009] proposed the application in DCE to brain tissue. Recent studies have shown the applicability of DCE MRI as diagnostic tool in other neuronal diseases, including stroke [Kassner et al., 2005] and multiple sclerosis [Ingrisch et al., 2012]. In brain tumors the measurement of tissue perfusion for assessment of blood-brain-barrier leakage or break-down can provide useful information for staging and assessment of therapy response [Møller et al., 2015; Jain, 2013].

From Signal to Contrast The extraction of CA concentration from signal intensities is a crucial part of DCE MRI data analysis, since pharmacokinetics are primarily deduced from concentrations. The contrast agent changes both longitudinal and transversal relaxation times, which in terms leads to a change of the measured signal intensities. In DCE MRI, the signal is dominated by the influence on the longitudinal *relaxivity* $R_1 = \frac{1}{T_1}$. T_2 effects play a minor role, since echo times are usually chosen very short. From the signal-time curves, contrast agent concentrations, or at least approximations thereof, can be derived again. The underlying mechanisms of the T_1 shortening effects derive from MR signal theory and are rather complex. However it has been shown that assumption of a linear relationship between relaxation rate and contrast agent concentration $C(t)$ is sufficient [Pintaske et al., 2006]

$$R_1(t) = R_{1,0} + r_1 \cdot C(t) \tag{3.9}$$

The time varying concentration, as measured with perfusion MRI, can thus be expressed as

$$C(t) = \frac{R_1(t) - R_{1,0}}{r_1} \tag{3.10}$$

The relation between signal intensity and relaxation time depends on a number of sequence specific factors, such as the coil sensitivity, the sequence flip angle and T_2 dependencies. For most sequences used in DCE MRI, these quantities can be merged into a time-independent constant $\Gamma(x)$. With this, the time varying signal intensity can be expressed as

$$S(t) = \Gamma(x) \cdot m_z(R(t)) \tag{3.11}$$

$m_z(R(t))$ describes the relation between longitudinal magnetization and relaxation rate. Assuming linearity between m_z and R leads to absolute and relative signal enhancement as approximations for the CA concentration:

$$C(t) = SE_{abs}(t) = \hat{k} \cdot (S(t) - S(0)) \tag{3.12}$$

$$C(t) = SE_{rel}(t) = \frac{R_{1,0}}{r_1} \cdot \frac{S(t) - S(0)}{S(0)} \tag{3.13}$$

For absolute signal enhancement, the proportionality constant $\hat{k}$ depends on the flip angle and coil sensitivity. These quantities cancel out for relative parameter comparisons, if $\hat{k}$ is equal in tissue and artery. This does not apply for relative signal enhancement, because the factor $\tilde{k} = R_{1,0}/r_1$ is independent of these quantities. However, $R_{1,0}$ is different in artery and tissue, leading to a scaling error of $R_{1,artery}/R_{1,tissue}$ in parameter estimates.

Analysis of Contrast Agent Kinetics The systemic transport of a CA bolus is described by indicator dilution theory, stating that the time course of the contrast agent distribution in tissue can be expressed as convolution of the concentration in a tissue feeding artery (AIF) with a so-called residue function, describing the tissue physiology and the contrast agent behavior. For a detail derivation, see section 3.4. Analysis in DCE MRI uses mathematical models based on the knowledge of contrast agent and tissue physiology to describe this residue function. Parameter estimation in pharmacokinetic modeling is straight forward from this point on. The goal is to find the set of n model parameters $\vec{\phi} = \{\phi_1, ..., \phi_n\}$ that best describes the experimental data. Convolution of the parameter dependent model representation of $R(t, \phi_i)$ with the measured AIF is fitted to the measured concentration time curves of the tissue with non-linear least square techniques (see figure 3.6).

It is obvious, that assessment of the right AIF is a crucial step in this analysis, as wrong estimation of the supplying influx time course can gravely influence the parameter estimates. Usually, $C_a(t)$ cannot be measured directly, but is deduced from the blood concentration $C_B(t)$ measured in a tumor supplying artery within the MRI image. C_a and C_B can be linked via the *hematocrit level* HCL

$$C_A(t) = \frac{C_B(t)}{(1 - HCL)} \tag{3.14}$$

In most cases, a literature value of $HCL = 0.45$ is used.

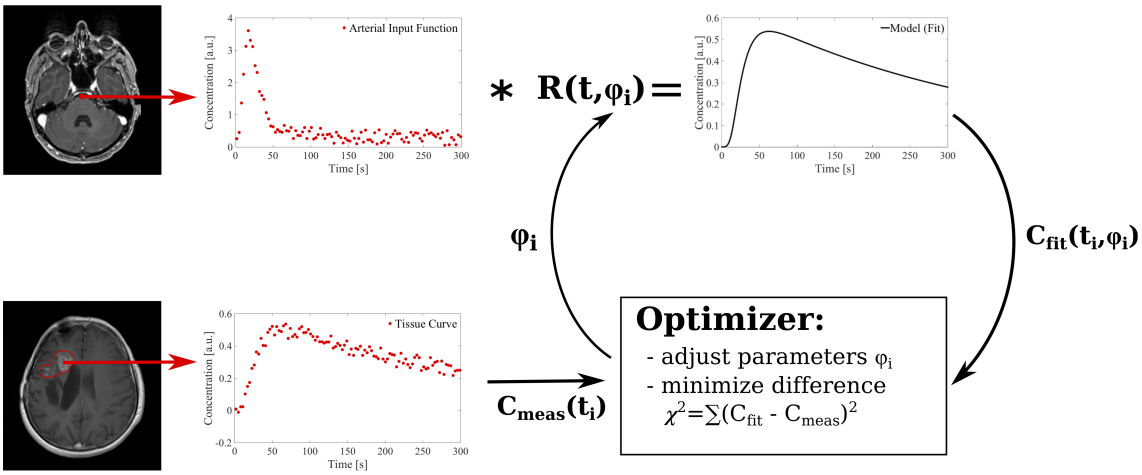

Figure 3.6: Principle of non-linear least square fitting on the example of concentration-time curves $C(t_i)$ in pharmacokinetic modeling of DCE MRI. From the dynamic image, the concentration-time curve of interest is extracted together with the arterial input function (AIF). Convolution of the AIF with the residue function $R(t, \phi_i)$, describing the tissue physiology and the contrast agent behavior, yields the theoretical concentration time curve of the contrast agent in tissue. In an iterative process, an optimizer adjusts the model parameters ϕ_i, until the similarity measure $\mathcal{X}^2$ (usually the sum of squared residuals) between theoretical and measured tissue concentration-time curve falls under a defined threshold.

3.3 Positron Emission Tomography

Standard MRI and CT are primarily used for imaging of anatomical structures and densities in the body. In neuro-oncology, MRI has been established as tool of choice for diagnosis and radiotherapy planning of brain tumors. However, the differentiation of tumor tissue from edematous, necrotic and fibrotic tissues is challenging. The accumulation of contrast agent in tumors, which is used for detection of malignant tissue, results from disruption of the blood-brain barrier. Accumulation can also be related to inflammation caused by surgery or radiation therapy though. In this case, *positron emission tomography* (PET) can help to distinguish tumor tissue.

3.3.1 Basic Principles

PET is an imaging technique in nuclear medicine, which enables the measurement of certain physiological processes, such as metabolism of a substance. The substance of interest is labeled with a radioactive isotope undergoing β^+-decay, and injected intravenously. Within the body, the emitted positrons annihilate with a next possible electron from the surrounding tissue atoms, emitting two back-to-back 180° photons of each 511 keV. These photons traverse and exit the body, and can be detected in coincidence measurements using a circular, scintillator-based detector around the patient. Reconstruction of the projected lines-of-response leads to a two dimensional visualization of the tracer distribution. Slice-wise measurements yield the 3D tracer distribution of the patient. In the body, the tracer accumulates at specific physiological sites, where it is metabolized. This accumulation can be seen in the PET images.

The intensity of accumulations can be evaluated by means of the *standardized uptake value* (SUV). SUV is defined as the ratio between decay corrected signal intensity [Bq/ml] and injected tracer activity per patient body weight. Considering decay correction of the injected activity for the time window between tracer injection and measurement, SUV is calculated as

$$SUV = \frac{A\left[\frac{\mathrm{Bq}}{\mathrm{ml}}\right]}{A_0\left[\frac{\mathrm{Bq}}{\mathrm{ml}}\right]/w\,[kg]} \cdot \frac{1}{\rho_{H_2O}\left[\frac{kg}{10^3 ml}\right]} \cdot e^{-ln(2)\cdot t/T} \tag{3.15}$$

where A is the tissue activity concentration, A_0 the initially injected activity and w the patient's body weight. t is the time passed between injection and measurement and T is the half-life of the tracer isotope. Segmentation and quantification of PET images is usually conducted with isocontours, which represent a percentage of the maximum SUV within a region or volume of interest.

3.3.2 Amino Acid PET with ^{18}F-FET

In nuclear medicine, radionuclides are bound to metabolic substances (pharmaceuticals), forming a so called radiopharmaceutical, often referred to as *tracer*. The detection of malignancies via PET is based on the different metabolisms of these tracers.

A prominent example is the radioactive tracer [^{18}F]-fluoro-2-deoxy-D-glucose (^{18}F-FDG). Deoxy-D-glucose is a type of sugar, which is labeled with the β^+ isotope ^{18}F with a half-life of 109.8 min. Fast-growing tumors have an increased glucose metabolism. Therefore, ^{18}F-FDG accumulates in such tumor cells and can be detected with a PET measurement. For detection of glioma, however, usage of ^{18}F-FDG is unsuitable due to the high glucose metabolism of the brain, which leads to an increased background signal. Tracer accumulation in tumor lesions can therefore not be sufficiently distinguished from the high background signal. In addition, ^{18}F-FDG is also taken up by inflammatory cells.

Amino acids (AA) serve as building blocks for proteins and precursors of hormones and neurotransmitters. Tumor cells frequently exhibit enhanced protein synthesis and amino acid transport [Huang and McConathy, 2013], whereas both processes are relatively low in healthy brain tissue. Hence radioactive labeled amino acids present potentially suitable compounds for detection of tumor tissue. The low uptake of AA in inflammatory tissue yields advantageous specificity of these tracers compared to ^{18}F-FDG [Del Sole et al., 2001]. Unlike in contrast enhanced MRI, a disrupted blood brain barrier is not a prerequisite for intra-tumoral AA accumulation.

For interpretation of tracer pharmacokinetic analysis, a detailed comprehension of the amino acid tracers metabolism is mandatory. Methyl or ethyl groups in most amino acid radiotracers prevent them from being incorporated into protein synthesis or metabolic pathways. Thus, tracer accumulation in tissues is mainly based on transport systems [Ishiwata et al., 1993]. After being transport into cells, different amino acid tracers present with specific metabolic fates, which can be used for tumor imaging. For most amino acid tracers, uptake is governed by transport via specific amino acid carrier systems, namely the sodium-independent amino acid transport system L. System L amino acid transporters, which transport a variety of neutral amino acids, play a superior roll in the tracer kinetics with respect to survival and growth of tumor cells. They are therefore widely expressed in primary human cancer cells [Imai et al., 2010; Zitron et al., 2013; Del Amo et al., 2008]. Since L-system transport is reversible [Verrey, 2003], efflux of non-metabolized amino acids is possible as well.

Various tracer combinations with amino acids have been studied for tumor imaging. Amongst them L-[methyl-^{11}C]methionine (MET) for PET and 3-[^{123}I]iodine-α-methyl-l-tyrosine (IMT) for *single photon emission computed tomography* (SPECT) represent the most used ones [Jager et al., 2001]. However, SPECT suffers from the lower spatial resolution compared to PET imaging. On the other hand, the short half-life of ^{11}C allows MET-PET at centers with on-site cyclotron only. These reasons resulted in the desire for a ^{18}F-labeled amino acid tracer. The most common of those tracers is O-(2-[^{18}F]fluoroethyl)-l-tyrosine (^{18}F-FET) [Wester et al., 1999], shown in figure 3.7, which enables the broad application of amino acid PET in clinical routine due to its easy production in sufficient amounts. ^{18}F-FET is metabolically stable and shows only minor degradation in the human body [Pauleit et al., 2003]. It was shown that ^{18}F-FET is not incorporated into proteins and does not participate in specific metabolic pathways [Pauleit et al., 2003]. The increased uptake derives from transportation only. Due to the lack of participation in protein synthesis and metabolism after transport, ^{18}F-FET uptake can be used for measuring amino acid transport rates. Heiss et al. [1999] presented that ^{18}F-FET uptake into tumor

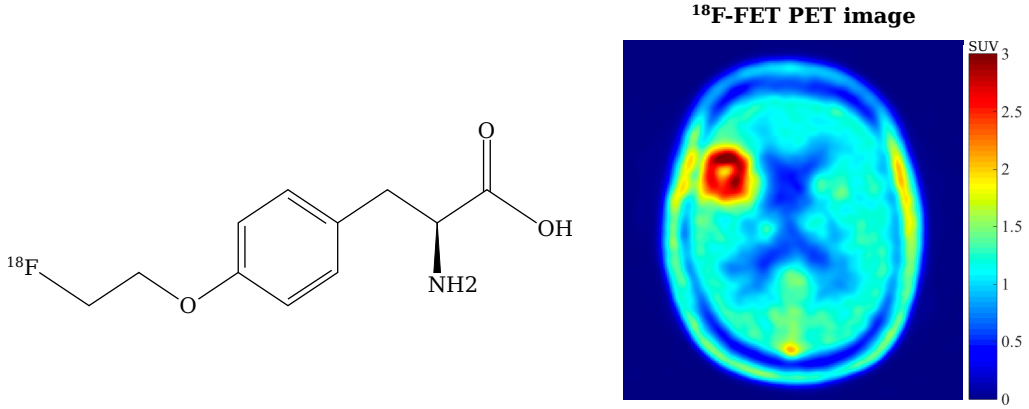

Figure 3.7: The O-(2-[^{18}F]fluoroethyl)-l-tyrosine molecule and its uptake distribution in a brain tumor patient. The tracer distribution is shown in units of the *SUV*.

cells is mainly caused by the L-type transport system. ^{18}F-FET presents with significantly lower uptake in inflammatory cells compared to ^{18}F-FDG and MET and thus provides higher specificity for differentiation between tumor tissue and inflammation. In summary, ^{18}F-FET shows little metabolism and remains chemically stable after accumulation in tumor tissue. Nevertheless the increased regional uptake of ^{18}F-FET in the brain is not 100% specific for glioma tissue. For instance, basal ganglia present with physiological uptake of ^{18}F-FET [Langen et al., 2006]. In addition, studies showed low urinary excretion corresponding to a high ^{18}F-FET concentration in the blood [Pauleit et al., 2003]. This leads to visualization of large vessels which can lead to misinterpretation of brain tumors with intense vascularization.

The infiltrative nature of high grade glioma results in difficulties for tumor extent detection and target delineation in radiotherapy. ^{18}F-FET PET offers the possibility to overcome these problems, as it offers high sensitivity and specificity for glioma tissue and high ^{18}F-FET SUV has been correlated with cell density [Pauleit et al., 2005; Stockhammer et al., 2008]. ^{18}F-FET positive volumes have been associated with relapse patterns of glioma patients after the application of chemotherapy [Weber et al., 2009] and have been shown to provide a prognostic value for progression-free and overall survival [Piroth et al., 2011]. Several authors studied response assessment [Dhermain et al., 2010] and applicability of ^{18}F-FET PET for radiotherapy planning [Grosu and Weber, 2010], [Weber et al., 2008], both in primary [Rosenschold et al., 2014] and recurrent glioma [Grosu et al., 2005]. The possibility for improved target delineation by usage of ^{18}F-FET PET is especially interesting with regards to the steep dose gradients in ion radiotherapy [Rieken et al., 2013].

3.3.3 Dynamic ^{18}F-FET PET

Dynamic PET acquisition is often used to study tissue physiology and uptake kinetics. The probably most common example is dynamic ^{18}F-FDG PET. Analysis of the time activity curves is analogue to evaluation of DCE MRI data. Pharmacokinetic models are fitted iteratively to the data in order to obtain parameter estimates of physiological quantities (see section 3.4.5). While most ^{18}F-FET PET studies rely on static uptake

images, recently it has been suggested that dynamic imaging can be useful for staging of glioma [Pöpperl et al., 2007]. Dynamic ^{18}F-FET PET has been presented in several studies, however analysis with pharmacokinetic models is rarely performed. Most studies either focus on the analysis of single frames [Weckesser et al., 2005] or resort to qualitative description of time-activity curve types [Jansen et al., 2014; Thon et al., 2015]. Pöpperl et al. [2006] introduced the method of *weighted frames* for grading of recurrent gliomas. The technique takes the physiological dynamics of ^{18}F-FET into account and quantifies the changes between time frames in order to account for the individual time-course. Thiele et al. [2009] used pharmacokinetic models among other methods for evaluation of the prognostic value of dynamic ^{18}F-FET PET in a group of nine high-grade glioma patients. However, dynamic data modeling was performed on time-activity curves averaged over the whole lesion, thus neglecting tumor heterogeneity. Furthermore limitations in their analysis software only allowed for qualitative investigation of the goodness of fit.

3.4 Pharmacokinetic Modeling and Indicator Dilution Theory

Pharmacokinetic modeling, sometimes also called tracer kinetic modeling, is the foundation for analysis of physiology studying time series in CT, MRI and PET. In fact, early models for DCE MRI derived from CT perfusion measurements and were built on the principles that had already been used to study metabolism kinetics in dynamic PET series. Since parameter estimation from pharmacokinetic models in both DCE MRI and PET is important for the course of this thesis, a general review of the basic principles, applicable to all modalities and studied substances, is presented. In the later sections, more detailed explanations of models applied in the respective imaging scenario and the meaning of the extracted parameters will be given. More detailed literature on the general theory of compartmental analysis can be found in Jacquez et al. [1985], and the dedicated applications on DCE MRI and PET are thoroughly reviewed in Sourbron and Buckley [2011] and Phelps [2004], respectively.

3.4.1 General Terms and Definitions

On a general scope, the analysis of the time course of a substance through the tissue is based on the *indicator dilution theory* (IDT). An *indicator* is a substance that is introduced into a physiological system and can be detected. Measuring the path of the indicator yields physiological information about the system. An important aspect is that the indicator must not change the system and its behavior. *Tracers* are a type of indicator with the same chemical composition as the studied systemic substance, but can be detected separately. Radioactive labeled substances used for PET, e.g. ^{18}F-FDG are tracers, whereas MRI contrast agents, such as gadolinium chelates, are typically indicators. For the following discussion, the behavior of the more general indicators will be reviewed.

Within a sample of tissue, the change of material of systemic substances is driven by influx through an entity of inlets ($i \in Inlets$) and outflux via a number of outlets ($o \in Outlets$), as shown in figure 3.8. The time an indicator particle needs for entering the tissue trough an inlet and leaving it through an outlet is referred to as *transit time*. Considering all inlets and outlets, this transit time has the form of a probability distribution $H(t)$. The *mean transit time* is the expectation value of $H(t)$.

The *volume of distribution* V is the volume of systemic substance containing the indicator. As the true volume of distribution is difficult to access, definition is often done by normalizing the volume of distribution to the volume of tissue. This normalized volume of distribution ν can thus take values between 0 and 1. The *concentration* $c(t)$ of the indicator in tissue is defined as the amount of indicator divided by the volume of distribution. The *tissue concentration* $C(t)$ is linked to $c(t)$ via

$$C(t) = \nu \cdot c(t) \tag{3.16}$$

The flux J is defined as the amount of indicator passing through an inlet or outlet per

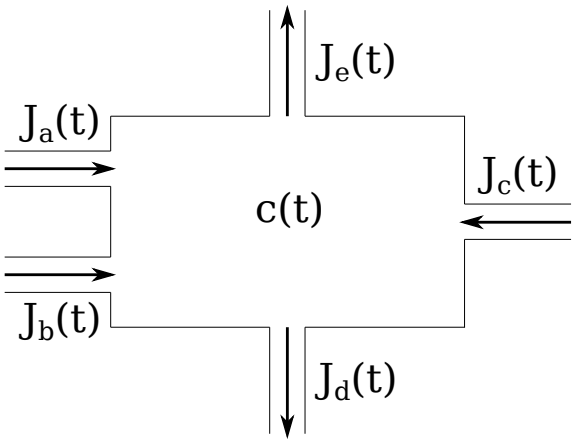

Figure 3.8: An element of tissue, having three indicator inlets [a, b, c] and two outlets [e, d]. The change of the indicator concentration $c(t)$ is the difference between total indicator influx $J_a(t) + J_b(t) + J_c(t)$ and total outflux $J_e(t) + J_d(t)$.

unit of time. The rate of change of the amount of indicator in the tissue sample can be expressed as the difference between all influx and outflux:

$$\frac{dC}{dt}(t) = \sum_{i \in Inlets} J_i(t) - \sum_{o \in Outlets} J_o(t) \tag{3.17}$$

3.4.2 Linear and Stationary Systems

In most cases it is safe to presume *linear* and *stationary* behavior of the indicator in tissue. Linear means, that the system response to the indicator influx is directly proportional to the amount of indicator influx. Stationary systems are systems where the response of the influx is independent of the arrival time, and in particular does not change during the measurement. For linear and stationary systems, the transit time distribution $H(t)$ acts as propagator for of the system [Meier and Zierler, 1954]:

$$\sum_{o \in Outlets} J_o(t) = \sum_{i \in Inlets} H_i(t) * J_i(t) \tag{3.18}$$

where $*$ denotes the convolution of $H_i(t)$ and $J_i(t)$. Using this, the concentration can be written in terms of a *residue function* $R(t)$ (see figure 3.9):

$$C_m(t) = \sum_{i \in Inlets} R_i(t) * J_i(t) \tag{3.19}$$

$$R_i(t) = 1 - \int_0^t H(t')dt' \tag{3.20}$$

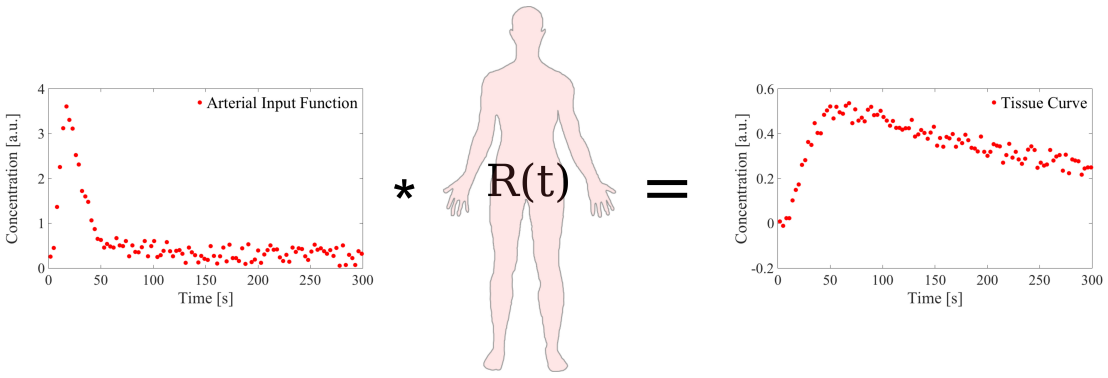

Figure 3.9: The time course of an indicator in tissue (measured concentration-time-curve) can be described as a convolution of the concentration in the arterial inlet (AIF) with a tissue and indicator specific residue function $R(t)$. The goal of pharmacokinetic analysis is to find this residue function.

$R_i(t)$ represents the fraction of entering particles with transit time larger than t, or in other words the number of particles, that are left in tissue at time t after entering at $t = 0$.

The goal of every pharmacokinetic analysis is to determine the residue function $R(t)$. This can be done using a model-free, purely numerical method often referred to as "deconvolution" [Rempp et al., 1994]. Alternatively, the tissue architecture and interactions can be modeled mathematically, which leads to a functional representation $R(t, \phi_i)$. $\{\phi_i\}$ is the set of model describing parameters. This technique is pursued in the following section.

3.4.3 Modeling Residue Functions: Compartmental Systems

Indicator behavior is often studied in *compartments*, which are defined as homogeneous and well-mixed macroscopic subunits of the physiological systems. Compartments describe the amount of substance that kinetically acts as homogeneous and well-mixed. A compartment does not necessarily need to be a physical volume or physiological space. It can also refer to a certain state of the indicator, say after a chemical interaction, for example in the case of ^{18}F-FDG. Multiple compartments interact via the exchange of material and thus form a compartmental system. The exchange is driven by fractional transfer coefficients, defined as the fraction of a the compartment material, that is transferred per unit of time.

In a linear compartment system, the influx and outflux are assumed to be directly proportional to the concentration [Sourbron and Buckley, 2011]

$$J_i(t) = k_i \cdot c(t) \tag{3.21}$$
$$J_o(t) = k_o \cdot c(t) \tag{3.22}$$

k_i and k_o are *exchange rates*, sometimes referred to as *clearance* of the inlet or outlet.

Inserting this relation into equation 3.18, the basic laws of interactions in compartment m can usually formulated as first order differential equation

$$\nu_m \frac{dc_m}{dt}(t) = \sum_{i \in Inlets} k_i \cdot c_i(t) - \sum_{o \in Outlets} k_o \cdot c_o(t) \tag{3.23}$$

Hence, a system of n differential equations leads to n coupled differential equations.

For $n \leq 3$, a closed-from analytical solution can be derived for functional representation of $R(t)$. Using the linear relation between flux and concentration 3.23 in the residue function formulation 3.19, the concentration in compartment m can be stated as:

$$C_m(t) = \sum_{i \in Inlets} k_i \cdot R_i(t) * c_i(t) \tag{3.24}$$

For a single compartment, the residue function can be expressed as a mono-exponential function, decaying with the mean transit time of the compartment:

$$R_m(t) = e^{-t/T_m} \text{ with } T_m = \frac{\nu_m}{\sum_{o \in Outlets} k_o} \tag{3.25}$$

In most cases, it is safe to assume that each compartment has only one inlet. In this case, the time-dependent total tissue concentration $C_T(t) = \sum_{m=1}^{n} \nu_m c_m(t)$ is related to the temporal course of the concentration in a supplying blood vessel $c_a(t)$ as

$$C_T(t) = k_p \cdot R(t) * c_a(t) \tag{3.26}$$

$$R(t) = \sum_{m=1}^{n} R_m(t) \tag{3.27}$$

The influx concentration $c_a(t)$is called *arterial input function* AIF and can be measured either directly from blood samples or from the signal changes in the image itself.

In summary, there are two ways of describing the time-dependent interplay of the concentrations of a multi-compartmental system and the time-course of total tissue concentration: either by the system of coupled differential equations, or by the convolution of the tissue residue function with the arterial input function. Solving differential equations with numerical algorithms can be time consuming, whereas convolutions can be performed very fast with modern computational algorithms.

3.4.4 Compartment Models in DCE MRI

DCE MRI is based on the concentration time course of MRI contrast agents in tissue. Contrast agents, such as gadolinium chelates, are extracellular contrast agent, thus their volume of distribution is restrained to the blood (*plasma*) and the *EES*. The microcirculation of these two compartments, having fractional volumes ν_p and ν_e, is generally described

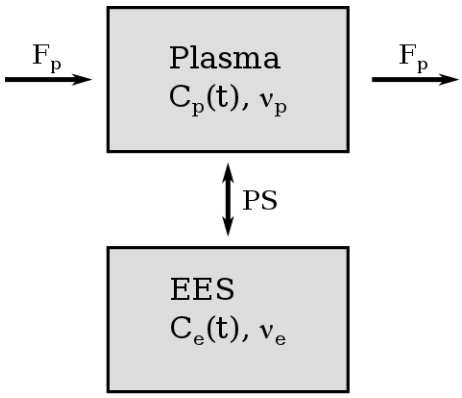

Figure 3.10: The two compartment exchange model describes microcirculation with two compartments: the plasma and the EES with fractional volumes ν_p and ν_e respectively. Contrast agent is transported from the blood (artery) into the capillary bed with plasma flow F_p. The rate of CA exchange over the capillary walls into the interstitial is the permeably-surface-area product PS.

with the *two compartment exchange model* (2CXM) [Brix et al., 2004], shown in figure 3.10.

CA is transported into the capillary bed through the artery with flux J_a and transported away through the venous drain J_v. From the plasma, the CA can cross over the capillary wall into the interstitial with flux J_e. This transport is bidirectional, hence the plasma is fed with an inlet flux J_i from the EES

$$J_a(t) = F_p \cdot c_a(t) \tag{3.28}$$
$$J_v(t) = F_p \cdot c_p(t) \tag{3.29}$$
$$J_e(t) = PS \cdot c_p(t) \tag{3.30}$$
$$J_i(t) = PS \cdot c_e(t) \tag{3.31}$$

$c_p(t)$ is the CA concentration in the capillaries (plasma) and $c_a(t)$ is the arterial concentration. F_p denotes the *plasma flow*, carrying indicator into the tissue. PS is the *permeability surface area product*, that quantifies transport over the capillary membrane. Permeability P is defined as the transport of indicator per unit of wall and per concentration. Since the area of the wall is unknown, P is integrated over the whole volume, leading to PS.

Following the formalism presented above, the concentration in the plasma compartment has two inlets (J_a and J_i) and two outlets (J_v and J_e). It can thus be written as

$$\nu_p \frac{dc_p(t)}{dt} = J_a + J_i - J_v - J_e \tag{3.32}$$
$$= F_p(c_a(t) - c_p(t)) - PS(c_p(t) - c_e(t)) \tag{3.33}$$

The interstitial volume exchanges tracer only with the plasma with the exchange rate PS, hence

$$\nu_e \frac{dc_e(t)}{dt} = PS(c_p(t) - c_e(t)) \tag{3.34}$$

The total tracer concentration in tissue yields

$$C_T(t) = \nu_p \cdot c_p(t) + \nu_e \cdot c_e(t) \tag{3.35}$$

The two mass balance equations yield residue functions $R_p(t)$ and $R_e(t)$:

$$R_p(t) = e^{-tK_1} + T_B K_2 \epsilon \left(e^{-tK_2} - e^{-tK_1}\right) \tag{3.36}$$

$$R_e(t) = (1 - T_B K_2)\epsilon \left(e^{-tK_2} - e^{-tK_1}\right) \tag{3.37}$$

$$R(t) = R_p(t) + R_e(t) \tag{3.38}$$

with the abbreviations

$$K_{1,2} = \frac{1}{2}\left(\frac{1}{T_p} + \frac{1}{T_e} \pm \sqrt{\left(\frac{1}{T_p} + \frac{1}{T_e}\right)^2 - 4\frac{1}{T_p}\frac{1}{T_e}}\right) \tag{3.39}$$

$$\epsilon = \frac{K_1 - T_B^{-1}}{K_1 - K_2} \tag{3.40}$$

T_p and T_e are the plasma and interstitial mean transit time, respectively, and T_B is the mean transit time of a hypothetical intravascular tracer. They are linked to the four parameters defining the model by

$$T_p = \frac{\nu_p}{PS + F_p} \; T_e = \frac{\nu_e}{PS} \; T_B = \frac{\nu_p}{F_p} \tag{3.41}$$

With this, the total tissue concentration can be written as

$$C_T(t) = F_p \left((1 - \epsilon)e^{-tK_1} + \epsilon \cdot e^{-tK_2}\right) * c_a(t) \tag{3.42}$$

The *extended Tofts model* (eTM) [Tofts et al., 1999] is widely used in clinical applications, where data quality is often insufficient to resolve additional structures, in particular the plasma flow. It derives from the 2CXM as approximation for the highly perfused regime by substituting the complex plasma residue function 3.37 with a delta distribution. Convolution with the arterial input concentration then yields:

$$c_t(t) = \nu_p \cdot c_a(t) + K_{trans} \cdot e^{-t\,K_{trans}/\nu_e} * c_a(t) \tag{3.43}$$

A very common notation is to write $k_{ep} = K_{trans}/\nu_e$. The eTM is an extension of the

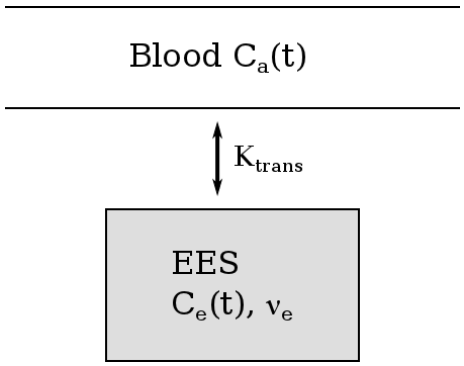

Figure 3.11: The classical Tofts model models contrast agent exchange between the blood and the interstitial volume directly. This assumption is only valid for weakly vascularized tissues with $\nu_p \approx 0$. In the high perfusion regime, the plasma residue function can be approximated by a delta distribution, leading to the extended Tofts model.

classical Tofts model [Tofts and Kermode, 1991], one of the initial models in compartmental analysis of DCE MRI, which assumes contrast agent exchange directly between blood and EES (see figure 3.11). The classical Tofts model is a one-compartment model with a single-exponential residue function, depending on two parameters: the transfer constant K_{trans} and the volume of the EES ν_e.

$$c_t(t) = K_{trans} \cdot e^{-t\, K_{trans}/\nu_e} * c_a(t) \tag{3.44}$$

The model assumptions hold true only for weakly vascularized tissue, where the capillary bed (plasma volume) can be neglected. In tumors this condition is not necessarily fulfilled.

3.4.5 Compartment Models in Dynamic PET

One of the main differences between tracer-kinetic modeling of dynamic PET and DCE MRI is that in PET, transport between two compartments does not necessarily have the same value in both directions. Since PET compartments often describe metabolic states of the tracer, it is possible that the transfer between the two states can happen at different rates or the chemical modulation of the tracer is not reversible and hence exchange between the compartments only works in one direction. The simplest model is the *one tissue compartment model* (1TCM), which is the PET analog the classical Tofts model in DCE MRI. It is a two compartment model that describes the tracer exchange between the blood pool and the tissue pool. Since the blood concentration is the measured AIF, $c_a(t)$, the remaining differential equation for the tissue concentration $c_1(t)$ yields an exponential residue function

$$c_1(t) = K_1 \cdot c_a(t) * e^{-k_2 \cdot t} \tag{3.45}$$

The *two tissue compartment model* (2TCM), as shown in figure 3.12, is a 3-compartment model. The compartments might describe for example the tracer in blood plasma, tracer in

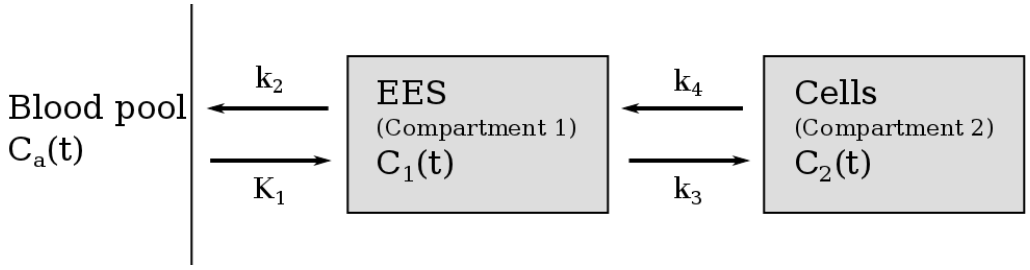

Figure 3.12: A general two tissue compartment model, describing the kinetics of a tracer that can be exchanged between the blood pool and the interstitial volume with exchange rates K_1 and k_2. From the interstitial space, the tracer can also be transported into cells. The transport process is quantified by the transport rates k_3 and k_4.

the EES and tracer in cells, respectively. Again, the concentration in the blood pool $c_a(t)$ is commonly measured directly, leaving two differential equations for the concentrations $c_1(t)$ and $c_2(t)$:

$$\frac{dc_1(t)}{dt} = K_1 c_a(t) - k_2 c_1(t) + k_4 c_2(t) - k_3 c_1(t) \tag{3.46}$$

$$\frac{dc_2(t)}{dt} = k_3 c_1(t) - k_4 c_2(t) \tag{3.47}$$

The analytical closed-form solution is given by

$$c_1(t) = \frac{K_1}{\alpha_2 - \alpha_1} c_a(t) * \left[(k_4 - \alpha_1)e^{-\alpha_1 t} + (\alpha_2 - k_4)e^{-\alpha_2 t}\right] \tag{3.48}$$

$$c_2(t) = \frac{K_1 k_3}{\alpha_2 - \alpha_1} c_a(t) * (e^{-\alpha_1 t} - e^{-\alpha_2 t}) \tag{3.49}$$

$$\text{with: } \alpha_{1,2} = \frac{(k_2 + k_3 + k_4) \mp \sqrt{(k_2 + k_3 + k_4)^2 - 4k_2 k_4}}{2} \tag{3.50}$$

A prominent example, where three compartments are needed is the tracer ^{18}F-FDG. The compartments describe ^{18}F-FDG in blood plasma, ^{18}F-FDG in tissue and phosphorylated ^{18}F-FDG in tissue, respectively. ^{18}F-FDG can diffuse nearly free between EES and cellular space, thus no distinction between these two in form of a compartment is necessary and they can be put together as the compartment "FDG in tissue". The phosphorylation process is not reversible, thus for ^{18}F-FDG, $k_4 = 0$ can be assumed.

For dynamic ^{18}F-FET-PET data, Thiele et al. [2009] used the 1TCM and 2TCM amongst other analysis approaches to determine the value of the determined parameters for the clinical outcome of patients with glioblastoma. The choice of a 2TCM topology was based on the bidirectional transport of ^{18}F-FET to tumor cells. It is hypothesized that after crossing the blood-brain barrier, ^{18}F-FET is taken up specifically by LAT2 transporters, a bidirectional L-type amino acid transporters regulating neutral amino acid transport from extracellular fluids into the cells, which is located on the membrane of tumor cells. Hence the 2TCM would represent ^{18}F-FET in the interstitial space after crossing the blood-brain

barrier and ^{18}F-FET in cells after uptake through LAT2. Their results showed better goodness-of-fit but less robust results amongst the patients studied for the 2TC model compared to the 1TCM. However they fitted mean TACs within the tumor volumes, thus neglecting possible heterogeneity, and accessed the goodness of fit on a visual basis.

3.4.6 Non-Compartmental Analysis

In cases where data quality does not allow for proper pharmacokinetic compartment modeling to be performed, one can resort to more simple, non-compartmental pharmacokinetic analysis of the concentration-time curves by determining curve describing parameters. Parameters in non-compartmental analysis are often deduced from statistical moment analysis. The zeroth moment of the concentration time curve, often referred to as *area under the curve* (*AUC*)

$$AUC = \int_0^T C(t)\, dt \tag{3.51}$$

is a popular parameter for "landscaping" of dynamic image series, as it yields stable results and is helpful for the assessment of tissue physiology. On the general scope of pharmacokinetic theory, the *AUC* of a substances concentration-time curve reflect the total amount of the substance reaching systemic circulation and thus enables comparison of bioavailability of the substance. For dynamic MRI using contrast agents in particular, the *AUC* is related to the blood volume, as shown by Rosen et al. [1991].

The ratio between the zeroth and first moment of the concentration time curve [Gibaldi and Perrier, 1982], [Riviere, 2011]

$$MRT = \frac{AUMC}{AUC} = \frac{\int_0^T t \cdot C(t)\, dt}{\int_0^T C(t)\, dt} \tag{3.52}$$

yields a parameter called *mean residence time* (*MRT*). *MRT* represents the elimination rate of a substance from the body and can be interpreted as "half-life" of the substance, describing its persistence in the body. It is inversely related to the elimination rate k_{el} of an open one-compartment model

$$k_{el} = \frac{1}{MRT} \tag{3.53}$$

Two further quantities, the *peak (plasma) concentration* C_{max} and the corresponding *time to peak* (*TTP*), are of potential interest for pharmacokinetics. The peak concentration marks the point at which alienated and absorbed amount of the substance are equal and is related to the absorption and elimination rates. The *TTP* is dependent on the absorption rate [DiPiro, 2010].

3.5 Image Processing

3.5.1 Registration

The clinical usage of medical images often resorts to complementary information gained from different imaging modalities. Thus, proper integration of the separate image data is often required. The task at hand is to bring the modalities in question into spatial alignment. This so-called registration procedure is a key pre-processing method in medical image computing and gains more and more importance due to a growing number and diversity of modalities. An apparent example is the combined usage of CT and MRI images in radiotherapy treatment planning.

In general, image registration tries to align corresponding anatomical or functional locations in different images. The goal is to find a transformation $T : (x, y, z) \rightarrow (x', y', z')$ mapping a point (x, y, z) in the source or moving coordinate system to the corresponding point (x', y', z') in the target coordinate system. An intra-subject registration aligns images from different modalities (multimodal) or different time points (serial) of one and the same subject. In other clinical settings, it is supposably useful to register images from different subjects for inter subject comparison. Both approaches involve the search for an optimal, or at least sufficient, geometric transformation, that maximizes image correspondence. Registration routines can be divided into 4 parts:

- The *transformation model* defines the geometric transformation between images. In general, one can distinguish between rigid, affine, projection and deformable transformations
- The degree of alignment is measured by the *similarity measure*. Feature based approaches aim at minimizing distances of corresponding features, such as reference points, within the image. However this strategy requires landmark detection or segmentation algorithms. Voxel based similarities on the other hand directly use image intensities in an attempt to measure the degree of similarity and spatial correspondence.
- An *optimization method* is used to optimize the similarity measure
- For assessment of accuracy and robustness, usually a *validation protocol* is defined to measure performance of the registration algorithm.

The complexity of the transformation model is characterized by the degrees of freedom involved. The simples transformation of image coordinates is the rigid transformation having 6 degrees of freedom, three from translational and three from rotational movements. Such rigid transformations are usually described in a transformation matrix with homogeneous coordinates: $y_i = a_{ij}x_j$, where x and y are the old and new coordinate vectors respectively. Images of the head can usually be transformed using these models, because the skull is rigid. Thus it is safe to assume, that it underlies no considerable changes, except growth in young patients. Other transformation include affine transformations, which include correction for scaling and shearing, and projection transformations, relating 3D and 2D images. A coordinate transformation that maps lines onto curves is called elastic or deformable transformation. Elastic transformations are often used for soft tissue mapping,

for example of the liver or lung. There are various approaches for similarity measures as well as optimization methods, but their review would go beyond the scope of this work. Hence they are not discussed further, but an overview can be found in Deserno [2011]. For registration of different image modalities in this work, the MatchPoint framework [Floca, 2009] integrated in MITK was utilized.

3.5.2 Segmentation

Segmentation is the process of dividing an image into semantically connected regions and can be seen as a pre-stage of classification. In medical applications it is used to define diagnostically or therapeutically relevant image areas, such as organ outlines or pathological target tissues. There are numerous approaches for segmentation, from manual and semi-automatic techniques to fully automatic algorithms. The following section presents an overview of segmentation techniques relevant to this work.

For many cases, manual segmentation by visually drawing the desired delineation is feasible, for example in target definition of GTV, CTV and PTV in radiotherapy. For some tasks, however, more sophisticated techniques, such as isocontours, Otsu thresholds or region growing are necessary to enable time-efficient analysis. Pixel-based approaches, that only consider the gray-scale intensity of each single pixel without consideration of the neighboring pixels, include static and adaptive thresholding techniques. Isocontours [Paulino et al., 2005], which are widely used for delineation of potential pathological uptake structures in PET, use static thresholds. They include all pixels within a given region with intensities exceeding a certain specified percentage of the maximum value in the region. The Otsu threshold is an adaptive thresholding technique, used for automated multi-segment determination based on an “object vs background” model. It determines histogram thresholds by minimizing the intra-class variance of the gray-scale values of the determined classes while maximizing the inter-class variance. Region growing (2D) and volume growing (3D) are agglomerative procedures, which is a type of region based method that considers only connected segments based on similarity measures. Starting from automatically or manually defined seed points, the algorithm iteratively includes neighboring pixels into the segment, if their corresponding similarity measure falls under a certain threshold, until no more spreading can be performed. The result of this algorithm is influenced by the number and position of seed points, as well as the applied similarity measure and its corresponding threshold. A completely different approach for multi-labeled, semi-automated image segmentation was proposed by Grady and Funka-Lea [2004]. For a given number of seed points, the algorithm assigns unlabeled voxels to a seed point that is most likely reached by a random walker starting from the pixel in question. The boundary constraints are applied as in graph theoretic electrical potentials. With these assumptions, the probability of the random walker first reaching a seed point is the solution to a Dirichlet problem with boundary conditions where the seed point in question is set to unity while others are fixed at zero.

3.5.3 Non-Linear Least Square Fitting

Parameter estimation in dynamic imaging is often performed by non-linear least square fitting of a pharmacokinetic model to a measured time course. The goal is to fit the model representing function to the measured curve in an iterative process, in order to find the set of model parameters that best describes the experimental data. Non-linear least square fitting fits the data by minimizing the sum of quadratic objective functions $f_i(x)$

$$\min_{\vec{x}} f(\vec{x}) = \sum_{i=1}^{m} f_i^2(\vec{x}) \tag{3.54}$$

Usually the sum of squared residuals , referred to as $\mathcal{X}^2$, is minimized with respect to the n model parameters $\vec{\phi} = \{\phi_1, ..., \phi_n\}$. This means that the objective functions take the form of the difference between the measured sample $C^*(t_i)$ and the model function $S(t_i, \vec{\phi})$ at time t_i in the measured time interval $t_i \in [t_0, T]$:

$$\min_{\vec{\phi}} \mathcal{X}^2(t, \phi_i) = \sum_{t_i=t_0}^{T} \left(C^*(t_i) - S(t_i, \vec{\phi}) \right)^2 \tag{3.55}$$

This poses an unconstraint optimization problem that can be solved by a number of different algorithms. The iteration process mostly breaks down to finding an approximation to the Hessian matrix. The above problem 3.55 can be written as

$$\min_{x} f(x) \sum_{i=1}^{m} f_i^2(x) = F(x)^T F(x) \tag{3.56}$$

with vector functions $F(x) = (f_1(x) f_2(x) ... f_m(x))^T$. The first derivative $\nabla f(x)$ follows according to the chain rule as

$$\nabla f(x) = \nabla F(x) F(x) \tag{3.57}$$

and hence the Hessian yields

$$\nabla^2 f(x) = \nabla F(x) \nabla F(x)^T + \sum_{i=1}^{m} f_i(x) \nabla^2 f_i(x) \tag{3.58}$$

Assuming that x^* is the solution to the optimization and $f(x^*) = 0$, then $f_i(x^*) = 0$ for all i and the model fits the data perfectly without errors. Using this, it follows that $F(x^*) = 0$ and thus $\nabla f(x^*) = 0$ as well, which would satisfy the first-order condition for an extremum. Furthermore, it implies that

$$\nabla^2 f(x^*) = \nabla F(x^*) \nabla F(x^*)^T > 0 \tag{3.59}$$

and hence the Hessian is positive semi-definite at the solution. From $F(x^*) = 0$ one can assume that $F(x) \approx 0$ for $x \approx x^*$. This leads to the approximation

$$\nabla^2 f(x) = \nabla F(x) \nabla F(x)^T + \sum_{i=1}^{m} \nabla^2 f_i(x) \approx \nabla F(x) \nabla F(x)^T \tag{3.60}$$

which only depends on first derivatives of $\{f_i\}$. Hence, if the model fits the data appropriately, the Hessian matrix can be found by using only first order derivatives. This is the approach of several methods for non-linear least square data fitting. The simplest algorithm is the Gauss-Newton method, which uses equation 3.61 directly to calculate a search direction from Newton's method

$$\nabla^2 f(x) p = -\nabla f(x) \tag{3.61}$$

$$\Rightarrow \nabla F(x) \nabla F(x)^T p = -\nabla F(x) F(x) \tag{3.62}$$

Solving for p gives the next iteration step $x \rightarrow x + p$. However, the Gauss-Newton method leads to poor results in cases, where the residuals at the solution are not small, because the function does not fit the data well.

The Levenberg-Marquardt algorithm is an extension of the Gauss-Newton method. It approximates the second term of the Hessian Matrix in equation 3.59 with the method of gradient descent by using

$$\sum_{i=1}^{m} f_i(x) \nabla^2 f_i(x) \approx \lambda I \tag{3.63}$$

with a scalar $\lambda \leq 0$

3.6 Classification and Machine Learning

Generative modeling of medical physiological interactions can be difficult in systems with complex underlying fundamental principles, since explicit mathematical formulations for all system influencing parameters have to be defined. Classification and pattern recognition tasks address this problem on an empirical, discriminative basis and are thus valuable tools for analysis of medical data, especially in the evaluation of large data cohorts (big-data). The search for recurrent patterns in data is interesting for the aim of the presented work as recurring image patterns on multi modal image sets present an chance for tissue classification and tumor growth prediction.

Pattern recognition tasks are often addressed with machine learning methods. On a given labelled training set, a general mapping is learned between the input data points and the corresponding classes that are known in advance. For the trainings set $\{X\}$ of observation variables x, the corresponding categories y, referred to as target vectors, are known in advanced. The result of the machine learning process is a function $y(x)$ that relates an input data point to an output category y. The *training phase* is the learning process of the assignment rule $y(x)$. In the *testing phase*, this rule is applied to a test set of previously unseen data points.

Regression algorithms attempt to predict a (possibly) continuous output value given a stream of input data. *Classification* algorithms deal with the task of assigning discrete categories to input data points. Most widely used classifiers are *support vector machines* (SVM) which can handle binary classifications problems with maximum-margin separation and good generalization for relatively little training data points at the same time. They project the data into a high dimensional space where it is easily separable. *Boosting* is another, iterative approach, building strong classifiers from linear combinations of many weak classifiers. They "boost" training examples one which the classifier works poorly, thus increasing their associated training weight. In *artificial neural networks*, which are inspired by working principles of the brain, a layered set of primitive units learns to predict output values for a given multi-dimensional input. In the feed-forward manner, each unit implements a non-linear transformation of its input and projects it down to the next layer. Learning is achieved by adjusting the weights between units. Tree-based models, based on *decision trees*, aim to exploit a training set in order to make prediction of the value of the target variable (class) for a new value of the input value.

3.6.1 Decision Trees

Decision Trees, as shown in figure 3.13, are tree-like graphs or models of decisions and their possible consequences. The so-called internal or split nodes represent a "test" on an characteristic attribute of the observation variable. Each outcome of a test, referred to as split, is represented by an outgoing branch from the split node. Terminal nodes, called leaves, represent the final classification or decision after all tests on the attributes are applied. The tests for decision making are organized hierarchically in a tree-like structure, and each way down the tree (lane) represents a classification rule. Given a previously unseen data point, the decision tree applies the predefined tests and the data point is sorted to a leaf node with a predictor, depending on the results of each test.

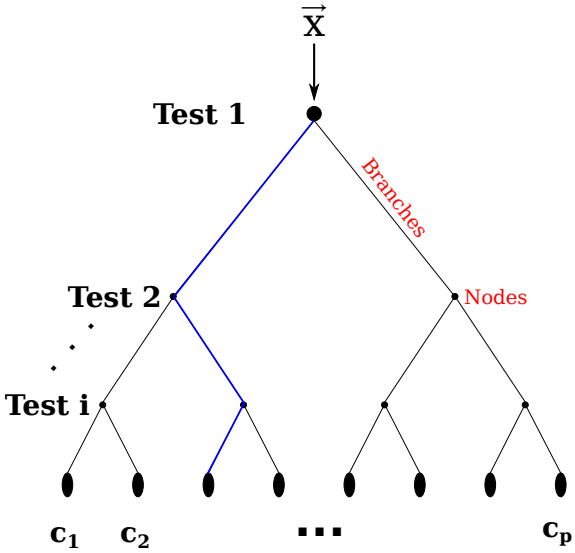

Figure 3.13: A decision tree is a hierarchical structure of tests on the attributes x_k of the observable $\vec{x}$. Each test results in a split of the node into branches. Each leaf represents a class c_j out of all p classes. After the observable is run down the tree (blue line) a certain class is assigned to it. During training, the parameters of the split at each node are optimize in such a manner that each of the N observables in the training sample $S = \left\{\vec{X}\right\} = \{\vec{x_1}, ..., \vec{x_N}\}$ is assigned with the right, previously known class.

Key to a decision tree is to establish all the test function associated to each internal node and the decision making predictors associated with each leaf. The concrete tree structure is learned automatically during training, by optimizing the parameters of the split functions at each internal nodes and the leaf predictors.

Using a training set of data points and the associated ground truth classes, the tree parameters are chosen to maximize the information gain of the split. The tree is grown from the training data, defined in terms of observation variables $\vec{x} = (x_1, ..., x_K)$ with K attributes, called features. The entire data set consists of N cases of $\vec{x}$: $S = \left\{\vec{X}\right\} = \{\vec{x_1}, ..., \vec{x_N}\}$. The cases $\vec{x_i}$ are each assigned a class label $c_m \in C = \{c_1, c_2, ..., c_M\}$ of all M available classes.

During growth of the tree, only a number of features $k < K$ is made available at each node. The node tries to find a classification of all training sample cases based on these k features, to find the best split of the cases into the p classes. If there are still wrongly classified cases in the child nodes, another test based on newly sampled k features is applied and the sample is split again. This process is repeated until all cases of the training sample are assigned to the right classes.

3.6.2 Random Forests

Breiman [2001] introduced the concept of *random forests*, an ensemble learning method for classification and regression problems. Random forests are built from a multitude of

uncorrelated, randomly trained *decision trees*. During training, a large number of trees is grown, each with a randomly sampled subset from the original data. For construction of the decision trees, $n < N$ cases are sampled with replacement from the original data S, building the training sample S'. This process is called out-of-bag bootstrapping. Usually $n = \frac{2}{3}$ is chosen. The sampling yields n pairs $\langle \vec{x} = (x_1, ..., x_K); c \rangle$ of samples $\vec{x}$ with K features and a corresponding class c.

In testing, a previously unseen data point is put down each of the trees in the forest. Each tree casts a "vote" for a class. The forest chooses the classification having the most votes over all trees in the forest. For regression problems, the output value is the mean prediction over all trees.

An important measure in classification and regression trees is the *Gini impurity*, a measure of the degree of incorrect classification of a sample if it is randomly labeled with a class. If f_i denotes the fraction of items labels with class c_i of all N samples $i \in \{1, 2, ..., N\}$, then the Gini impurity is calculated as

$$I_G(f) = \sum_{i=1}^{N} f_i(1 - f_i) = \sum_{i \neq k} f_i f_k \tag{3.64}$$

Classification errors can be mainly attributed to two things: correlation between the forest trees and lack of strength of each individual tree. A key aspect of the decision forest is the fact, that its component trees are all randomly different from one another, thereby improving the classification results. Correlation is decreased by introducing randomness in two different ways

1. Random training data set sampling: The training data set are sampled randomly. This is called bagging and refers to out-of-bag bootstrapping of the original data into training subsets
2. Randomized node optimization: Not all k available attributes of the data points are made available, but a number $k < K$ is specified such that at each node, k variables are selected at random out of the k and the best split on these m is used to split the node.

Random forests present a number of advantages for addressing classification problems. They run efficient on large data sets without the danger of overfitting and can handle a large number of both input variables and features. Furthermore they provide an estimate on variable importance and an error estimation of the classification result can be assessed.

3.7 The Medical Imaging Interaction Toolkit

In order to test different imaging modalities and protocols for their potential to contribute to an improved multi-parametric model of the tumor and tissue physiology, the necessity arises to display and analyze the various medical images from CT, MRI and PET. There is large collection of software solutions for visualization and image processing of medical data, commercial solutions coupled to imaging scanners as well as stand-alone open source software. A detailed review of these tools can be found in Wolf [2010]. Commercial software, such as MatLab [MatLab®, www.mathworks.com] and MeVis [MeVis®, www.mevislab.de], are closed "black-boxes", that allow no adaptation and flexibility for user specification. Open source extensible software, such as the 3D slicer [Gering et al., 1999] or OsiriX [Rosset et al., 2004], are ready-to-use end-user applications which can be extended by custom code. They provide high support on the graphical user interface (GUI) front end level, however their adaptability in terms of framework design is limited. Software toolkits on the other hand provide a high level of flexibility and user specification. Modern toolkits are often constructed as object oriented class libraries providing support for specific tasks with a high level of adaptability and flexibility. For medical imaging, they define a set of implemented methods and algorithms for image processing, visualization as well as data management. Nevertheless they are confined within their dedicated purpose and lack the possibility of easy end-user application with a graphical user interface. The medical imaging interaction toolkit MITK [Wolf et al., 2005] provides a good compromise between high development flexibility and support of end-user application interfaces. MITK is a free open-source software toolkit that supports development of interactive medical imaging software. It started as an in-house solution for reliable software development in medical imaging in the department of medical and biological informatics at the DKFZ. Originally designed only as a toolkit for support of interactive multi-view applications, recent developments have added an optional layer on the application level and an open-source end-user application using Qt for the GUI, shown in figure 3.14. With this, it represents a flexible yet easy to use software system covering all steps of a clinical workflow, including data handling and image analysis [Nolden et al., 2013]. MITK is implemented in C++ and released open-source in order to allow users application builds without any restrictions or obligations. It can be built under Windows, Mac OS and Linux, using the cross-platform, open-source build-system Cmake [www.cmake.org]. The graphical user interface is provided via the platform independent library Qt [www.qt.io]. The implementation follows a data-centric concept, which enables multiple consistent 2D and 3D views on the same data. The core is based on the Insight Segmentation and Registration Toolkit (ITK, www.itk.org) and the Visualization Toolkit (VTK, www.vtk.org), reusing as much as possible from these toolkits and adding missing features required for interactive image processing. It offers the use of further packages, e.g. Qt [www.qt.io], Boost [www.boost.org], DCMTK [www.dcmtk.org], OpenCV [Bradski and Kaehler, 2008] or SOFA [Allard et al., 2007], however inclusion of these is not necessarily required. The ITK is the most widely used toolkit in medical image processing, providing a large number of multi-dimensional image processing algorithms, especially for registration and segmentation tasks. The large collection of filters and file readers enable access to many file formats for MITK. The VTK is a popular toolkit for visualization of data. It includes the infrastructure for scalar, vector, tensor texture and volume visualization as well as a large number of algorithms for 3D computer graphics and image processing. MITK

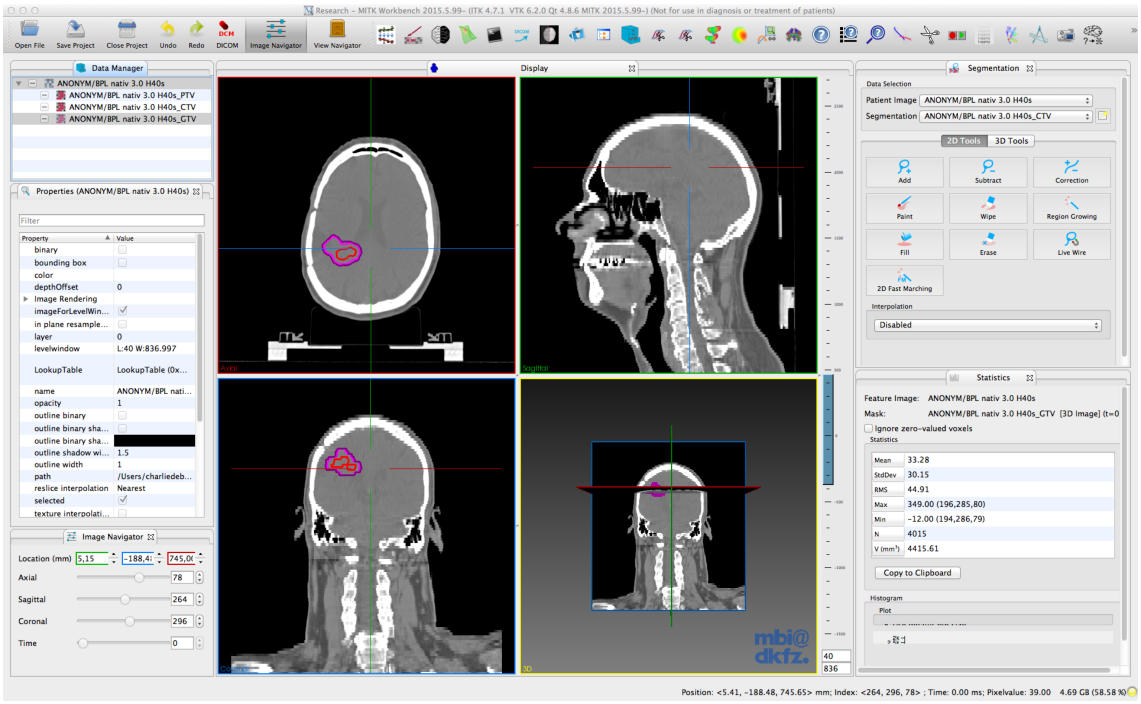

Figure 3.14: The *MITK workbench* provides a Qt based application interface for 3D display (3 views: axial, sagittal and coronal), processing and analysis of radiological images. Segmentation of the an image (in this case a treatment planning CT) can be performed with various 2D and 3D algorithms. The statistics plugin enables basic statistical analysis of image intensities within contours. Structure sets from treatment planning (GTV (red), CTV (magenta) and PTV(purple)) can be loaded via DICOM RT import.

uses the visualization pipeline for flexible combination of VTK-based and OpenGL-based rendering.

Originally MITK was intended as a toolkit and not an application or application framework and thus only contained basic support for building complete applications. In this role it allows the construction of applications specifically tailored for a medical image analysis task, providing only those features to the user (physician) that are required. Constant evolution and a growing number of users have led to the introduction of an extensions to offer support on the application-level, including a user interface concept and a ready-to-use application frame for rapid prototyping. The toolkit itself can also be used within existing software. Algorithms and routines are grouped in modules. A module represents a C++ class library covering a specific problem domain. Thus we implemented the basic fitting infrastructure for pharmacokinetic modeling of dynamic image data into a dedicated module. Framework functionalities are located in plugins, and a generic plugin framework enables easy development of service-oriented and modular systems. These plugins build enclosed workflows for a specific image processing task. The PET SUV calculation (section 4.3.1) and the model fitting configuration of perfusion MR data (section 4.2.1) are implemented as plugins, which can be accessed from the graphical user interface.

MITK supports DICOM[1] import and retrieval and the corresponding grouping of image slices into datasets for static as well as time resolved images. Additional features include volume visualization, measurements and statistics calculations of images and ROIs. It offers a variety of interactive slice-based and 3D segmentation tools, including several manual drawing tools, 2D and 3D region growing, absolute and Otsu thresholding amongst others. Morphological image operations, such as erosion and dilation, and Boolean operations (differences, unions, intersections) of segmentations are supported. New developments have introduced the import and visualization of RT structure sets and dose distributions via RT DICOM, which is an essential tool for the analysis and workflows presented in this work. For registrations, the MatchPoint framework [Floca, 2009] was used. A separate application MITK-Diffusion offers a number of plugins for image analysis and diagnosis on diffusion-weighted MR [Fritzsche et al., 2012].

[1]Digital Imaging and Communications in Medicine

3.8 Patient Data

Exemplary data for all studies involving patient data was taken from recurrent high grade glioma patients treated at the HIT[2] facility, more specifically data from the *CINDERELLA* trial (NCT01166308) [Combs et al., 2010] and data based on the CINDERELLA treatment protocol (CINDERELLA analog). These patients, who underwent a prior course of standard photon RT for the primary tumor, were irradiated with fractionated carbon therapy using single doses of 3 GyE (grey equivalent) and 10 to 16 fractions. Unlike patients with primary brain tumors, no surgery was performed, which allows the direct co-registration and comparison of pre- and post-treatment imaging modalities. The treatment volumes for irradiation with carbon ions were defined as the contrast enhanced region in T_1 weighted MRI, plus a safety margin of 5 mm.

Due to study purposes, some of these patients received multimodal imaging sequences. Aside from standard imaging protocols such as CT, T_1-weighted MRI with and without contrast agent and T_2-FLAIR sequences, the CINDERELLA protocol included functional MRI sequences for dynamic perfusion MRI (both DCE and DSC), DWI and susceptibility weighted MRI (*SWI*) sequences.

All patients received T_1-weighted MRI with and without contrast agent for the purpose of treatment planning, however in several cases these MRIs were acquired at external centers. The T_1-weighted MRI scans performed at the Heidelberg university clinic were conducted with a T_1 weighted MPRAGE sequence ($T_R = 1770$ ms, $T_E = 3.57$ ms, $\alpha = 15°$) at a 3T Siemens Verio MRI scanner with a resolution of $0.78 \times 0.78 \times 1.0\,\text{mm}^3$.

For all patients structure sets containing the treatment volumes *GTV* (gross tumor volume), *CTV* (clinical target volume) and *PTV* (planning target volume), based on the treatment planning CT and the T_1-weighted contrast enhanced MRI, and the calculated dose distributions from carbon irradiation treatment planning were available in the RT DICOM format.

26 patients received PET scans using the ^{18}F-FET tracer within 2 month prior to radiotherapy. Measurements were taken using a Siemens Biograph 6 PET scanner 30 to 40 minutes after intravenous injection of 150 MBq and 220 MBq of ^{18}F-FET.

From these 26 patients, 18 patients showed neuro-radiologically confirmed progressive diseases at an available follow-up examination, which was necessary for the presented studies in order to investigate the potential of the imaging modalities to predict tumor progress (see figure 3.15, left side). The other patients either exhibited stable disease at the time of the presented studies or follow up data was not available. All of the following studies were performed on data from the cohort of these 18 patients. From treatment planning MRI, the following sequences were available:

- 11 patients received dynamic ^{18}F-FET PET. The dynamic data was acquired for 40 min in 20 frames (6×20 s,8×60 s, 5×300 s).
- Except for two subjects, all patients also had received T_2 weighted FLAIR MRI (Resolution: $0.89 \times 0.89 \times 5\,\text{mm}^3$, $T_R = 8500$ ms, $T_E = 135$ ms $T_I = 2400$ ms).

[2] Heidelberger Ionenstrahl-Therapiezentrum

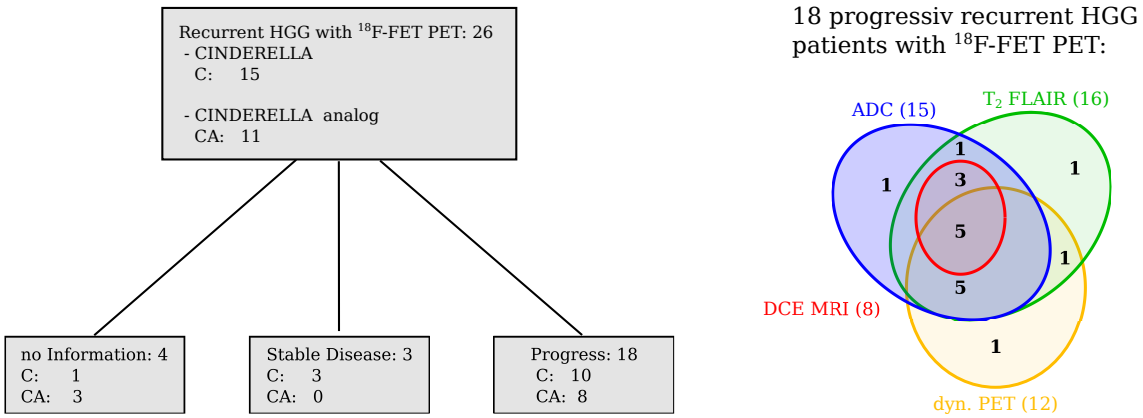

Figure 3.15: Available data from recurrent high grade glioma patients in the CINDERELLA trial or CINDERELLA affiliated. The left side shows the distribution of different endpoints (progress, stable disease, no information) of the 26 patients that received ^{18}F-FET PET scans. The Venn diagram on the right side illustrates the available multi-modal image data of the 18 patients, who presented with progressive disease.

- The scans performed at the university clinic included diffusion weighted MRI of six directions (Protocol *EPI_DIFF_b1200*, $T_R = 5000$ ms, $T_E = 83$ ms) at a resolution of $1.77 \times 1.77 \times 5\,\text{mm}^3$, providing parameter maps of the ADC and for two patients also maps of the FA. For 15 out of the 18 patients, ADC maps were available. In two cases, the maps of FA were available as well.
- For four patients, DCE MRI data was acquired with a T_1 weighted volumetric interpolated brain examination (VIBE) sequence at a resolution of 0.898mm×0.898mm×5mm and 21 equidistant time steps at a temporal sampling rate of 12.26 s. The sequence protocol *fl3d1* used $T_R = 5.54$ ms, $T_R = 2.52$ ms and a flip angle of 10°. As contrast agent bolus, the gadolinium chelate "Gadovist" was used.
- For eight patients, dynamic contrast enhanced T_2 weighted MRI series (DSC MRI) were available, however they were not used in the presented work.

Five patients in the cohort received additional MRI scans with the CINDERELLA protocol on the first and last day of radiotherapy. One additional patient received additional MRI on the last day of therapy only. These MRI studies provided ADC maps, FA maps and DCE MRI data in one, three and four additional patients. All of the 18 patients showed progressive diseases within a year (11 months) after radiotherapy. In 8 cases, the progression confirming MRI scan included all sequences from the CINDERELLA protocol.

All relevant patient data is summarized in table 3.1. The available data from different modalities is illustrated in figure 3.15 on the left side. Only five patients could provide with a complete multi-modal data set.

Table 3.1: Overview of patient histological diagnosis (Histology (primary tumor/recurrent tumor)), irradiation scheme (Dose (fractionation)), progress after the end of RT (Progress) and available image data (T_2 FLAIR, ADC maps, FA maps, DCE MRI data and dynamic ^{18}F-FET PET data) of the recurrent high grade glioma cohort with 18F-FET PET scans. Checkmarks mark the available data from imaging scans prior to RT. Blue checkmarks indicated that the respective sequence is available from the MRI on the first day of RT (one day before radiotherapy), instead of the planning MRI.

ID	Histo. (initial/recurrent)	Dose [GyE] (# fractions)	Progress [month]	FLAIR (T_2)	ADC	FA	DCE MRI	PET dyn.
1	Astro (II/III)	30 (10)	1	✓	✓	✓	✓	✓
2	GBM (IV/IV)	33 (11)	8.1	✓	✓	✓	✓	✓
3	GBM (IV/IV)	33 (11)	0.9	✓	✓	✓	✓	✓
4	Astro (II/IV)	33 (11)	1	✓	✓	✓	✓	×
5	GBM (IV/IV)	33 (11)	1	✓	✓	×	✓	×
6	GBM (IV/IV)	33 (11)	3.3	✓	✓	×	✓	×
7	GBM (IV/IV)	36 (12)	2.1	✓	✓	×	✓	✓
8	GBM (IV/IV)	39 (13)	9.9	✓	✓	✓	✓	✓
9	Astro (II/III)	39 (13)	0.9	×	✓	×	×	×
10	GBM (IV/IV)	39 (13)	2.5	×	×	×	×	✓
11	GBM (IV/IV)	30 (10)	6.6	✓	×	×	×	×
12	Astro (III/III)	33 (11)	3.1	✓	✓	×	×	✓
13	Oligo (III/III)	39 (13)	3.4	✓	✓	×	×	✓
14	Astro (III/III)	33 (11)	3.5	✓	✓	×	×	×
15	GBM (IV/IV)	39 (13)	8.5	✓	✓	×	×	✓
16	GBM (IV/IV)	39 (13)	1.4	✓	✓	×	×	✓
17	GBM (IV/IV)	30 (10)	11.5	✓	✓	×	×	✓
18	Astro (II/III)	33 (11)	3.5	✓	×	×	×	✓

4 Results

The goal of the presented thesis was to investigate the predictive value of parameters derived from perfusion MRI and amino acid PET with respect to tissue classification. The medical imaging interaction toolkit (MITK, Wolf et al. [2005]) was used as common software basis, as it covers all parts of basic image processing, including DICOM[1] import, registration, segmentation, binary image operations and statistics. Analysis software tools not yet available in MITK were developed during the course of the thesis.

A modality independent software module for fitting of dynamic data with user specific model functions was designed and implemented. The toolkit was intended in particular for pharmacokinetic modeling, but its design enables application to all different kinds of fitting tasks on 4D data sets. Software structure and implementation concepts are presented in chapter 4.1.

From this dynamic data analysis module, two dedicated plugins with specified analysis workflow and graphical user interface (GUI) were developed for application in pharmacokinetic modeling of dynamic contrast enhanced magnetic resonance imaging (DCE MRI) and dynamic positron emission tomography (PET) data.

The DCE MRI analysis plugin is briefly presented in section 4.2.1. The plugin was used to study perfusion data from recurrent high-grade glioma patients. The aim was to assess the ability of the determined parameters to identify tumor tissue at risk. Furthermore a simulation tool for generation of synthetic DCE MRI data from parameter images by inversion of the parameter estimating process was developed based on the dynamic data analysis module. With the simulation and fitting tools, studies on the 2 compartment exchange model (2CXM) were performed, in order to investigate accuracy and robustness of the parameter estimates depending on different configuration aspects of the fitting routine (section 4.2.3).

Plugins developed for analysis of PET images are presented in section 4.3.1. Two plugins were implemented for the evaluation of endpoint static PET images, the *SUV* calculation plugin and the isocontour plugin. These tools were used to study different segmentation techniques of the endpoint static ^{18}F-FET PET data, investigating the contour overlap with the treatment planning contours from contrast enhanced T_1 weighted MRI and with the progress tumor volume.

Furthermore a plugin for pharmacokinetic analysis of dynamic PET data was derived from the dynamic data analysis module. Suitability of different pharmacokinetic models for fitting the dynamic ^{18}F-FET were studied. Results are presented in section 4.3.3.

Using the presented software and results, a workflow for multimodal image analysis was

[1] Digital Imaging and Communications in Medicine

developed, which is described in section 4.4. The implementation of a method for combined analysis of the various image-derived parameters based on random forest machine learning is presented. Exemplary results of a classification analysis for tumor progress prediction are shown in section 4.4.3.

4.1 The MITK Dynamic Data Analysis Module

The presented thesis resorted to pharmacokinetic analysis of DCE MRI and dynamic PET data, particularly in combination with other imaging modalities. Hence, the need for a software solution, that can address the task of fitting in both modalities, is apparent. MITK was used to implement a software module for analyzing dynamic image data by means of non-linear least square (NLLS) fitting with a specified model function. The module provides necessary base classes for all data processing steps. It was designed with high modularity, allowing a large degree of flexibility and user specific definitions. The module is modality independent, thus application is not limited to a specific analysis purpose, e.g. pharmacokinetic modeling in DCE MRI, but can be used for various fitting tasks. Two dedicated applications with graphical user interfaces for pharmacokinetic modeling of DCE MRI and dynamic PET data were implemented in ready-to-use plugins. Applications of the model fitting routine and the non-compartmental analysis extension are shown in studies on data from DCE MRI (section 4.2) and dynamic PET (4.3).

4.1.1 Core Module and Fitting Framework Concepts

The presented module offers a software framework for iterative fitting of a measured data by means of NLLS, described in section 3.5.3.

Figure 4.1 schematically shows the module structure and interplay between individual components: Data fitting is an optimization problem with the aim of finding the parameter set $\{\phi_i\}$, that best describes the measured *sample* $C^*[t]$. Hence, the central position of the module is held by the *optimizer*, whose task is the minimization of a *similarity measure*, i.e. an objective function. The crucial point of the data analysis is the theoretical model, referred to as *model function*, which is the functional representation $f(t, \phi_i)$ of the course of data points. For a given set of parameters, on which optimization should be performed, this function calculates the corresponding *signal* $C(t, \phi_i)$. The *cost function* links the model specific function and the generalized optimization routine. The parameter set in question is passed from the optimizer through this function down to the model, which returns the theoretical signal. The cost function then calculates the specified similarity measure, describing the deviation between measured data sample and fitted model function. Usually the sum of quadratic difference between the sample and theoretical signal, referred to as sum of squared residuals $\mathcal{X}^2$, is used as objective function, but other definitions of objective functions are possible as well.

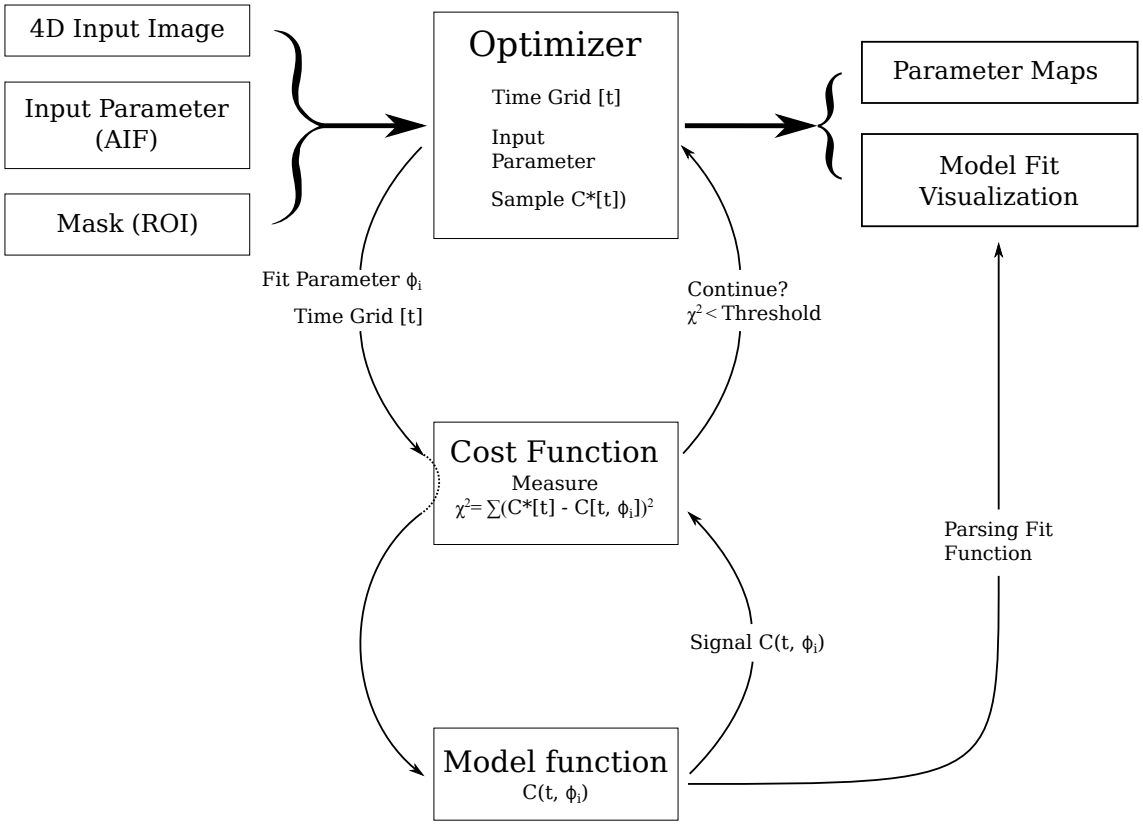

Figure 4.1: Structure and workflow of the dynamic data analysis module. From the input image, *temporal grid* $[t]$ and signal-time curve are extracted in every voxel. If necessary, the signal is converted to concentration units, yielding the *sample* $C^*[t]$. The *optimizer* passes the time grid, together with an estimate for the *fit parameters* ϕ_i, to the *model* via the *cost function*. The model calculates the theoretical concentration time curve (*signal* $C(t, \phi_i)$) and passes it back to the cost function. The *similarity measure* (e.g. sum of squared residuals $\mathcal{X}^2$) is calculated and passed to the optimizer. The optimizer then adjusts the parameter estimates. This routine is repeated, until the measure satisfies certain stopping criteria. Final parameters are stored in *parameter maps*. The fit in every voxel can be evaluated using the *modelfit view*, which displays the measured sample and the fitted curve, reconstructed directly from the model function and the parameter values. Each block is its own software element and can be changed or expanded by the user without influencing the others.

The framework structure of the core module allows for easy implementation of own model functions, optimizers and optimization measures. The fitting framework supports pixel-based and region-based fitting. Measured data curves, represented by arrays of intensity values at sampling points, and the corresponding sampling grids (e.g. the time grid $[t_i]$ of typical dynamic data sets) are extracted in both cases. For region-based fitting, an averaged sample curve is calculated from the arithmetic mean of all pixels within a defined region at each time-point. The pixel-based approach fits the sample curve of each spatial coordinate (3D pixel) separately. Fitting can be performed on any data sampling strategy, since sampling grids are extracted for each frame of the image data directly. This procedure allows for support of equidistant, as well as arbitrary sampling.

Model specific properties, such as model and variable names, functional domain, etc., are defined in *parameterizers*. Static input values used for signal calculation and default values for start parameters and constrains are specified in the parameterizers as well. Within the framework, each model has its own class that defines the mathematical curve representation, and a corresponding parameterizer. New models can be derived from model base classes, which define the fundamental functionalities of each model. Instantiation and management of models and their parameterizers are handled by model specific factories, which are generated automatically.

The entire fitting routine is incorporated in ITK [www.itk.org] image filters to perform fitting on single voxel basis and allow for parallel computing. As a default optimizer the Levenberg-Marquardt algorithm was chosen, a combination of the Gauss-Newton method and the method of gradient descents, providing good robustness. This optimizer was used because of its fast convergence through the definition of multi-valued objective functions. The corresponding objective function is defined as the individual squared residuals, rather than their sum.

The initial parameter values for optimization are passed to the optimizer via delegates. The delegates allow different strategies for definition of start parameters, e.g. global scalar values for all curves or local values represented by images, with each pixel being a set of start parameter values. The delegate has a default state, used when the initial values have not been specified by the users. Various forms of initial values specification and extraction are possible (scalar value, image, look-up-tables, etc.). The tuple of start parameters can be accessed, for example by the optimizer, via the current optimized pixel index. Value constrains can be imposed on the different parameters in order to limit optimization search space, or to exclude values without physical meaning. Upper and lower constraint values with a certain tolerance bandwidth can be defined for each parameter and for parameter combinations, e.g. the sum of two parameters. Violation of constraints during optimization result in penalties that drastically increase the measure and hence, drive the optimizer away from such values.

4.1.2 Visualization

The resulting parameter estimates are stored in 3D images, with one image for every parameter. Additional parameters for evaluation, like the sum of squared residuals, or other derived quantities, can be defined. The user can navigate through the different parameter maps, overlay them with different modalities, change the color map and access single pixel values. For research purposes, the option of accessing the final optimizer state in parameter maps was included, giving overview over the stopping criteria, number of iterations and constraint violations.

In order to allow detailed evaluation of data and fits, an extension of the module for visualization was implemented. Every fitting task performed on a data set generates a user identifier (UID), linked to a specific fit configuration. Together with the model information from the parameterizer, this UID is assigned to all output images created in the fit as a property, allowing for comparison of fits with different models or parameter combinations of the same data. The modelfit view can access the fit properties linked through the UID

and display the fitted curves together with the measured raw data points. The fitted curve is directly reconstructed online with the according fit parameters.

4.1.3 AIF-based Models

Pharmacokinetic models often depend on an arterial input function (AIF), since indicator dilution theory postulates the tissue concentration-time course as convolution of the indicator influx with a specific response function. Therefore, additional base classes handling models which use an AIF, were defined. The AIF can be extracted from the dynamic image by segmentation of a respective blood vessel. The extracted curve is averaged over all pixels in the contour and registered with the parameterizers. The AIF can be displayed in the modelfit view together with the fitted data. For AIF-based models, calculation of the theoretical signal is often based on indicator dilution theory and requires either convolution of AIF and residue function, or directly solving differential mass balance equations. Both approaches can be handled by the module. The convolution is performed in position space, rather than frequency space. Since the residue functions are mostly represented by exponential terms, using linear interpolation of the AIF between the sampling points yields a recursive analytical expression for the convolution integral [Ingrisch, 2012] (see Appendix). Solutions of differential equations can be found by using the Runge-Kutta algorithm (see Appendix), implemented in the boost library [www.boost.org], which is incorporated in MITK.

4.1.4 Non-Compartmental Analysis Tool

Pixel-wise fitting can be time consuming. Thus, it is rarely used to analyze whole image scans, but rather for focused analysis of certain regions. For general assessment of the whole image topology, and identification of areas potentially interesting for dedicated pharmacokinetic analysis, calculation of semi-quantitative curve parameters from non-compartmental analysis is often used as a preprocessing step (see chapter 3.4.6). The software module was extended for easy implementation of such parameter calculations in a functor-filter style. The underlying workflow extracts the intensity courses from the image and passes them to the definition of the parameter. The current plugin implementation offers modality independent derivation of parameters *AUC* (area under the curve), *AUMC* (area under the first moment curve), *TTP* (time to peak), C_{max} (peak intensity) and *MRT* (mean residence time) from 4D image. For applications in DCE MRI and dynamic PET, the image intensities can be converted to concentration (rel. SE or abs. SE) or *SUV* values for normalization, respectively, prior to semi-quantitative parameter calculations. The calculated parameter values are stored in 3D images.

4.2 DCE MRI

The analysis of image time series from dynamic contrast enhanced MRI by means of pharmacokinetic modeling played a major role throughout the course of this thesis. Parameter estimates from perfusion MRI allow for assessment of tissue hemodynamics and

provide insight into blood-brain-barrier leakage and tumor angiogenesis [Møller et al., 2015]. Software solutions available prior to this thesis presented with a number of disadvantages. Most of these tools are stand-alone solutions, developed to serve a single analysis purpose. Thus, comparison of the data with other imaging modalities, and combination analysis are difficult to perform. Commercial software, e.g. *Dynalab* [*MeVisLAB*, 2016], are usually black-boxes with rigid analysis configurations. To overcome these limitations, the dynamic data analysis module was used to implement a plugin for model fitting of DCE data. In the following section this tool is presented. Its usage and advantages are illustrated on exemplary studies of the assessment of arterial input functions and the evaluation of non-compartmental analysis of DCE MRI data from high-grade glioma patients. Inversion of the fitting routine can yield concentration-time curves from a given set of model parameters. This approach was used to implement a simulation software tool for DCE MRI data. Data simulations allowed studies of accuracy, stability and robustness of parameter estimation in pharmacokinetic modeling. The difference between two different functional definitions of the 2 compartment exchange model (2CXM) were investigated and the influence of the initial values of model parameters on the outcome of the optimization routine was studied.

4.2.1 Software Developments

The DCE MRI Plugin

The MITK dynamic data analysis provides a modality independent, highly flexible software tool for model fitting of dynamic data. The module was used to design a plugin for pharmacokinetic analysis of DCE MRI data. Two model functions of widely used pharmacokinetic models in DCE MRI were implemented:

- The extended Tofts model, described by equation 3.44.
- The 2 compartment exchange model (2CXM). For this model, two approaches for defining the model can be used: two differential mass balance equations (3.34 and 3.35) or convolution of the arterial concentration with the residue function (equation 3.39). The plugin supports both versions.

Pharmacokinetic models in DCE MRI are usually defined with respect to contrast agent concentration time courses, hence the acquired image intensity has to be converted to concentration values before fitting. As discussed in section 3.2.5, the relation between CA concentration and MRI signal can be expressed in terms of relative or absolute signal enhancement (rel. SE and abs. SE) with respect to the baseline signal $S(t = 0)$. For the DCE MRI fitting tool, conversion with both options is supported.

The DCE MRI analysis plugin allows fitting of the dynamic image with a pixel- or region-based strategy. The AIF can be either derived from an image (the same image, that measures the tissue of interest, or a separately acquired one) or loaded from a file (for example if an AIF from a patient collective is used). The configuration of the fitting routine can be specified with several parameters. Constraints can be imposed on the parameters, in order to exclude unreasonable parameter values and limit the search space, which in terms decreases computation time. Starting values of the parameters can be defined as

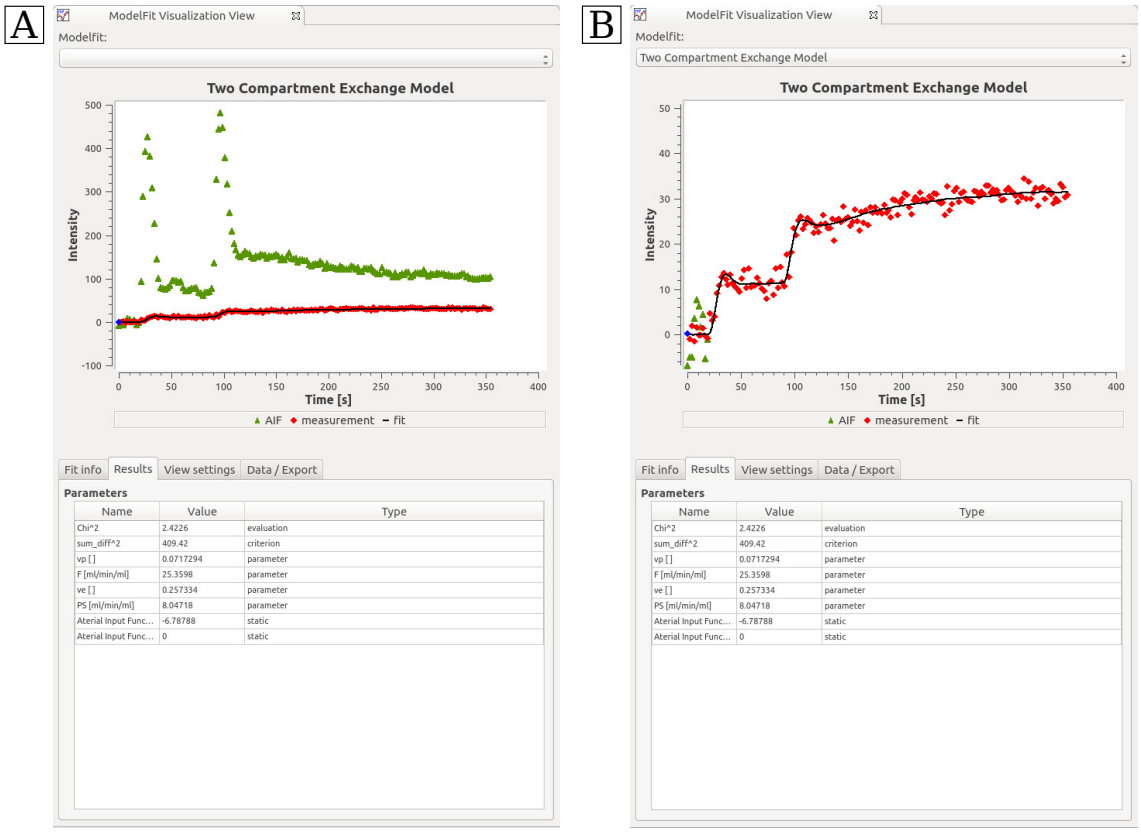

Figure 4.2: A: Exemplary application of the developed DCE MRI plugin for pharmacokinetic modeling. A simulated concentration-time-curve (input parameters: $\tilde{F}_p = 25\frac{\text{ml}}{\text{min}\cdot 100\text{ml}}$, $\widetilde{PS} = 5\frac{\text{ml}}{\text{min}\cdot 100\text{ml}}$, $\tilde{v}_p = 0.1$, $\tilde{v}_e = 0.15$) was fitted with the two compartment exchange model. The raw data and resulting fit curve are displayed in the modelfit view. B shows the arterial input function (green), data points (red) and fit curve (black). In the right panel, the y-axis is reset for better visibility of data points and fitted curves. In the lower table of the plugin view, parameter estimates are listed: $F_p = 25.36\frac{\text{ml}}{\text{min}\cdot 100\text{ml}}$, $PS = 8.05\frac{\text{ml}}{\text{min}\cdot 100\text{ml}}$, $v_p = 0.072$ and $v_e = 0.257$.

static values for all pixels, or as local start parameter values defined in an image. This option allowed for evaluation of the influence of parameter starting values on the outcome of the optimization routine, discussed in section 4.2.3.

Figure 4.2 illustrates the functionality of the DCE MRI pharmacokinetic modeling tool. A simulated concentration-time curve (red dots) and the corresponding fit curve (black line), displayed in the modelfit view, are shown. The utilized arterial input function is shown in green (4.2A). The concentration in tissue is much lower than in the artery. Therefore, figure 4.2B shows the tissue curve with a magnified y-axis. The input parameters, used for curve simulation, were $\tilde{F}_p = 25\frac{\text{ml}}{\text{min}\cdot 100\text{ml}}$, $\widetilde{PS} = 5\frac{\text{ml}}{\text{min}\cdot 100\text{ml}}$, $\tilde{v}_p = 0.1$ and $\tilde{v}_e = 0.15$. The fit yielded parameter estimates $F_p = 25.36\frac{\text{ml}}{\text{min}\cdot 100\text{ml}}$, $PS = 8.05\frac{\text{ml}}{\text{min}\cdot 100\text{ml}}$, $v_p = 0.072$ and $v_e = 0.257$. The deviations between input values and fitting estimates of the model parameters are discussed in detail in section 4.2.3

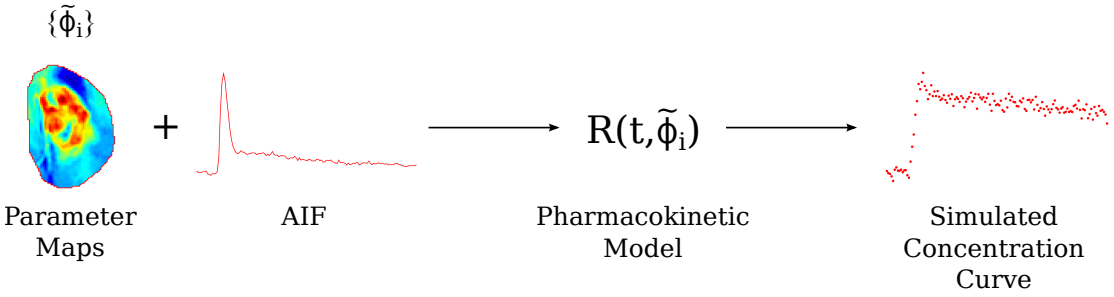

Figure 4.3: Functionality of the DCE MRI data simulation tool. Using the respective set of model parameters $\{\tilde{\phi}_i\}$ in form of images (maps), and an arterial input function (AIF), the theoretical concentration-time curve is calculated from the pharmacokinetic model $R(t, \tilde{\phi}_i)$. Random numbers from a Gaussian distribution are added to the curve in order to account for noise. The resulting synthetic curve can be used for *in-silico* validation of the fitting routine.

The DCE Data Simulation Tool

The high flexibility of the dynamic data analysis module, and the possibility for the user to specify the optimizer configuration, opened the opportunity to study certain aspects of NLLS fitting in pharmacokinetic kinetic analysis. Based on the dynamic data analysis module, a simulation tool for DCE MRI data was developed, which enables generation of synthetic perfusion MRI data.

Data simulation is performed by inversion of the fitting process, as illustrated in figure 4.3: 3D maps of the model parameters $\{\tilde{\phi}_i\}$ and an arterial input function are used to calculate the corresponding concentration-time curves from the model function. To simulate noise, random numbers from a Gaussian distribution are added to the data points. The width of the noise is calculated from the contrast-to-noise ratio (CNR), defined as ratio between the maximum concentration of the arterial input and the standard deviation of the Gaussian noise. The temporal resolution of the synthetic DCE MRI image is defined through the sampling of the AIF.

The resulting concentration-time curves are stored in 4D images. These simulated images can be used as input for the fitting routing. This procedure allows for *in-silico* validation of the fitting routine. The effects of different configurations on the parameter estimates can be studied by directly comparing the fitting results to the original parameter values used for data synthesis.

4.2.2 Studies on Measured DCE MRI Data

DCE MRI data from recurrent high grade glioma patients was investigated with respect to the applicability of pharmacokinetic modeling and the surrogate value of determined values for detection of tumor tissue at risk. Three patients were selected for exemplary studies. The patients were chosen based on good visibility of the arterial tree in the brain, which is vital for assessment of the arterial input function. The arterial tree was visualized with the 3D volume rendering tool in MITK.

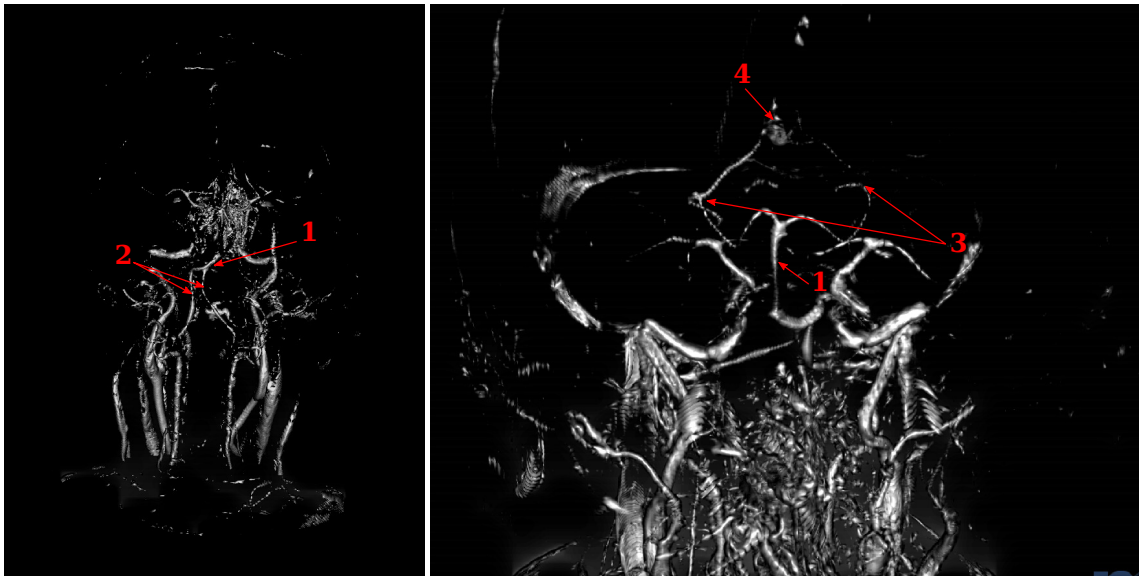

Figure 4.4: 3D view of vessel structure, resulting from volume rendering (patient n^o 3). Rendering of the T_1 weighted contrast enhanced MRI was used to assess the arterial tree in the brain and to identify vessels for AIF measurement. Locations which were used for AIF assessment are indicated with red arrows (basilar artery: 1, carotid arteries: 2, middle cerebral arteries: 3, frontal cerebral artery: 4).

Figure 4.4 shows two views of the arterial tree in patient n^o 3 as an example for volume rendering from the T_1 weighted contrast enhanced MRI. The vessels of interest (basilar artery: 1; left and right internal carotid artery: 2; left and right middle cerebral artery: 3; anterior cerebral artery: 4) are marked with red arrows.

Only two patients in the available data cohort provided DCE MRI data prior to radiotherapy, together with an adequately visible arterial tree: patients n^o 2 and n^o 3. Thus, an additional patient, who received DCE MRI sequences before radiotherapy, but no ^{18}F-FET PET scan, was used (referred to as patient A).

AIF assessment in recurrent high grade glioma patients: inter-patient variability and measurement locations

Correct determination of the arterial concentration (arterial input function AIF) is vital for parameter estimation in DCE MRI. Dispersion and delay of the CA bolus through the body have to be considered, since the administered bolus is not of an ideal, delta-function-like shape. Thus, the AIF should be determined in a feeding artery as close as possible to the tissue of interest. However, in the brain, the image resolution of the dynamic scans is typically in the order of millimeters, hence smaller vessels are difficult to assess.

The following study investigated the feasibility of quantifying hemodynamics with pharmacokinetic analysis of DCE MRI data in individual patients. Problems in AIF estimation arose due to low temporal resolution of the image ($\Delta t = 12.26\,\mathrm{s}$). Temporal under-sampling is likely to result in missing the first pass of the bolus, which would yield an underestimation of the arterial concentration. In order to study, whether the AIF can be assessed in

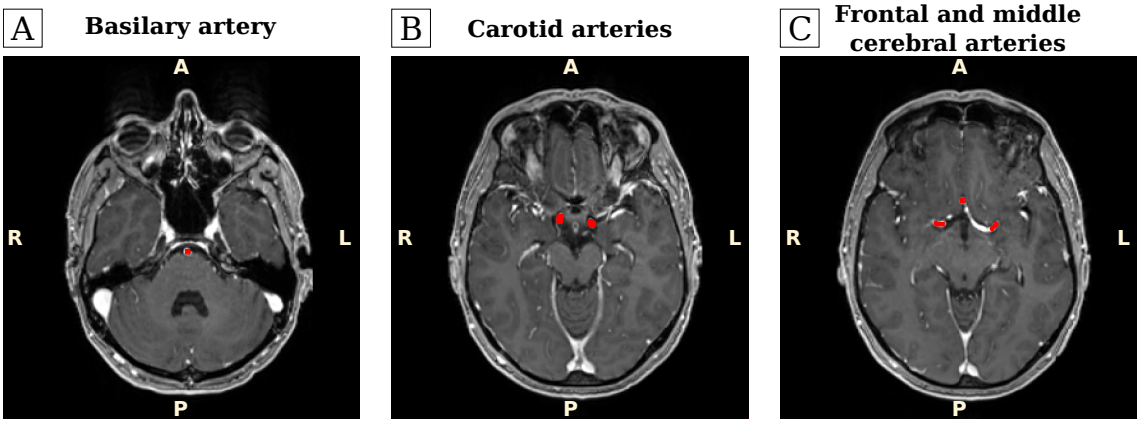

Figure 4.5: Contours for measurement of different arterial input functions (red) in six large brain feeding arteries: Basilar artery (A), left and right internal carotid artery (B), anterior cerebral artery and left and right middle cerebral artery (C). The vessels were segmented with help of the contrast enhanced T_1 weighted MRI, here shown in patient n^o 3 for illustration.

the available data with sufficient quality, arterial concentration curves were measured at different locations in the brain in the three selected patients. Six large feeding arteries of the brain were segmented in one to three slices:

- The basilar artery, located at the junction between medulla oblongata and pons (9-32 pixels)
- The left and right internal carotid artery, the major paired artery on each side of the neck (6-23 pixels)
- The anterior cerebral artery, a pair of arteries originating from the internal carotid artery, supplying the frontal and superior medial parietal lobes (15-24 pixels)
- The left and right middle cerebral artery, arising from the internal carotid for blood supply of the cerebrum (12-42 pixels)

The number in brackets denotes the minimum and maximum size of the contour. Segmentations of the different arteries were drawn using the static, high resolution contrast enhanced T_1 weighted MR image for localization. Figure 4.5 shows the T_1 weighted contrast enhanced MRI of patient n^o 3 in three transversal slices. Contours of the basilar artery (A), the left and right internal carotid artery (B) as well as the anterior cerebral artery and left and right middle cerebral artery (C) are drawn in red on the image.

The large slice thickness of dynamic scans (≈ 5 mm) made segmentation difficult, since the vessels were visible only in one slice in several cases. Dynamic series were converted to concentration in terms of relative signal enhancement (rel. SE, $\tilde{k} = 1$). The concentration-time curves from all pixels in a region were averaged, resulting in one arterial input curve each.

The extracted concentration time curves in different arteries of each patient are shown in the left column of figure 4.6. All six measured arterial concentration curves (basilar artery: black, left carotid artery: blue, right carotid artery: cyan, left middle artery: red,

right middle artery: magenta, frontal cerebral artery: green) in arbitrary units of relative signal enhancement are plotted over the measurement time for patients n^o 2 (top), n^o 3 (middle) and patient A (bottom; no ^{18}F-FET PET). A distinct peak in the concentration is visible only in the basilar artery (black) in patient n^o 3. The left and right internal carotid show small peaks. In patient n^o 2, only the left internal carotid artery shows higher concentration in the early measurement phase. All other vessels exhibited no peak. In patient A, concentration shows a similar time course in all arteries, with a small enhancement in the beginning of the measurement. However, compared to typical arterial concentrations, this peak is too low. Overall, concentrations time courses in the middle and frontal cerebral arteries exhibited little to no peak behavior.

Information on the administered dose of contrast agent, or a curve with higher temporal sampling, were not available. Thus, it is difficult to determine, whether the curves are representative for the time course of the arterial concentration. It is likely, that the concentration peak is underestimated, as it is measured at most in one time point. Hence the probability of missing the true peak is high. Intra-serial registration of the individual time slices was not performed, thus the possibility of misalignment cannot be excluded. However, the spatial resolution of the dynamic image ($0.898\,\text{mm} \times 0.898\,\text{mm} \times 5\,\text{mm}$) is lower than the observed movement in-between serial images, especially in the axial plane.

In a second step, the arterial concentration was measured in the three largest vessels (basilar artery, carotid artery left and right) for one patient at four different time points:

- MRI used for treatment planning, 2 weeks before radiotherapy (red)
- MRI done on the first day of radiotherapy (blue)
- MRI done on the last day of radiotherapy, 14 days after the first fraction (green)
- MRI done at the first follow-up, one month after therapy (black)

The arterial concentration-time curves in the basilar artery (top), right carotid artery (middle) and left carotid artery (bottom) are shown in the right column of figure 4.6. The results show, that none of the investigated arteries provide a stable estimate of the AIF, since concentration-time curves vary greatly between different measurements.

The deviation is unlikely to be a treatment induced effect, because these vessels were not exposed to irradiation. Again, no clear distinction of the peak is possible. Results showed, that the data acquired with the study protocol does not provide sufficient quality for appropriate pharmacokinetic modeling, because the arterial concentration cannot be determined properly.

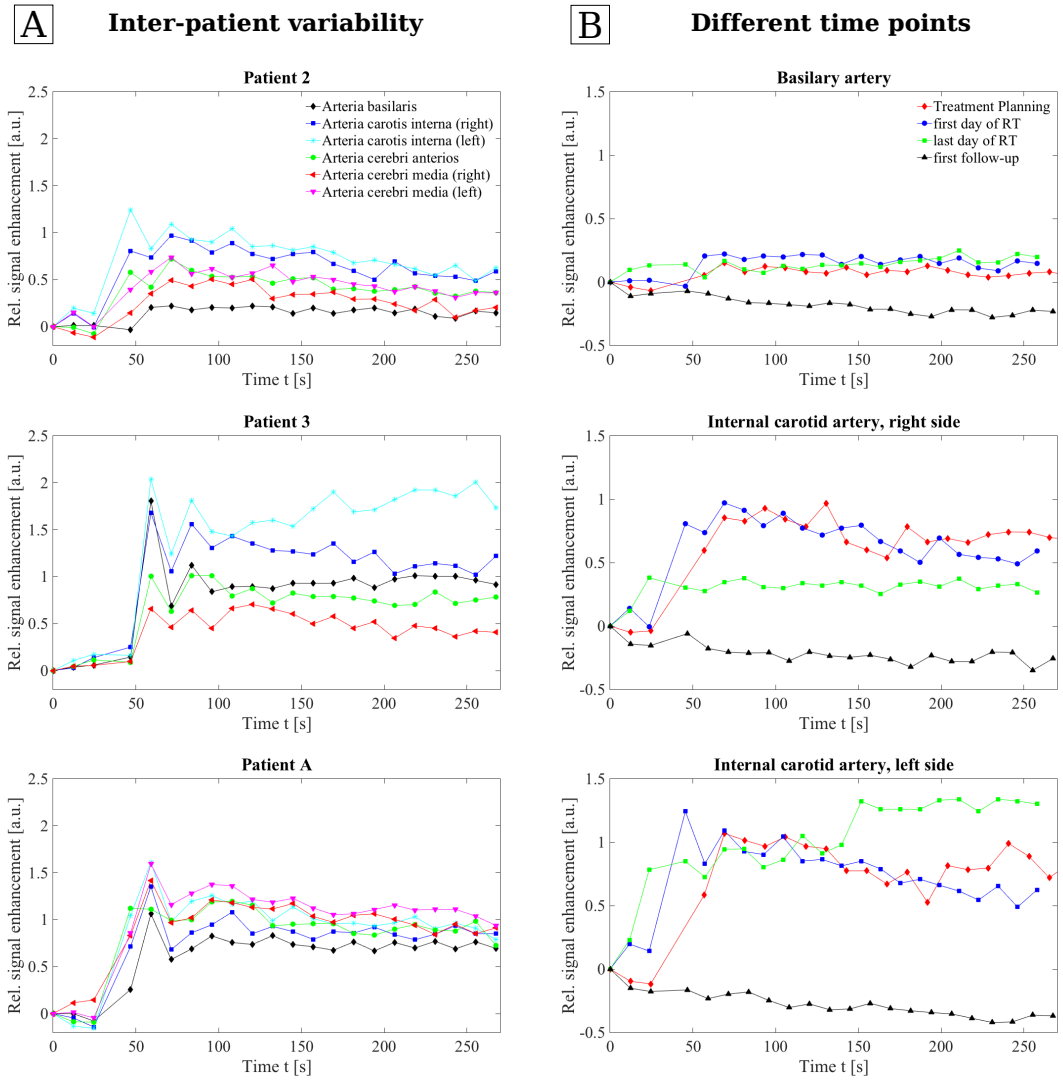

Figure 4.6: A: Arterial concentration-time curves (AIF) in patients 2 (top), 3 (middle) and A (bottom) for assessment of inter-patient variability and best measurement location. Curves were measured from DCE MRI data acquired on the first day of radiotherapy in six different large brain arteries: the basilar artery (black), left and right carotid artery (blue and cyan), left and right middle artery (red and magenta) and frontal cerebral artery (green).
B: Arterial concentration-time curves in three large brain arteries in patient n^o 2, measured at four different time points over the course of radiotherapy, for assessment intra-patient variability. The curves were measured in the basilar artery (top), right (middle) and left (bottom) carotid artery. DCE MRI images were acquired at treatment planning (red), on the first day of radiotherapy (blue), on the last day of radiotherapy (green) and at the first follow-up examination (black). For all cases, signal intensity was converted to concentration in terms of relative signal enhancement.

Perfusion parameter monitoring under therapy: temporal development of semi-quantitative curve parameters (*AUC*, *MRT*, C_{max}) from DCE MRI in treatment volumes over the course of radiotherapy

Assessment of the AIF showed, that the available DCE MRI data is not suitable for dedicated pharmacokinetic modeling, due to coarse temporal sampling. However, one can resort to determining semi-quantitative parameters from non-compartmental analysis, describing the curve shape (c.f. section 3.4.6). In the next study, the software tool for non-compartmental analysis was used to investigate semi-quantitative parameters in different volumes over the time course of radiotherapy treatment. The goal was to evaluate the extent, to which any of these parameters could possibly provide more insight into tumor tissue. The same three patients from the above study were investigated. Dynamic images from four different time points over the course of radiotherapy were analyzed. The time series were registered to the treatment planning CT and converted into concentration by means of relative signal enhancement (rel. SE, $\tilde{k} = 1$). This was done as normalization step.

DCE MRI from four different time points was investigated:

- MRI done on the first day of radiotherapy
- MRI done on the last day of radiotherapy, 14 days after the first fraction
- MRI done at the first follow-up, one month after therapy
- MRI done at the second follow-up, three months after therapy

The four quantitative curve describing parameters *AUC* (*area-under-the-curve*), *MRT* (*mean-residence-time*), *TTP* (*time-to-peak*) and C_{max} (*maximum concentration*) were calculated in each voxel. Parameters were then measured within the three different volumes, illustrated in figure 4.7:

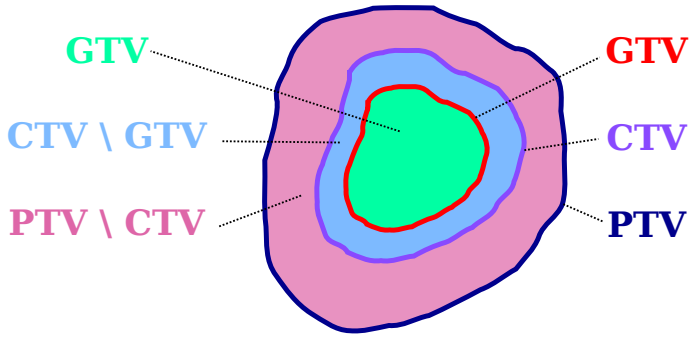

Figure 4.7: Semi-quantitative parameters *AUC*, *MRT*, C_{max} and *TTP* from non-compartmental analysis of DCE MRI data were investigated in three different volumes: the macroscopically visible tumor volume *GTV* (green), in the estimated microscopic outliers of the tumor added by the *CTV* ($CTV \setminus GTV$, blue) and in the additional safety area from the *PTV* ($PTV \setminus CTV$, pink).

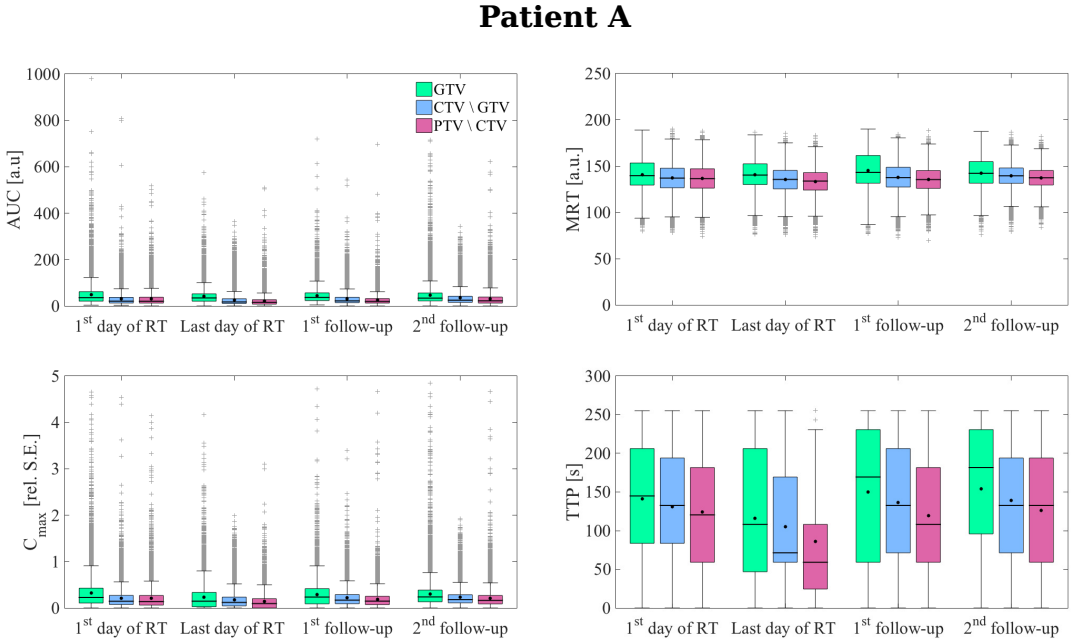

Figure 4.8: Semi-quantitative parameters *AUC*, *MRT*, C_{max} and *TTP* from non-compartmental analysis of DCE MRI data in patient A. DCE MR images were acquired at treatment planning, on the first day of radiotherapy, on the last day of radiotherapy and at the first follow-up examination. Parameters were analyzed within the gross tumor volume *GTV* (green), the estimated microscopic outliers of the tumor $CTV \setminus GTV$ (blue) and the additional safety area accounting for irradiation uncertainties $PTV \setminus CTV$ (pink). The whiskers are defined as first/third quartile -/+ 1.5 IQR. The parameter median is represented by the black line, the black dot shows the mean value.

- Within the macroscopically visible tumor volume *GTV* (green)
- In the estimated microscopic outliers of the tumor, that the *CTV* includes, calculated by subtracting *GTV* from *CTV*: $CTV \setminus GTV$ (blue)
- In the additional safety area accounting for irradiation uncertainties (*PTV*), calculated by subtracting the *CTV* from the *PTV*: $PTV \setminus CTV$ (pink)

In figures 4.8, 4.9 and 4.10, the distributions of each of the measured parameters within these three volumes at the respective time points is presented in patients n^o 2, 3 and A, respectively. Patient A did not receive a ^{18}F-FET PET scan.

The *AUC* is shown in the top left box plot of each figure panel. The parameter was clearly enhanced in *GTV*, compared to the two target volume extensions in patient n^o 3. In patient n^o 2, the measured *AUC* within the *GTV* volume spread wider and a slight tendency towards higher values was observed. This indicates enhanced heterogeneity of the tissue within the *GTV*. In the other two volumes, the parameter was stable. Patient n^o 3 exhibited almost no differences in *AUC* between volumes. *MRT*, plotted in the top right of the figure panels, showed a slight enhancement within the *GTV* in patients n^o 2 and n^o 3. This effect was not observed in patient A. In this case, the measured values for *MRT* were stable over time and in different volumes. The distribution of the maximum

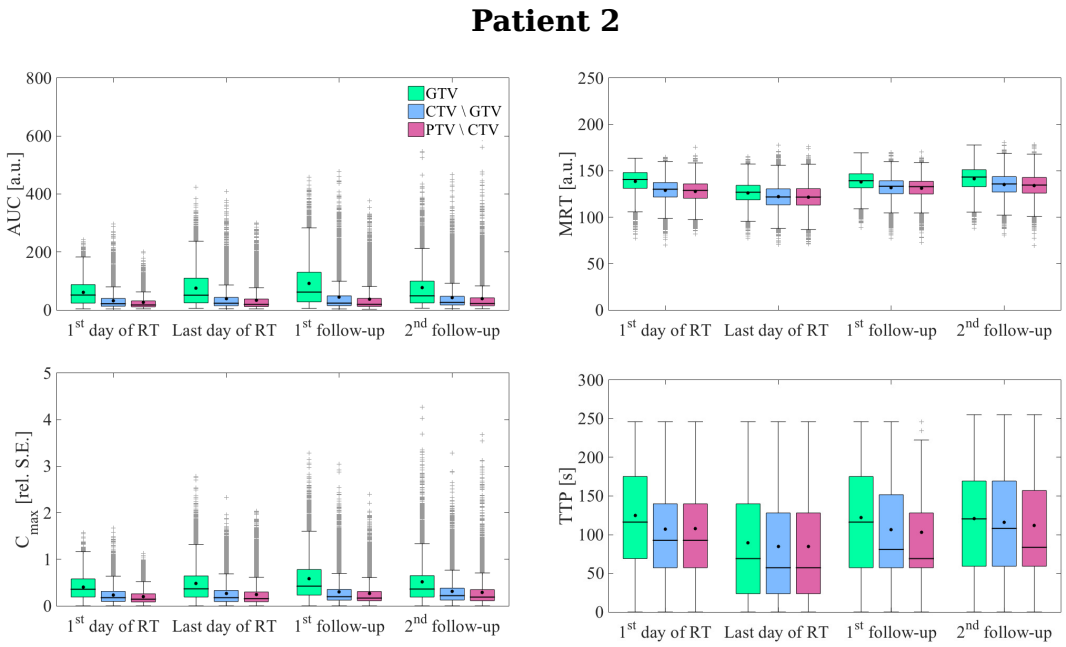

Figure 4.9: Semi-quantitative parameters *AUC*, *MRT*, C_{max} and *TTP* from non-compartmental analysis of DCE MRI data in patient n^o 2. DCE MR images were acquired at treatment planning, on the first day of radiotherapy, on the last day of radiotherapy and at the first follow-up examination. Parameters were analyzed within the gross tumor volume *GTV* (green), the estimated microscopic outliers of the tumor $CTV \setminus GTV$ (blue) and the additional safety area accounting for irradiation uncertainties $PTV \setminus CTV$ (pink). The whiskers are defined as first/third quartile -/+ 1.5 IQR. The parameter median is represented by the black line, the black dot shows the mean value.

concentration C_{max} is shown in the bottom left box plot. The parameter differed between volumes in patient n^o 3. In patient n^o 2, the differences were less distinct, whereas no difference in parameters was observed in patient A. The bottom right box plot displays the parameter *TTP*, which exhibited large variances, thus no dedicated conclusion could be drawn.

In patient n^o 3, a gradual descent of all parameters was observed between treatment volumes. Over time, the parameters decreased from the first day of radiotherapy to the first follow up examination and increased again at the second follow up. Both effects were not observed in the other two patients. All parameters derived from patient A presented with large stability over time and no differences between the treatment volumes.

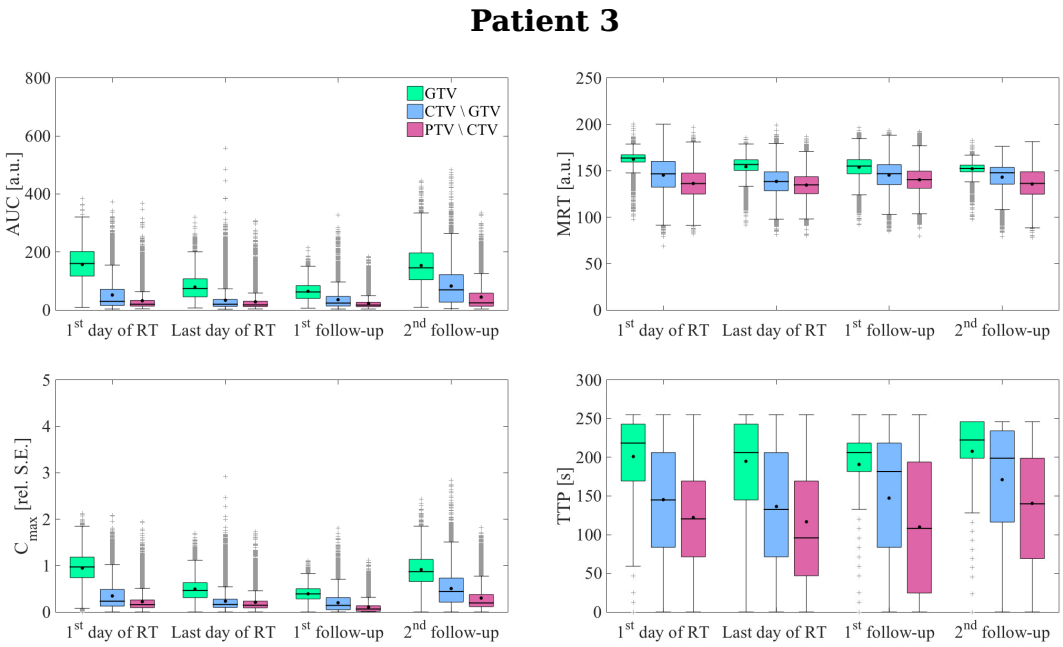

Figure 4.10: Semi-quantitative parameters *AUC*, *MRT*, C_{max} and *TTP* from non-compartmental analysis of DCE MRI data in patient n^o 3. DCE MR images were acquired at treatment planning, on the first day of radiotherapy, on the last day of radiotherapy and at the first follow-up examination. Parameters were analyzed within the gross tumor volume *GTV* (green), the estimated microscopic outliers of the tumor $CTV \setminus GTV$ (blue) and the additional safety area accounting for irradiation uncertainties $PTV \setminus CTV$ (pink). The whiskers are defined as first/third quartile -/+ 1.5 IQR. The parameter median is represented by the black line, the black dot shows the mean value.

Figure 4.11 illustrates maps of the semi-quantitative parameters within the *PTV* for patient n^o 3. *AUC* and C_{max} presented with similar patterns of parameter distributions. *TTP* showed noisy parameter values and less stability, compared to the other parameters. All parameter maps indicated tumor volume deviation from the *GTV* contour (indicated as black inner contour).

Tumor progress of patient n^o 3 was confirmed at the first follow up examination date (one month after radiotherapy). In order to assess parameter difference within tumor regrowth, the progress tumor volume $GTV_{Prog.}$ was delineated based on T_1 weighted contrast enhanced MRI. The progress *P* was defined as the difference between progress tumor volume $GTV_{Prog.}$ and initial tumor volume *GTV*

$$P = GTV \setminus GTV_{Prog.} \tag{4.1}$$

For comparison of parameter values in tumor to healthy tissue conditions, a reference contour "*ROI*" was drawn on the contra-lateral side of the brain. *ROI* was of similar size as *GTV*.

Figure 4.12 shows the distribution of parameters *AUC* (top left), *MRT* (top right), C_{max} (bottom left) and *TTP* (bottom right) with the three volumes *GTV* (green), *P* (blue) and *ROI* (pink) in patient n^o 3 on the first day of radiotherapy and at the progress confirming

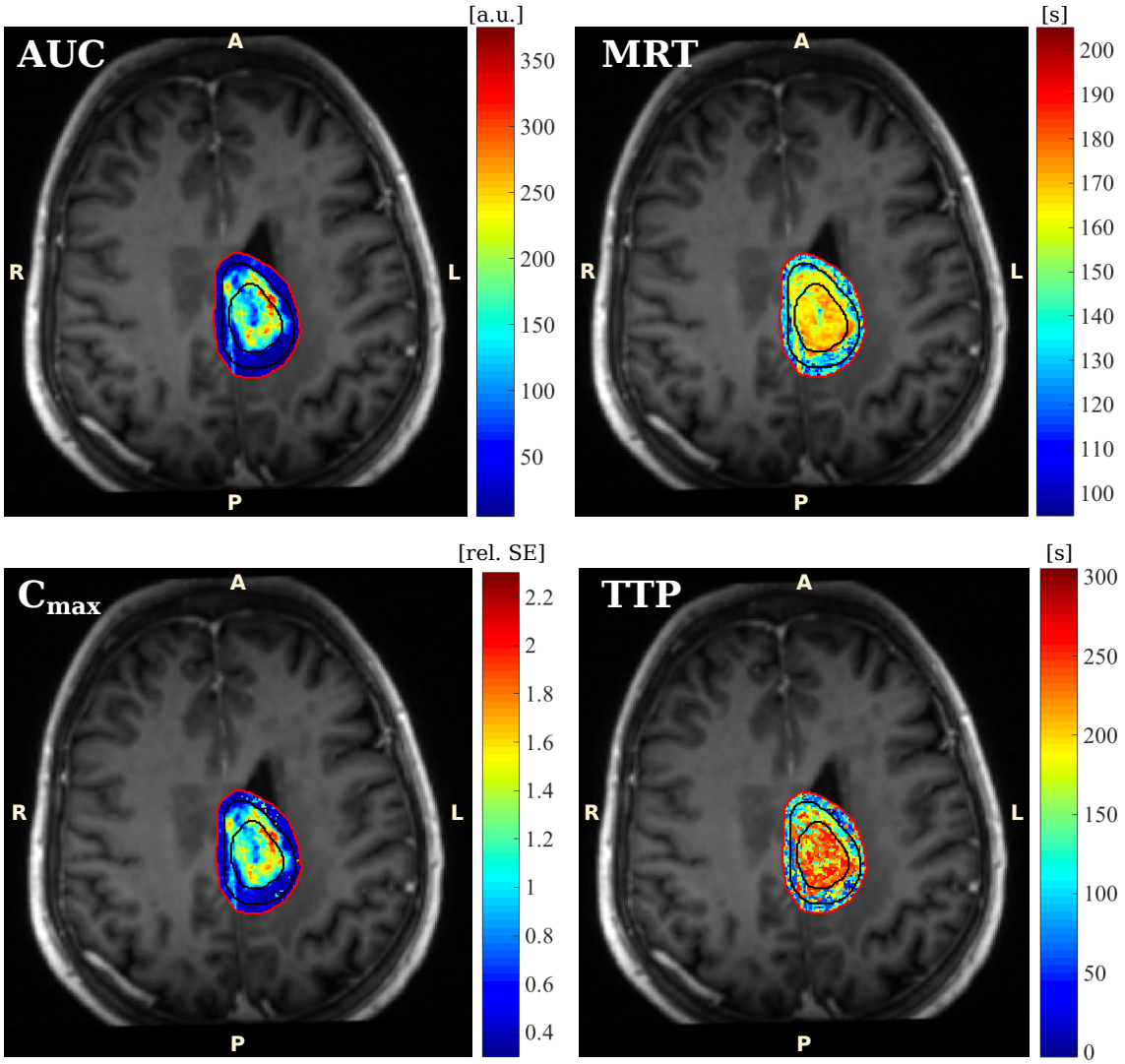

Figure 4.11: Parameter maps of semi-quantitative parameters *AUC*, *MRT*, C_{max} and *TTP* from non-compartmental analysis of DCE MRI data, acquired on the first day of radiotherapy, in patient n^o 3. Parameters were calculated within the *PTV* red outer contour). Here, they are shown as overly of the static, T_1 weighted contrast enhanced MRI for localization. *GTV* and *CTV* contours are indicated in black.

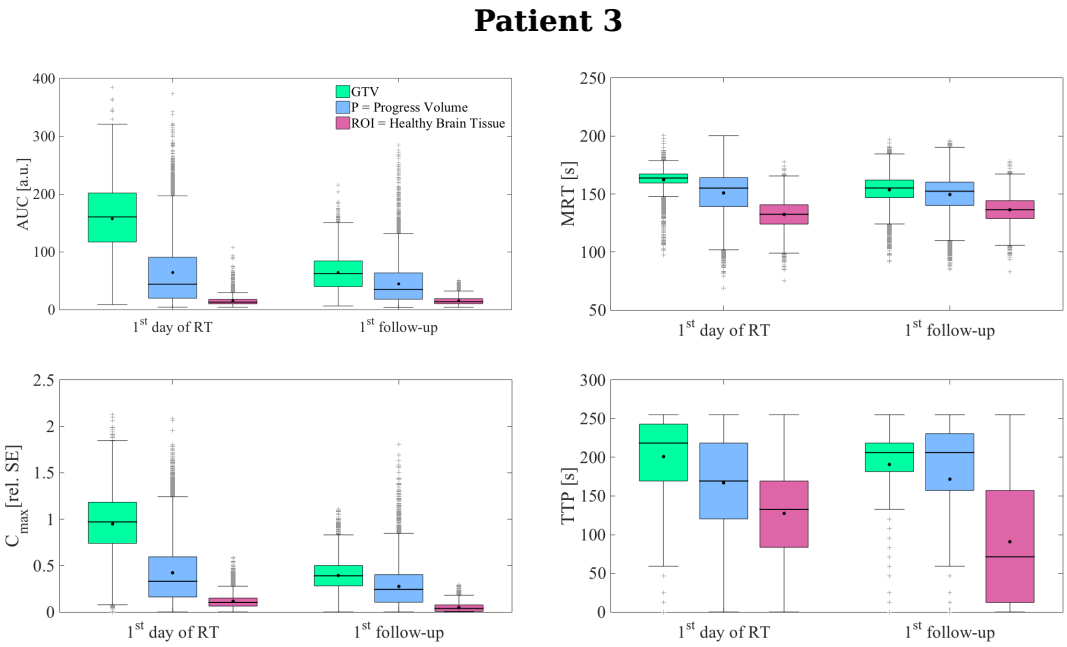

Figure 4.12: Semi-quantitative parameters *AUC*, *MRT*, C_{max} and *TTP* from non-compartmental analysis of DCE MRI data in patient n^o 3. Data was acquired at the first day of radiotherapy and at the progress confirming follow-up date. Parameters were investigated in the treatment planning *GTV* (green), in the progress tumor volume $P = GTV \setminus GTV_{Prog.}$ (blue) and in reference healthy brain tissue *ROI* (pink). The whiskers are defined as first/third quartile -/+ 1.5 IQR. The parameter median is represented by the black line, the black dot shows the mean value.

follow-up examination. A gradual descent between the three different volumes can be observed for all four parameters. The parameter values in the progress volume and healthy brain remain stable between the two examination dates, while *AUC* and C_{max} decrease within the *GTV*.

The results indicate, that parameters from non-compartmental analysis could be helpful surrogates for tissue classification, as they seem to exhibit distinction between the different volumes and tissue types. However, result differed distinctively between patients. For further deductions, more patients need to be investigated. While the semi-quantitative parameters provided a good measure for tissue separation in patient n^o 3, they showed only small differences between the different volume in patient n^o 2. This patient, however, presented with a small overall tumor volume and slow progressive growth: $GTV = 5627\text{mm}^3$, $P = 591\,\text{mm}^3$. Progress in this patient was detected 8 months after irradiation, whereas patient n^o 3 presented with progress already 1 month after therapy. This suggests, that differences in the semi-quantitative parameters from DCE MRI could distinguish between fast and slow growing progress. *TTP* however provides a wide spread distribution of values and thus, represents an unstable parameter.

4.2.3 Studies on Simulated DCE MRI Data

The two-compartment exchange model (2CXM) describes the compartments *plasma* and *interstitial volume* with fractional volume v_p and v_e and their exchange in terms of plasma flow F_p and permeability-surface area product PS. The model function is defined by a system of two coupled differential equations [Brix et al., 2010]. A closed-form analytic solution as convolution of a biexponential residue function with the arterial concentration derives from indicator dilution theory. Several studies on model feasibility and comparison between different models have been performed [Sourbron et al., 2009; Luypaert et al., 2012; Brix et al., 2009]. However, little attention has been given to technical aspects of the fitting routine [Luypaert et al., 2010].

The perfusion simulation tool allowed for generation of synthetic DCE MRI data. For this data, the ground truth of model parameters is known. Thus, fitting of simulated curves with the model fitting tool allows for *in-silico* validation and error assessment of the optimization routine. The purpose of the following studies was to evaluate the results of parameter estimates with the 2CXM. Different data scenarios and fit configuration were tested with respect to accuracy, robustness and computation speed, by fitting simulated concentration time curves in image space, and evaluating the resulting parameter maps. Image based perfusion data was simulated using the developed simulation software tool. Concentration-time curves were calculated with the convolution approach of the model function of the 2CXM, using image based parameter sets $[F_p, PS, v_p, v_e](x, y, z)$ and a measured arterial input function from a double-bolus injection, acquired in the middle cerebral artery (temporal resolution of 2.11 s, Ingrisch et al. [2012]). A noise level of CNR = 300 was applied to the data. All simulated curves were fitted with the 2CXM, using the previously presented DCE MRI plugin. In order to assure model consistency and limit the optimizer search space to physically reasonable values, parameter constraints were applied. The fractional volumes can only have values between 0 and 1, and their sum cannot exceed a value of 1:

$$0 < v_p, v_e < 1 \tag{4.2}$$

$$v_p + v_e < 1, \tag{4.3}$$

Plasma flow and permeability cannot be negative, and should, for the sake of meaningful parameter estimates, not exceed 100 [ml/min/100ml]. For PS, values larger then -1 were allowed in order to cover the range of intact blood-brain-barrier ($PS = 0$) with a certain deviation tolerance.

$$0 < F_p < 100 \left[\frac{\text{ml}}{\text{min} \cdot 100\text{ml}}\right] \tag{4.4}$$

$$-1 < PS < 100 \left[\frac{\text{ml}}{\text{min} \cdot 100\text{ml}}\right] \tag{4.5}$$

The optimizer configuration and start parameters were kept constant for all fits, except in section 4.2.3, where the influence of the start parameters itself was investigated.

Table 4.1: Parameter combinations of the simulated concentration-time curves for homogeneous parameter images. Together with a measured arterial input function, each of the parameter combinations was used to simulate a homogeneous 30×30 pixel dynamic image (169 time points, temporal resolution 2.1 s). These images were fitted for assessment of robustness, precision and computational time of parameter estimates.

	F_p $\left[\frac{\text{ml}}{\text{min 100ml}}\right]$	PS $\left[\frac{\text{ml}}{\text{min 100ml}}\right]$	v_p $[-]$	v_e $[-]$
Reference	25	5	0.1	0.15
Low F_p	5	5	0.1	0.15
Low PS	25	2	0.1	0.15
Low v_p	25	5	0.05	0.15
Low v_e	25	5	0.1	0.05

Assessment of accuracy, robustness and computation time of 2CXM parameter estimates using differential equations compared to convolution

The model function of the 2CXM is defined by the two coupled differential equations 3.34 and 3.35 . A closed-form analytic solution as convolution of a bi-exponential residue function with the arterial concentration derives from indicator dilution theory (equation 3.39). For parameter estimation with the non-linear least squares method, the residuals can be calculated by either numeric convolution of the closed-form solution, or by directly solving the differential equations (e.g. using the Runge-Kutta algorithm). The following study compared both strategies in terms of accuracy, robustness and computation speed by fitting simulated concentration time curves in image space, and quantitative and qualitative evaluation of the resulting parameter maps.

Accuracy and robustness were evaluated on concentration-time curves derived from the five different parameter combinations listed in table 4.1. One reference condition was used with parameter values similar to those of a brain tumor ($F_p = 25\frac{\text{ml}}{\text{min 100ml}}$, $PS = 5\frac{\text{ml}}{\text{min 100ml}}$, $v_p = 0.1$ and $v_e = 0.15$). The other four curves were set in a way that three of the parameters were left at reference values, while the remaining parameter was set to a low value.

Figure 4.13 illustrates the simulated concentration time curves. In the top left the utilized arterial input function is plotted in green. The other five panels show representative curves for each of the five parameter combinations: Reference (top right), low plasma flow (middle left), low permeability (middle right), low plasma volume (bottom left) and low interstitial volume (bottom right). For illustration, the reference curve shows the simulated curve without noise (black line) in comparison to the used curve with Gaussian random noise

(red dots). With each of the five parameter combinations, a homogeneous 30×30 pixel concentration image of time-resolved concentration curves was simulated.

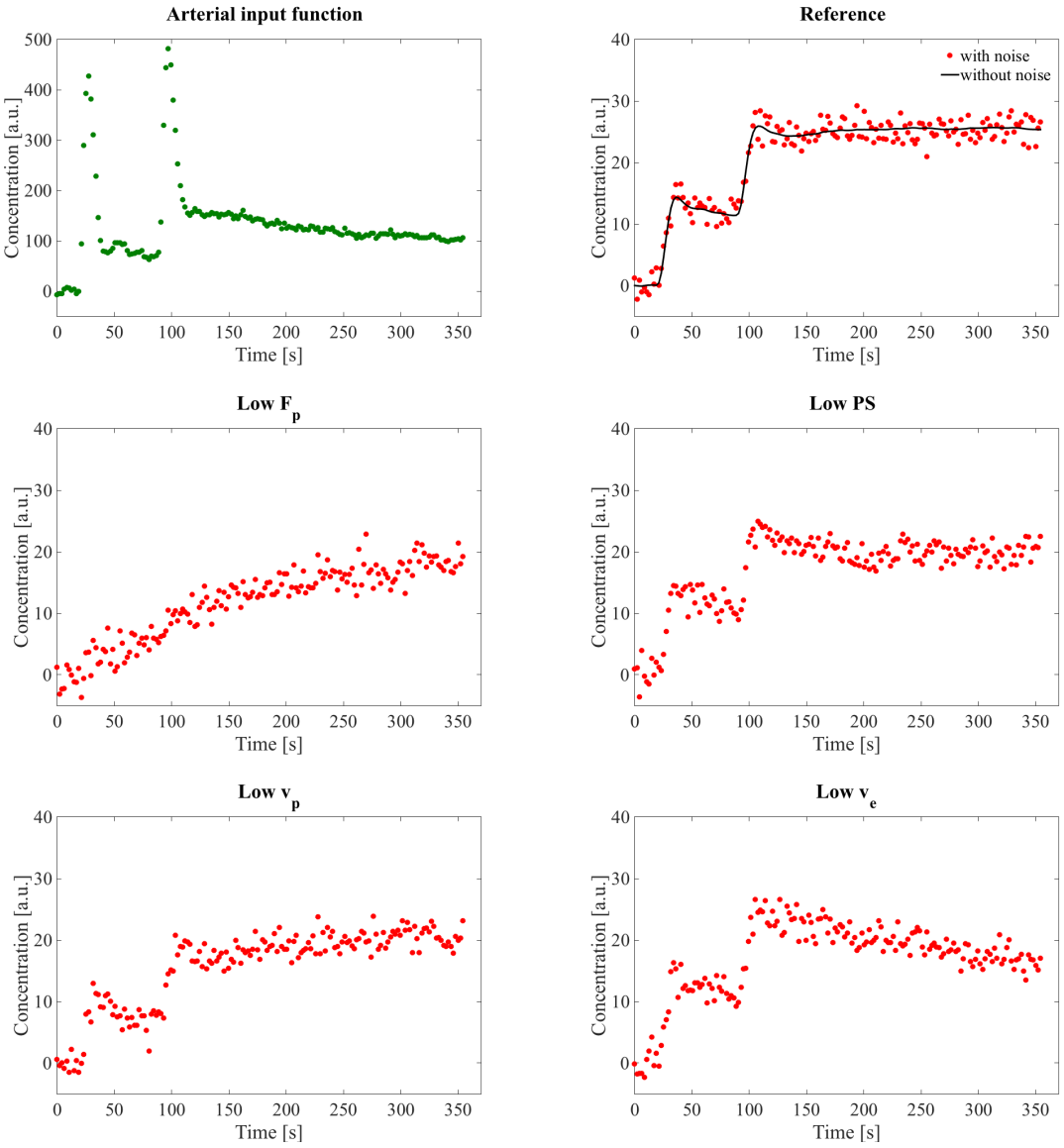

Figure 4.13: The arterial input curve used for simulations and representative simulated concentration-time curves of the homogeneous parameter images for reference values, low F_p, low PS, low v_p and low v_e, listed in table 4.1. For illustration, the reference curve shows the simulated curve without noise (black line) in comparison to the used curve with Gaussian random noise (red dots). The AIF was taken from measurements of a double bolus injection in the middle cerebral artery (temporal resolution of 2.11 s, [Ingrisch et al., 2012]).

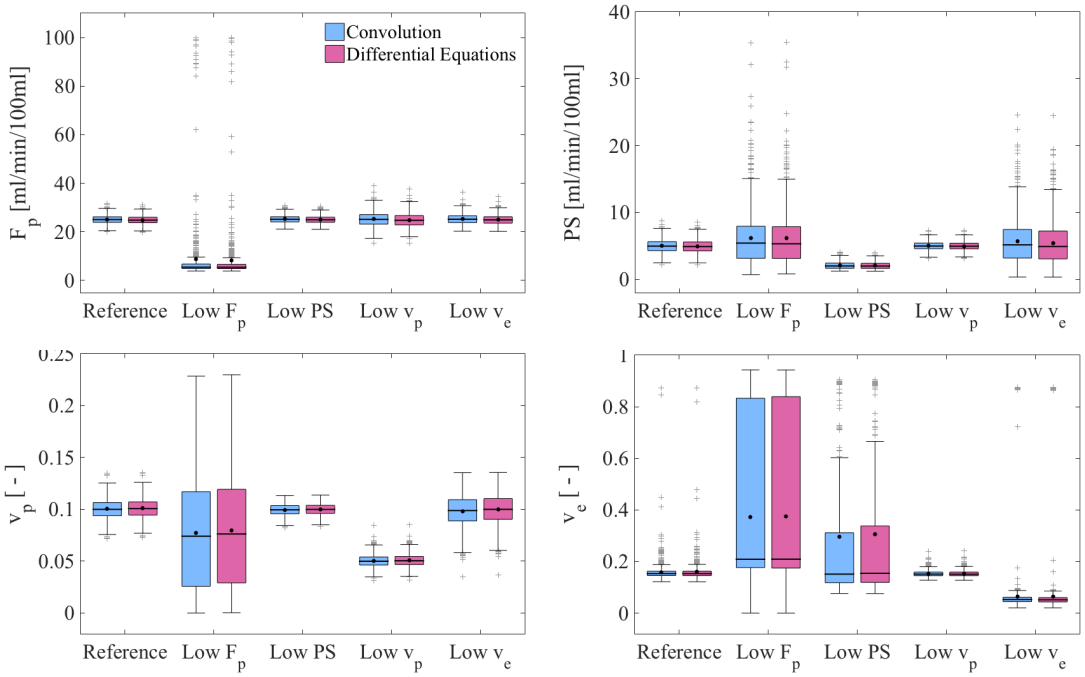

Figure 4.14: Results of parameter estimates for F_p, PS, v_p and v_e from fitting homogeneous 30×30 pixel images of five different parameter combinations (table 4.1) with the convolution model function (blue) and with the differential equation approach (pink), respectively. The whiskers are defined as first/third quartile -/+ 1.5 IQR. The parameter median is represented by the black line, the black dot shows the mean value.

The resulting dynamic images were fitted using both approaches of the 2CXM model function. The differential equations were solved using the boost [www.boost.org] implementation of the Runge-Kutta method. For the convolution approach, the arterial input function was interpolated linearly. The resulting fitted parameters were compared to the input value by calculating the bias, e.g. the difference between input value and the mean of the fitting result, and the variance of the mean.

Figure 4.14 shows box plots of the resulting parameter estimates for F_p, PS, v_p and v_e, comparing the fit results using the convolution (blue) to the fit results using the differential mass balance equations (pink) for all five curve types. The parameter median is represented by the black line, the black dot shows the mean value. The convolution and the differential equation approach yielded similar results for a given parameter combination. The fitting result for v_e yielded a poor estimate with many outliers. The mean and median parameter estimates differed strongly. For low values of F_p, both fitting strategies yielded poor fit stability, large uncertainties and many outliers.

Precision was evaluated by subtracting the mean parameter estimate from the original input value. The results of the precision in each of the five parameter scenarios are presented in figure 4.15 for the four model parameters F_p (top left), PS (top right), v_p (bottom left) and v_e (bottom right). The error bars indicate the standard deviation of the mean. The mean estimates of F_p compared to the true value showed no considerable deviation except

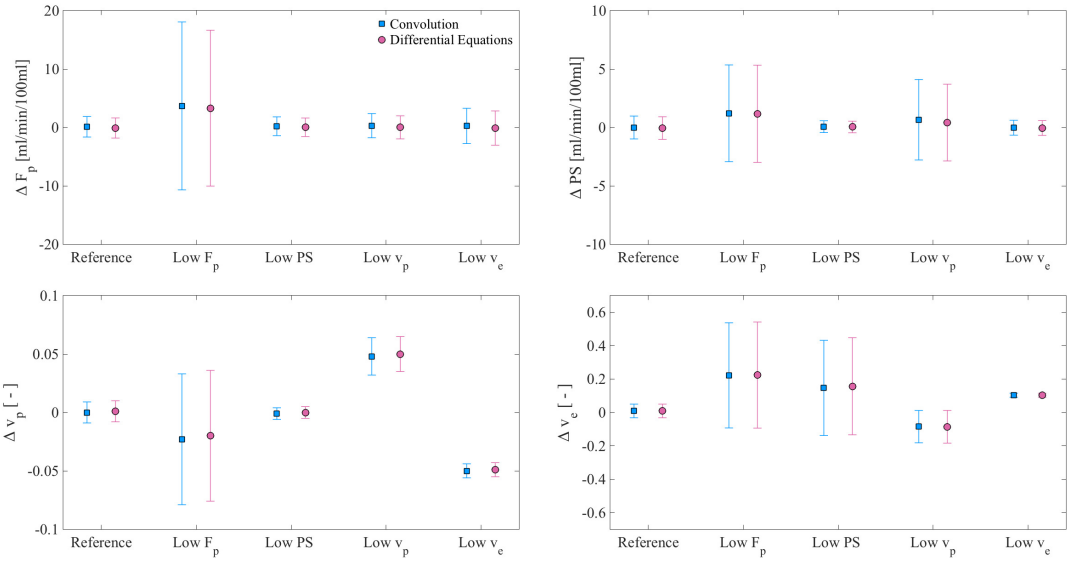

Figure 4.15: Accuracy and precision of parameter estimates for F_p, PS, v_p and v_e from fitting homogeneous 30×30 pixel images of five different parameter combinations (table 4.1) with the convolution (blue) and Runge-Kutta (pink) approach, in terms of deviation from the true value and variance. The data points show the accuracy calculated as the difference from the mean parameter estimate of all 900 fitted curves to the true input value. The error bars represent the precision in terms of standard deviation of the mean.

for low F_p. For the reference situation as well as low PS and low v_e, parameter estimates of PS and v_p were close to the original values.

The optimization time per pixel required for fitting with the convolution model function (blue) compared to the approach of solving the differential mass balance equations (pink) is illustrated in figure 4.16. The convolution approach excelled in terms of computational time, as it is three orders of magnitude faster than the differential equations.

Influence of fitting start parameters on the parameter estimates in the 2CXM in image based simulation studies

The influence of starting values on parameter estimates has been mentioned, however, it was never studied in depth [Brix et al., 2009]. The developed DCE MRI fitting tool allows definition of starting values for each parameter, not only as scalar values, but also on a pixel-wise basis in form of images. This opens the opportunity to study the influence of different starting value combinations and graphically visualize it. The parameter combinations defined in section 4.2.3 were used to simulate homogeneous 15×60 pixel concentration images of 169 time points. These synthetic images were fitted with the 2CXM, using the convolution approach.

The start parameters were defined in 15×60 pixel images as well. Each start parameter was either constant over the whole image, or varying between 15 different values along the x-axis. The values used are listed in table 4.2: The initial values of F_p varied between

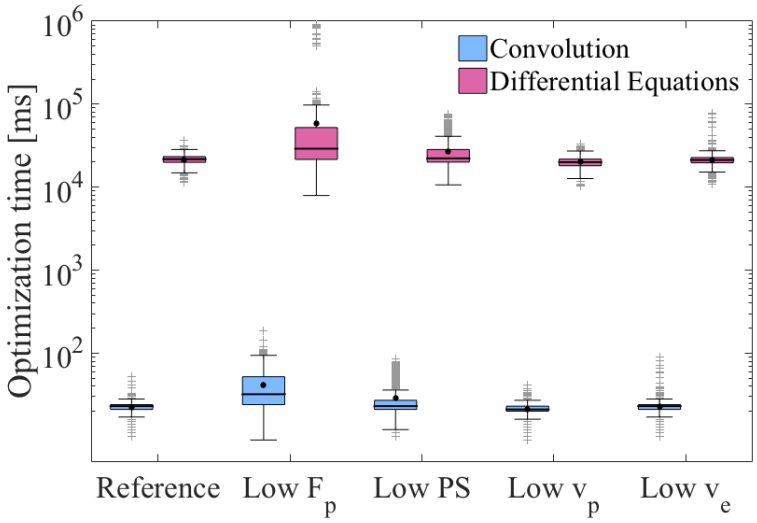

Figure 4.16: Optimization time per pixel for fitting homogeneous 30×30 pixel images of five different parameter combinations (table 4.1) with the convolution (blue) and Runge-Kutta (pink) approach, respectively. The whiskers are defined as first/third quartile -/+ 1.5 IQR. The parameter median is represented by the black line, the black dot shows the mean value.

2.5 [ml/min/100ml] and 37.5 [ml/min/100ml] in steps of 2.5 [ml/min/100ml]. The initial values for PS ranged from 0 [ml/min/100ml] to 15 [ml/min/100ml] in unity steps. v_p and v_e both had initial values ranging from 0.02 to 0.3 in steps of 0.2.

Table 4.2: Initial values for model parameters, studied in the fitting routine. Homogeneous 15×60 pixel images, simulated with different parameter sets (table 4.1), were fitted. The starting value of one parameter took 15 different values along the x-axis, while the other starting values were kept at a fixed value. This procedure was applied to all for parameters.

Parameter	fixed value	variation
$F_p \left[\frac{\text{ml}}{\text{min 100ml}}\right]$	25	2.5, 5, ... , 35, 37.5
$PS \left[\frac{\text{ml}}{\text{min 100ml}}\right]$	5	0, 1, 2, ... , 13, 14
v_p [−]	0.1	0.02, 0.04, ... , 0.3
v_e [−]	0.155	0.02, 0.04, ... , 0.3

Hence, each curve type was fitted with 4 different start parameter configurations, with one parameter varying and the other 3 staying fixed at constant values:

- F_p = varying, PS = const , v_p = const, v_e = const
- F_p = const, PS = varying , v_p = const, v_e = const
- F_p = const, PS = const , v_p = varying, v_e = const
- F_p = const, PS = const , v_p = const, v_e = varying

Each curve type was fitted 60 times with each of the start parameter configuration in order to allow calculation of mean parameter estimates.

In order to evaluate accuracy of the parameter estimates in more detail, the fitted values of all four model parameters P_{fit} were compared to the respective input values $P_{original}$, used for simulation, by means of the relative error:

$$E_{rel}(x, y, z, n) = \frac{P_{fit}(x, y, z, n) - P_{original}(x, y, z, n)}{P_{original}(x, y, z, n)} \tag{4.6}$$

For every curve type and every initial optimizer value configuration, the relative deviation of the fitting result to the original value was calculated for F_p, PS, v_p and v_e, and averaged over all 60 values of the same initial optimizer value configuration. This approach yielded $15 \times 5 \times 4$ error maps for each of the four model parameters. Figure 4.17 shows the relative errors on parameter estimates on F_p (A) and PS (B) for the five different curve types (x-axis). Each map results from fits with one of the starting values varying, F_p, PS, v_p, v_e from top to bottom. The variation in the respective parameter is indicated on the y-axis. The errors on parameter estimates on v_p (C) and v_e (D) are mapped in the same manner in figure 4.18.

Parameter estimates for F_p In general, parameter estimates of F_p showed low errors, except for curves with low F_p, which is consistent with the results from the 4.2.3. For low start value of F_p, the error on the estimate of F_p increased in all five curve types. Otherwise, the errors showed no dependency on the start value for F_p and PS. For curve with low F_p, the averaged parameter estimates indicated dependency on the start value for v_p and v_e. To investigate this further, the calculated mean error on the parameter estimate for curves with low plasma flow is plotted in figure 4.19. The x-axis represents the varying initial value for v_p (top) and v_e (bottom). The error bars denote the standard deviation. The graphics show that mean error on F_p does not depend on either of the starting values within the standard deviation.

Parameter estimates for PS Errors on the estimate for PS were higher, compared to errors for F_p. The error was increased for low start values of F_p and PS. Curve types with low F_p or low v_e showed higher errors on the estimate for PS. There was no visible dependency with the start value of any of the parameters.

Parameter estimates for v_p The errors on estimates of v_p were low, except for curve with low F_p. Error were increased for very low start values of F_p and PS. Otherwise no visible dependency with the start values of any of the parameters was found. For curve types with low F_p, the estimate on v_p seemed to exhibit dependency with the start value for v_p, especially at low starting values. The plot in figure 4.20 shows the calculated mean error on the parameter estimate for curves with low plasma flow over the varying initial value of v_p. No dependency of the error is visible within the standard deviation (error bars).

Parameter estimates for v_e The errors on v_e showed the highest errors of all estimates, especially for low F_p and low PS curves. The errors were distinctively larger if the start value for PS was set to 0. Apart from this, no dependency with the start parameter values was found.

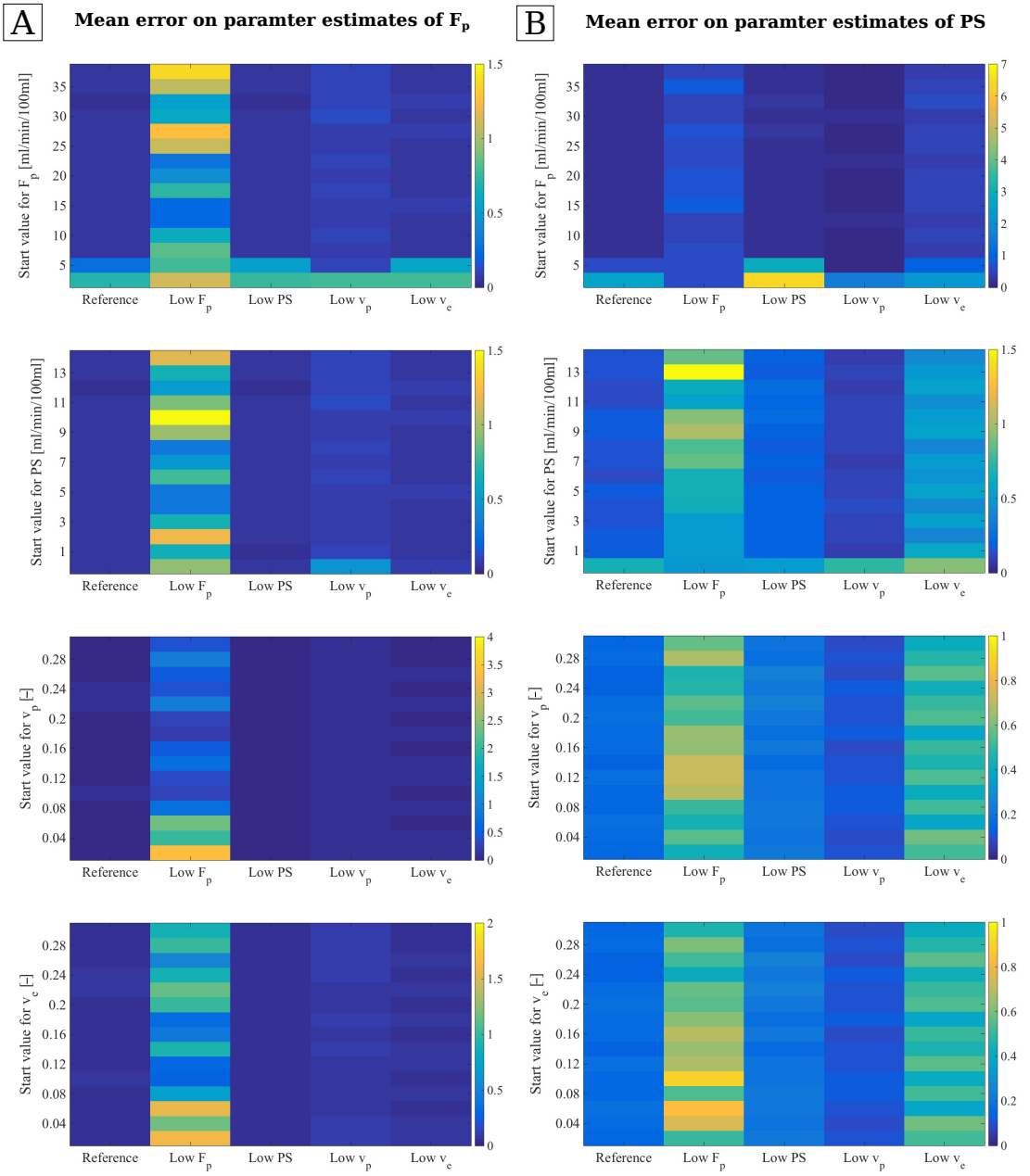

Figure 4.17: Relative errors of parameter estimates of F_p (A) and PS (B), from fits with varying initial values of F_p, PS, v_p and v_e (top to bottom). The starting value of one parameter took 15 different values, here displayed on the y-axis, while the other starting values were kept at a fixed value. Parameter estimates were averaged over 60 curves and the relative error was calculated with respect to the original parameter value, used for data simulation. The five different curve types, displayed on the x-axis, used the input parameter combination for simulation described in table 4.1.

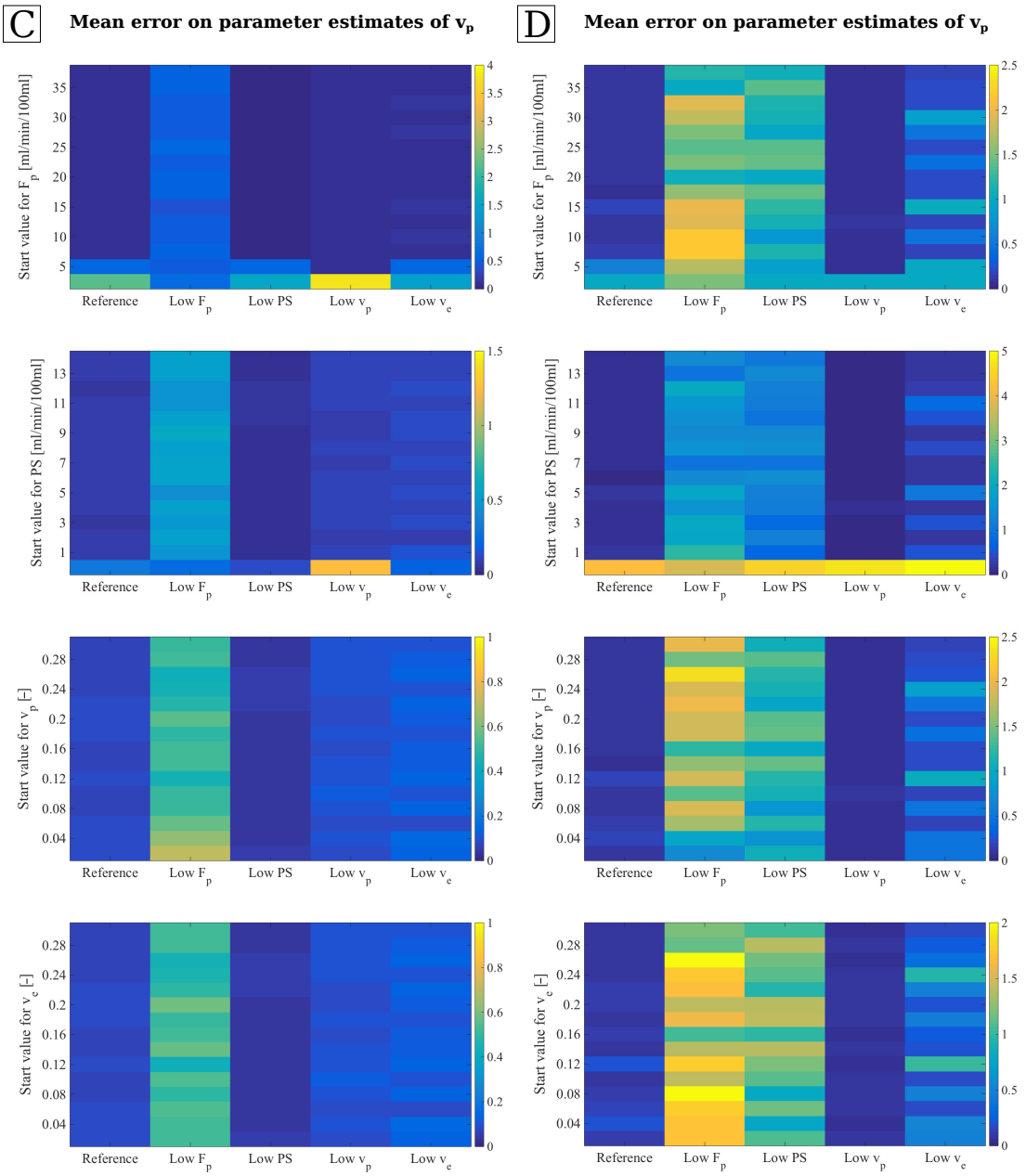

Figure 4.18: Relative errors of parameter estimates of v_p (C) and v_e (D), from fits with varying initial values of F_p, PS, v_p and v_e (top to bottom). The starting value of one parameter took 15 different values, here displayed on the y-axis, while the other starting values were kept at a fixed value. Parameter estimates were averaged over 60 curves and the relative error was calculated with respect to the original parameter value, used for data simulation. The five different curve types, displayed on the x-axis, used the input parameter combination for simulation described in table 4.1.

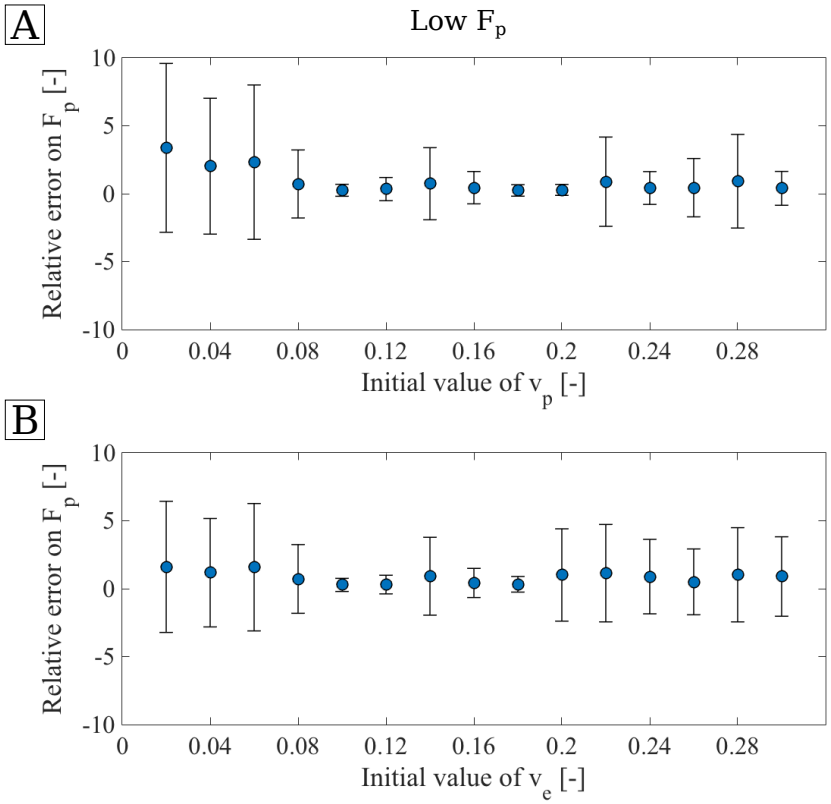

Figure 4.19: Relative errors on parameter estimates of F_p with varying initial values of v_p (A) and v_e (B) for concentration curves with low F_p. The starting value of one parameter took 15 different values along the x-axis, while the other starting values were kept at a fixed value. Parameter estimates were averaged over 60 curves and the relative error was calculated with respect to the original parameter value, used for data simulation. The error bars represent the standard deviation of the mean.

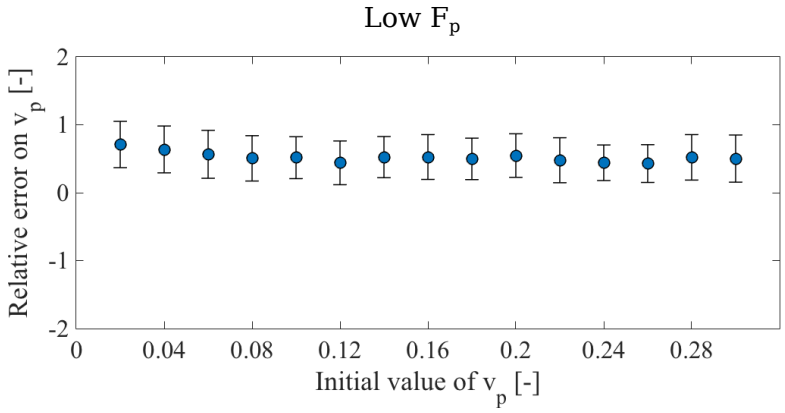

Figure 4.20: Relative errors on parameter estimates of v_p with varying initial values of v_p, for concentration curves with low F_p. The starting value of one parameter took 15 different values along the x-axis, while the other starting values were kept at a fixed value. Parameter estimates were averaged over 60 curves and the relative error was calculated with respect to the original parameter value, used for data simulation. The error bars represent the standard deviation of the mean.

4.3 ^{18}F-FET PET

Evaluation of data from ^{18}F-FET PET imaging was particularly interesting for this thesis, since metabolic information from tracer uptake reveals properties of amino acid transport rates in glioma tissue and has been shown to correlate with cell density [Pauleit et al., 2005]. To include PET data into the multi-modal image analysis, software plugins for evaluation of PET images were implemented in MITK. The tools were further used to analyze ^{18}F-FET PET data from recurrent high grade glioma patients. Tumor segmentations on static endpoint ^{18}F-FET PET images, derived from different contouring techniques, were compared to the gross tumor volume (GTV) and to the volume of tumor progress at follow-up.
For analysis of dynamic ^{18}F-FET PET scans, two pharmacokinetic models of tracer dilution, i.e. the one tissue compartment model (1TCM) and the two tissue compartment model (2TCM), were fitted to the measured time-activity curves (TAC) and results were compared for assessment of robustness and model feasibility. Furthermore, semi-quantitative parameters from non-compartmental analysis were investigated with respect to different tissue volumes.

4.3.1 Software Developments

The PET SUV Calculation Plugin

So far, it was only possible to display PET images in MITK as grey scale values of the intensity, but no further PET specific analysis could be performed. For dedicated analysis of the ^{18}F-FET PET data, a tool for calculation of the standardized uptake value (SUV) in each image pixel was developed. The plugin requires definition of the time interval between tracer injection and measurement, the amount of injected activity, the patient body weight and the tracer isotope. These parameters can be entered manually or read directly from the DICOM data, if the corresponding tags are set. The SUV is calculated with these values according to formula 3.16. Calculation of the SUV image is based on the ITK image filter concept, which handles looping over the image pixels and thus, covers the question of correct pixel access. This approach allows for parallel computing, improving the computational time efficiency. 3D and 4D data sets are supported.
The plugin was used to calculated the SUV_{max} values from ^{18}F-FET PET scans of the 18 recurrent high grade glioma patients. The values for *injected activity*, *patient body weight* and *time to measurement* were determined from the DICOM tags. For calculation of the *time to measurement*, the time stamps of DICOM tags "Acquisition Time" (0008|0032) and "Radiopharmaceutical Start Time" (0018|1072) were subtracted from each other.

Validation of the calculated SUV was done by comparing the resulting SUV_{max}, derived from the MITK statistics plugin, to reference values ($SUV_{max,ref}$) mentioned in the patient's medical report from nuclear medicine. Medical reports stating $SUV_{max,ref}$ were for six patients. The calculated and reference SUV_{max} are listed in table 4.3. The values calculated with the presented plugin were consistent with those from nuclear medicine reports.

Table 4.3: SUV_{max} calculated with the developed MITK plugin, compared to $SUV_{max,ref}$ values, that were noted in the medical reports from nuclear medicine.

Patient n^o	Plugin calculation SUV_{max} [−]	Medical report $SUV_{max,ref}$ [−]
3	2.89	2.9
7	4.57	4.6
8	3.28	3.3
10	3.38	3.4
14	2.49	2.5
15	3.40	3.4

The Isocontour Plugin

In nuclear medicine, segmentation and quantification of PET images is usually performed using isocontours (see section 3.5.2). A plugin for derivation of isocontours from custom defined contours was developed for MITK. However, the threshold value for these contours is not standardized (c.f. chapter 3.3) and various values are used throughout the literature. Thus, the tool enables flexible definition of the percentage threshold. The user needs to provide a three dimensional contour, which roughly confines the lesion of interest. The contour can be drawn manually, via thresholding or other segmentation techniques. Together with the PET image, the tool extracts all pixels with values exceeding the defined percentage threshold on the maximum intensity value within the contour. Isocontour delineation can be performed on PET raw data as well as SUV images. To allow inter-patient comparison, the isocontour plugin offers the option to normalize the entire image by dividing the pixel values through the maximum value in the isocontour. This option was used for SUV feature images in the prediction analysis, presented in section 4.4.3.

The SUV calculation plugin enables superposition of standard T_1 weighted contrast enhanced MRI with the SUV image, as illustrated in figure 4.21. Isocontours (50%: black contour, 70%: light blue contour) can be drawn on basis of the SUV image and compared to the radiotherapy planning contours (GTV: red contour).

Dynamic PET Analysis Plugin

PET image acquisition can also be performed dynamically, in order to study tissue physiology and extract information on metabolic exchange rates and transport properties. As discussed in section 3.3.3 the time course of the tracer uptake can be described by pharmacokinetic models (tissue compartment models) with varying number of compartments,

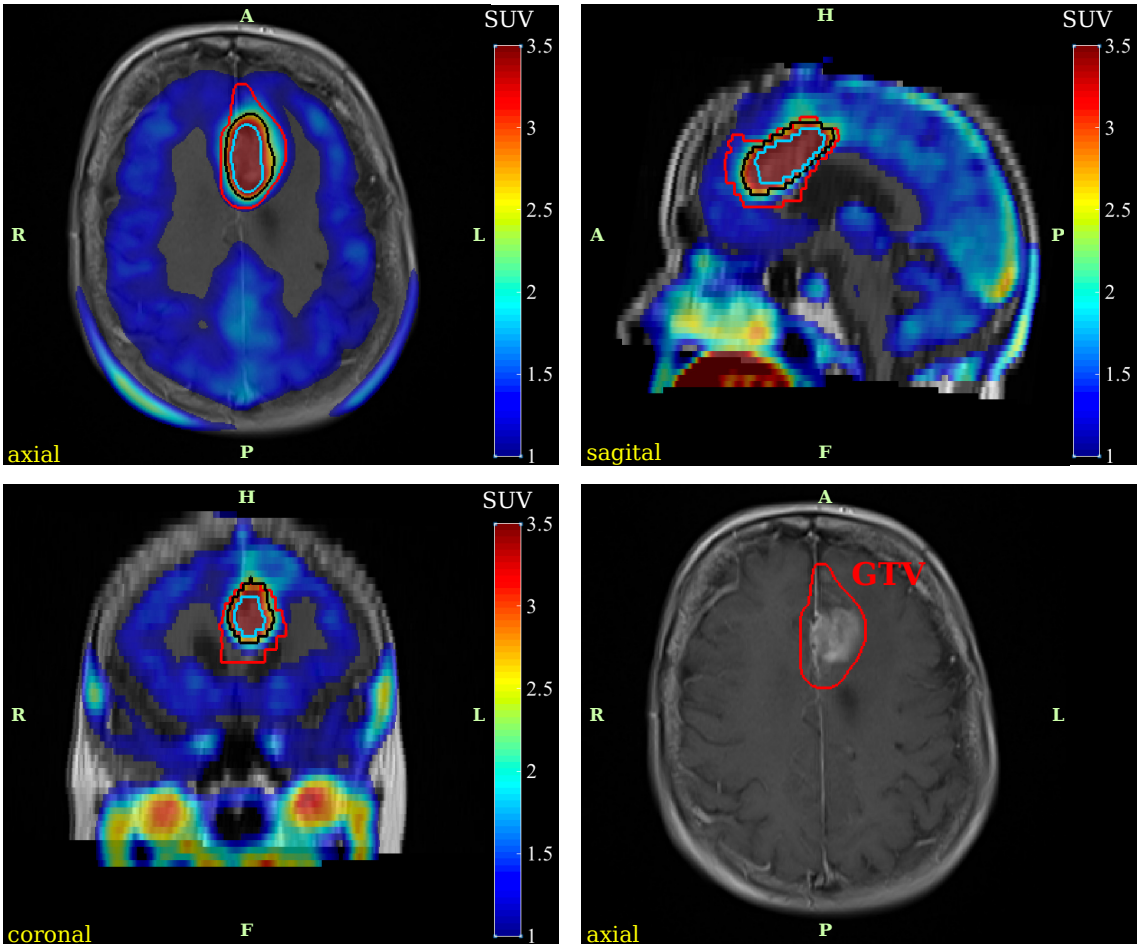

Figure 4.21: The MITK *SUV* calculation plugin allows for overlay of standard T_1 weighted contrast enhanced MRI (right bottom) with the *SUV* image (colored), calculated from ^{18}F-FET PET scans. Isocontours can be drawn on basis of the *SUV* image and compared to the radiotherapy planning contours. Here, the isocontour 50% (black contour) and 70% (light blue contour) are compared to the treatment planning GTV (red contour).

depending on the system transport and metabolic states of the tracer in question. A plugin for analysis of time activity curves with such models was implemented, using the dynamic data analysis module. The two tissue compartment model (2TCM), generally used for dynamic studies of the ^{18}F-FDG tracer, and a simple one tissue compartment model (1TCM) were implemented. They represent potential candidates for analysis of dynamic ^{18}F-FET data. Definition of an arterial input function and the fit configuration (starting values and constraints of model parameters) were implemented similarly to the DCE MRI analysis tool. Unlike in DCE MRI, conversion to concentration of the 4D images is not explicitly necessary in pharmacokinetic modeling of PET, since the raw data images are naturally in concentration units of [Bq/ml]. Nevertheless, the data can be transformed to *SUV* with the afore mentioned *SUV* calculation plugin (section 4.3.1).

4.3.2 Analysis of Endpoint Static ^{18}F-FET PET

In the following study, the value of ^{18}F-FET PET contouring for detection of areas at risk for tumor progress formation was investigated on 18 recurrent high-grade glioma patients, who received ^{18}F-FET PET scans prior to radiotherapy. The goal was to assess the volumes added to standard treatment volume with PET-based delineation, and compare them to the progression volumes of the tumor found at follow-up.

Six different segmentation techniques were applied to contour lesions in ^{18}F-FET PET images: isocontours of 40%, 50%, 60% and 70%, and two semi-automated segmentation algorithms: 3D region growing (RG) and the multi-labeled random walker (RW) (see chapter 3.5.2). For the semi-automated segmentation algorithms, the implementations in the VIRTUOS treatment planning system [Bendl et al., 1993] were used and the resulting contours were imported in MITK.

The maximum SUV (SUV_{max}) was determined for each lesion using the SUV calculation plugin presented above. For normalization to healthy brain tissue, a region of similar size to the lesion, providing stable SUV values, was contoured in the contralateral part of the brain, in three slices around the SUV_{max} presenting slice. The reference SUV of the contralateral healthy brain, SUV_{ref}, was determined as mean SUV within this region. The *tumor-specific uptake ratio* TUR was calculated as

$$TUR = \frac{SUV_{max}}{SUV_{ref}} \tag{4.7}$$

Not every contouring technique could be applied in every patient, since the level of uptake varies greatly between patients. In patients with generally low uptake, application of low isocontour thresholds (40% and 50%) was not reasonable, because these thresholds included background values. Application of isocontours 40%, 50% and 60% failed in 10 patients (55%), 6 patients (33%) and 4 patients (22%), respectively. From the TUR, tolerance values for adequate and reasonable application of the different isocontours could be derived

- Isocontour 40%: $TUR \geq 2.72$
- Isocontour 50%: $TUR \geq 2.10$
- Isocontour 60%: $TUR \geq 1.62$

The isocontour 70% failed in one patient (patient n^o 13), because of very low $TUR = 1.13$. For one patient, contouring with 3D region growing and the multi-label random walker was not possible due to failed registration in VIRTUOS (patient n^o 9). In two patients (n^o 16 and n^o 18), the random walker segmentation failed for unknown reasons.

Tumor regrowth $GTV_{Prog.}$ was delineated based on the T_1 weighted contrast enhanced MRI, acquired at the first progress-confirming follow-up. All studied patients received different irradiation doses, due to the dose escalation scheme of the trial. The influence of the dose was, however, not considered in this study.

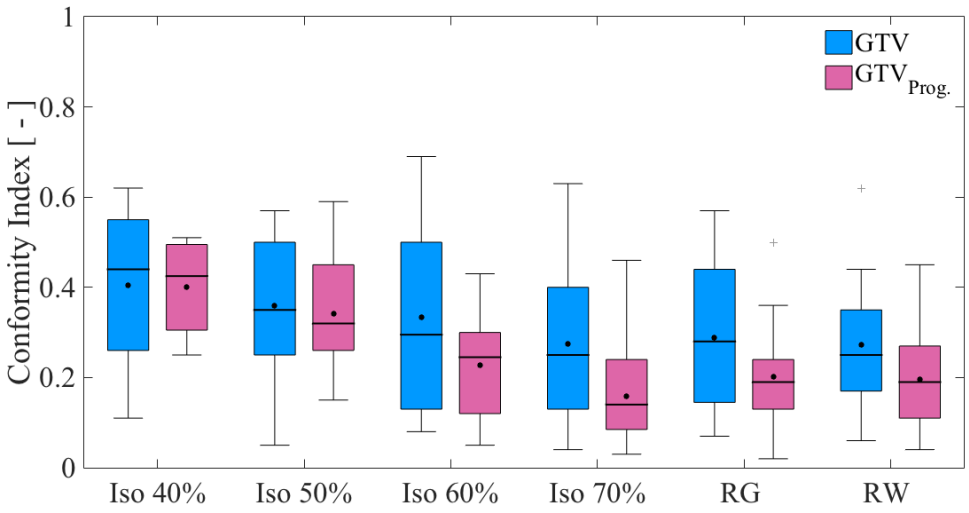

Figure 4.22: Conformity index of different PET-based contouring techniques with respect to the treatment planning GTV (blue) and the progress tumor volume $GTV_{Prog.}$ (pink). Conformity indices C_{GTV} and $C_{Prog.}$ were calculated as intersection between intersection between PET-based and MRI-based contours (GTV and $GTV_{Prog.}$), divided by their union. The whiskers are defined as first/third quartile -/+ 1.5 IQR. The median is represented by the black line, the black dot shows the mean value.

PET-based contours were compared to the GTV and $GTV_{Prog.}$ by calculation of the intersection between contours for each patient and normalizing it to the union. This yielded the conformity index C:

$$C_{GTV} = \frac{PET \cap GTV}{PET \cup GTV} \qquad C_{Progress} = \frac{PET \cap GTV_{Prog.}}{PET \cup GTV_{Prog.}} \tag{4.8}$$

Table 4.4 lists the SUV_{max}, TUR and the contouring technique yielding the largest conformity index with GTV and $GTV_{Prog.}$ together with the corresponding value, respectively.

Results of the conformity indices with GTV (blue) and $GTV_{Prog.}$ (pink) are plotted in figure 4.22, for the different contouring methods along the x-axis. The isocontour of 60% yielded the highest conformity with the treatment planning GTV most often (six cases), closely followed by the isocontours of 40% and 50%. However, figure 4.22 shows that on average, the isocontour of 40% yielded the highest conformity with a mean value of $C_{GTV}(\text{iso } 40\%) = 0.40 \pm 0.2$. For patient n^o14, the conformity between GTV and PET contour was low for all contour techniques, with a maximum value of $C_{GTV} = 0.08$ for the isocontour of 60%. This was due to a very small GTV volume in general ($V_{GTV} = 634\text{mm}^3$).

Figure 4.23 shows the correlation between the SUV_{max} and PET contour yielding the largest conformity with the GTV (blue dots) and with the $GTV_{Prog.}$ (red cross). At the first glance, a roughly linear relation could be assumed.

For detailed insight into the congruence between ^{18}F-FET PET-active region and tumor progress volume, GTV was subtracted from the PET-based contours, yielding the volume $A = PET \setminus GTV$. A denotes the volume, which shows enhanced PET tracer uptake but

Table 4.4: Results for the largest conformity index between PET contour and treatment planning GTV, and between PET contour and tumor volume $GTV_{Prog.}$ at progress, respectively. For every patient, the SUV_{max} of the lesion was calculated and decided by the reference SUV_{ref} in healthy brain tissue (*uptake-to-noise ratio* TUR). Conformity indices C_{GTV} and $C_{Prog.}$ were calculated as intersection between intersection between PET-based and MRI-based contours (GTV and $GTV_{Prog.}$), divided by their union. Column 4 lists the contouring technique that yielded the larges conformity index (column 5) for overlap with the GTV. Column 6 lists the contouring technique that yielded the highest conformity index (column 7) for overlap with the $GTV_{Prog.}$.

Patient	SUV_{max} [−]	TUR [−]	Best match GTV	C_{GTV} [−]	Best match $GTV_{Prog.}$	$C_{Prog.}$ [−]
1	3.87	3.46	Iso 50%	0.28	Iso 40%	0.25
2	1.83	1.63	RW	0.39	Iso 70%	0.46
3	2.89	3.66	Iso 60%	0.69	Iso 40%	0.49
4	3.98	2.74	Iso 60%	0.50	Iso 50%	0.59
5	1.26	1.62	RG	0.31	Iso 70%	0.27
6	3.75	4.17	Iso 40%	0.53	Iso 40%	0.51
7	4.57	3.20	Iso 40%	0.56	Iso 40%	0.44
8	3.28	2.80	Iso 40%	0.62	Iso 40%	0.50
9	2.74	2.71	Iso 60%	0.64	Iso 60%	0.30
10	3.38	4.07	Iso 40%	0.54	Iso 40%	0.34
11	3.00	2.61	Iso 50%	0.51	Iso 40%	0.40
12	1.97	1.50	Iso 70%	0.49	RW	0.28
13	1.08	1.13	RW	0.23	RW	0.04
14	2.49	2.59	Iso 60%	0.08	Iso 50%	0.50
15	3.40	3.43	Iso 60%	0.49	Iso 40%	0.27
16	1.52	2.05	Iso 60%	0.20	Iso 60%	0.50
17	2.79	2.56	Iso 50%	0.22	Iso 50%	0.32
18	1.16	1.43	Iso 70%	0.40	Iso 70%	0.07

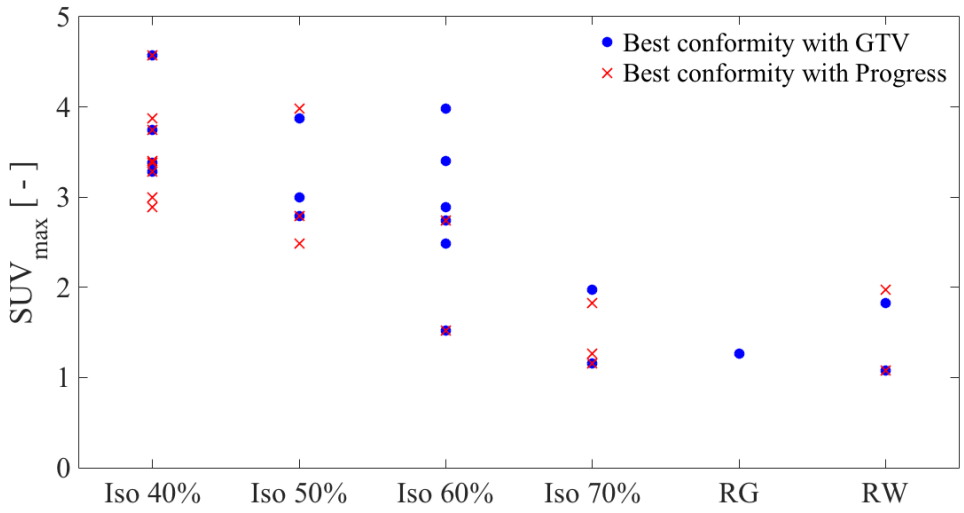

Figure 4.23: Relation between SUV_{max} and the PET-based contour, which yielded the best conformity index with the GTV (blue dots) and $GTV_{Prog.}$ (red crosses).

no MRI contrast-agent uptake. The volume difference between $GTV_{Prog.}$ and treatment planning GTV was calculated, $P = GTV_{Prog.} \setminus GTV$, similar to the approach in section 4.2.2. Figure 4.24 schematically shows the different contours GTV (red), $GTV_{Prog.}$ (blue) and PET-based contour (green), and the respective volumes P (light blue), A (light green), derived from them. The intersection between the two volumes, $I = P \cup A$ (pink), was used as indicator for evaluation of the ability to detect potential tissue at risk with ^{18}F-FET PET.

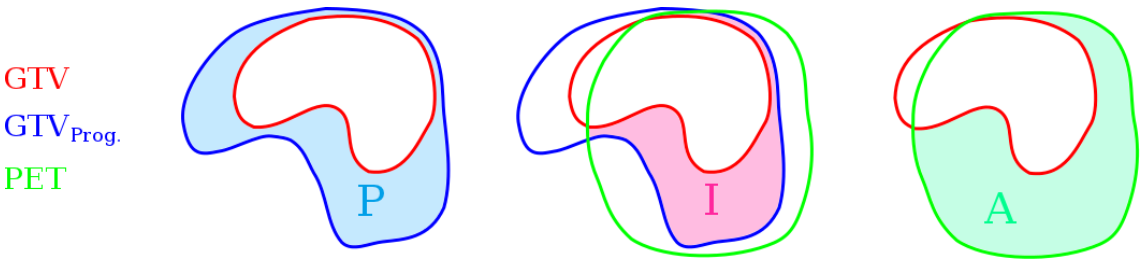

Figure 4.24: Different volumes that were investigated for quantification of the overlap of progress and PET-based contours. The GTV (red), the progress tumor volume $GTV_{Prog.}$ (blue) and the PET-based contour (green) were used for analysis. The volume differences between PET-based contour and GTV is the defined as $A = PET \setminus GTV$. Progress was defined as difference between GTV and $GTV_{Prog.}$ (blue): $P = GTV_{Prog.} \setminus GTV$. The intersection $I = P \cup A$ (pink), was used as indicator for evaluation of the ability to detect potential tissue at risk with ^{18}F-FET PET.

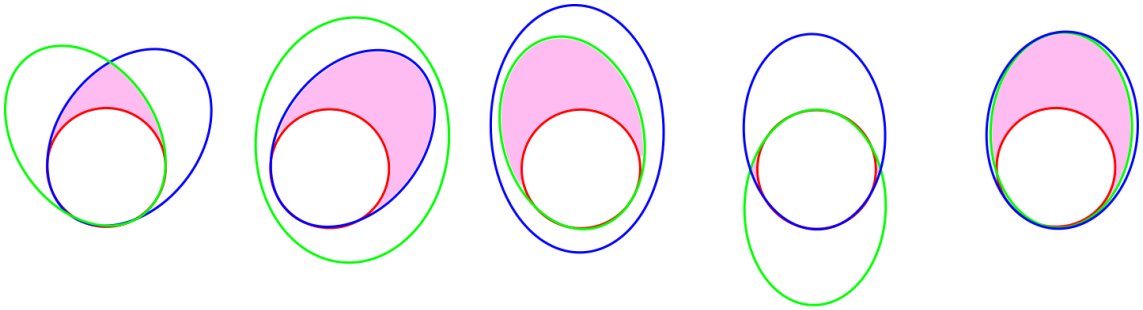

Figure 4.25: Illustration of different scenarios for comparisons between GTV (red), progress tumor volume $GTV_{Prog.}$ (blue) and the PET-based contour (green), with corresponding values for sensitivity and specificity. If the PET-derived contour is very large, sensitivity will be close to 1 and specificity will be smaller than 1. If GTV was delineated broadly, specificity will be close to 1, but sensitivity will be small. Good coverage of the tumor progress volume by the PET-active area exists only, if both sensitivity and specificity are close to 1.

Two parameters quantifying the degree of overlap between tumor progress and ^{18}F-FET PET volumes were defined:

$$\text{Sensitivity: } Se = \frac{P \cup A}{P} = \frac{I}{P} \tag{4.9}$$

$$\text{Specificity: } Sp = \frac{P \cup A}{A} = \frac{I}{A} \tag{4.10}$$

The different scenarios for overlap between GTV (red), $GTV_{Prog.}$ (blue) and PET-based contour (green), and the values for sensitivity and specificity, that they lead to, are illustrated in figure 4.25. If the PET-derived contour is very large, which is the case especially for low isocontour thresholds, sensitivity will be close to 1 and specificity will be smaller than 1. On the other hand, if GTV was delineated broadly, specificity will be close to 1, but sensitivity will be small. Good coverage of the progress volume by the PET-active area exists only, if both sensitivity and specificity are close to 1.

In all cases, the false prediction of the PET-based contour (false positives), i.e. the volume that would be added to the GTV by ^{18}F-FET PET, but is not associated with progress, can be derived as:

$$f.p. = \frac{A \setminus I}{A} = 1 - \frac{I}{A} = 1 - Sp \tag{4.11}$$

In the same manner, the false negatives, i.e. parts of the progress volume that are not detected by the PET-based contour, yield

$$f.n. = \frac{P \setminus I}{P} = 1 - \frac{I}{P} = 1 - Se \tag{4.12}$$

Results for sensitivity (blue) and specificity (pink) of the different PET contouring techniques are shown in figure 4.26 for each patient. The isocontour of 40% clearly yielded the highest conformity with regards to the progress tumor volume $GTV_{Prog.}$ in most cases and on average with a mean value of $C_{Progress}(\text{iso } 40\%) = 0.40 \pm 0.1$. However, the results displayed in figure 4.26 indicate, that isocontour 50% presented the best relation between high sensitivity and high specificity with respect to the tumor progress volume. In general, specificity was close to one in most patients for the large isocontour thresholds (60% and 70%) as well as region growing and random walker technique. On the other hand, sensitivity was generally low for these patients. This effect arose mostly due to large GTV contours for treatment planning, that completely enclosed the smaller PET-contours. In patient n^o 6 and n^o 7, the isocontours of 60% and 70%, as well as the region growing and random walker algorithms did not add any volume to the GTV ($A = 0$).

4.3.3 Analysis of Dynamic ^{18}F-FET PET

Pharmacokinetic modeling of dynamic ^{18}F-FET PET using the 1TCM and 2TCM

Few studies have investigated the possibility of pharmacokinetic modeling on ^{18}F-FET PET [Thiele et al., 2009]. Using the PET fitting plugin, feasibility of pharmacokinetic analysis for the available dynamic ^{18}F-FET PET data was investigated. The standard one tissue compartment model (1TCM) provides a simple but stable representation of the ^{18}F-FET tracer in plasma and tissue. The bidirectional transport of ^{18}F-FET into cells by system L would justify usage of the two tissue compartment model (2TCM), representing ^{18}F-FET exchange between the three compartments "blood", "interstitial volume" and "cells".

Applicability of the 1TCM and the 2TCM for analysis of dynamic ^{18}F-FET PET time-activity curves in high grade glioma patients was investigated on seven patients, for which segmentation with the isocontour 50% was applicable. All patients had received dynamic and endpoint static ^{18}F-FET PET prior to radiotherapy.

Based on the endpoint static image, isocontour 50% was drawn around the lesion, as illustrated in figure 4.27. The standard T_1 weighted contrast enhanced MRI image (left) is displayed together with the GTV (red) of three patients (n^o 1: top, n^o 7: middle, n^o 8: bottom), compared to the isocontour 50% (purple) on corresponding SUV maps (right). Isocontour 50% was chosen, as it presented the best results in terms of sensitivity and specificity in the afore mentioned study. However, it can be seen, that the PET contour and GTV differ in size in all three patients. There is a distinct mismatch between GTV and isocontour in patient n^o 1.

Within the isocontours, time-activity curves of each voxel were fitted with the 1TCM and 2TCM, yielding maps for each parameter k_i. Positivity constraints were imposed on all exchange rate parameters, $0 \leq k_i$, because they are defined in terms of unidirectional flux. For the 2TCM, the fractional blood volume V_B is normalized to a volume element of tissue. Thus, the additional condition $0 \leq V_B \leq 1$ was applied. For evaluation of fit quality, parameter maps of the sum of squared residuals $\mathcal{X}^2$ were studied.

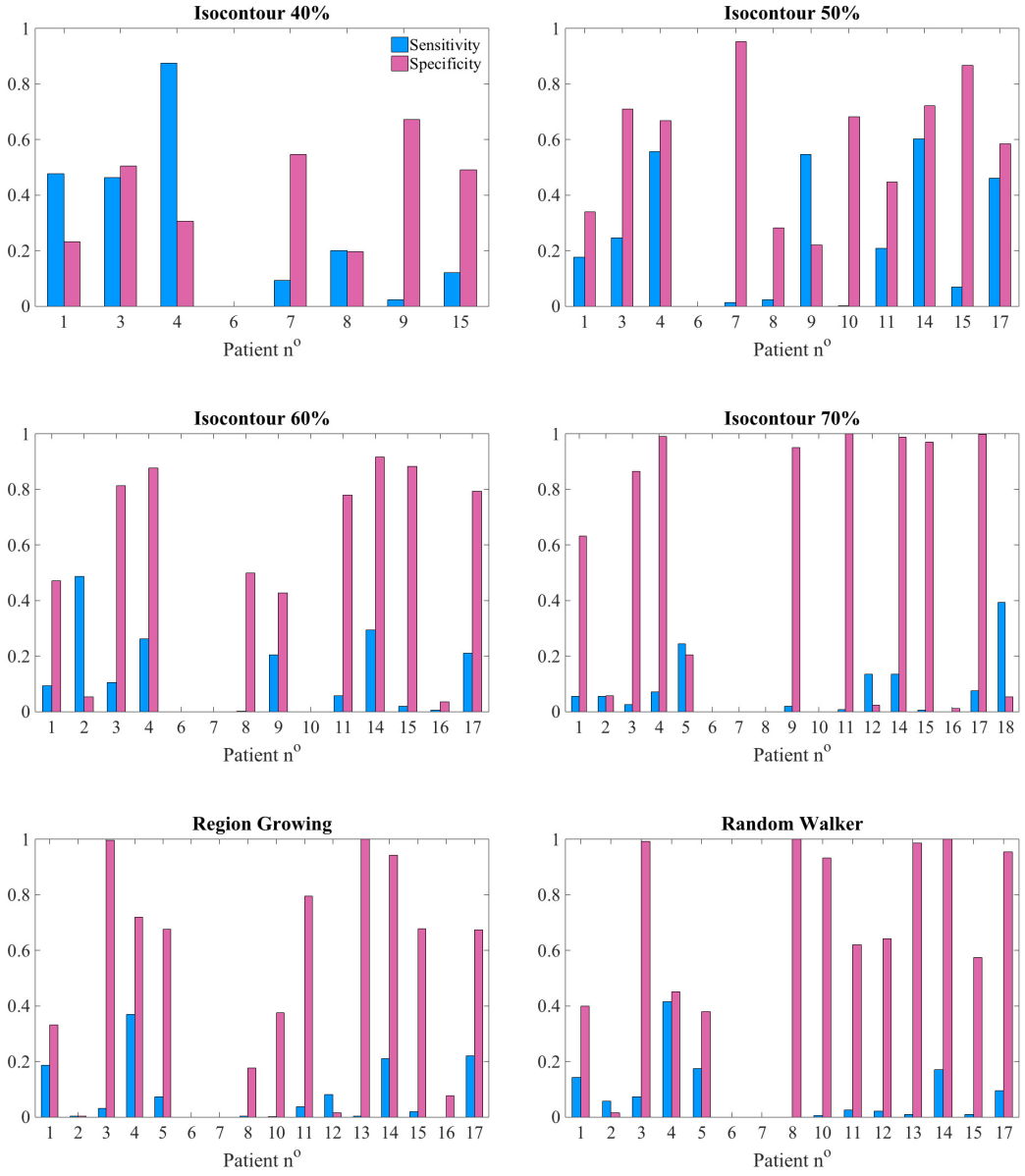

Figure 4.26: Results for sensitivity (blue) and specificity (pink) in every patient, for different PET-based contouring techniques. Sensitivity is calculated as intersection between progress tumor volume $P = GTV_{Prog.} \setminus GTV$ and volume added to the GTV by the PET-based contour $A = PET \setminus GTV$, normalized to the volume P added to the GTV by tumor progress. Specificity is defined as intersection between progress tumor volume $P = GTV_{Prog.} \setminus GTV$ and volume added to the GTV by the PET-based contour $A = PET \setminus GTV$, normalized to the volume A added to the GTV by the PET-based contour. Higher sensitivity and specificity indicate better coverage of tumor progress by PET-active volume. False prediction of the PET-based contour (false positives), i.e. the volume that would be added to the GTV by ^{18}F-FET PET, but is not associated with progress, can be calculated as $1 - Specificity$. False negatives, i.e the part of the progress volume that is not detected by the PET-based contour, can be calculated as $1 - Sensitivity$.

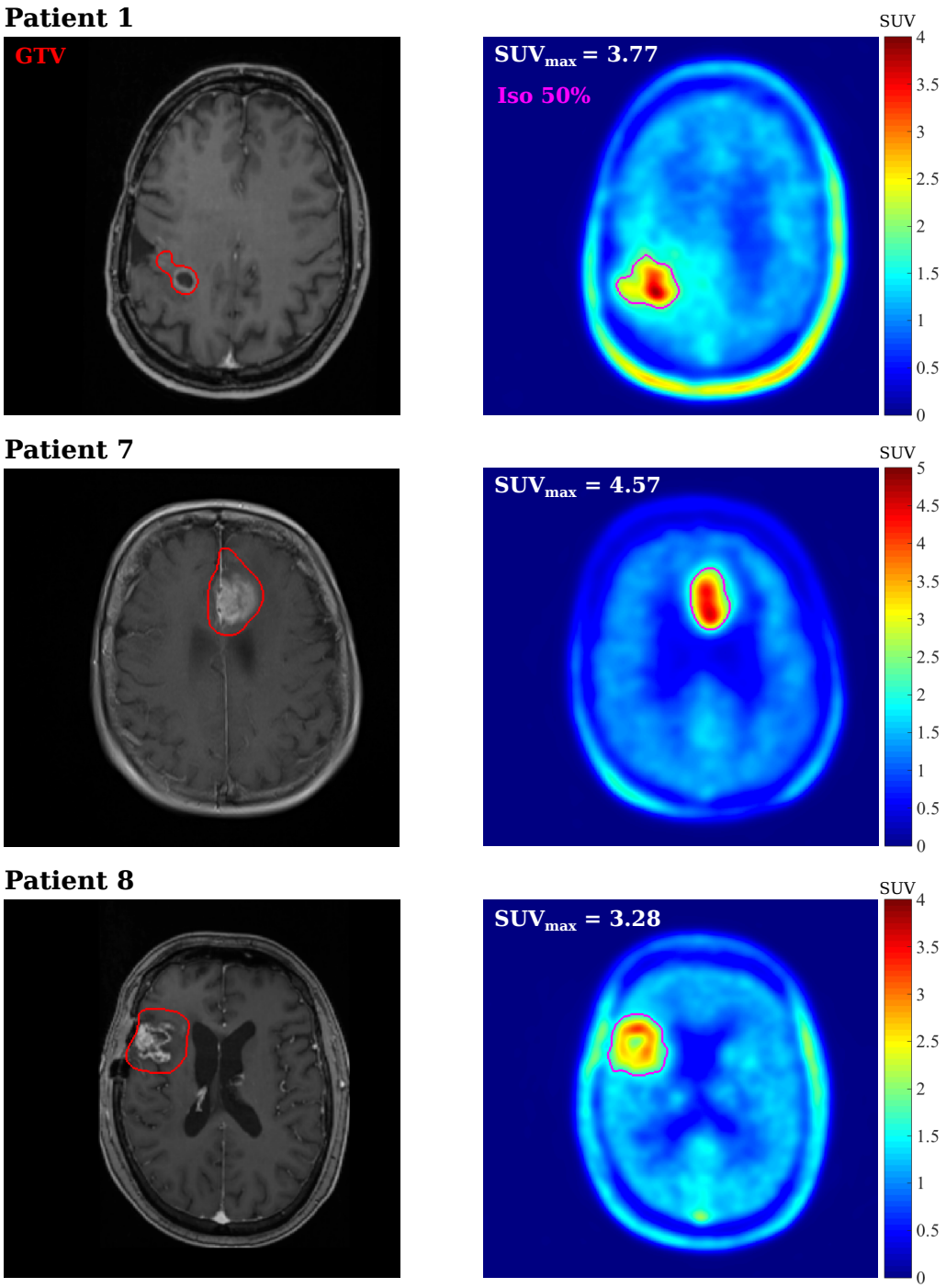

Figure 4.27: T_1 weighted, contrast enhanced MRI (left) and the macroscopic visible tumor volume GTV (red contour), compared to SUV maps from ^{18}F-FET PET (right) and isocontour 50% (purple contour) for patients n^o 1, 7 and 8.

Table 4.5: Mean values and standard deviation of parameter estimates from fits with the one tissue compartment model (1TCM, K_1 and k_2) and the two tissue compartment model (2TCM, K_1, k_2, k_3, k_4 and V_B) for seven different patients. Parameters were averaged within the isocontour 50%.

Patient	1TCM		2TCM				
n^o	K_1 [$\frac{1}{\text{min}}$]	k_2 [$\frac{1}{\text{min}}$]	K_1 [$\frac{1}{\text{min}}$]	k_2 [$\frac{1}{\text{min}}$]	k_3 [$\frac{1}{\text{min}}$]	k_4 [$\frac{1}{\text{min}}$]	V_B [$-$]
1	0.07 ± 0.02	0.12 ± 0.04	0.09 ± 0.08	0.63 ± 1.32	0.19 ± 0.33	0.09 ± 0.28	0.03 ± 0.01
3	0.18 ± 0.09	0.32 ± 0.18	15.62 ± 179	136.16 ± 1540	0.15 ± 0.24	0.15 ± 0.30	0.09 ± 0.04
7	0.17 ± 0.08	0.23 ± 0.14	88.31 ± 554	810 ± 4524	0.37 ± 0.36	0.15 ± 0.38	0.06 ± 0.04
8	0.15 ± 0.10	0.31 ± 0.27	0.17 ± 2.8	1.01 ± 27	0.14 ± 0.26	0.14 ± 0.27	0.09 ± 0.06
10	0.89 ± 7.2	2.34 ± 20.1	19.55 ± 166	210.33 ± 1624	0.28 ± 0.35	0.11 ± 0.21	0.04 ± 0.03
15	0.29 ± 1.4	0.73 ± 4.7	0.37 ± 0.43	2.08 ± 2.46	0.24 ± 0.15	0.09 ± 0.05	0.03 ± 0.04
17	0.10 ± 0.05	0.23 ± 0.15	75.6 ± 340	1086 ± 4665	0.29 ± 0.34	0.09 ± 0.14	0.04 ± 0.02

Table 4.5 presents the results for mean parameter estimates from the 1TCM and 2TCM with corresponding standard deviations, averaged within the isocontour 50%, for all seven patients.

Parameter estimates from the 1TCM yielded reasonable results, with values in plausible physiological ranges and adequate standard deviations, except for patient n^o 10. The estimated values are comparable to the results found by Thiele et al. [2009].

Parameter estimates resulting from fits with the 2CXM were less stable. In several cases, the mean parameter estimates yielded unreasonably high values, pointing at decreased fit stability and outliers. The large mean values and standard deviations for K_1 and k_2 from the 2TCM hinted at overfitting. Estimates for k_3, k_4 and V_B were more plausible, however since the model seems to overfit the data, these results are not reliable. Furthermore, the values exhibit enhanced standard deviations.

Overall, the results suggest, that two out of the five model parameters from the 2TCM are not needed to describe the data. The 1TCM could be extended with a third parameter, similar to the extended Tofts model, for improved description of the time-activity curves.

This heterogeneity can also be seen in figure 4.28, showing maps of the parameter estimates from fitting with the 1TCM (top row) and 2TCM (middle and bottom row) for patient n^o 1. The parameter estimates from the 1TCM exhibit tumor heterogeneity beyond the one observed in the SUV map (see figure 4.27). This result indicates, that parameter estimates from dynamic FET PET can provide a more detailed insight on tumor heterogeneity, compared to endpoint static acquisition.

The maps obtained from fitting the 2TCM presented with even larger heterogeneity (voxels without color coding (transparent) present values $0 < v < 10^{-5}$). The parameter estimates from the 2TCM fit exhibit enhanced clustering and large outlier values.

Three different areas within the parameter map of K_1 from the 1TCM were chosen to illustrate the curve shape in hot spots and cold spots (see figure 4.29, left). For these

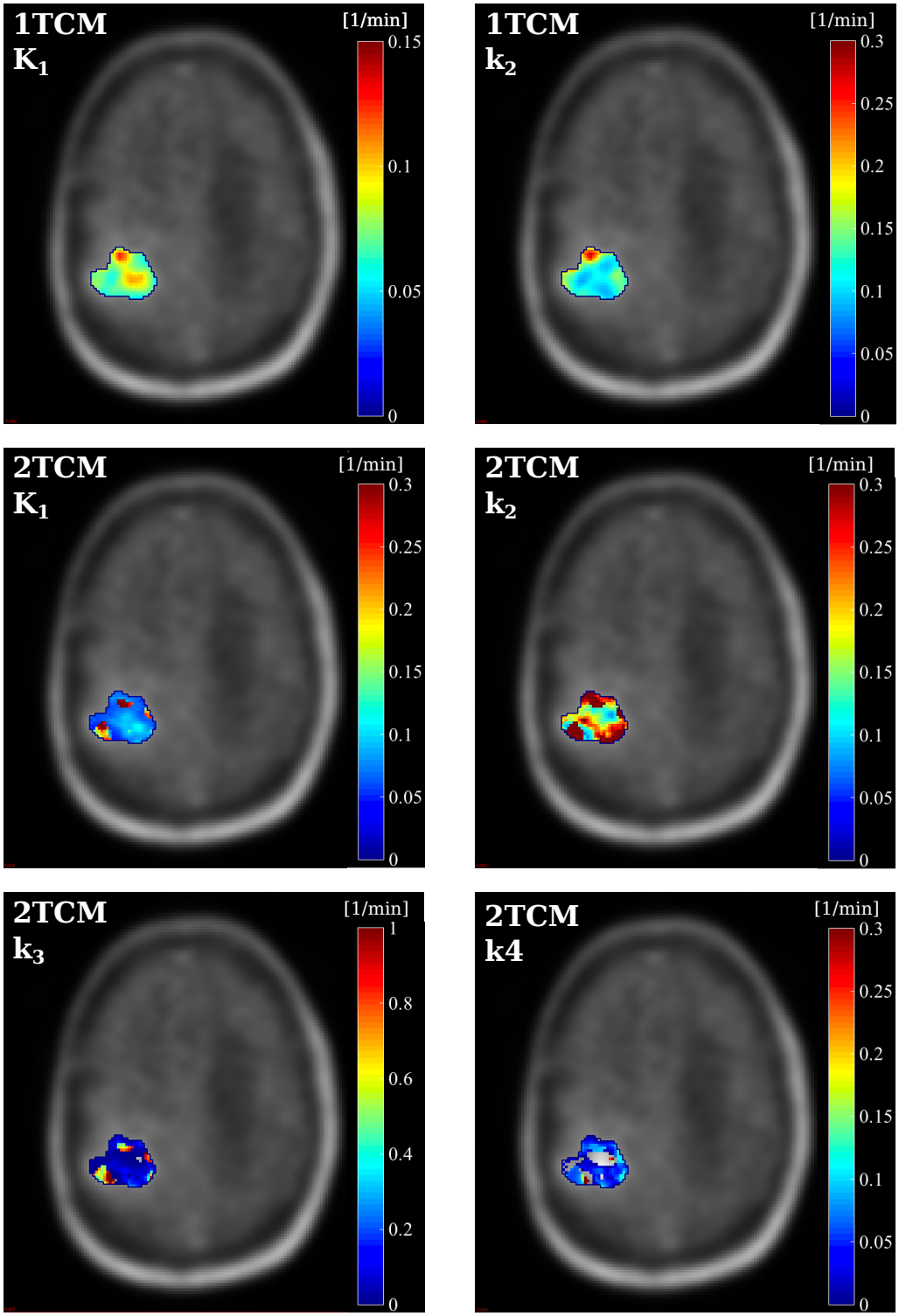

Figure 4.28: Maps of parameter estimates within the isocontour 50% (colored) from fitting time-activity curves of patient n^o 1 with the one tissue compartment model (1TCM K_1 an k_2) and the two tissue compartment model (2TCM K_1, k_2, k_3, k_4). The parameters are displayed on the PET raw data image (grey scale). All parameters are in units of $\left[\frac{1}{\text{min}}\right]$. Voxels within the isocontour containing values of less than 10^{-5} are not color-coded, due to a visualization limitation of MITK.

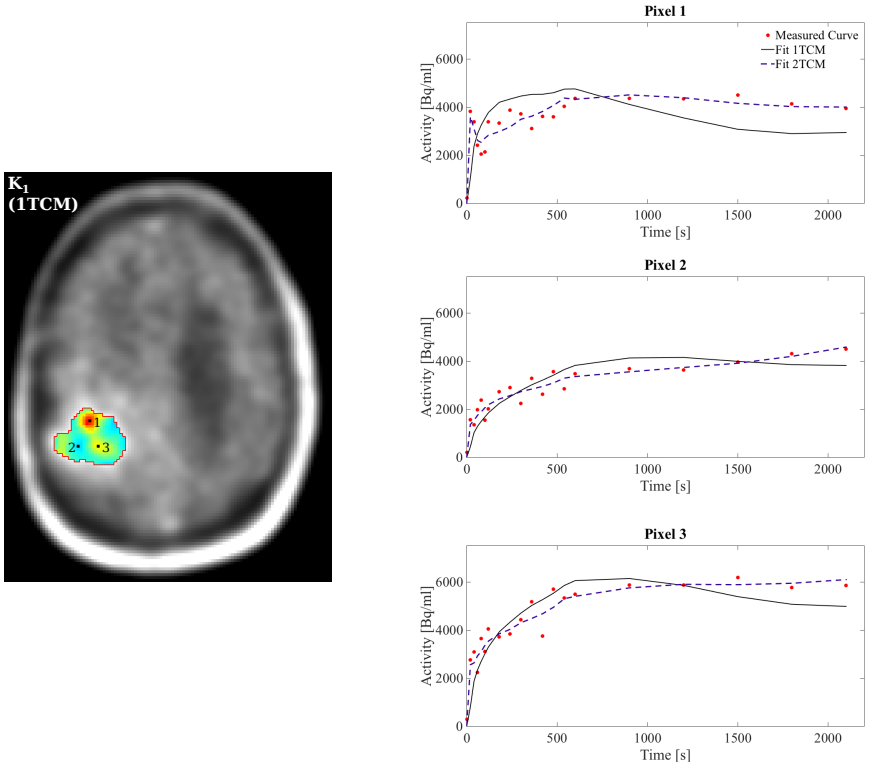

Figure 4.29: Measured time-activity curves (red dots) and fitted model curves from the one tissue compartment model (black line) and the two tissue compartment model (blue dotted line) for 3 representative voxels in patient n^o 1. The voxels were placed in distinct hot spots/cold spots, illustrated in the parameter map of K_1 from fitting with the 1TCM (left image).

three voxels, representative measured TACs with fit curves from the 1TCM and 2TCM are shown in figure 4.29 (right). It could be observed, that the 2TCM seemed to fit the data better.

For a more general assessment of the fit quality of both models, the $\mathcal{X}^2$ values from fits with the 1TCM (blue) and 2TCM (pink) in three patients are plotted in figure 4.30. The median is represented by the black line, the black dot shows the mean value. As expected the 2TCM fits yielded lower $\mathcal{X}^2$, since the increased number of parameters offer more degrees of freedom. However, more outliers to large $\mathcal{X}^2$ values were observed with the 2TCM, and the values were wider spread.

In summary, even though the 2TCM seemed to yield better fits, the results indicated overfitting and less robust fits. It is likely, that the acquired image quality (temporal sampling and noise level) is not sufficient to resolve the physiological detail level described with the 2TCM. The parameter estimates obtained with the 1TCM fit offered increased stability.

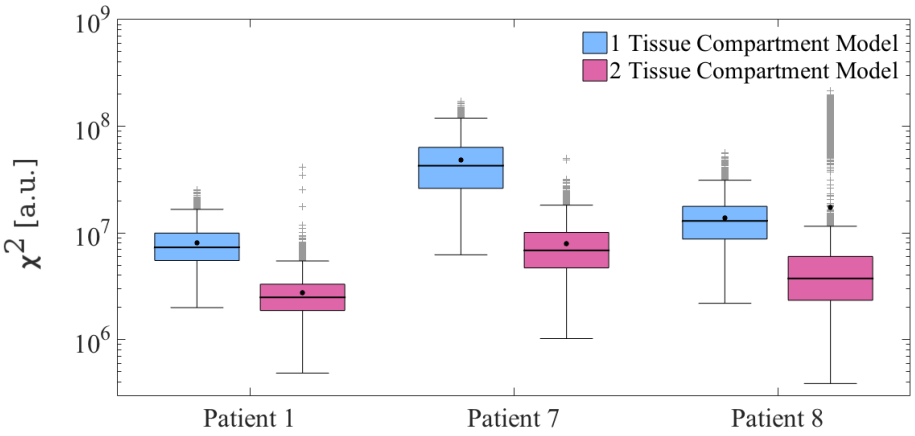

Figure 4.30: Sum of squared residuals $\mathcal{X}^2$, resulting from fits of time-activity-curves with the one tissue compartment model (blue) and the two tissue compartment model (pink) model within the isocontour 50%, for patients n^o 1, 7 and 8. Due to the large values, $\mathcal{X}^2$ is displayed on a logarithmic scale. The whiskers are defined as first/third quartile -/+ 1.5 IQR. The median is represented by the black line, the black dot shows the mean value.

Non-compartmental analysis of dynamic ^{18}F-FET PET: Evaluation of semi-quantitative parameters in different tissue volumes

Pharmacokinetic modeling on the whole acquired ^{18}F-FET PET image is very time consuming, since a large number of pixels have to be fitted. Furthermore, the requirements and assumptions of the compartmental models are not met in all tissue structures of the brain. For example, it is not advisable to define a single arterial input curve for the entire head. Thus, the possibility of using semi-quantitative parameters from non-compartmental analysis for possible applicability in the multi-modal image analysis approach was investigated, similar to the study presented in section 4.2.2.

For the seven patients mentioned above, the dynamic ^{18}F-FET PET image was registered to the treatment planning CT and converted to SUV images. The parameters of AUC, MRT and SUV_{peak} ($= C_{max}$) were calculated on the entire image. Mean values and standard deviations of the three parameters, averaged within the isocontour 50%, are listed in table 4.6 for each patient. MRT provided a very stable measure with low standard deviation and little variance among different patients. SUV_{peak} was naturally lower than the SUV_{max} (c.f. table 4.4), since SUV_{peak} was averaged over the entire contour, whereas SUV_{max} represents a single voxel with the highest uptake. AUC exhibited large parameter differences and high standard deviations, representing the afore mentioned heterogeneity within the volume.

Similar to the analysis of semi-quantitative parameters in DCE MRI data, the values of parameters from non-compartmental analysis of dynamic ^{18}F-FET PET were investigated in three different volumes: the GTV, the progress $P = GTV \setminus GTV_{Prog.}$ and a healthy tissue reference region. The latter two volumes were both already defined in section 4.3.2.

Figure 4.31 shows the resulting mean values with standard deviation of the parameters AUC (top), MRT (middle) and SUV_{peak} (bottom) for all seven patients. The values were

Table 4.6: Semi-quantitative parameter mean values and standard deviations from non-compartmental analysis of ^{18}F-FET PET time-activity curves of several different patients. Parameters were averaged within the isocontour 50%.

Patient	AUC [a.u.]	MRT [s]	SUV_{peak} [−]
Patient 1	4590 ± 798	1011 ± 22	2.59 ± 0.43
Patient 3	3695 ± 744	1011 ± 28	2.12 ± 0.37
Patient 7	5850 ± 1075	1011 ± 25	3.32 ± 0.58
Patient 8	4276 ± 724	1039 ± 32	2.52 ± 0.39
Patient 10	3970 ± 649	1000 ± 35	2.31 ± 0.51
Patient 15	4135 ± 639	1010 ± 26	2.42 ± 0.50
Patient 17	3112 ± 527	1033 ± 29	1.82 ± 0.30

averaged over the GTV (blue diamond), the progress volume P (green square) and in the healthy tissue reference region (pink circle). The MRT provides a stable measure with little differences between different patients. The parameter does not help to distinguish between tumor, progress and healthy tissue though. Only for patient n^o 15, the value of $MRT = 951 \pm 48$ was measured in the healthy tissue reference region was lower than in the other patients. However, the values are consistent within the error bars. The larger standard deviation in this case indicates enhanced heterogeneity of the measured values, which was also observed in SUV_{peak}.

In AUC and SUV_{peak}, variations between the different volumes could be observed, especially between the GTV and the other two volumes. The individual values of these two parameters were similar in most patients. Only patient n^o 17 exhibited no difference in AUC between the three different volumes. It was observed that the measured values in the progress volume and healthy tissue region were similar to those of the other patients, but AUC in the GTV was distinctively lower. The average AUC within the isocontour 50 % also took the lowest value in this patient: $AUC = 3112 \pm 527$. The patient also showed no difference in SUV_{peak} between different volumes and a low mean $SUV_{peak} = 1.82 \pm 0.3$ within the isocontour. AUC and SUV_{peak} exhibited very similar parameter behavior. In patients n^o 1 and 3, they show distinct differentiation between GTV, progress and healthy tissue. This result does not translate to the other patients though, as in these cases the parameters differ only between GTV and the other two tissue types.

In summary, the results indicate that parameters from non-compartmental analysis of ^{18}F-FET PET time-activity curves might provide a good measure to distinguish tumor tissue. However, they are able to detect the progressive volume only to an extent.

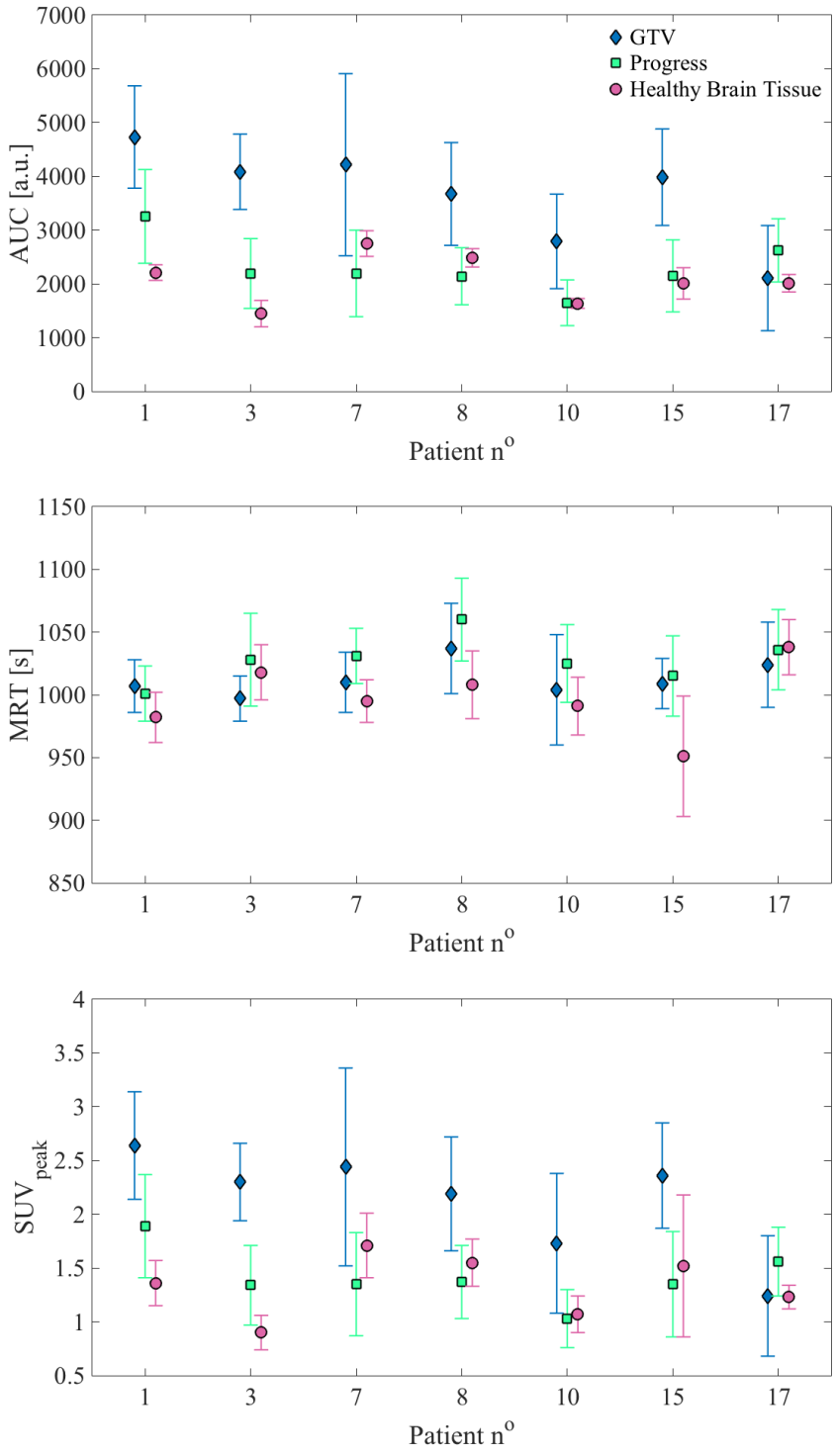

Figure 4.31: Semi-quantitative parameters *AUC*, *MRT* and SUV_{peak} (= C_{max}) from non-compartmental analysis of dynamic ^{18}F-FET PET data of seven patients. Parameter mean values were averaged within the treatment planning *GTV* (blue diamond), the progress tumor volume $P = GTV \setminus GTV_{Prog.}$ (green square) and healthy brain tissue (pink circle). Error bars denote the standard deviation of the mean.

4.4 Multi-Modal Image Analysis using Random Forest Machine Learning

The presented analysis software, together with the already available MITK tools, made pre-processing of all different presented modalities from the multimodal image set possible.

The aim of the following study was to find *rules* in terms of parameter combinations, which are able to predict the probability for tumor progression in each pixel. Various machine learning algorithms can be used to address this classification problem. The presented work resorted to random forest classification, because of its capability to handle a multitude of different samples and features. Of course, it is possible to address the classification problem with other algorithms and techniques, such as support vector machines or clustering algorithms. However, these approaches do not naturally extent for multiple classes. Furthermore they are at risk of running into boundaries concerning computational capacity, when confronted with large data sets.

The forest is trained to assign each pixel with a tissue morphology describing class, based on intensities from various imaging modalities. This pixel wise identification of tumor tissue based on radiological images acquired prior radiotherapy could be used to support and improve planning target delineation. The method was initially introduced by Weber et al. [2015], who used random forest mainly grown from features of diffusion weighted MRI for training and prediction of tumor growth.

The following section presents a workflow for the described analysis of image pre-processing and random forest machine learning, based on developed and already existing tools in MITK. An example analysis on a small set of patient data is shown for illustration of the functionality and results.

4.4.1 Software Developments

The software library VIGRA [Köthe et al., 2008] includes an implementation of random forests for classification and regression problems. The library, together with the infrastructure for handling of features and classes in training and testing, was incorporated into MITK by Weber et al. [2015]. Based on this *classification module*, a command line tool for classification of the available data of recurrent high grade glioma patients was developed.

The different types of images used for classification are referred to as *feature images*. In the language of classification, an image pixel (referenced by its image index i) represents a sample $\vec{x}$. The intensity from the K different imaging modalities are the samples attributes, or *features*, $\vec{\Theta} = (\Theta_1, \Theta_2, ..., \Theta_K)$. The *class mask* defines the assignment of the samples to one of the $m = 1, ..., M$ classes c_m (target vectors) in an integer valued image.

In VIGRA, the features of each pixel are stored as rows in the *feature matrix*. In this matrix, each row represents a sample $\vec{x}$. The first column is the samples pixel index i, the following columns represent each the corresponding value of a feature image. For several patients, the samples from each patient are listed after one another. Thus, for N patients with K features and p_n samples in patient $n = \{1, ..., N\}$, the feature matrix is a $\left(\sum_{n=1}^{N} p_n\right) \times (K + 1)$ matrix with rows $[i, \Theta_1, ..., \Theta_K]$. The *class matrix*, which stores the

assignment of the samples to the corresponding class, consists of only two columns, the pixel index and the class index $[i, c_m]$.

The workflow of the random forest is illustrated in figure 4.32. For training (left side), a set of patients with corresponding feature images, on which classification should be performed, is selected. The developed classification tool loads the required images for training from an input file, defining the list of training patients and features, together with the corresponding class mask. From these images, the feature and class matrices are extracted.

Configuration of the random forest is read from a separate configuration file. The following random forest parameters can be defined:

- *Minimum split node size:* The number of samples in a node required for the node to split further. If the number of samples in the node is below this threshold, the node does not split, even if classification is not yet perfect.
- *Tree count:* How many trees are grown for the forest.
- *Tree depth:* How many splits are grown at most
- *Precision:* The splitting precision
- *Fraction:* Specifies the fraction of the total number of samples used for training of a tree (out-of-bag sampling).
- *Sample with replacement:* Boolean value if out-of-bag sampling is performed with or without replacement

The split criterion is the Gini impurity. In principle, it is possible to derive the *test*, that is applied to split a node, from linear combinations of multiple features. However, in the presented work, this option was not exploited, and splitting of a node was based on applying a threshold to a single feature.

The configured forest is trained to learn classification rules based on the feature matrix and class matrix. The fully trained forest can afterwards be used for *prediction*, i.e testing, on previously unseen feature images of new patients, as indicated on the right hand side of figure 4.32. The patients for testing are defined in the input file as well. The feature images in question are loaded with a prediction mask, defining the pixels on which classification should be performed, and the feature matrix is extracted. All samples in the testing feature matrix are run down the trees in the forest and the resulting voted class of each pixel is stored in a prediction image, similar to a class mask. The predicted classification image can be loaded and evaluated in MITK.

4.4.2 Development of a Classification Workflow

The inclusion of physiological imaging modalities was especially interesting for this thesis, focusing on the predictive value of metabolic parameters from FET-PET and hemodynamic parameters from DCE MRI. As shown before, the available DCE MRI data was not suitable for pharmacokinetic analysis. Hence, semi-quantitative curve-describing parameters from non-compartmental analysis were used. Data from dynamic and endpoint static ^{18}F-FET-PET scans was included, because it provides high sensitivity and specificity of ^{18}F-FET

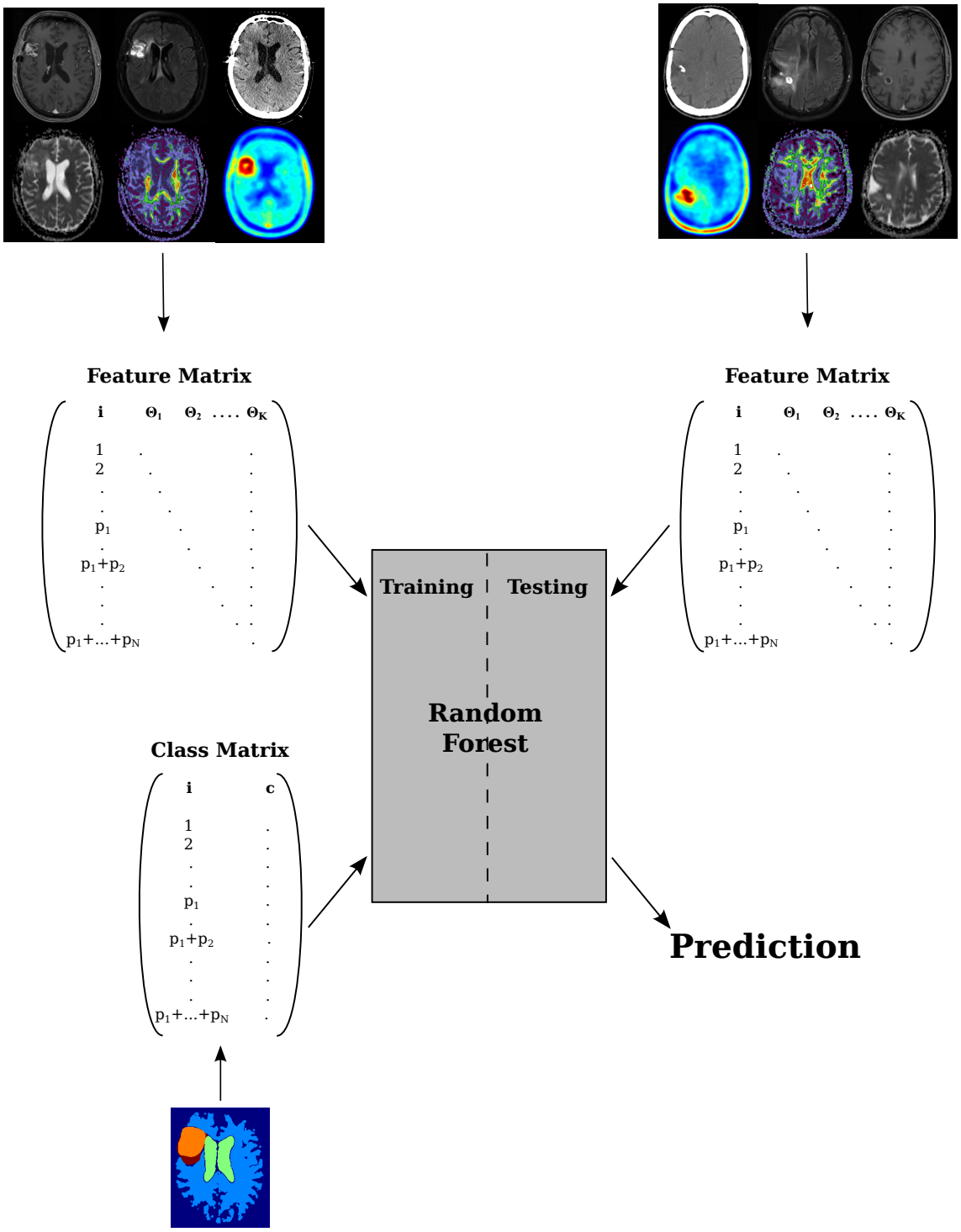

Figure 4.32: Workflow of the random forest implementation. From the multimodal image data set and the class mask, the feature matrix and class mask used for training are extracted and passed to the forest. The forest growth a multitude of decision trees for classification of the samples (image pixels) with the associating classes (defined in class mask). The trained forest can then be used for prediction on a feature matrix from a previously unseen image data set. The prediction result is a class mask as well that can be loaded and displayed in MITK.

for glioma tissue and high *SUV* has been correlated with cell density [Pauleit et al., 2005]. Maps of the apparent diffusion coefficient (ADC) from diffusion weighted MRI and T_2 weighted MRI images using FLAIR were also used as features. The *ADC* has been shown to correlate with cellularity [Ellingson et al., 2012] and the heavy T_2 weighting from FLAIR sequences induces strong contrast for edema. Furthermore, the irradiated dose distribution, derived from Monte Carlo simulations of the carbon ion irradiation plan, was included. Fractionation differences in the patients were only accounted for through the total applied dose.

All image raw data was imported from the CHILI PACS system [CHILI®, HIT Research Data Base] in DICOM format. For each patient, all relevant images were loaded in MITK. Co-registration to the treatment planning CT and interpolation to the same spatial resolution was done using the *Matchpoint* multimodal rigid registration algorithm for head and neck images [Floca, 2009]. Pre-processing of the feature images was performed in order to calculate feature maps. The *SUV* images from endpoint static ^{18}F-FET PET were normalized by division through the SUV_{max} of the lesion, since tracer uptake varies greatly between patients (see section 4.3). Parameter images of *AUC*, *MRT* and C_{max} were derived from DCE MRI data, as shown in section 4.2.2. The dynamic ^{18}F-FET-PET data was converted to 4D *SUV* images and parameters *AUC*, *MRT* and SUV_{max} were derived with non-compartmental analysis from *SUV*-time curves. Pharmacokinetic analysis with compartment models was not suitable, since large amounts of pixels would need to be fitted. Furthermore, the requirements and assumptions of the compartmental models are not met in all tissue structures of the brain, which would lead to wrong estimates and bias the analysis. From diffusion MRI, the native parameter maps of the *ADC* and fractionated anisotropy (FA) were used. The T_2 FLAIR image was z-transformed to account for the qualitative nature of MRI images and inter-patient variability. The dose distribution, representing the dose value in [cGyE] in each pixel, was loaded from RT DICOM files and stored as feature images.

Each image pixel was assigned with one of the class labels listed in table 4.7. Segmentation of patients into anatomical structures was performed for definition of the class masks. The treatment planning *GTV* was used as contour for assignment of pixels to the class *initial tumor volume* c_3. The ventricles were segmented based on the T_1 weighted MRI, using 3D region growing, and assigned to the class *CSF* (c_1). In cases, were the *GTV* included parts of the ventricles, it was subtracted from the *CSF* volume. The *progress tumor volume* c_4 was labeled according to segmentation of $GTV_{Prog.}$, from which the *initial tumor volume* and *CSF* were subtracted. The *CSF* was ranked above the progress, because the goal was determination of progress tissue at risk in the initial state and thus, progress originating from healthy tissue expulsion was not of interest.

Background was segmented by applying the Otsu threshold to the CT image, segmenting it into 4 regions. The inner content of the skull was made subject to a closing operation (erosion followed by dilation), and the result was used for further processing. Using the 3D region growing technique with a lower threshold than before, cerebrospinal fluid including the sulci was segmented. This contour was subtracted from the inner skull content. Afterwards, an opening operation (dilation followed by erosion) was performed for smoothing the contours. From the remaining volume the contours of *initial tumor*, *progress*

Table 4.7: Different class labels used for tissue classification. The "background" class includes pixels outside of the head, bone structures, skin, structures of the spine and jaws, etc. The "CSF" class is defined in order to account for ventricles and resection cavities. "Initial tumor volume" was determined from the treatment planning GTV. "Progress was calculated as $GTV_{Prog.} \setminus GTV$.

Class	Description	Index
c_0	Background	0
c_1	Cerebrospinal fluid (CSF)	1
c_2	Healthy (white and grey) brain matter	2
c_3	Initial tumor volume	3
c_4	Progressive tumor volume	4

and *CSF* were subtracted. The remaining pixels were assigned to the *healthy brain tissue* (c_2) class.

An example of a class mask is shown in the middle panel of figure 4.33. The integer value image is laid over the T_1 weighted contrast enhanced MRI (left panel). The color coding shows *background* (c_0, transparent), *CSF* (c_1, green), *healthy brain matter* (c_3, light blue), *initial tumor volume GTV* (c_4, orange) and *progress tumor volume* from the follow up MRI (c_4, red).

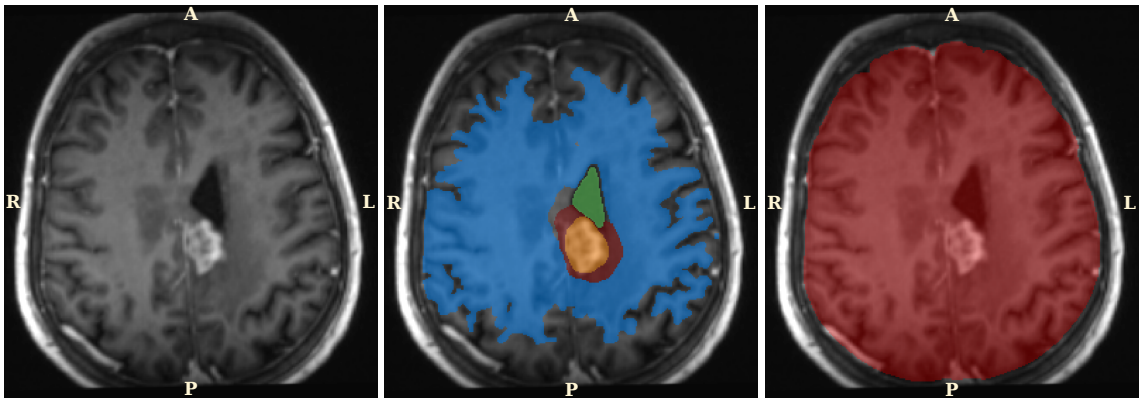

Figure 4.33: Class mask of patient n^o 3 used for training (middle) and testing (right). The corresponding T_1 weighted contrast enhanced MRI is shown on the left. Class labels are background (c_0, dark blue), CSF (c_1, green), healthy brain matter (c_3, light blue), initial tumor volume GTV (c_4, orange) and progress tumor volume from the follow up MRI (c_4, dark red).

4.4.3 Tumor Progression Prediction

To illustrate the developed workflow of classification analysis, an example analysis was performed on a sample set of eight recurrent high grade glioma patients.

For training and prediction, patients were selected, for which a large variety of imaging data was available: patient n^o 1 to 8. Feature images from seven of these patients were

Table 4.8: Different combinations of patients and features used for training of the random forest. Prediction was performed on patient n^o 3.

	Patient n^o	Feature						
		T_2 FLAIR	ADC	FA	DCE MRI (MRT, AUC, C_{max})	SUV	dyn. PET (MRT, AUC, SUV_{peak})	DOSE
#1	1, 2, 4, 5, 6, 7, 8	✓	✓	×	✓	✓	×	×
#2	1, 2, 4, 5, 6, 7, 8	✓	✓	×	✓	✓	×	✓
#3	1, 2, 8	✓	✓	✓	✓	✓	✓	✓
#4	1, 2, 4, 5, 6, 7, 8	✓	✓	×	✓	×	×	✓

used for training in four different combinations. The grown forest was tested for tumor progress prediction in the remaining patient (n^o 3). Prediction in the testing phase was performed on the entire volume within the skull, shown in the right panel of figure 4.33. Training was performed with different combinations of patients and features. Table 4.8 lists the different patients by number that were used for training of the forest. The respective feature images that were used for training and prediction are indicated with a check mark.

The random forest was configured to grow 500 trees (*tree count*) with each a depth of 10 split levels (*tree depth*). The *minimum split node size* was set to 2. Out-of-bag sampling was performed with replacement on two third of the data (*fraction* = $\frac{2}{3}$).

Figure 4.34 illustrates the resulting classification maps (predictions) of patient n^o 3 from all four training combinations in three representative slices. In the top row, the manually defined *class mask* of said patient is shown for comparison of certain structures, i.e. the "true" location of ventricles, initial tumor and progress volume. The rows below show the corresponding slices in the resulting classification images, for the four different prediction combinations (table 4.8). The color coding shows again *background* (c_0, transparent), *CSF* (c_1, green), *healthy brain matter* (c_3, light blue), *initial tumor volume GTV* (c_4, orange) and *progress tumor volume* from the follow up MRI (c_4, red).

All four training combinations yielded roughly accurate classification of brain tissue and ventricle. To some extent, sulci are detected as well. Smaller structures were not assessed, most likely because of the low spatial resolution of most feature images. All training configurations predicted larger initial tumor volumes compared to the actual *GTV* contour from treatment planning.

Combination #1 barely classified any pixels as *progressed tumor*. However, the predicted *initial tumor volume* is comparable to the combined volume of tumor and progress in the class mask. The difference between predictions #1 and #2 was inclusion of the irradiated dose distribution. This led to a reduction of "noisy" pixels throughout the brain, wrongly classified as *initial tumor volume*. Furthermore, consideration of the dose distribution led to an increased predicted *progressed tumor volume* at the edges of the initial tumor volume.

Combination #3 utilized less patients for training and more features, including the parameters from non-compartmental analysis of the dynamic FET-PET curves. The prediction

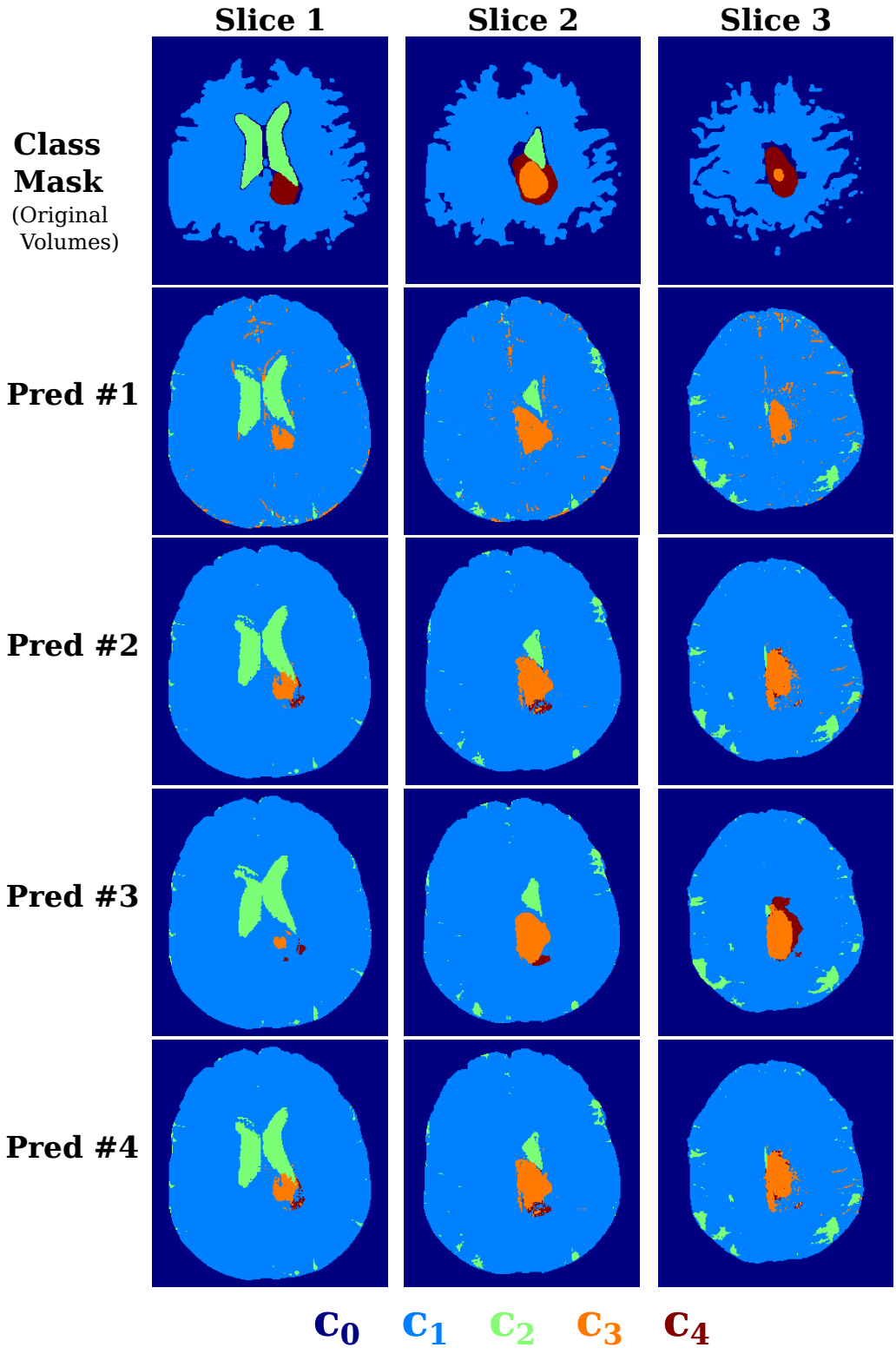

Figure 4.34: Results from predictions on patient n^o 3 with training configurations 1 to 4 in three different images slices compared to the class mask. The color coding shows *background* (c_0, dark blue), *CSF* (c_1, green), *healthy brain matter* (c_3, light blue), *initial tumor volume GTV* (c_4, orange) and *progress tumor volume* from the follow up MRI (c_4, dark red).

yielded sharper contours and less outlier pixels, compared to the other configurations. This is natural, since more patients provide increased heterogeneity of the training collective, making it more difficult for the forest to find precise classification rules. In the top slice (slice 3), prediction #3 estimated the larges progress tumor volume, compared to the other scenarios. This progress volume is close to the volumes defined in the class mask.

Combination #4 was chosen almost identical to combination #2, however, it did not include the normalized SUV as feature. This combination was chosen to investigate whether the SUV has a large impact on the classification result. This seems, however, not to be the case, since prediction #2 an #4 yield almost identical results.

In the following, the two predicted volumes *initial tumor mass* $ITM_{Pred.}$ and *progressed tumor mass* $PTM_{Pred.}$ are studied in detail. The predicted volumes were compared to the original *initial tumor volume* GTV and *progressed tumor volume* $GTV_{Prog.}$ in terms of sensitivity and specificity, similar to section 4.3.2. For sensitivity, the intersection between mask volume and predicted volume was divided by the mask volume

$$Se = \frac{V_{Pred.} \cap V_{Mask}}{V_{Mask}} = \frac{I}{V_{Mask}} \tag{4.13}$$

The specificity was calculated as intersection between mask volume and prediction volume, divided by the prediction volume:

$$Sp = \frac{V_{Pred.} \cap V_{Mask}}{V_{Pred.}} = \frac{I}{V_{Pred.}} \tag{4.14}$$

Figure 4.35 presents results of sensitivity (blue) and specificity (pink) for predicted volumes compared to the original volumes in the class mask. Four combinations of comparison were possible, that are illustrated in respective schematics next to the bar plot:

1. Left top panel: Comparison of $ITM_{Pred.}$ (light blue) compared to GTV (orange)
2. Left bottom panel: Comparison of $ITM_{Pred.}$ (light blue) compared to $GTV_{Prog.}$ (red)
3. Right top panel: Comparison of $PTM_{Pred.}$ (dark blue) compared to GTV (orange)
4. Right bottom panel: Comparison of $PTM_{Pred.}$ (dark blue) compared to $GTV_{Prog.}$ (red)

For prediction configuration #1, nearly no volume was classified as *progressed tumor*, hence the comparisons to GTV and $GTV_{Prog.}$ yielded same values for sensitivity and specificity. The intersection between $ITM_{Pred.}$ and $GTV_{Prog.}$ yielded highest specificity for all predictions: $Sp_{\#1} = 0.88$, $Sp_{\#2} = 0.73$, $Sp_{\#3} = 0.79$, $Sp_{\#4} = 0.73$. The highest sensitivity was found in the comparison between PTM_{Pred} and GTV: $Se_{\#1} = 0.92$, $Se_{\#2} = 0.97$, $Se_{\#3} = 0.98$, $Se_{\#4} = 0.97$. These sensitivity values close to 1 indicate that the predicted progress tumor volume includes the actual initial tumor almost entirely. However, specificity was low in this comparison. This means, that a large additional volume was added by the prediction that did not contain tumor tissue. Overall, comparison between $ITM_{Pred.}$ and $GTV_{Prog.}$ yielded the best relation between good sensitivity and specificity. This result suggests, that the gained information from the modalities used in

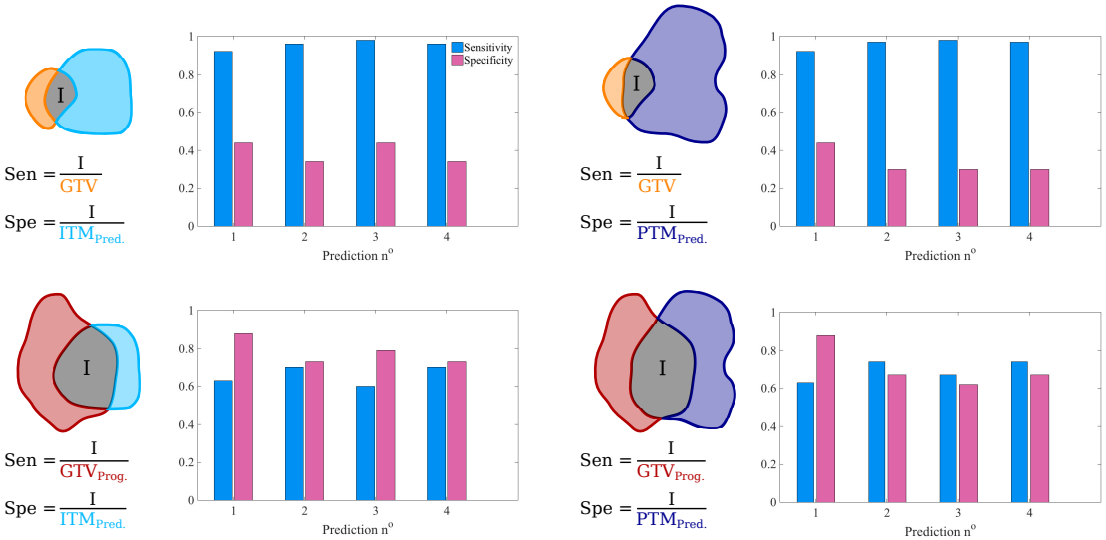

Figure 4.35: Sensitivity (blue) and specificity (pink) for predicted volumes *initial tumor mass* $ITM_{Pred.}$ (light blue) and *progressed tumor mass* $PTM_{Pred.}$ (dark blue) resulting from four different training configurations (prediction n^o), compared to original volumes GTV (orange) and $GTV_{Prog.}$ (red). Schematics of the compare volumes are drawn next to each bar plot, respectively (left side). I denotes the intersection between the two investigated volumes. Respective formulas for calculation of sensitivity and specificity are listed for each case.

forest training provide with an improved target volume, compared to usage of T_1 contrast enhanced MRI alone.

The presented results illustrate different prediction scenarios, based on the available image data. However, for dedicated analysis and more reliable results, training and prediction with only one data sample is insufficient. In theory, a large number of training patients and a large number of testing patients is required. Due to the limited amount of available image data, this was not possible. Nevertheless, validation of the prediction results can be performed to an extend by using the *leave-one-out* method, thus creating several data sets from one available data set. The concept is based on the above used approach of training on data from seven patients and predicting on the remaining patient. The testing patient is permuted through the cohort, thus "creating" eight samples form the initial one. This method provides a compromise between the limited amount of data and a sufficient number of training sets. Tissue classification was predicted on each patient with a forest grown from the remaining patients, using training configuration #2.

In figure 4.36 sensitivity (blue) and specificity (pink) of the predicted tumor volume for all patients are presented, together with schematics of the four volume combinations, in the same manner as before. In the intersection between $PTM_{Pred.}$ and GTV, sensitivity was high ($Se > 0.8$) for most patients. In patient n^o 6, sensitivity was comparably low $Se = 0.28$. Then again, patient n^o 6 presented with maximum specificity $Sp = 1$. Low sensitivity and high specificity could be observed in all volume comparisons of patient n^o 6. The effect resulted from the fact, that GTV was contoured broadly, thus, it enclosed the predicted volumes entirely.

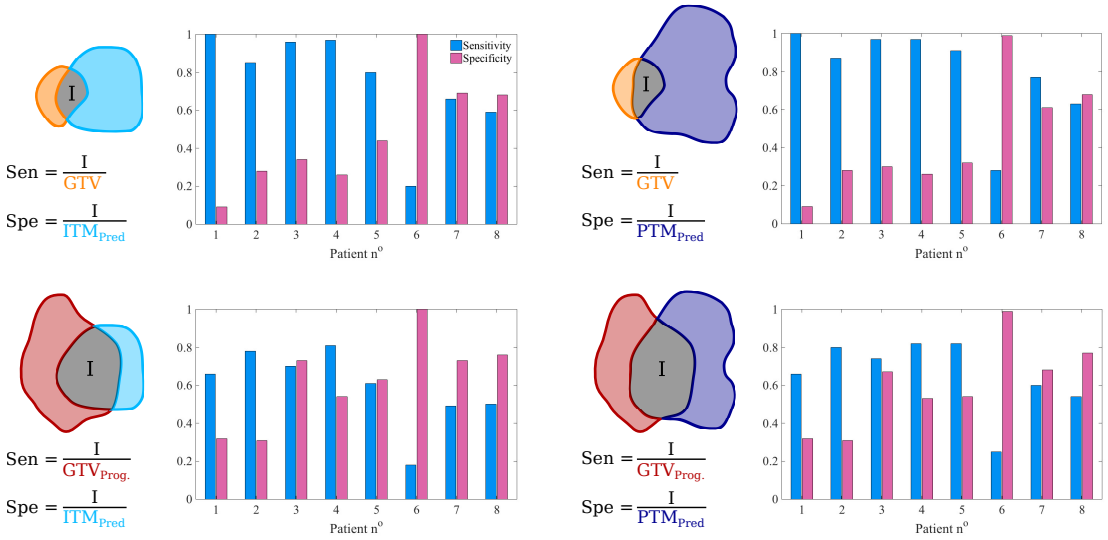

Figure 4.36: Sensitivity (blue) and specificity (pink) for predicted volumes *initial tumor mass* $ITM_{Pred.}$ (light blue) and *progressed tumor mass* $PTM_{Pred.}$ (dark blue) of different patients (patient n^o) , compared to original volumes GTV (orange) and $GTV_{Prog.}$ (red). Schematics of the compare volumes are drawn next to each bar plot, respectively (left side). I denotes the intersection between the two investigated volumes. Respective formulas for calculation of sensitivity and specificity are listed for each case. Training configuration #2 was used for all predictions.

Table 4.9 lists mean values and standard deviations of sensitivity and specificity, averaged over all patients, for the different volume comparisons (intersections).

The averaged sensitivity was highest for the overlap between $PTM_{Pred.}$ and GTV with a value of $Se = 0.8 \pm 0.24$. Thus, the predicted progress tumor volume is able to detect the actual initial tumor almost entirely. However, for this case, specificity had the lowest mean value (0.44 ± 0.29). Specificity was lower in general, with a maximum average value of $Sp = 0.63 \pm 0.23$ for the overlap between $ITM_{Pred.}$ and $GTV_{Prog.}$. In this case, sensitivity features the lowest value of 0.59 ± 0.20. Hence, the prediction would add a large percentage of treated volume that is not tumor. The question, whether the predicted volume is compatible with healthy tissue sparing depends on the actual tumor volume and is thus to be decided for every patient individually.

Table 4.9: Mean values with standard deviations of sensitivity and specificity for comparison between predicted and original tumor volumes. Values are averaged over all patients.

Volume Intersection I	Sensitivity	Specificity
$ITM_{Pred.} \cap GTV$	0.75 ± 0.27	0.47 ± 0.29
$ITM_{Pred.} \cap GTV_{Prog.}$	0.59 ± 0.20	0.63 ± 0.23
$PTM_{Pred.} \cap GTV$	0.80 ± 0.24	0.44 ± 0.29
$PTM_{Pred.} \cap GTV_{Prog.}$	0.65 ± 0.19	0.60 ± 0.23

5 Discussion

The main objective of the presented thesis was development of a workflow for multi-modal, multi-parametric analysis of radiological images from different modalities. The developed approach enables investigation of DCE MRI and dynamic contrast enhanced magnetic resonance imaging (DCE MRI) as well as positron emission tomography (PET) for the surrogate value of extracted parameters with respect to tumor tissue identification. Progressive growth is a common problem in radiotherapy of patients with high grade glioma, leading to poor overall survival. Usage of multimodal information from various physiological imaging techniques for assessment of microscopic outliers and heterogeneity of the tumor could improve target delineation in radiotherapy and thus prevent tumor recurrences.

To achieve this goal, the first step was to provide a common analysis framework for all image modalities of interest. The framework should enable all necessary preprocessing and analysis steps required for concurrent evaluation of different patients and images. Therefore, the medical imaging interaction toolkit (MITK) was employed to address this task. Additional software tools were developed and implemented, providing means for quantitative analysis of PET images and both pharmacokinetic modeling as well as non-compartmental analysis of data from DCE MRI and dynamic PET.

Since parameters derived from DCE MRI and dynamic ^{18}F-FET PET were especially interesting to this work, several analyses on patient data were performed. Technical aspects of quantitative pharmacokinetic modeling in DCE MRI were addressed using synthetic data, in order to evaluate accuracy, precision and robustness of parameter estimates of the analysis routine. The aim of these studies was illustration of the evaluation procedure and feasibility assessment of certain features of interest to multimodal image analysis. Contouring methods for ^{18}F-FET PET images were investigated on 18 patients, gaining more insight on the overlap between tracer uptake regions and macroscopically visible tumor extents, derived from T_1 weighted contrast enhanced MRI. The goal was to estimate the extent to which the metabolic information from ^{18}F-FET PET can predict patterns of tumor progression.

The presented software extensions to MITK enabled development of a workflow for preprocessing of multi-modal patient data sets. The aim was to combine information from different modalities for predictions on tumor progression patterns with the help of classification algorithms. A command line tool for classification of data into healthy and malignant structures was developed based on random forest machine learning. Together with the multimodal patient data set, this tool sets up the environment to train a forest on a subset of data to learn classification rules based on the various image intensities, in order to assign each pixel from a previously unseen testing patient with a tissue morphology describing class. For illustration of the possible classification options, enabled with the presented

work, an example analysis for tumor progress prediction was performed on a sample of eight recurrent high grade glioma patients.

5.1 Software Developments

5.1.1 Dynamic Data Analysis Module

Analysis of dynamic data is part of various image processing approaches and analysis steps. The most prominent example is pharmacokinetic modeling of dynamic measurements from various imaging modalities such as magnetic resonance imaging (MRI) [Tofts and Kermode, 1991; Sourbron and Buckley, 2011], computed tomography (CT) [Kiessling et al., 2004; Brix et al., 2010] and positron emission tomography (PET) [Phelps, 2004; Carson, 2005]. However, there are a number of different applications for generalized fitting of 4D data. Assessment of interstitial fluid pressure and flow velocity was presented by Hompland et al. [2012] by fitting of peritumoral contrast enhanced rims in MRI with exponential models. Stahl et al. [2015] determined temperature induced stimulation of brown adipose tissue by linear fits of fat fraction maps over temperature decreases, derived from time resolved DIXON MRI [Dixon, 1984] measurements. Fitting certain physiological and biological image parameters over several study time points during follow up can be used to assess treatment response in radiotherapy.

All these evaluation routines share a common principle: relevant parameters are estimated by fitting a model representing function to the measured curve in an iterative process, in order to find the set of model parameters that best describes the experimental data. This task is usually performed by non-linear least square (NLLS) optimization techniques. NLLS iteratively fits the data by minimizing the sum of quadratic objective functions $f_i(x)$ with respect to the n model parameters (see section 3.5.3) [NIST/SEMATECH, 2013].

A software module for analysis of 4D image data by means of NLLS fitting was developed in this thesis. Originally, the software module was intended for pharmacokinetic modeling in perfusion MRI.

Parameter estimation in DCE MRI is usually performed by NLLS fitting of a pharmacokinetic model to a measured concentration-time curve [Sourbron and Buckley, 2011]. Numerous tools are available for such analysis, however they present with certain disadvantages.

Commercial software, such as *Dynalab* [*MeVisLAB*, 2016] or *MK-model* [Holford, 1994], is usually of a closed-source form and software code cannot be accessed, which makes error assessment difficult in cases of fit failure or problematic DICOM import. Furthermore, these solutions are often limited in the number of available models and implementation of own developments is difficult. Some authors resort to MatLab®, www.mathworks.com [Kershaw and Buckley, 2006]. The obtained results are, however, challenging to transfer into medical image processing tools. In some cases, commercial software programs for DICOM workstations and radiological image processing offer tools to analyze data (e.g. Siemens Tissue4D™), however mostly standard protocols are supported without room for research developments. In addition, these software solutions are commonly “black-boxes”

with hidden configuration aspects and rigid algorithmic routines. Hence few aspects of the fitting process can be changed and studied. The IDL software tool MINPACK MPFIT [Moré, 1978; Markwardt, 2009] is an open-source solution used by many authors [Ingrisch and Sourbron, 2013; Luypaert et al., 2012]. Few open-source solutions for analysis of DCE MRI data exist, that are integrated into DICOM workstations [Zöllner et al., 2016; Haider et al., 2015; Sung, 2015]. However, these tools are often designed to serve a single analysis purpose.

Most authors resort to in-house developed software tools, e.g. the VIRTUOS BioImage module [Neff, 2005; Sourbron et al., 2009]. This approach presents the disadvantage of complicated comparison between results. Most in-house solutions require conversion and transfer of the data from DICOM workstations [Sourbron, 2010]. Furthermore the software tools are often designed for only a specific analysis purpose and hence integration of other image processing steps, e.g. segmentation or registration, and comparison of modalities are difficult [Sourbron, 2010].

To overcome these limitations and allow for integration of dynamic data from MRI and PET into the multimodal image analysis approach, the dynamic data analysis module was developed for MITK. The goal was to design and implement an independent, flexible and reusable software module that can be used for dynamic data modeling of DCE MRI as well as dynamic PET data. Furthermore, it should offer a high degree of freedom for definition of fitting configurations. The module was designed with characteristics of a software toolkit as well as a framework. The toolkit nature allows for integration of existing functionalities and models into other software tools, for example intravoxel incoherent motion imaging (IVIM) [Koh et al., 2011]. The framework structure provides an established fitting infrastructure, which can be appended with own implementations of models, optimizers and cost functions.

Raw data and fit results can be assessed visually with the modelfit view, which offers pixel-wise evaluation of analysis results. The arterial input function (AIF) and fitted curves from different models can be compared directly to the measured data. Quantitative evaluation of fit results is possible via parameter maps (images) and the optimization measure $\mathcal{X}^2$.

An extension for calculation of semi-quantitative curve describing parameters enables non-compartmental analysis for data of less quality. In analogy to the model function for fitting, further parameters in terms of the calculation function can be easily implemented by the developer without having to deal with the underlying framework. Calculation of these parameters is very fast on a voxel wise basis for entire images. This approach can be used for landscaping of tissue structures, which are then fitted with the region-based approach to improve fit stability for detailed assessment of physiological parameters [Gibaldi and Perrier, 1982; O'Connor et al., 2008].

One major advantage of the presented MITK dynamic data modeling software is its high modularity, making it superior to other software solutions. This feature provides decoupling of the fitting routine from input images. Thus, the individual components are modality independent and can be used for development of software tools with different study and analysis purposes. Decoupling of the model function from the rest of the optimization routine allows for simple implementation of other models by the user without concern for

the rest of the module. Additionally, the stand-alone functionality of the fitting routine enables concrete studies of different aspects of optimization, such as optimization algorithm, optimizer configuration and similarity measure.

For the presented applications of the dynamic data analysis module in DCE MRI and dynamic PET, the Levenberg-Marquardt optimizer [www.itk.org] was used. This optimizer is widely utilized and presents with good stability and fast convergence due to the multivalued cost function [Ahearn et al., 2005].

The developed software module allows for a number of studies on technical aspects of the model fitting routine. Investigating the influence of different optimizers, such as Powell optimization or particle swarm optimization, on the outcome of pharmacokinetic modeling can be used for error assessment in both DCE MRI and dynamic PET. Furthermore, different approaches for cost functions can be investigated. A native selection for the cost function is the sum of squared residuals instead of the multivalued squared residual cost function.

Since MITK can be used as a toolkit, application of the dynamic data analysis module does not depend on usage of a graphical user interface. Hence, the software module can be incorporated into scripting environments and command line tools, giving the opportunity of (semi-)automatic analysis of large patient data sets.

Two dedicated applications for pharmacokinetic analysis of DCE MRI and dynamic PET data were developed from the module. A plugin with dedicated workflow and graphical user interface for pharmacokinetic modeling of DCE MRI data was implemented. Model functions of the two compartment exchange model [Brix et al., 2004] and the extended Tofts model [Tofts and Kermode, 1991] are available. Application of the plugin was shown in the studies on simulated perfusion data. Compared to other tools for DCE MRI data analysis, the plugin offers enhanced flexibility for definition of the fit configuration in terms of initial parameter values, model parameter constraints and conversion from signal intensities to concentration units. The modelfit view offers visual assessment of the goodness of fit not only for regional averaged curves, but on a single-pixel basis. Because of the modular structure of the underlying dynamic data analysis module, the plugin can be easily expanded by the user with own model implementations as well as different optimizers and cost functions. Linkage of the module to MITK offers a large collection of image preprocessing options that is not available in most other DCE MRI analysis software solutions. For example, inter- and intra-serial registration can be performed with the Matchpoint registration framework [Floca, 2009]. As shown in the study on non-compartmental parameters from DCE MRI data, combination of the plugin with RT DICOM import allows for study of hemodynamic parameters within treatment volumes from radiotherapy. MITK offers a large variety of segmentation tools. Arterial input function (AIF) and region segmentation for pharmacokinetic analysis can be facilitated by using images from other modalities or sequences.

An extension to the module in form of a simulation tool for creation of synthetic DCE MRI data was developed and used to study different aspects of parameter estimation in pharmacokinetic modeling. Data simulation is a popular tool in pharmacokinetic analysis of perfusion MRI for studies on model feasibility and comparison between models [Sourbron et al., 2009; Brix et al., 2009; Luypaert et al., 2012; Ingrisch, 2012]. Often, authors resort

to the Java-based simulation system JSIM [www.physiome.org/jsim]. The simulation tool presented in this thesis allows for simulation beyond single concentration-time curves, on whole 4D data sets. In addition, the approach is image-based, which facilitates assessment of parameter estimates resulting from fits of the synthetic data and enables data transfer.

For analysis of dynamic PET, similar challenges arise with the existing software solution as for DCE MRI The available software solution PMOD [PMOD®] is used by several authors [Dimitrakopoulou-Strauss et al., 2001; Mikolajczyk et al., 1998]. However this tool is a commercial solution and expansion or changes in the configuration and available models were not possible. Thus, the dynamic data analysis module was used to design a dynamic PET analysis plugin. The plugin offers the same functionalities as the DCE MRI analysis plugin. Its application was shown in the study on model feasibility for dynamic ^{18}F-FET PET data, discussed in section 5.3.1.

Both tools are used by several groups within the DKFZ[1] for evaluation of both DCE MRI and dynamic PET data.

For broadened analysis of DCE MRI data in various organs, implementation of further pharmacokinetic models is necessary. The concentration of MRI contrast agents in plasma cannot only be described by a compartment but also by the *plug-flow* approach [Larson et al., 1987], which models the capillary as a tube system and accounts for concentration gradients along these tubes. With this approach, the *tissue homogeneity model* [Johnson and Wilson, 1966] and the *distributed parameter model* [Sangren and Sheppard, 1953] derive as two region models. Approximations of these models, such as tissue uptake models, are used for various organ studies and in analysis of *arterial spin labeling* perfusion MRI. Dynamic susceptibility contrast (DSC) MRI offers assessment of perfusion parameters such as the cerebral blood flow, cerebral blood volume and mean transit time [Rosen et al., 1991]. DSC uses deconvolution for finding the residue function from indicator dilution theory [Rempp et al., 1994]. Evaluation of DSC data, has not been explored in this thesis so far. However, analysis of concentration curves from DSC MRI could as well be addressed with the presented software module.

Simulation studies can be pursued further, concerning error estimation in different parameter regimes or influence of optimizer configuration.

The simulation framework could be extended for PET data. This would also allow for combination with Monte Carlo simulations of PET acquisition, and hence, modeling the data quality for dynamic PET scans.

5.1.2 PET Software Developments

PET data is usually analyzed directly at clinical workstations belonging to the scanner, e.g. the Siemens® syngo system, or commercial software (e.g. ROVER [ABX advanced biochemical compounds]). This approach leads to the disadvantage that analysis can only be performed with tools provided by the manufacturer. Furthermore, it is often desired to compare and overlay PET data with various other modalities, especially in the context of radiotherapy, which cannot be done intuitively at scanner workstations. Open-source

[1] Deutsches Krebsforschungszentrum

solutions, for example RT_IMAGE [Graves et al., 2007], can overcome these drawbacks. On the other hand, they are often limited in the analysis of other modalities, like MRI.

In order to evaluate PET data together with other investigated modalities, software tools were implemented in MITK. The MITK plugin for calculation of the standardized uptake value (SUV) provides a simple but helpful tool for analysis of endpoint static images from PET. The tool does not only provide mean and maximum SUV within a contour but rather in every pixel of the entire image. This allows for display adjustments and single value evaluation of SUV, as well as segmentations based on SUV values (e.g. thresholding). Mean and maximum SUV of a lesion can be easily computed with the statistics plugin. SUV calculations were validated on six patients by comparing SUV_{max} values determined with the plugin to values mentioned in the medical reports.

Though isocontours are a simple thresholding technique, they constitute a well-established part of PET analysis workflows [Paulino et al., 2005; Zaidi and El Naqa, 2010]. The developed isocontour plugin allows definition of various percentiles, and thus, the user can try different thresholds to find the most suitable for the analysis. A drawback of the tool is its limitation of segmentations to the predefined contour boundaries. Even though the 3D interpolation technique of MITK allows for fast definition of the contour, care must still be taken with regards to other tracer-enhancing, non-pathological structures. The tool could be improved by allowing extension of the isocontour over the predefined contour within a connected region, similar to region growing.

5.2 DCE MRI

After over 20 years of research, DCE MRI has turned out to be a popular method for characterization of tissue physiology in various diseases. Measurement of tissue perfusion allows assessment of blood-brain barrier leakage or break-down, an often considered aspect for diagnosis and staging of brain cancer [Sourbron et al., 2009; Larsson et al., 2009; Møller et al., 2015]. Recent studies have shown the applicability of perfusion MRI as diagnostic tool in other neuronal diseases, including stroke [Kassner et al., 2005] and multiple sclerosis [Ingrisch et al., 2012]. Furthermore, quantification of tumor angiogenesis through measurement of micro-vascularization is used in numerous studies for malignancy characterization and monitoring of treatment response in various tumor entities, including brain, breast and prostate [Møller et al., 2015; Brix et al., 2004; Buckley et al., 2004]. Perfusion quantification is based on dynamic measurements of administration of a contrast agent (CA) bolus and the subsequent temporal changes in image signal, which are dependent on local capillary blood supply and extravasation of the contrast agent into the surrounding tissue. DCE MRI data were investigated for the purpose of this thesis, because hemodynamic parameters describing tissue perfusion and permeability could provide detailed physiological insight into tumor heterogeneity.

5.2.1 Studies on Measured DCE MRI Data

AIF determination is a big challenge in DCE MRI, even if the data is acquired at appropriate temporal resolution Sourbron [2014, 2010]. Various organs present with different challenges

in estimation of the arterial concentration. In the brain, arteries directly feeding the tissue of interest can rarely be assessed. Measurements of arterial concentration in large, easily accessible vessels require correction for dispersion and delay of the bolus in pharmacokinetic models. If the arterial concentration is measured in the carotid arteries, inflow effects are likely to distort the true contrast agent (CA) concentration, as they present with signal enhancement even in the absence of CA [Kim et al., 2002]. In small vessels, on the other hand, partial volume effects complicate correct estimation of the arterial concentration. All these aspects have to be considered when choosing a strategy for AIF measurement specifically tailored for the investigation at hand. One approach to overcome the obstacles of AIF measurements is fitting a sum of gamma-variate functions to the measured arterial concentration, and use the fitted curve as AIF [Sourbron et al., 2009]. Another approach is averaging the AIF of several patients [Weinmann et al., 1983]. The resulting curve, together with scaling factors for individual patient corrections, can be used as standardized AIF on the entire patient set [Degani et al., 1997; Simpson et al., 1999]. To allow for this option, the fitting tool offers loading of an AIF from an external, comma-separated value (CSV) file. The study on AIF assessment revealed insufficient quality of the available DCE MRI data due to temporal under-sampling. The arterial concentration resulting from the bolus injection cannot be determined adequately from the images, especially in the peak area. Thus, the data is not suitable for quantitative pharmacokinetic analysis.

If data quality from perfusion MRI is insufficient for proper pharmacokinetic modeling to be performed, one can resort to non-compartmental analysis by calculation of semi-quantitative, curve describing parameters. These parameters can be used to assess basic features of tissue physiology and hemodynamics [O'Connor et al., 2014, 2012, 2008]. In the presented thesis, non-compartmental analysis was enabled through extension of the dynamic data analysis module. Analysis of parameters from non-compartmental analysis of DCE MRI data from recurrent high grade glioma patients was performed in three patients. The goal was to illustrate the workflow and applicability of such an analysis with the developed tools. Data sets of several time points during the course of radiotherapy were investigated. Semi-quantitative parameters exhibit differences between different treatment volumes. There was a distinct difference in parameters between gross tumor volume (GTV) and the volumes added by clinical target volume (CTV) and planning target volume (PTV). No consistent tendency of functional dependence of the parameters over the time course of radiotherapy was observed.

Parameters from compartmental analysis were also compared in the progressive tumor volume and healthy tissue for one patient. These preliminary results showed, that a closer look and more detailed studies of the parameters from non-compartmental analysis with larger patient numbers could be interesting for the pursued multi-modal image analysis approach for tumor tissue identification. Parameters from non-compartmental analysis could be helpful surrogates for tissue classification. This is the basis further studies with more patients to widen the scope of the technology which was developed in this thesis.

5.2.2 Studies on Simulated DCE MRI Data

Various models for pharmacokinetic analysis of DCE MRI data have been proposed. Feasibility and comparison between different models have been studied by several authors [Sourbron et al., 2009; Brix et al., 2009], especially under consideration of the Akaike information criterion [Luypaert et al., 2012; Ingrisch, 2012]. Parameters from perfusion MRI data are usually estimated by non-linear least square fitting (NLLS) of the pharmacokinetic model to the measured time courses of the CA concentration derived from image signals [Sourbron et al., 2009; Brix et al., 2010].

NLLS-fitting by minimizing the sum of quadratic objective functions with respect to model parameters (see section 3.5.3) poses an unconstraint optimization problem that can be solved by a number of different optimization routines. One major challenge in NLLS the fact, that the determined minimum of the objective function does not necessarily represent the global minimum [NIST/SEMATECH, 2013]. Thus, parameter estimates yield ambiguous results that can differ from the true values. Ability of the optimization algorithm to find the true minimum depends on a number of requirements imposed on both data quality and technical configuration of the fitting routine. The importance of correct data acquisition for input of pharmacokinetic analysis has been shown in a study on the effects of temporal sampling and noise level of the acquired image data [Luypaert et al., 2010]. Apart from this, little attention was given to technical aspects of the fitting routine and their influence on the parameter estimates.

Two studies on accuracy and robustness of parameter estimates from pharmacokinetic modeling with the two compartment exchange model were performed, based on simulated concentration time curves. The closed-form analytical convolution and differential equations for definition of the model function yielded similar results in terms of accuracy and precision. Fitting with the closed form solution is superior in computational time. Both approaches are limited in accuracy for situations with low blood flow. The model parameter or the fractional interstitial volume shows great instability and little reliability in all cases. However, results are representative only to an extent, since one type of arterial input function and one noise level were used. Furthermore, stability assessment was performed with the small number of different curve types. A statistical analysis was not conducted, because the examined samples, i.e. the simulated concentration time curves, are not statistically independent. The individual curves were functionally identical for the given parameter set and differed only in noise. Hence, statistical evaluation of the results would be unreasonable.

Nevertheless, the presented results revealed that different parameter combinations yielded different levels of accuracy and robustness of the fit.

It has been hypothesized that the choice of initial parameter values influences the optimization routine, and thus, the parameter estimates [Brix et al., 2009]. In the presence of several local minima for the similarity measure, initial position will determine the direction of optimization. Under these circumstances, it is possible for the optimizer to find a local minimum, close to the initial values, rather than the correct global minimum for the parameter estimate. This problem is also known in the area of dynamic PET, where various strategies are used to find the optimal set of initial values [Boxenbaum et al., 1974; Yaqub

et al., 2006]. In DCE MRI, necessity for the appropriate choice of starting parameters has been mentioned, but it has never been studied in depth to the best of the author's knowledge.

The influence of starting values for model parameters on the outcome of the fitting process was investigated using simulated concentration-time curves. Results showed that accuracy and precision of parameter estimates are influenced by the initial values less than expected. Estimates on F_p and PS are sensitive to their own start values at low values. Apart from that, no clear relation between start value and error on the parameter estimate was found. However, only the effects of varying one start parameter were investigated. For further clarification, the next step would include variation of start values of two parameters simultaneously. Again, it should be considered that only one type of AIF was used.

For detailed quantification of fitting accuracy and possible inter-parameter dependencies, further studies have to be performed. Using the image based approach within the simulation framework, a large number of parameter combinations can be simulated and results can be visually assessed. From the resulting large variety of parameter estimates, regions of increased or decreased stability and accuracy can be deduced. These regions can be studied again as representative parameter sets on a large number of curves, in order to find a model for the error on parameter estimates, which could be integrated into the fitting routine.

5.3 ^{18}F-FET PET

Amino acid PET is a promising modality for detection and characterization of brain tumors, because it offers high sensitivity and specificity for glioma tissue. Uptake of the ^{18}F-FET tracer has been correlated with cell density [Pauleit et al., 2005; Stockhammer et al., 2008]. Various authors have investigated correlation ^{18}F-FET positive volumes with tumor progression [Weber et al., 2009] and progression-free and overall survival [Piroth et al., 2011]. Applicability of ^{18}F-FET PET for radiotherapy planning and its capability to improved target delineation have been shown in several studies [Grosu and Weber, 2010; Weber et al., 2008]. Thus, inclusion of data from ^{18}F-FET PET was desired for the presented multi-modal multi-parametric analysis approach.

5.3.1 Studies on Dynamic ^{18}F-FET PET

To the best of the author's knowledge, pharmacokinetic modeling on dynamic ^{18}F-FET PET data has been performed so far by a single group [Thiele et al., 2009]. Thus, the question which model suites best the tracer kinetics is still unanswered. In principle, the kinetics of ^{18}F-FET can be modeled with the two tissue compartment model (2TCM) due to the bidirectional transport of ^{18}F-FET through system L. The compartments represent ^{18}F-FET in blood or plasma ($c_a(t)$), in EES and in the cells. However, if data quality is not sufficient, the five parameters in the 2TCM can lead to overfitting. In this case parameter estimates are inconclusive. The one tissue compartment model (1TCM) on the other hand is widely used in dynamic PET, as it is a simple representation of the tracer transport between blood and tissue. Most studies either focus on the analysis of single frames [Weckesser et al., 2005] or resort to qualitative description of time-activity curve

types [Jansen et al., 2014; Thon et al., 2015]. The approach of Pöpperl et al. [2006] using weighted frames provides an alternative analysis strategy.

The implementation of a GUI-based analysis workflow for pharmacokinetic modeling of dynamic PET data allowed investigation of the feasibility of describing the time activity curves from dynamic FET-PET scans with two widely used tracer kinetic models, the one tissue and two tissue compartment model.

Since dynamic acquisition of ^{18}F-FET PET scans, described in section 3.3.3, might reveal further details of tumor physiology, analysis of this data was of high interest. The developed dynamic data analysis module allowed implementation of a tool for voxel wise pharmacokinetic fitting of TACs from dynamic ^{18}F-FET PET and assessment of parameter estimates as well as fitting quality.

Available data from recurrent high grade glioma patients provided dynamic ^{18}F-FET PET scans for twelve patients. The data acquisition mode of non-equidistant time sampling steps provided high temporal sampling in beginning of measurement, in order to catch the bolus arrival in the arteries. At later measurement time points, coarser sampling is sufficient to assess curve tendencies. These conditions allowed for appropriate estimation of arterial concentration in the carotid arteries. In five patients, the afore described study on the endpoint static image showed that tracer uptake is too low for reasonable application of the isocontour 50%. For the remaining seven patients, voxel-wise fits of the model functions of the 1TCM and the 2TCM were performed within the volume of the isocontour 50%, in order to study applicability and robustness of both models for the available ^{18}F-FET PET dynamic data.

The resulting parameter maps for fitting estimates of K_1 (1TC), k_2 (1TC), K_1 (2TC), k_2 (2TC), k_3 (2TC), k_4 (2TC) and V_B (2TC) were averaged within the isocontour 50%. Large errors in terms of standard deviations, especially in parameter estimates with the 2TCM, indicated decreased robustness of this model. Closer investigations of the parameter maps and fit curves revealed, that increased number of degrees of freedom in the 2TCM (five free fitting parameters) support overfitting of the curve. In general, two out of the five parameters seemed to be unnecessary for description of the curve and hence, were estimated with illegitimate values. Nevertheless, the enhanced degree of freedom of the 2TCM yields smaller $\mathcal{X}^2$ values. Additional fitting parameters allow a better adaption of the model curve to the measured data points. However, a large number of outliers in parameter estimates and $\mathcal{X}^2$ in an unreasonably large value regime revealed decreased robustness of the fits and hint at insufficient data quality of the measurements to assess the complex physiological interplay described by the 2TCM. For stable parameter estimates, the 1TCM provides a good approach. These results are in concordance with findings of Thiele et al. [2009].

Like in DCE MRI, deriving semi-quantitative curve parameters from non-compartmental analysis provides an alternative evaluation method to pharmacokinetic modeling [DiStefano, 1982; Gibaldi and Perrier, 1982; Riviere, 2011]. For this thesis, non-compartmental analysis was performed in these seven patients. The semi-quantitative parameters AUC (area under the curve) and SUV_{peak} exhibited differences between initial tumor volume, progressive tumor volume and healthy tissue. The MRT (mean residence time) showed stable values with little variations between patients. However in five of the seven patients, the MRT

was slightly higher in the tumor progress volume compared to the *GTV* and healthy brain tissue. The evaluated parameters could be helpful markers in tissue classification.

5.3.2 Studies on Endpoint Static ^{18}F-FET PET

The *SUV* calculation and the isocontour segmentation plugin implementations made quantitative studies of PET data with MITK possible. This option is particularly interesting for combination with other modalities (MRI) and information from radiotherapy treatment planning, e.g. structure sets and dose distributions. Both tools were used for a study of endpoint static ^{18}F-FET PET data from recurrent high grade glioma patients.

The prognostic value of ^{18}F-FET PET, and the effects of its inclusion into the radiotherapy treatment planning procedure, have been investigated by various authors [Grosu et al., 2005]. There is no gold standard for delineation of lesions in PET images in general [Lee, 2010]. The level the tracer uptake, which has to be considered pathological and hence included into segmentation, is unclear and presumably varies between tracers. The *SUV* somewhat normalizes the measured activity to the patient, however, the assumption of $SUV \approx 1$ for normal tissue is based on assuming free diffusion of the tracer and a tissue density of water throughout the whole patient body. These assumptions are valid only to an extent, and thus thresholding the *SUV* for values larger than 1 does not yield satisfying results, even under consideration of the noise level [Keyes Jr et al., 1995]. Isocontours are widely used in clinical routine. Nonetheless, there is no standard threshold and different centers use different values.

Selection of an appropriate segmentation algorithm is crucial for interpretation and quantitative evaluation of ^{18}F-FET tracer uptake in brain lesions [Zaidi and El Naqa, 2010]. Vees et al. [2009] compared different contouring methods on ^{18}F-FET-PET images of high-grade glioma patients to the standard delineation based on contrast-enhanced T_1 weighted MRI. Investigated segmentation techniques included manual delineation, a fixed cutoff of $SUV > 2.5$, isocontours of 40% and 50%, a signal-to-background ratio (SBR) based adaptive threshold, a gradient finder based on the Marr-Hilldreth operator and 3D region growing. Results showed, that PET-based contours were usually smaller than the MRI-based segmentation, however ^{18}F-FET-PET was able to detect lesions not visible in MRI. In 33% of the cases, PET-based contours included substantial volumes outside of the MRI based *GTV*. The fixed cutoff $SUV > 2.5$ and the gradient finder yielded poor results. The SBR thresholding yielded best performance and most reliable results.

In the presented work, segmentation volumes resulting from different contouring techniques were compared to treatment planning gross tumor volume and tumor progress volume. For delineation of the PET active lesions in 18 recurrent high grade glioma patients, isocontours of 40%, 50%, 60% and 70%, and two semi-automated segmentation algorithms, 3D region growing (RG) and the multi-labeled random walker (RW), were used. The maximum *SUV* in all 18 lesions varied between 1.08 and 4.57, which is low compared to uptake of tracers like 18F-FDG.

It could be observed that applicability of certain contours depends on the level of tracer uptake. In order to use isocontours of low percentiles (i.e. 40% and 50%) with reasonable

outcome, the tracer uptake gradient between lesion and background has to exceed certain thresholds. Application criteria could be formulated in terms of thresholds on the ratio between maximum and reference SUV values (tumor-specific uptake ratio).

Conformity between MRI-based contours of GTV and PET-active regions were only valid to an extent, with a maximum conformity index of $C_{GTV} \approx 0.6$. With decreasing maximum uptake, smaller contours (larger isocontour thresholds, region growing and random walker) yielded better conformity. In some cases substantial mismatches between PET and MRI contours could be observed.

Conformity of the PET-based contours with the $GTV_{Prog.}$ was generally lower than with the treatment planning GTV. Overall, larger contours (isocontour 40%) yielded better conformity with the $GTV_{Prog.}$. Detailed study revealed that the isocontour 50% provides best trade-off between sensitivity and specificity of all PET-based contours, with respect to tumor progress volume. In summary, no contouring technique showed clear superiority.

With regards to the presented results, it is questionable, wither definition of a fixed contouring method for delineation of lesions in ^{18}F-FET PET images is meaningful. The large heterogeneity of tracer uptake between patients suggests that the contouring method should be chosen individually adjusted to the patient, depending on the amount of tracer uptake. This hypothesis is supported by the relation between SUV_{max} and best conformity yielding contour, illustrated in figure 4.23. At the first glance, a roughly linear relation could be assumed. Logistic regression could provide a more realistic estimate on the relation between SUV_{max} and suitable contouring technique, as it accounts for saturation of the conformity index in low and high value regimes.

In this study, the irradiated dose and its 3D distribution were not considered, even though it obviously influences the formation of progressive tumor volume and thus the overlap between PET-based contours and progressive tumor GTV_{FU}. At first glance, no relation between dose and conformity, sensitivity of specificity could be observed. A more detailed study of the effects of the applied dose is however easily applicable with the presented software environment.

5.4 Multi-Modal Image Analysis using Random Forest Machine Learning

The previously presented software tools allowed for multi-modal, multi-parametric image analysis and development of a framework for prediction of tumor growth patterns. Most approaches for simulating tumor growth are based on generative modeling. This approach can be difficult in systems with complex underlying fundamental principles, since explicit mathematical formulations for all system influencing parameters have to be defined. Swanson et al. [2000] presented a method for modeling tumor expansion velocity in grey and white brain matter using diffusion-reaction-equations. Several authors have applied diffusion tensor imaging for modeling diffusion processes in tissue [Jbabdi et al., 2005; Swanson et al., 2003; Konukoglu et al., 2010].

This thesis was based on the approach of Weber et al. [2015], who presented a discriminative modeling approach using random forest machine learning. However, the presented work

used a novel approach of including metabolic and hemodynamic surrogate parameters, derived from amino acid PET and DCE MRI, in combination with information from radiotherapy treatment planning for prediction of tumor tissue volumes.

The random forest algorithm was chosen to perform classification of data because of its capacity for multi-class pattern recognition and efficiency on large data sets, without the danger of overfitting. With the ability to handle a large number of both input variables and features, random forests are suitable for the task at hand, where hundreds of thousands of pixels from each patient need to be classified. A command line tool was developed for easy setup of forest training and prediction. In principle, it is possible to start forest training and prediction directly within MITK with loaded feature images. However, if a large amount of data (many different patients and/or features) should be investigated this procedure is inefficient.

Applicability of the established analysis workflow was shown on retrospective data of eight patients with recurrent high grade glioma, for which sufficient multi-modal image data was available. Besides hemodynamic parameters, derived from DCE MRI, and metabolic quantities estimated from both endpoint static and dynamic ^{18}F-FET PET, parameters from diffusion weighted and T_2 FLAIR MRI sequences were included for forest training. Furthermore, the irradiated dose was considered in the analysis, as it influences the formation of progress patterns significantly. All image preprocessing steps were done with MITK. Performance of the classification workflow was tested with four different training configurations and subsequent prediction of tumor growth patterns with the resulting forests in one patient.

In general, the presented predictions could identify the tumor volume rather well without usage of standard modalities like T_1 weighted contrast enhanced MRI. The classification results based on physiological modalities suggested larger GTV volumes. Inclusion of the predicted initial and progressive tumor volumes would yield a larger treatment planning contour, which might include micro-invasions of surrounding healthy tissue. Using the calculated dose distribution from radiotherapy planning smoothened and improved the classification result.

In order to increase the number of testing and training samples, the *leave-one-out* method was used for tissue classification of all eight patients. Training was performed on seven patients with the feature images T_2 FLAIR MRI, ADC maps from diffusion MRI, normalized SUV values from endpoint static ^{18}F-FET PET, semi-quantitative parameters AUC, MRT and C_{max} (SUV_{max}) from dynamic MRI and PET measurements, and the calculated dose distribution. The patient used for testing was permuted through all eight patients. Results were evaluated in terms of sensitivity and specificity of the predicted volumes for "initial tumor" and "progressed tumor" with respect to the "ground truth" defined in the class mask. Sensitivity was high in most patients. The maximum sensitivity of 0.80 ± 0.24 was found in the predicted progressed tumor mass with respect to the mask defined GTV. Specificity was lower. The highest specificity was found in the comparison between predicted progressed tumor mass compared to the mask defined $GTV_{Prog.}$ with an average value of 0.60 ± 0.23.

Prediction results were not optimal with 100% sensitivity and specificity. However, sensitivity and specificity were larger compared to results of the study on ^{18}F-FET PET

alone. Especially the predicted "progressed tumor" volume yielded good results except in one patient. The presented study provides a novel approach for tissue classification. Results show, that tumor tissue can be predicted using only functional and metabolic imaging modalities. Furthermore, the prediction analysis detected initial tumor volumes, larger than those visible in the T_1 weighted contrast enhanced MRI and CT images. Other investigation could assess absolute predicted volumes with respect to additional doses applied to non-tumorous tissues. This trade-off between volumes receiving unnecessarily high doses and good tumor coverage is essential for therapy planning in radiation oncology.

The random forest classification tool that was developed in this work performed in terms of computational time and efficiency, as well as easy configuration of training and testing conditions. Parallel computing made the algorithm reasonably fast and efficient in terms of computational storage. No difficulties were encountered with larger training sets (6 patients, 10 features, roughly 10^5 pixel per patient). In principle, resolution of the prediction is determined by image with highest spatial resolution. At this resolution two image positions (pixels) are possibly different in their attributes and hence can be distinguished from one another in classification. However, dominant features with lower spatial resolution will distort this and hence, influence the prediction resolution.

Manual data preprocessing is inevitable but time consuming. One of most time consuming steps presents export of raw data from the CHILI PACS[2] [CHILI®, HIT Research Data Base]. Coupling of the analysis routine to the PACS could facilitate this step and thus, speed up data preparation. Some steps of the preprocessing workflow could partly be done automatically, e.g. image registration and most calculations of feature maps. This approach is, however, hindered by the large heterogeneity of the available data. Not every modality is available for every patient. Inclusion of data acquired at external centers implies differing sequence and acquisition parameters for same feature images. Some procedures have to be performed manually nonetheless, in particular creation of class masks for forest training.

Prediction results of a forest depend greatly on finding the right cohort (sample) for training. In the presented work, patients with recurrent high grade glioma were chosen. These patients did not undergo surgery and thus, direct mapping of imaging pixels before and after therapy is possible. Furthermore, the patients received irradiation from a single plan, i.e. no boost was applied, and radiation was delivered from a single beam direction. This made direct study of images before and after radiotherapy possible without distortion factors from different treatment courses between patients. For analysis of data from primary tumors, an adequate classification protocol has to be found.

Another issue is quantification and interpretation of prediction results for evaluation. The used class mask does not necessarily provide the ground truth, describing the true tumor extent.

Patients investigated were diagnosed with both glioblastoma and anaplastic astrocytoma. It has yet to be investigated, whether these entities should be separated in the classification process. Furthermore, the question of the sample size has to be discussed. It was shown, that the number of patients used for training influences the prediction outcome. On the one hand, more patients lead to statistically more relevant and trustworthy results, due to

[2] picture archiving and communication system

an increased number of samples. On the other hand, a larger variety of patients introduces an increased degree of heterogeneity, which makes it more difficult for the forest to find generalized classification rules.

The endpoint, on which training is performed, can be varied. In this study, additionally grown tumor volume at the first progress confirming follow up was used. This was due to the fact that the study aimed to investigate whether the progressive regions possibly arise from underestimation and thus, under dosage, of the tumor extend at planning. The goal was to identify these regions in advance using additional physiological imaging modalities. The GTV was used as definition of initial tumor volume, because the progress was also defined in terms of contrast enhancing region in the T_1 weighted MRI. Using a cohort of patients with favorable outcome (disease free, stable disease) could be used to learn adequate rules for target volume definition. Predictions from the resulting forest could be used for guidance in GTV delineation.

Further studies should be done to investigate the appropriate choice of features on which classification should be performed. In this work, focus was put on parameters from physiological imaging modalities. Weber et al. [2015] used data from diffusion weighted MRI together with several distance and texture measures, accounting for the distance of each pixel from primary tumor site and nerve fiber paths, describing tissue structure. These parameters could be combined with the presented multi-modal features for improved classification with both anatomical and physiological tissue properties. Another option is considering further information from treatment planning. For ion therapy, range uncertainties of the distal edge could be included to find possible regions of under-dosage at the steep dose gradients.

Feature importance analysis can be used to determine the parameters most relevant for correct classification. These parameters could be considered accordingly with increased weighting in clinical treatment planning and target delineation.

The presented workflow can be used for longitudinal data analysis of several time points in order to study progress formation and growth. It might be especially interesting to investigate consecutive time points from follow up over a long time period. This setup excludes the possibility of pseudo-progression and could yield a deeper understanding of the differences between fast and slow growing tumors.

The presented workflow uses the random forest algorithm for tissue classification. Random forests also present the opportunity for regression analysis, which might be more suitable for yielding the probability of each pixel being or becoming tumor. The regression results could be included as “probability maps” into the treatment planning routine.

6 Summary

The goal of radiotherapy is to induce destruction of the tumor while spearing the surrounding healthy tissue. Target delineation, i.e. the definition of the tumor extent, is based on radiological images, which allow for differentiation between tumor and normal tissue. Current standard definition of radiotherapy target volumes is based on contouring anatomical information from computed tomographic (CT) images, providing information on the tissue density distribution. Detection of tumor fronts for primary brain tumors (glioma) is limited due to diffuse infiltration patterns of the surrounding normal brain. These tumors often exhibit breakdown of the blood-brain-barrier. This effect can be assessed using contrast agent enhanced T_1 weighted magnetic resonance imaging (MRI). Usage of biological imaging, e.g. amino acid tracer positron emission tomography (PET), can provide further information.

The presented thesis aimed to improve radiotherapy target delineation of high grade glioma using an integrative image analysis approach. Focus was set on physiological imaging modalities, including metabolic and functional images from PET as well as diffusion and perfusion MRI. Amino acid tracers for PET provide enhanced uptake in glioma tissue, which has been shown to correlate with cell density in the literature. Several authors have shown that usage of ^{18}F-FET can increase survival time significantly by improving treatment planning. Perfusion and diffusion MRI have been established as a useful diagnostic tool in various brain diseases in several studies. Dynamic contrast enhanced (DCE) perfusion imaging enables quantification of tissue micro-circulation and micro-vascularization by measuring hemodynamic parameters, such as cerebral blood flow and volume. Diffusion weighted imaging enables assessment of nerve fiber structures and the derived apparent diffusion coefficient, which has been shown to correlate with cellularity by a number of authors.

Data from recurrent high grade glioma patients, included in the CINDERELLA trial [Combs et al., 2010] at the HIT[1] facility, was studied. Image data from this study included standard imaging protocols (CT and T_1-weighted MRI with and without contrast agent), as well as T_2 fluid attenuation inversion recovery sequences, functional MRI sequences for perfusion, diffusion weighted and susceptibility weighted imaging sequences.

The first step was to investigate of the surrogate value of these modalities. Parameter assessment was studied with respect to the physiological correlates, as well as parameter stability and robustness. For this purpose, software tools for the quantitative analysis of the available image data were developed. The medical imaging interaction toolkit (MITK) was used as a common software basis. For analysis of dynamic image series, a software module for extraction and fitting of signal-time curves with a dedicated model function was

[1] Heidelberger Ionenstrahl-Therapiezentrum

implemented. In principle, the developed module can be used for any kind of 4D dynamic data modeling. In the context of this work, it was mainly used for pharmacokinetic modeling of indicator behavior in dynamic PET and DCE MRI. An extension to the model provides means for calculation of semi-quantitative, curve-describing parameters from non-compartmental analysis, e.g. the area under the curve and mean residence time. Additionally, a tool was developed for calculation of standardized uptake values (SUV), a widely used clinical measure for assessment of tracer uptake in PET. Segmentation of PET images is usually done using isocontours, a percentage thresholding method. Hence, a plugin for automatic delineation of isocontours with a variable threshold was implemented.

Model feasibility of two pharmacokinetic models was studied for dynamic ^{18}F-FET PET data in seven patients. The results showed, that the two tissue compartment model represents, in principle, a feasible description of ^{18}F-FET kinetics. However, the one tissue compartment model yielded better results with regards to stability and robustness. Furthermore, non-compartmental analysis of time-SUV curves were performed, yielding semi-quantitative parameters in different tissue volumes. Parameters differed in initial and progressed tumor volume compared to healthy tissue, leading to surrogate parameters in tumor assessment.

DCE MRI data were investigated for feasibility to pharmacokinetic modeling in three sample patients using the presented software tools. Assessment of the arterial concentration showed, that the acquired data were not suitable for dedicated pharmacokinetic modeling analysis due to low temporal resolution. Non-compartmental analysis of the concentration-time curves yielded semi-quantitative parameters, which could be shown to differ between target volumes from radiotherapy planning and progressive tumor volume. Hence, they could provide stable measures for tissue classification.

Pharmacokinetic modeling provides a complex analysis method that is prone to error, if not used properly. Parameters are usually estimated by fitting a model function to measured data using standard non-linear least squares methods (NLLS). NLLS poses an unconstrained optimization problem that does not necessarily yield a unique solution. Different factors concerning data quality as well as optimization algorithmic can influence the outcome, since the optimizer might find a local minimum instead of the global one. In the literature, several studies on model feasibility and comparison between different models have been performed. However, little attention was given to technical aspects of the fitting routine. The high flexibility of the presented dynamic data analysis software, and the possibility for specifying both model function and optimizer configuration, gave the opportunity to study certain aspects of non-linear least square fitting in tracer-kinetic modeling. During the course of this work a simulation tool for perfusion data was developed, which allows for generation of synthetic perfusion MRI data. The tool works opposite to the fitting process, using a model function and maps of the corresponding parameters to calculate the resulting concentration-time curve and store it in a 4D image. Synthetic DCE MRI data, created with the simulation tool, was used for two studies on accuracy and robustness of parameter estimates in DCE MRI with the two compartment exchange model. This model is defined by two coupled first-order differential equations, which can be solved analytically or by direct integration. Both strategies were compared for different parameter scenarios on synthetic 4D images. The resulting parameter estimates were evaluated in

terms of accuracy, precision and computational speed. Both approaches yielded similar results in parameter determination, the convolution excelled in computational speed. It has been mentioned by several authors, that the choice of initial parameter values has an influence on the optimization routine and thus the parameter estimates. In the presence of several local minima for the cost function within the search space, the initial position will determine the direction of the optimization. Under these circumstances, it is likely, that the optimizer does not choose the correct global minimum for the parameter estimate but rather a local one lying closer to the initial values. The necessity for adequate choice of starting parameters has not been studied before. Since the presented fitting module allows definition of starting values for each parameter on a pixel-wise basis in form of images, the influence of the optimization parameter start values could be studied in the presented work. Results show that the influence of starting values of the optimization routine on the accuracy of the parameter estimates was less than expected.

The second step of analyzing multimodal image data from primary brain tumor patients conducted studies on comparison between parameter from different modalities. The goal was to investigate the extent, to which combined image information could yield conclusive information. Such an analysis was enabled with the developed software tools. Inclusion of radiotherapy parameters was used to assess mismatches between modalities. The prognostic value of ^{18}F-FET PET with respect to tumor recurrence was analyzed on different PET delineation techniques, including isocontours of 40%, 50%, 60% and 70% and the two semi-automatic segmentation algorithms, 3D region growing and the multi-label random walker. The volumes that these PET-based contours added to the treated gross tumor volume from radiotherapy planning, were compared to the progression patterns of the tumor in follow-up examinations. The results showed that no contouring technique was clearly superior and could provide high conformity, sensitivity and specificity with regards to the progressive tumor volumes in all patients. Since the level of tracer uptake varies greatly between patients, results suggested, that an appropriate contouring technique should be chosen based on tracer uptake in the lesion compared to the healthy brain tissue background.

The results of these comparison studies were not satisfying. Thus, a novel integrative approach was pursued as third step. A technique for combining information from multimodal imaging was developed and tested in this thesis, in order to find physical models describing the tumor progress formation. The above mentioned modalities and software tools were used for prediction of tumor progression patterns based on multimodal image classification with a random forest machine learning algorithm. All images from relevant modalities can be loaded and preprocessed within MITK, including registration, segmentation and calculation of the necessary features. A command line tool for automatic training configuration of a random forest with the desired group of patients and features, and subsequent prediction boasted on classification of previously unseen patient data. Exemplary prediction analysis of tumor progression was performed with different training configurations on a small set of patients with recurrent high grade glioma in order to illustrate functionality of the workflow and classification results. The developed software environment provides the means for a number of different studies on multi-modal multi-parametric data sets with regards to tumor growth patterns. Classification and regression analysis can be performed on large patient cohorts, with regard to recurrences as well as longitudinal growth behavior

of tumors. Further studies on the appropriate set of features, patients and investigated endpoints have to be conducted in the future.

To conclude, this thesis presented a novel approach for quantitative, integrative analysis of multimodal image data that was developed, established and tested on real patient data.

Appendix

Runge-Kutta method

The Runge-Kutta method is an iterative method for approximation of solutions to ordinary differential equations. The differential equations form the following initial value problem:

$$\begin{aligned}
y'(x) &= f(x, y(x)) \\
y_1'(x) &= f_1(x, y_1(x), ..., y_n(x)) \\
y_2'(x) &= f_2(x, y_1(x), ..., y_n(x)) \\
&... \\
y_n'(x) &= f_n(x, y_1(x), ..., y_n(x)) \\
&\text{with initial vaule:} \\
y(x_0) &= y_0
\end{aligned}$$

Defining a step size h, such as $x_i = x_0 + ih$, then the solution $y(x)$ to the initial value problem can be approximated with a functionw_i, that can be calculated iteratively using:

$$\begin{aligned}
w_0 &= x_0 \\
k_1 &= h \cdot f(x_i, w_i) \\
k_2 &= h \cdot f(x_i + \frac{h}{2}, w_i + \frac{k_1}{2} \\
k_3 &= h \cdot f(x_i + \frac{h}{2}, w_i + \frac{k_2}{2} \\
k_4 &= h \cdot f(x_i + h, w_i + k_3) \\
w_{i+1} &= w_i + \frac{1}{6}(k_1 + 2k_2 + 2k_3 + k_4)
\end{aligned}$$

This method is referred to as 4^{th} order Runge Kutta.

Convolution with arterial input functions

The convolution of two functions $f(t), g(t)$ is defined as

$$(f * g)(t) = \int_{-\infty}^{+\infty} f(t - \tau) \cdot g(\tau) d\tau$$

Indicator dilution theory states that the concentration time course of an indicator can be described by convolution of the indicator influx $c_a(t)$ (arterial concentration) with a model specific residue function $R(t, \phi_i)$. For closed-form analytical solutions, this residue function is a sum of exponential functions $R_n = e^{-\lambda_n t}$ with decay constants λ_n. The arterial concentration is usually measured from image data, thus it is provided as discrete array $c_a[t_i]$ at sampling time points $t_i \in [t_0, T]$. With this, the convolution yields

$$\begin{aligned} C_n(t) = (R_n * c_a)(t) &= \int_{-\infty}^{+\infty} R(t-\tau) c_a(\tau) d\tau \\ &= \int_{t_0}^{T} e^{-\lambda_n (t_i - \tau)} c_a(\tau) d\tau \end{aligned}$$

This approach requires evaluation of $c_a(\tau)$ at all times τ. Approximating the integral via a sum of discrete sample points leads to major errors in estimating $C(t)$, especially if temporal sampling t_i is low. Ingrisch [2012] proposed linear interpolation of the arterial concentration

$$\begin{aligned} \Delta t &= t_{i+1} - t_i \\ m &= \frac{c_a(t_{i+1}) - c_a(t_i)}{\Delta t} \\ \rightarrow c_a(\tau) &= c_a(t_i) + m \cdot (\tau - t_i) \end{aligned}$$

Using this approach, an iterative formula for calculation of $C(t_i) := Y_i$ can be found. If Y_i is known, the subsequent element Y_{i+1} can be calculated via

$$\begin{aligned} Y_{i+1} &= \int_{t_0}^{t_{i+1}} e^{-\lambda_n (t_{i+1} - \tau)} c_a(\tau) d\tau \\ &= \int_{t_0}^{t_i} e^{-\lambda_n (t_{i+1} - \tau)} c_a(\tau) d\tau + \int_{t_i}^{t_{i+1}} e^{-\lambda_n (t_{i+1} - \tau)} c_a(\tau) d\tau \\ &= \int_{t_0}^{t_i} e^{\lambda_n \tau} e^{-\lambda (t_i - t_i + t_{i+1})} c_a(\tau) d\tau + \int_{t_i}^{t_{i+1}} e^{-\lambda_n (t_{i+1} - \tau)} c_a(\tau) d\tau \\ &= \int_{t_0}^{t_i} e^{-\lambda_n (t_i - \tau)} e^{-\lambda (t_{i+1} - t_i)} c_a(\tau) d\tau + \int_{t_i}^{t_{i+1}} e^{-\lambda_n (t_{i+1} - \tau)} c_a(\tau) d\tau \\ &= Y_i \cdot e^{-\lambda (t_{i+1} - t_i)} + \int_{t_i}^{t_{i+1}} e^{-\lambda_n (t_{i+1} - \tau)} c_a(\tau) d\tau \end{aligned}$$

The first sampling point can be assumed as $C(t_0) = 0$, since the contrast agent concentration is usually zero at the beginning of the measurement. The second integral can be derived as

$$
\begin{aligned}
I &= \int_{t_i}^{t_{i+1}} e^{-\lambda_n(t_{i+1}-\tau)} c_a(\tau) d\tau \\
\lambda_n &= e^{-\lambda_n(t_{i+1}-\tau)} \left\{ \int_{t_i}^{t_{i+1}} (c_a(t_i) - mt_i) e^{\lambda_n \tau} d\tau + \int_{t_i}^{t_{i+1}} m\tau e^{\lambda_n \tau} d\tau \right\} \\
&= \frac{c_a(t_i) - mt_i}{\lambda_n}(1 - e^{-\lambda \Delta\tau}) + \frac{m}{\lambda^2}\left[(\lambda_n t_{i+1} - 1) - e^{-\lambda_n \Delta t}(\lambda_n t_i - 1)\right]
\end{aligned}
$$

With this, the convolution of the exponential residue function with the discretely sampled arterial concentration $c_a(t)$ yields

$$
\begin{aligned}
C_n(t_0) &= 0 \\
C_n(t_{i+1}) &= (R_n * c_a)(t) \\
&= C(t_i) \cdot e^{-\lambda(t_{i+1}-t_i)} + \frac{c_a(t_i) - mt_i}{\lambda_n}(1 - e^{-\lambda \Delta\tau}) \\
&+ \frac{m}{\lambda^2}\left[(\lambda_n t_{i+1} - 1) - e^{-\lambda_n \Delta t}(\lambda_n t_i - 1)\right]
\end{aligned}
$$

Bibliography

Abragam, A. [2007], *Principles of Nuclear Magnetism*, Oxford University Press.

ABX advanced biochemical compounds GmbH, Radeberg, G. [2015], 'ROI Visualization, Evaluation and Image Registration.', Accessed on: 04/30/2016. `http://www.abx.de/rover/index.php/overview.html`.

Ahearn, T., Staff, R., Redpath, T. and Semple, S. [2005], 'The use of the Levenberg-Marquardt curve-fitting algorithm in pharmacokinetic modelling of DCE-MRI data.', *Physics in Medicine and Biology* **50**(9), N85.

Allard, J., Cotin, S., Faure, F., Bensoussan, P.-J., Poyer, F., Duriez, C., Delingette, H. and Grisoni, L. [2007], 'Sofa-an open source framework for medical simulation.', in *MMVR 15-Medicine Meets Virtual Reality*, Vol. 125, IOP Press, pp. 13–18.

Bendl, R., Pross, J., Keller, M., Bürkelbach, J. and Schlegel, W. [1993], 'VIRTUOS - A program for VIRTUal radiotherapy Simulation.', in *Computer Assisted Radiology/Computergestützte Radiologie*, Springer, pp. 676–682.

Bernstein, M. A., King, K. F. and Zhou, X. J. [2004], *Handbook of MRI pulse sequences*, Elsevier.

Bille, J. and Schlegel, W. [2002], *Medizinische Physik 2: Medizinische Strahlenphysik*, Berlin Heidelberg New York: Springer-Verlag.

Boost C++ Libraries [2016], Boost Software License. `http://www.boost.org/`.

Boxenbaum, H. G., Riegelman, S. and Elashoff, R. M. [1974], 'Statistical estimations in pharmacokinetics.', *Journal of Pharmacokinetics and Biopharmaceutics* **2**(2), 123–148.

Bradski, G. and Kaehler, A. [2008], *Learning OpenCV: Computer vision with the OpenCV library*, O'Reilly Media, Inc.

Breiman, L. [2001], 'Random forests.', *Machine Learning* **45**(1), 5–32.

Brix, G., Griebel, J., Kiessling, F. and Wenz, F. [2010], 'Tracer kinetic modelling of tumour angiogenesis based on dynamic contrast-enhanced CT and MRI measurements.', *European Journal of Nuclear Medicine and Molecular Imaging* **37**(1), 30–51.

Brix, G., Kiessling, F., Lucht, R., Darai, S., Wasser, K., Delorme, S. and Griebel, J. [2004], 'Microcirculation and microvasculature in breast tumors: pharmacokinetic analysis of dynamic MR image series.', *Magnetic Resonance in Medicine* **52**(2), 420–429.

Brix, G., Zwick, S., Kiessling, F. and Griebel, J. [2009], 'Pharmacokinetic analysis of tissue microcirculation using nested models: multimodel inference and parameter identifiability.', *Medical Physics* **36**(7), 2923–2933.

Brynolfsson, P., Nilsson, D., Henriksson, R., Hauksson, J., Karlsson, M., Garpebring, A., Birgander, R., Trygg, J., Nyholm, T. and Asklund, T. [2014], 'ADC texture - An imaging biomarker for high-grade glioma?', *Medical Physics* **41**(10), 101903.

Buckley, D. L., Roberts, C., Parker, G. J., Logue, J. P. and Hutchinson, C. E. [2004], 'Prostate Cancer: Evaluation of Vascular Characteristics with Dynamic Contrast-enhanced T1-weighted MR Imaging - Initial Experience 1.', *Radiology* **233**(3), 709–715.

Carson, R. E. [2005], 'Tracer kinetic modeling in PET', in *Positron Emission Tomography*, Springer, pp. 127–159.

Chavaudra, J. and Bridier, A. [2001], 'Definition of volumes in external radiotherapy: ICRU reports 50 and 62.', *Cancer Radiothérapie: Journal de la Société Française de Radiothérapie Oncologique* **5**(5), 472.

CHILI PACS, HIT Research Data Base [2016], CHILI GmbH.

CMake [2016], Kitware Inc. `https://www.cmake.org/`.

Combs, S. E., Burkholder, I., Edler, L., Rieken, S., Habermehl, D., Jäkel, O., Haberer, T., Haselmann, R., Unterberg, A., Wick, W. et al. [2010], 'Randomised phase I/II study to evaluate carbon ion radiotherapy versus fractionated stereotactic radiotherapy in patients with recurrent or progressive gliomas: the CINDERELLA trial.', *BMC Cancer* **10**(1), 533.

De Coene, B., Hajnal, J. V., Gatehouse, P., Longmore, D. B., White, S. J., Oatridge, A., Pennock, J., Young, I. and Bydder, G. [1992], 'MR of the brain using fluid-attenuated inversion recovery (FLAIR) pulse sequences.', *American Journal of Neuroradiology* **13**(6), 1555–1564.

Degani, H., Gusis, V., Weinstein, D., Fields, S. and Strano, S. [1997], 'Mapping pathophysiological features of breast tumors by MRI at high spatial resolution.', *Nature Medicine* **3**(7), 780–782.

Del Amo, E. M., Urtti, A. and Yliperttula, M. [2008], 'Pharmacokinetic role of L-type amino acid transporters LAT1 and LAT2.', *European Journal of Pharmaceutical Sciences* **35**(3), 161–174.

Del Sole, A., Falini, A., Ravasi, L., Ottobrini, L., De Marchis, D., Bombardieri, E. and Lucignani, G. [2001], 'Anatomical and biochemical investigation of primary brain tumours.', *European Journal of Nuclear Medicine* **28**(12), 1851–1872.

Deserno, T. M. [2011], *Biomedical Image Processing*, Springer.

Deutsche Krebshilfe [2016], Accessed on: 02/10/2016. `http://www.krebshilfe.de/wir-informieren/ueber-krebs/krebszahlen.html?L=`.

Dhermain, F. G., Hau, P., Lanfermann, H., Jacobs, A. H. and van den Bent, M. J. [2010], 'Advanced MRI and PET imaging for assessment of treatment response in patients with gliomas.', *The Lancet Neurology* **9**(9), 906–920.

Dimitrakopoulou-Strauss, A., Strauss, L. G., Schwarzbach, M., Burger, C., Heichel, T., Willeke, F., Mechtersheimer, G. and Lehnert, T. [2001], 'Dynamic PET 18F-FDG studies in patients with primary and recurrent soft-tissue sarcomas: impact on diagnosis and correlation with grading.', *Journal of Nuclear Medicine* **42**(5), 713–720.

DiPiro, J. T. [2010], *Concepts in Clinical Pharmacokinetics*, ASHP.

DiStefano, J. [1982], 'Noncompartmental vs. compartmental analysis: some bases for choice.', *American Journal of Physiology-Regulatory, Integrative and Comparative Physiology* **243**(1), R1–R6.

Dixon, W. T. [1984], 'Simple proton spectroscopic imaging.', *Radiology* **153**(1), 189–194.

DKFZ Atlas of Cancer Mortality [2010], Accessed on 04/19/2016. `https://www.dkfz.de/en/forschung/index.html`.

E. Yankeelov, D. R. P. and Price., R. R. [2011], *Quantitative MRI in Cancer*, CRC Press.

Ellingson, B. M., Cloughesy, T. F., Zaw, T., Lai, A., Nghiemphu, P. L., Harris, R., Lalezari, S., Wagle, N., Naeini, K. M., Carrillo, J. et al. [2012], 'Functional diffusion maps (fDMs) evaluated before and after radiochemotherapy predict progression-free and overall survival in newly diagnosed glioblastoma.', *Neuro-oncology* p. nor220.

Essig, M., Hawighorst, H., Schoenberg, S. O., Engenhart-Cabillic, R., Fuss, M., Debus, J., Zuna, I., Knopp, M. V. and van Kaick, G. [1998], 'Fast fluid-attenuated inversion-recovery (FLAIR) MRI in the assessment of intraaxial brain tumors.', *Journal of Magnetic Resonance Imaging* **8**(4), 789–798.

Essig, M., Metzner, R., Bonsanto, M., Hawighorst, H., Debus, J., Tronnier, V., Knopp, M. V. and Kaick, G. [2001], 'Postoperative fluid-attenuated inversion recovery MR imaging of cerebral gliomas: initial results.', *European Radiology* **11**(10), 2004–2010.

Floca, R. [2009], 'MatchPoint: on bridging the innovation gap between algorithmic research and clinical use in image registration.', in *World Congress on Medical Physics and Biomedical Engineering, September 7-12, 2009, Munich, Germany*, Springer, pp. 1105–1108.

Fritzsche, K. H., Neher, P. F., Reicht, I., van Bruggen, T., Goch, C., Reisert, M., Nolden, M., Zelzer, S., Meinzer, H.-P., Stieltjes, B. et al. [2012], 'MITK diffusion imaging.', *Methods of Information in Medicine* **51**(5), 441.

Gaspar, L. E., Fisher, B. J., Macdonald, D. R., Leber, D. V., Halperin, E. C., Schold, S. C. and Cairncross, J. G. [1992], 'Supratentorial malignant glioma: patterns of recurrence and implications for external beam local treatment.', *International Journal of Radiation Oncology* Biology* Physics* **24**(1), 55–57.

Gering, D. T., Nabavi, A., Kikinis, R., Grimson, W. E. L., Hata, N., Everett, P., Jolesz, F. and Wells, W. M. [1999], 'An integrated visualization system for surgical planning and guidance using image fusion and interventional imaging.', in *Medical image computing and computer-assisted intervention–MICCAI'99*, Springer, pp. 809–819.

Gibaldi, M. and Perrier, D. [1982], *Pharmacokinetics, 2nd Edition*, Dekker, New York.

Grady, L. and Funka-Lea, G. [2004], 'Multi-label image segmentation for medical applications based on graph-theoretic electrical potentials.', in *Computer Vision and Mathematical Methods in Medical and Biomedical Image Analysis*, Springer, pp. 230–245.

Graves, E. E., Quon, A. and Loo, B. W. [2007], 'RT_Image: an open-source tool for investigating PET in radiation oncology.', *Technology in Cancer Research & Treatment* **6**(2), 111–121.

Grosu, A.-L. and Weber, W. A. [2010], 'PET for radiation treatment planning of brain tumours.', *Radiotherapy and Oncology* **96**(3), 325–327.

Grosu, A. L., Weber, W. A., Franz, M., Stärk, S., Piert, M., Thamm, R., Gumprecht, H., Schwaiger, M., Molls, M. and Nieder, C. [2005], 'Reirradiation of recurrent high-grade gliomas using amino acid PET (SPECT)/CT/MRI image fusion to determine gross tumor volume for stereotactic fractionated radiotherapy.', *International Journal of Radiation Oncology* Biology* Physics* **63**(2), 511–519.

Haider, M., Yeung, I. and Jaffray, D. [2015], 'The DCE Tool for ClearCanvas', Accessed on: 04/30/2016. `http://thedcetool.com/`.

Hajnal, J. V., Bryant, D. J., Kasuboski, L., Pattany, P. M., De Coene, B., Lewis, P. D., Pennock, J. M., Oatridge, A., Young, I. R. and Bydder, G. M. [1992], 'Use of fluid attenuated inversion recovery (FLAIR) pulse sequences in MRI of the brain.', *Journal of Computer Assisted Tomography* **16**(6), 841–844.

Heiss, P., Mayer, S., Herz, M., Wester, H.-J. et al. [1999], 'Investigation of transport mechanism and uptake kinetics of O-(2-[18F] fluoroethyl)-L-tyrosine in vitro and in vivo', *The Journal of Nuclear Medicine* **40**(8), 1367.

Holford, N. [1994], 'MK-MODEL, a quantitative modelling system for pharmacologists, version 5'.

Hompland, T., Ellingsen, C., Øvrebø, K. M. and Rofstad, E. K. [2012], 'Interstitial fluid pressure and associated lymph node metastasis revealed in tumors by dynamic contrast-enhanced MRI', *Cancer Research* **72**(19), 4899–4908.

Huang, C. and McConathy, J. [2013], 'Radiolabeled amino acids for oncologic imaging.', *Journal of Nuclear Medicine* **54**(7), 1007–1010.

Husstedt, H., Sickert, M., Köstler, H., Haubitz, B. and Becker, H. [2000], 'Diagnostic value of the fast-FLAIR sequence in MR imaging of intracranial tumors.', *European Radiology* **10**(5), 745–752.

Imai, H., Kaira, K., Oriuchi, N., Shimizu, K., Tominaga, H., Yanagitani, N., Sunaga, N., Ishizuka, T., Nagamori, S., Promchan, K. et al. [2010], 'Inhibition of L-type amino acid transporter 1 has antitumor activity in non-small cell lung cancer.', *Anticancer research* **30**(12), 4819–4828.

Ingrisch, M. [2012], Quantification of cerebral hemodynamics with dynamic contrast-enhanced MRI, PhD thesis, Ludwig-Maximilians-Universität München.

Ingrisch, M. and Sourbron, S. [2013], 'Tracer-kinetic modeling of dynamic contrast-enhanced MRI and CT: a primer', *Journal of Pharmacokinetics and Pharmacodynamics* **40**(3), 281–300.

Ingrisch, M., Sourbron, S., Morhard, D., Ertl-Wagner, B., Kümpfel, T., Hohlfeld, R., Reiser, M. and Glaser, C. [2012], 'Quantification of perfusion and permeability in multiple sclerosis: dynamic contrast-enhanced MRI in 3D at 3T.', *Investigative Radiology* **47**(4), 252–258.

Ishiwata, K., Kubota, K., Murakami, M., Kubota, R., Sasaki, T., Ishii, S. and Senda, M. [1993], 'Re-evaluation of amino acid PET studies: can the protein synthesis rates in brain and tumor tissues be measured in vivo?', *Journal of Nuclear Medicine: official publication, Society of Nuclear Medicine* **34**(11), 1936–1943.

Jacquez, J. A. et al. [1985], *Compartmental analysis in biology and medicine*, Elsevier, Amsterdam.

Jager, P. L., Vaalburg, W., Pruim, J., De Vries, E. G., Langen, K.-J. and Piers, D. A. [2001], 'Radiolabeled Amino Acids: Basic Aspects and Clinical Applications in Oncology.', *Journal of Nuclear Medicine* **42**(3), 432–445.

Jain, R. [2013], 'Measurements of tumor vascular leakiness using DCE in brain tumors: clinical applications.', *NMR in Biomedicine* **26**(8), 1042–1049.

Jansen, N. L., Suchorska, B., Wenter, V., Eigenbrod, S., Schmid-Tannwald, C., Zwergal, A., Niyazi, M., Drexler, M., Bartenstein, P., Schnell, O. et al. [2014], 'Dynamic 18F-FET PET in newly diagnosed astrocytic low-grade glioma identifies high-risk patients.', *Journal of Nuclear Medicine* **55**(2), 198–203.

Jbabdi, S., Mandonnet, E., Duffau, H., Capelle, L., Swanson, K. R., Pélégrini-Issac, M., Guillevin, R. and Benali, H. [2005], 'Simulation of anisotropic growth of low-grade gliomas using diffusion tensor imaging.', *Magnetic Resonance in Medicine* **54**(3), 616–624.

Johnson, J. A. and Wilson, T. A. [1966], 'A model for capillary exchange.', *American Journal of Physiology–Legacy Content* **210**(6), 1299–1303.

Kassner, A., Roberts, T., Taylor, K., Silver, F. and Mikulis, D. [2005], 'Prediction of hemorrhage in acute ischemic stroke using permeability MR imaging.', *American Journal of Neuroradiology* **26**(9), 2213–2217.

Kershaw, L. E. and Buckley, D. L. [2006], 'Precision in measurements of perfusion and microvascular permeability with T1-weighted dynamic contrast-enhanced MRI.', *Magnetic Resonance in Medicine* **56**(5), 986–992.

Keyes Jr, J. W. et al. [1995], 'SUV: standard uptake or silly useless value?', *Journal of Nuclear Medicine* **36**(10), 1836–1839.

Kiessling, F., Boese, J., Corvinus, C., Ederle, J., Zuna, I., Schoenberg, S., Brix, G., Schmähl, A., Tuengerthal, S., Herth, F. et al. [2004], 'Perfusion CT in patients with advanced bronchial carcinomas: a novel chance for characterization and treatment monitoring?', *European Radiology* **14**(7), 1226–1233.

Kim, Y., Rebro, K. and Schmainda, K. [2002], 'Water exchange and inflow affect the accuracy of T1-GRE blood volume measurements: Implications for the evaluation of tumor angiogenesis.', *Magnetic Resonance in Medicine* **47**(6), 1110–1120.

Knutsson, L., Ståhlberg, F. and Wirestam, R. [2010], 'Absolute quantification of perfusion using dynamic susceptibility contrast MRI: pitfalls and possibilities.', *Magnetic Resonance Materials in Physics, Biology and Medicine* **23**(1), 1–21.

Koh, D.-M., Collins, D. J. and Orton, M. R. [2011], 'Intravoxel incoherent motion in body diffusion-weighted MRI: reality and challenges.', *American Journal of Roentgenology* **196**(6), 1351–1361.

Konukoglu, E., Clatz, O., Menze, B. H., Stieltjes, B., Weber, M.-A., Mandonnet, E., Delingette, H. and Ayache, N. [2010], 'Image guided personalization of reaction-diffusion type tumor growth models using modified anisotropic eikonal equations.', *Medical Imaging, IEEE Transactions on* **29**(1), 77–95.

Köthe, U. et al. [2008], 'VIGRA-Vision with Generic Algorithms', *Cognitive Systems Group, University of Hamburg, Germany* .

Langen, K.-J., Hamacher, K., Weckesser, M., Floeth, F., Stoffels, G., Bauer, D., Coenen, H. H. and Pauleit, D. [2006], 'O-(2-[18 F] fluoroethyl)-L-tyrosine: uptake mechanisms and clinical applications.', *Nuclear Medicine and Biology* **33**(3), 287–294.

Larson, K. B., Markham, J. and Raichle, M. E. [1987], 'Tracer-kinetic models for measuring cerebral blood flow using externally detected radiotracers.', *Journal of Cerebral Blood Flow & Metabolism* **7**(4), 443–463.

Larsson, H. B., Courivaud, F., Rostrup, E. and Hansen, A. E. [2009], 'Measurement of brain perfusion, blood volume, and blood-brain barrier permeability, using dynamic contrast-enhanced T1-weighted MRI at 3 tesla.', *Magnetic Resonance in Medicine* **62**(5), 1270–1281.

Lee, J. A. [2010], 'Segmentation of positron emission tomography images: some recommendations for target delineation in radiation oncology.', *Radiotherapy and Oncology* **96**(3), 302–307.

Luypaert, R., Ingrisch, M., Sourbron, S. and de Mey, J. [2012], 'The Akaike information criterion in DCE-MRI: Does it improve the haemodynamic parameter estimates?', *Physics in Medicine and Biology* **57**(11), 3609.

Luypaert, R., Sourbron, S., Makkat, S. and de Mey, J. [2010], 'Error estimation for perfusion parameters obtained using the two-compartment exchange model in dynamic contrast-enhanced MRI: a simulation study', *Physics in Medicine and Biology* **55**(21), 6431.

Markwardt, C. B. [2009], 'Non-linear least squares fitting in IDL with MPFIT.', *arXiv preprint arXiv:0902.2850* .

Meier, P. and Zierler, K. L. [1954], 'On the theory of the indicator-dilution method for measurement of blood flow and volume.', *Journal of Applied Physiology* **6**(12), 731–744.

MeVisLAB [2016], MeVis Medical Solutions and Fraunhofer MEVIS. `http://www.mevislab.de/`.

Mikolajczyk, K., Szabatin, M., Rudnicki, P., Grodzki, M. and Burger, C. [1998], 'A JAVA environment for medical image data analysis: initial application for brain PET quantitation.', *Medical Informatics* **23**(3), 207–214.

Møller, S., Lundemann, M., Law, I., Poulsen, H. S., Larsson, H. B. and Engelholm, S. A. [2015], 'Early changes in perfusion of glioblastoma during radio-and chemotherapy evaluated by T1-dynamic contrast enhanced magnetic resonance imaging.', *Acta Oncologica* **54**(9), 1521–1528.

Moré, J. J. [1978], 'The Levenberg-Marquardt algorithm: implementation and theory.', in *Numerical Analysis*, Springer, pp. 105–116.

Mugler, J. P. and Brookeman, J. R. [1990], 'Three-dimensional magnetization-prepared rapid gradient-echo imaging (3D MP RAGE).', *Magnetic Resonance in Medicine* **15**(1), 152–157.

Mugler, J. P. and Brookeman, J. R. [1991], 'Rapid three-dimensional T1-weighted MR imaging with the MP-RAGE sequence.', *Journal of Magnetic Resonance Imaging* **1**(5), 561–567.

Neff, T. [2005], Verbesserung der Zielvolumendefinition in der Strahlentherapieplanung durch den Einsatz der biologischen Bildgebung., PhD thesis, Universität Mannheim: sn.

NIST/SEMATECH [2013], 'e-Handbook of Statistical Methods', Accessed on: 04/30/2016. `http://www.itl.nist.gov/div898/handbook/`.

Nolden, M., Zelzer, S., Seitel, A., Wald, D., Müller, M., Franz, A. M., Maleike, D., Fangerau, M., Baumhauer, M., Maier-Hein, L. et al. [2013], 'The medical imaging interaction toolkit: challenges and advances.', *International Journal of Computer Assisted Radiology and Surgery* **8**(4), 607–620.

Nöth, U., Hattingen, E., Bähr, O., Tichy, J. and Deichmann, R. [2015], 'Improved visibility of brain tumors in synthetic MP-RAGE anatomies with pure T1 weighting.', *NMR in Biomedicine* **28**(7), 818–830.

O'Connor, J. P., Jackson, A., Asselin, M.-C., Buckley, D. L., Parker, G. J. and Jayson, G. C. [2008], 'Quantitative imaging biomarkers in the clinical development of targeted therapeutics: current and future perspectives.', *The Lancet Oncology* **9**(8), 766–776.

O'Connor, J. P., Jackson, A., Parker, G. J., Roberts, C. and Jayson, G. C. [2012], 'Dynamic contrast-enhanced MRI in clinical trials of antivascular therapies.', *Nature Reviews Clinical Oncology* **9**(3), 167–177.

O'Connor, J., Tofts, P., Miles, K., Parkes, L., Thompson, G. and Jackson, A. [2014], 'Dynamic contrast-enhanced imaging techniques: CT and MRI', *The British Journal of Radiology* .

Pauleit, D., Floeth, F., Hamacher, K., Riemenschneider, M. J., Reifenberger, G., Müller, H.-W., Zilles, K., Coenen, H. H. and Langen, K.-J. [2005], 'O-(2-[18F] fluoroethyl)-L-tyrosine PET combined with MRI improves the diagnostic assessment of cerebral gliomas.', *Brain* **128**(3), 678–687.

Pauleit, D., Floeth, F., Herzog, H., Hamacher, K., Tellmann, L., Müller, H.-W., Coenen, H. H. and Langen, K.-J. [2003], 'Whole-body distribution and dosimetry of O-(2-[18F] fluoroethyl)-L-tyrosine.', *European Journal of Nuclear Medicine and Molecular Imaging* **30**(4), 519–524.

Paulino, A. C., Koshy, M., Howell, R., Schuster, D. and Davis, L. W. [2005], 'Comparison of CT-and FDG-PET-defined gross tumor volume in intensity-modulated radiotherapy for head-and-neck cancer.', *International Journal of Radiation Oncology* Biology* Physics* **61**(5), 1385–1392.

Phelps, M. E. [2004], *PET: molecular imaging and its biological applications*, Springer Science & Business Media.

Physiome Project, National Simulation Resource, U. o. W. [2015], 'JSIM', Accessed on: 04/30/2016. `http://www.physiome.org/jsim/`.

Pintaske, J., Martisosian, P., Graf, H., Erg, G., Lodemann, K.-P., Claussen, C. D. and Schick, F. [2006], 'Relaxivity of gadopentetate dimeglumine (Magnevist), gadobutrol (Gadovist), and gadobenate dimeglumine (MultiHance) in human blood plasma at 0.2, 1.5 and 3 Tesla.', *Investigative Radiology* **41**(3), 213–221.

Piroth, M. D., Pinkawa, M., Holy, R., Klotz, J., Nussen, S., Stoffels, G., Coenen, H. H., Kaiser, H. J., Langen, K. J. and Eble, M. J. [2011], 'Prognostic value of early [18 F] fluoroethyltyrosine positron emission tomography after radiochemotherapy in glioblastoma multiforme.', *International Journal of Radiation Oncology* Biology* Physics* **80**(1), 176–184.

PMOD Modeling Software [2016], PMOD Technologies Ltd. `https://www.pmod.com/web/`.

Pöpperl, G., Kreth, F. W., Herms, J., Koch, W., Mehrkens, J. H., Gildehaus, F. J., Kretzschmar, H. A., Tonn, J. C. and Tatsch, K. [2006], 'Analysis of 18F-FET PET for grading of recurrent gliomas: is evaluation of uptake kinetics superior to standard methods?', *Journal of Nuclear Medicine* **47**(3), 393–403.

Pöpperl, G., Kreth, F. W., Mehrkens, J. H., Herms, J., Seelos, K., Koch, W., Gildehaus, F. J., Kretzschmar, H. A., Tonn, J. C. and Tatsch, K. [2007], 'FET PET for the evaluation of untreated gliomas: correlation of FET uptake and uptake kinetics with tumour

grading.', *European Journal of Nuclear Medicine and Molecular Imaging* **34**(12), 1933–1942.

Rempp, K. A., Brix, G., Wenz, F., Becker, C. R., Gückel, F. and Lorenz, W. J. [1994], 'Quantification of regional cerebral blood flow and volume with dynamic susceptibility contrast-enhanced MR imaging.', *Radiology* **193**(3), 637–641.

Rieken, S., Habermehl, D., Giesel, F. L., Hoffmann, C., Burger, U., Rief, H., Welzel, T., Haberkorn, U., Debus, J. and Combs, S. E. [2013], 'Analysis of FET-PET imaging for target volume definition in patients with gliomas treated with conformal radiotherapy.', *Radiotherapy and Oncology* **109**(3), 487–492.

Riviere, J. E. [2011], *Comparative pharmacokinteics: principles, techniques and applications*, John Wiley & Sons.

Rosen, B. R., Belliveau, J. W., Buchbinder, B. R., McKinstry, R. C., Porkka, L. M., Kennedy, D. N., Neuder, M. S., Fisel, C. R., Aronen, H. J., Kwong, K. K. et al. [1991], 'Contrast agents and cerebral hemodynamics.', *Magnetic Resonance in Medicine* **19**(2), 285–292.

Rosenschold, P. M., Costa, J., Engelholm, S. A., Lundemann, M. J., Law, I., Ohlhues, L. and Engelholm, S. [2014], 'Impact of [18F]-fluoro-ethyl-tyrosine PET imaging on target definition for radiation therapy of high-grade glioma.', *Neuro-oncology* p. nou316.

Rosset, A., Spadola, L. and Ratib, O. [2004], 'OsiriX: an open-source software for navigating in multidimensional DICOM images.', *Journal of Digital Imaging* **17**(3), 205–216.

Rowley, H. A., Grant, P. E. and Roberts, T. [1999], 'Diffusion MR imaging. Theory and applications.', *Neuroimaging Clinics of North America* **9**(2), 343–361.

Rydberg, J. N., Hammond, C. A., Grimm, R. C., Erickson, B. J., Jack Jr, C. R., Huston 3rd, J. and Riederer, S. J. [1994], 'Initial clinical experience in MR imaging of the brain with a fast fluid-attenuated inversion-recovery pulse sequence.', *Radiology* **193**(1), 173–180.

Sangren, W. and Sheppard, C. [1953], 'A mathematical derivation of the exchange of a labeled substance between a liquid flowing in a vessel and an external compartment.', *The Bulletin of Mathematical Biophysics* **15**(4), 387–394.

Siemens, Erlangen, G. [2016], 'Tissue4D', Accessed on: 04/30/2016. `https://www.healthcare.siemens.de/magnetic-resonance-imaging/options-and-upgrades/clinical-applications/tissue-4d`.

Simpson, N. E., He, Z. and Evelhoch, J. L. [1999], 'Deuterium NMR tissue perfusion measurements using the tracer uptake approach: I. Optimization of methods.', *Magnetic Resonance in Medicine* **42**(1), 42–52.

Sourbron, S. [2010], 'Technical aspects of MR perfusion.', *European Journal of Radiology* **76**(3), 304–313.

Sourbron, S. [2014], 'An introduction to Dynamic Contrast Enhanced MRI.', in *22rd Annual meeting of the International Society of Magnetic Resonance in Medicine (ISMRM 2014)*, Vol. 22, International Society of Magnetic Resonance in Medicine (ISMRM).

Sourbron, S. and Buckley, D. L. [2011], 'Tracer kinetic modelling in MRI: estimating perfusion and capillary permeability.', *Physics in Medicine and Biology* **57**(2), R1.

Sourbron, S., Ingrisch, M., Siefert, A., Reiser, M. and Herrmann, K. [2009], 'Quantification of cerebral blood flow, cerebral blood volume, and blood–brain-barrier leakage with DCE-MRI.', *Magnetic Resonance in Medicine* **62**(1), 205–217.

Stahl, V., Maier, F., Floca, R. O., Berger, M. C., Berriel Diaz, M., Freitag, M. T., Weber, M.-A., Dimitrakopoulou-Strauss, A. and Nagel, A. [2015], 'In vivo Assessment of Cold Stimulation Effects on the Fat Fraction of Brown Adipose Tissue using DIXON MRI.', in *23rd Annual meeting of the International Society of Magnetic Resonance in Medicine (ISMRM 2015)*, Vol. 23, International Society of Magnetic Resonance in Medicine (ISMRM).

Stockhammer, F., Plotkin, M., Amthauer, H., Van Landeghem, F. K. and Woiciechowsky, C. [2008], 'Correlation of F-18-fluoro-ethyl-tyrosin uptake with vascular and cell density in non-contrast-enhancing gliomas.', *Journal of Neuro-oncology* **88**(2), 205–210.

Stupp, R., Mason, W. P., Van Den Bent, M. J., Weller, M., Fisher, B., Taphoorn, M. J., Belanger, K., Brandes, A. A., Marosi, C., Bogdahn, U. et al. [2005], 'Radiotherapy plus concomitant and adjuvant temozolomide for glioblastoma.', *New England Journal of Medicine* **352**(10), 987–996.

Sugahara, T., Korogi, Y., Kochi, M., Ikushima, I., Shigematu, Y., Hirai, T., Okuda, T., Liang, L., Ge, Y., Komohara, Y. et al. [1999], 'Usefulness of diffusion-weighted MRI with echo-planar technique in the evaluation of cellularity in gliomas.', *Journal of Magnetic Resonance Imaging* **9**(1), 53–60.

Sung, K. [2015], 'DCE Tool', Accessed on: 04/30/2016. `http://kyungs.bol.ucla.edu/software/DCE_tool/DCE_tool.html`.

Swanson, K. R., Alvord, E. and Murray, J. [2000], 'A quantitative model for differential motility of gliomas in grey and white matter.', *Cell Proliferation* **33**(5), 317–329.

Swanson, K. R., Bridge, C., Murray, J. and Alvord, E. C. [2003], 'Virtual and real brain tumors: using mathematical modeling to quantify glioma growth and invasion.', *Journal of the Neurological Sciences* **216**(1), 1–10.

The Insight Segmentation and Registration Toolkit ITK [2016], Kitware Inc. `http://www.itk.org`.

The MathWorks MATLAB Products and Services [2016], The MathWorks Inc. `http://www.mathworks.com/`.

The OFFIS DICOM Toolkit DCMTK [2016], OFFIS e.V. `http://www.dcmtk.org/`.

The Qt software framework [2016], Qt Company. `http://www.qt.io`.

The Visualization Toolkit VTK [2016], Kitware Inc. `http://www.vtk.org`.

Thiele, F., Ehmer, J., Piroth, M. D., Eble, M. J., Coenen, H. H., Kaiser, H.-J., Schaefer, W. M., Buell, U. and Boy, C. [2009], 'The quantification of dynamic FET PET imaging and correlation with the clinical outcome in patients with glioblastoma.', *Physics in Medicine and Biology* **54**(18), 5525.

Thon, N., Kunz, M., Lemke, L., Jansen, N. L., Eigenbrod, S., Kreth, S., Lutz, J., Egensperger, R., Giese, A., Herms, J. et al. [2015], 'Dynamic 18F-FET PET in suspected WHO grade II gliomas defines distinct biological subgroups with different clinical courses.', *International Journal of Cancer* **136**(9), 2132–2145.

Tofts, P. S., Brix, G., Buckley, D. L., Evelhoch, J. L., Henderson, E., Knopp, M. V., Larsson, H. B., Lee, T.-Y., Mayr, N. A., Parker, G. J. et al. [1999], 'Estimating kinetic parameters from dynamic contrast-enhanced T 1-weighted MRI of a diffusable tracer: standardized quantities and symbols.', *Journal of Magnetic Resonance Imaging* **10**(3), 223–232.

Tofts, P. S. and Kermode, A. G. [1991], 'Measurement of the blood-brain barrier permeability and leakage space using dynamic MR imaging. 1. Fundamental concepts.', *Magnetic Resonance in Medicine* **17**(2), 357–367.

Vees, H., Senthamizhchelvan, S., Miralbell, R., Weber, D. C., Ratib, O. and Zaidi, H. [2009], 'Assessment of various strategies for 18F-FET PET-guided delineation of target volumes in high-grade glioma patients.', *European Journal of Nuclear Medicine and Molecular Imaging* **36**(2), 182–193.

Verrey, F. [2003], 'System L: heteromeric exchangers of large, neutral amino acids involved in directional transport.', *Pflügers Archiv* **445**(5), 529–533.

Walker, M. D., Strike, T. A. and Sheline, G. E. [1979], 'An analysis of dose-effect relationship in the radiotherapy of malignant gliomas.', *International Journal of Radiation Oncology* Biology* Physics* **5**(10), 1725–1731.

Weber, C., Götz, M., Binczyck, F., Polanska, J., Tarnawski, R., Bobek-Billewicz, B., Meinzer, H.-P., Stieltjes, B. and Maier-Hein, K. [2015], 'Überwachtes Lernen zur Prädiktion von Tumorwachstum.', in *Bildverarbeitung für die Medizin 2015*, Springer, pp. 473–478.

Weber, D. C., Casanova, N., Zilli, T., Buchegger, F., Rouzaud, M., Nouet, P., Vees, H., Ratib, O., Dipasquale, G. and Miralbell, R. [2009], 'Recurrence pattern after [(18) F] fluoroethyltyrosine-positron emission tomography-guided radiotherapy for high-grade glioma: a prospective study.', *Radiotherapy and Oncology* **93**(3), 586–592.

Weber, D. C., Zilli, T., Buchegger, F., Casanova, N., Haller, G., Rouzaud, M., Nouet, P., Dipasquale, G., Ratib, O., Zaidi, H. et al. [2008], '[(18) F] Fluoroethyltyrosine-positron emission tomography-guided radiotherapy for high-grade glioma.', *Radiation Oncology* **3**(1), 1.

Weckesser, M., Langen, K., Rickert, C., Kloska, S., Straeter, R., Hamacher, K., Kurlemann, G., Wassmann, H., Coenen, H. and Schober, O. [2005], 'O-(2-[18F] fluorethyl)-L-tyrosine

PET in the clinical evaluation of primary brain tumours.', *European Journal of Nuclear Medicine and Molecular Imaging* **32**(4), 422–429.

Weinmann, H., Laniado, M. and Mützel, W. [1983], 'Pharmacokinetics of GdDTPA/dimeglumine after intravenous injection into healthy volunteers.', *Physiological Chemistry and Physics and Medical NMR* **16**(2), 167–172.

Wester, H. J., Herz, M., Weber, W., Heiss, P. et al. [1999], 'Synthesis and radiopharmocology of 0-(2-[18F] fluoroethyl)-L-Tyrosine for tumor imaging.', *The Journal of Nuclear Medicine* **40**(1), 205.

Wetzel, S. G., Johnson, G., Tan, A. G., Cha, S., Knopp, E. A., Lee, V. S., Thomasson, D. and Rofsky, N. M. [2002], 'Three-dimensional, T1-weighted gradient-echo imaging of the brain with a volumetric interpolated examination.', *American Journal of Neuroradiology* **23**(6), 995–1002.

WHO Cancer Fact Sheet N° 297 [2015], Accessed on: 02/10/2016. `http://www.who.int/mediacentre/factsheets/fs297/en/`.

Wolf, I. [2010], 'Toolkits and software for developing biomedical image processing and analysis applications.', in *Biomedical Image Processing*, Springer, pp. 521–544.

Wolf, I., Vetter, M., Wegner, I., Böttger, T., Nolden, M., Schöbinger, M., Hastenteufel, M., Kunert, T. and Meinzer, H.-P. [2005], 'The medical imaging interaction toolkit.', *Medical Image Analysis* **9**(6), 594–604.

Yaqub, M., Boellaard, R., Kropholler, M. A. and Lammertsma, A. A. [2006], 'Optimization algorithms and weighting factors for analysis of dynamic PET studies.', *Physics in Medicine and Biology* **51**(17), 4217.

Zaidi, H. and El Naqa, I. [2010], 'PET-guided delineation of radiation therapy treatment volumes: a survey of image segmentation techniques.', *European Journal of Nuclear Medicine and Molecular Imaging* **37**(11), 2165–2187.

Zitron, I. M., Kamson, D. O., Kiousis, S., Juhász, C. and Mittal, S. [2013], 'In vivo metabolism of tryptophan in meningiomas is mediated by indoleamine 2, 3-dioxygenase 1.', *Cancer Biology & Therapy* **14**(4), 333–339.

Zöllner, F. G., Daab, M., Sourbron, S. P., Schad, L. R., Schoenberg, S. O. and Weisser, G. [2016], 'An open source software for analysis of dynamic contrast enhanced magnetic resonance images: UMMPerfusion revisited.', *BMC Medical Imaging* **16**(1), 1.

List of Figures

List of Tables

Acknowledgements

An dieser Stelle möchte ich die Gelegenheit nutzen und mich bei all jenen herzlich bedanken, die mir in den letzten 3 Jahre geholfen und mich unterstützt haben, und damit zum Gelingen dieser Arbeit beigetragen haben.

Zuallererst möchte ich meinem Doktorvater Prof. Jürgen Debus danken, der trotz seines vollen Terminkalenders immer Zeit fand, mir bei Fragen weiterzuhelfen. Zudem bedanke ich mich bei meinem Gruppenleiter Amir Abdollahi für die Unterstützung und Betreuung der letzten drei Jahre.

Prof. Oliver Jäckel danke ich für die fachliche Unterstützung, insbesondere von physikalischer Seite, und einige wertvolle Anregungen und Ideen für Studien.

Zwei Menschen haben maßgeblich zum Gelingen dieser Arbeit beigetragen. Mit ihrem Rat standen sie mir immer zur Seite, haben bei Projekten geholfen, mir viel beigebracht und dabei nie die Geduld verloren.

Deshalb danke ich Ralf Floca, der sich mit mir in das Abenteuer “Perfusions-Modellierung” gestürzt hat. Er hat mir fast alles über Softwaredesign und objektorientiertes Programmieren beigebracht, was ich heute weiß, und mir in vielen mühsamen Stunden Revision und Diskussion geholfen, das MITK “Dynamic Data Modeling“ Software Tool zu dem zu machen, was es heute ist. Danke Ralf!

Zum anderen danke ich Michael Ingrisch, der mir die physikalischen Grundlagen der Perfusions-Bildgebung, mit all ihren Vorzügen wie auch Tücken, nahegebracht hat und immer mir mit seinem Fachwissen immer zur Seite stand, wenn ich mich auf den Irrwegen des Publikationsdschungels verlaufen hatte. Du warst immer nur einen Anruf entfernt, wenn ich kurz vorm Verzweifeln war und deine Anregungen, Diskussionen und Ratschläge haben mir immer geholfen, wenn ich nicht mehr weiter wusste. Danke Michi!

Ich möchte mich außerdem bei Ali Afshar-Orohmie für seine Hilfe und Expertise im Bereich der PET Bildgebung bedanken. Ich danke auch meiner Arbeitsgruppe, der Abteilung für translationale Radioonkologie, und insbesondere meinem Büronachbarn Maximilian Knoll. Sein weitreichendes medizinisches Fachwissen und Grundverständnis für Informatik waren in vielen anregenden Gesprächen und fachlichen Diskussionen hilfreich.

Außerdem bedanke ich mich bei den Mitgliedern der Abteilung “Medizinische Physik in der Radiologie” des DKFZ und meiner Adoptiv-Arbeitsgruppen am 7 Tesla MRT für viele schöne Mittags- und Kaffeepausen, erlebnisreiche Fußballspiele und eine tolle Konferenz. Vor allem danke ich Kristian Rink und Vanessa Stahl für ihr Engagement, mir die Grundlagen der MRT und ein Minimum an praktischem Wissen zu vermitteln.

Stellvertretend für die Abteilung “Medizinische und Biologische Informatik” des DKFZ und das MITK Team danke ich Marco Nolden. Ein besonderer Dank für ihre Hilfe in allen

Softwarefragen gilt Andreas Fetzer und Christian Weber. Stellvertretend für das Team der Medizinphysik am HIT möchte ich mich bei Malte Ellerbrock bedanken. Für Ihre Unterstützung und Hilfe danke ich außerdem Nina Bougatf und Andrea Mairani.

Natürlich danke ich auch all meinen Freunden und Bekannten die mich durch mein Physik Studium und die Promotion begleitet haben und die letzten 9 Jahre in Heidelberg unvergesslich gemacht haben.

Last but not least danke ich natürlich meiner Familie für all die liebevolle Unterstützung während Promotion und Studium. Ohne sie wäre all dies niemals möglich gewesen.

Erklärung

Ich versichere, dass ich diese Arbeit selbstständig verfasst habe und keine anderen als die angegebenen Quellen und Hilfsmittel benutzt habe.

Heidelberg, den 02. Mai 2016 .....